

Washington University in St. Louis

## Washington University Open Scholarship

---

All Theses and Dissertations (ETDs)

---

January 2009

### Oxygen-Enhanced Combustion: Theory and Applications

Scott Skeen

*Washington University in St. Louis*

Follow this and additional works at: <https://openscholarship.wustl.edu/etd>

---

#### Recommended Citation

Skeen, Scott, "Oxygen-Enhanced Combustion: Theory and Applications" (2009). *All Theses and Dissertations (ETDs)*. 325.

<https://openscholarship.wustl.edu/etd/325>

This Dissertation is brought to you for free and open access by Washington University Open Scholarship. It has been accepted for inclusion in All Theses and Dissertations (ETDs) by an authorized administrator of Washington University Open Scholarship. For more information, please contact [digital@wumail.wustl.edu](mailto:digital@wumail.wustl.edu).

WASHINGTON UNIVERSITY IN ST. LOUIS  
School of Engineering and Applied Science  
Department of Energy, Environmental, and Chemical Engineering

Dissertation Examination Committee:

Richard L. Axelbaum, Chair

Ramesh K. Agarwal

Pratim Biswas

Raimo J. Hakkinen

Himadri B. Pakrasi

Jay R. Turner

OXYGEN-ENHANCED COMBUSTION: THEORY AND APPLICATIONS

by

Scott A. Skeen

A dissertation presented to the School of Engineering  
of Washington University in partial fulfillment of the  
requirements for the degree of

DOCTOR OF PHILOSOPHY

August 2009  
Saint Louis, Missouri

## ABSTRACT OF THE DISSERTATION

Oxygen-Enhanced Combustion: Theory and Applications

by

Scott A. Skeen

Doctor of Philosophy in Energy, Environmental, and Chemical Engineering

Washington University in St. Louis, 2009

Research Advisor: Professor Richard L. Axelbaum

In the broadest sense, oxygen-enhanced combustion (OEC) refers to the use of oxygen to improve combustion and/or process characteristics. When a stream of oxygen is available, a wide range of flame configurations is possible. This work considers two specific configurations of OEC and is divided into two parts. In Part I, fundamental experimental and numerical flame studies explore the combustion of gaseous fuel/inert mixtures in oxygen-enriched air or pure oxygen under well-defined conditions. Part II targets a more practical application by considering the combustion of solid fuels in a variety of oxygen/carbon dioxide mixing scenarios.

For gaseous non-premixed flames, combining fuel-dilution with oxygen-enrichment can dramatically alter the flame structure (i.e. the relationship between the local temperature and local species concentrations). The extent of fuel-dilution and oxygen-enrichment can be quantified by the stoichiometric mixture fraction,  $Z_{st}$ , with fuel/air flames characterized by

$Z_{st}$  values closer to zero and diluted-fuel/oxygen flames characterized by  $Z_{st}$  values closer to unity. Changes in flame structure resulting in less fuel and more oxygen in the region of high temperature have been identified as the primary cause for reduced soot formation in high  $Z_{st}$  flames. Local temperature-species relationships resulting in soot-free conditions have been shown to correlate with a single conserved scalar, the local atomic carbon-to-oxygen ratio (C/O). A simple model has been developed suggesting that for soot-free conditions to exist, the local C/O ratio and local temperature must be below critical values, i.e.  $C/O < (C/O)_{cr}$  and  $T < T_{cr}$ . For high  $Z_{st}$  flames, the local critical C/O ratio was associated with the increased presence of oxidizing species on the fuel side of the flame. This argument was supported by experimental and numerical results showing that for high  $Z_{st}$  flames appreciable concentrations of molecular oxygen are observed at the location of maximum temperature ( $x_{T_{max}}$ ). Nevertheless, the significance of the local critical C/O ratio has not been fully explained and the role of oxidizing species on the fuel side of the flame in soot suppression has not been verified. Moreover, the mechanisms responsible for the presence of appreciable oxygen at the location of maximum temperature in high  $Z_{st}$  flames have not been evaluated. These issues are addressed in Part I of this work.

In Part I, coflow flame experiments were performed to compare and evaluate the influence of flame structure on soot formation when operating under normal and inverse flame conditions. Flame structure was shown to influence soot formation in a similar fashion for normal and inverse flames when the effects of residence time were removed. The simple model previously discussed was modified to account for finite-rate chemistry and residence time effects, and was correlated with experimental data leading to the determination of the critical local temperature and critical local C/O ratio for soot inception in ethylene flames.

The presence of appreciable oxygen at the location of maximum temperature was investigated using a flame code with detailed chemistry. The mechanisms responsible for  $O_2$  at  $x_{T_{max}}$  in high  $Z_{st}$  flames were determined and explained. This phenomenon was attributed to a shifting of the location of maximum temperature relative to the location of oxygen depletion, and the temperature shift was explained by considering the variations in the heat release profile at high  $Z_{st}$ .

A second numerical investigation was also conducted to evaluate the significance of the local critical C/O ratio as a parameter describing soot-free conditions, the role of oxidizing species at this location, and changes that occur in the chemical pathway to the formation of soot precursors at high  $Z_{st}$ . The critical local C/O ratio was shown to correspond to the edge of the radical pool for flames of any  $Z_{st}$ , and oxidizing species did not appear to accelerate soot precursor oxidation at high  $Z_{st}$  as previously thought. A reverse pathway analysis was used to determine the dominant chemical pathway leading to the formation of soot precursors. At high  $Z_{st}$ , a key soot precursor formation step was observed to reverse leading to the destruction of propargyl ( $C_3H_3$ ) to form acetylene ( $C_2H_2$ ) as opposed to benzene ( $C_6H_6$ ) and phenyl ( $C_6H_5$ ). The existence of soot-free flames at long residence times was attributed to this phenomenon.

In Part II of this work, a form of OEC currently being considered as an enabling technology for carbon dioxide capture from pulverized coal (PC) utility plants, termed *oxy-fuel combustion*, was considered. Oxy-fuel combustion utilizes oxygen and recycled flue gases (RFG) as the oxidizer instead of air, therefore the concentration of oxygen in the coal carrier stream, as well as any other concentric stream or quiescent environment, is a variable. The viability of oxy-fuel combustion can be enhanced by its ability to reduce capital and

operational costs by, for example, lowering the emissions of nitrogen oxide species (NO<sub>x</sub>) in situ. Studies have demonstrated that oxy-fuel combustion can lower NO<sub>x</sub> emissions by as much as 70% when compared to conventional coal/air combustion, largely due to the reduction of recycled NO<sub>x</sub> to molecular nitrogen when interacting with hydrocarbon species in the flame.

This work investigates the potential for reduced NO<sub>x</sub> emissions under oxy-fuel conditions through variations in the gas composition of the fuel carrier and concentric oxidizer streams. Nitric oxide (NO) emissions were measured during the combustion of PC and PC/sawdust mixtures under air-fired and oxy-fuel conditions. The effects of excess oxygen, secondary oxidizer swirl, carrier gas flow rate, and sawdust cofiring on NO emissions were investigated. Under oxy-fuel conditions, the effect of varying the compositions of the carrier gas and concentric oxidizer streams on NO emissions was also investigated. Under the optimal oxy-fuel conditions, NO emissions were reduced by 20% when compared to air-firing. Cofiring coal with sawdust that contained less fuel bound nitrogen did not reduce the NO emissions under air-fired or oxy-fuel conditions. Changing the adiabatic flame temperature by varying the oxygen concentration in the concentric oxidizer stream did not significantly influence NO emissions until the temperature was too low and flame instabilities were observed. When increasing the oxygen concentration in the coal carrier gas a critical local stoichiometric ratio was observed that led to increased NO emissions.

# Acknowledgments

This work was funded by the National Aeronautics and Space Administration and the United States Department of Energy under the University Coal Research Program.

Deep gratitude is expressed to my advisor Dr. Richard L. Axelbaum for providing me the opportunity to perform this work and for his guidance, support, and tremendous insights.

I would also like to thank the members of my dissertation committee Professors Ramesh K. Agarwal, Pratim Biswas, Raimo J. Hakkinen, Himadri B. Pakrasi, and Jay R. Turner. The assistance and support of my colleagues in the Laboratory for Advanced Combustion and Energy Research is also acknowledged.

Special thanks is given to Dr. Ben M. Kumfer, who developed the soot inception model presented in Chapter 4, and who provided assistance during the construction and operation of the coal system. Gratitude is also expressed to Yosef Santer for his tremendous contributions to the coal system and experiments.

Scott A. Skeen

*Washington University in St. Louis*

*August 2009*

Dedicated to Stefanie, Saida, and Harmon, who make every day bright.



# Contents

<b>Abstract .....</b>	<b>ii</b>
<b>Acknowledgments.....</b>	<b>vi</b>
<b>Contents .....</b>	<b>viii</b>
<b>List of Tables .....</b>	<b>xi</b>
<b>List of Figures .....</b>	<b>xii</b>
<b>1 Introduction.....</b>	<b>1</b>
<b>2 Research Objectives.....</b>	<b>7</b>
2.1 Part I Objectives.....	8
2.2 Part II Objectives .....	9
<b>Part I Fundamental Non-Premixed Gaseous Flame Studies.....</b>	<b>11</b>
<b>3 Background.....</b>	<b>12</b>
3.1 Non-premixed Combustion of Gaseous Fuels.....	12
3.1.1 Equilibrium Flame Structure.....	13
3.1.2 Soot.....	18
3.1.3 Flame Structure and Soot Formation .....	20
<b>4 Measuring and Modeling Soot Inception Limits in Laminar Diffusion Flames .....</b>	<b>25</b>
4.1 Introduction .....	25
4.2 Experimental Methods .....	28
4.3 Results and Discussion.....	31
4.4 Conclusions.....	47
<b>5 Structural Changes in OEC Resulting in the Presence of Appreciable Oxygen at the Location of Maximum Temperature .....</b>	<b>49</b>
5.1 Introduction .....	49
5.2 Numerical .....	51
5.3 Preliminary analysis: comparing the detailed chemistry with the flame sheet approximation .....	53
5.4 Results and Discussion.....	55

5.4.1 Characterizing oxygen depletion .....	55
5.4.2 Maximum temperature shift at high $Z_{st}$ .....	58
5.5 Conclusions.....	70
<b>6 Structural Effects on Soot Precursor Kinetics Resulting in Soot-Free Flames .....</b>	<b>72</b>
6.1 Introduction .....	72
6.2 Numerical .....	73
6.3 Results and Discussion.....	74
6.4 Conclusions.....	92
<b>Part II Air-Fired and Oxy-Fuel Combustion of Coal and Coal/Biomass Mixtures ...</b>	<b>94</b>
<b>7 Background .....</b>	<b>95</b>
7.1 Coal.....	96
7.1.1 Coal Formation and Characterization .....	96
7.1.2 Coal Usage and Resources.....	96
7.1.3 Coal and Global Climate Change.....	97
7.1.4 Oxy-Coal Combustion for CCS .....	99
7.2 Biomass.....	102
7.2.1 Biomass Resources .....	103
7.2.2 Oxy-Coal/Biomass Cofiring.....	105
7.3 Physical Processes of Solid Fuel Combustion .....	108
7.3.1 Heating and Drying.....	108
7.3.2 Devolatilization.....	108
7.3.3 Volatiles Oxidation.....	109
7.3.4 Char Oxidation .....	110
7.3.5 Ignition and Flame Stability .....	112
7.4 Nitrogen Oxides.....	115
7.4.1 Thermal NO <sub>x</sub> .....	115
7.4.2 Prompt NO <sub>x</sub> .....	116
7.4.3 Fuel NO <sub>x</sub> .....	116
7.4.4 Conventional NO <sub>x</sub> Reduction Strategies.....	117
7.4.5 Oxy-Fuel Combustion for NO <sub>x</sub> Reduction .....	119
7.4.6 Biomass Cofiring for NO <sub>x</sub> Reduction .....	124
7.5 Summary.....	126
<b>8 Nitric Oxide Emissions from Coal and Coal/Biomass Combustion Under Air-Fired and Oxy-Fuel Conditions.....</b>	<b>127</b>
8.1 Introduction .....	127
8.2 Experimental.....	132
8.3 Results and Discussion.....	140

8.3.1 Air-fired Conditions .....	140
8.3.2 Summary of Air-fired Results .....	148
8.3.3 Oxy-fuel Conditions.....	149
8.4 Conclusions .....	159
<b>9 Summary and Recommendations .....</b>	<b>163</b>
9.1 Part I Summary.....	163
9.2 Part I Recommendations.....	165
9.3 Part II Summary .....	166
9.4 Part II Recommendations.....	169
9.4.1 System Modifications .....	169
9.4.2 Future Work .....	170
<b>Appendix A Flame Equilibrium Formulation .....</b>	<b>173</b>
<b>Appendix B Reaction Mechanism Used in Chapter 6.....</b>	<b>179</b>
<b>Appendix C 30 kWth Coal Combustor Standard Operating Procedure (SOP).....</b>	<b>200</b>
C.1 Preliminaries .....	200
C.2 Ignition.....	200
C.3 Coal Delivery.....	201
C.4 Shutdown.....	201
<b>References .....</b>	<b>203</b>
<b>Curriculum Vitae.....</b>	<b>212</b>

# List of Tables

Table 4.1. Input parameters for sooting limit flames.....	32
Table 4.2. Selected properties of sooting limit flames .....	35
Table 5.1. Flame Parameters.....	53
Table 5.2. Dominant reactions in four different heat zones.....	63
Table 6.1. Flame parameters .....	74
Table 7.1. Potential biomass resources adapted from refs. [23, 24].....	104
Table 8.1. Fuel properties.....	138
Table 8.2. Summary of experimental operating conditions .....	139

# List of Figures

Figure 3.1. Illustration of equilibrium structure of (a) ethylene/air $Z_{st} = 0.064$ and (b) diluted-ethylene/oxygen $Z_{st} = 0.78$ flames at $T_{ad} = 2370$ K. Filled area indicates the region of high temperature ( $T/T_{ad} \geq 0.7$ ). .....	18
Figure 3.2. Schematic of counterflow flames at (a) $Z_{st} = 0.064$ (ethylene/air) and (b) $Z_{st} = 0.78$ (diluted-ethylene/oxygen) .....	23
Figure 4.1. Schematic diagram of burner for normal and inverse coflow flames. ....	29
Figure 4.2. Photographs of (a) normal and (b) inverse sooting limit flames. The sooting limit is observed at a height of 8 mm from the burner tip. ....	30
Figure 4.3. Sooting limit flame temperature vs stoichiometric mixture fraction for normal and inverse flames. Case 1: Constant flame height of 16 mm. ....	33
Figure 4.4. Sooting limit flame temperature vs stoichiometric mixture fraction for normal and inverse flames. Case 2: Constant gas exit velocity. ....	36
Figure 4.5. Comparison of measured inverse flame sooting limits and the model (line) obtained with $E_a = 31$ kcal/mol; $C_0 = 780$ K <sup>-1</sup> s <sup>-1</sup> , $\tau = 22.4$ ms and $(C/O)_{cr} = 0.53$ . ....	41
Figure 4.6. Representation of the collapse of the soot formation zone with increasing $Z_{st}$ . ....	42
Figure 4.7. Flame sheet approximation results for Cases 1, 2, and 3 from Fig. 4.6 showing shrinking of soot formation zone due to convergence of low-temperature ( $T_{kin}$ ) and low C/O ratio (high-temperature $T_{C/O}$ ) boundaries. ....	45
Figure 4.8. Representation of the sooting zones of four flames with varying flame temperatures. ....	47
Figure 5.1. Flame sheet approximation (solid) and numerical solution (dash-dot) for (a) ethylene/air ( $Z_{st} = 0.064$ ) and (b) diluted-ethylene/oxygen ( $Z_{st} = 0.78$ ). ....	55
Figure 5.2. Oxygen mole fraction and net rate of oxygen consumption for flames at (a) $Z_{st} = 0.064$ , (b) $Z_{st} = 0.4$ , and (c) $Z_{st} = 0.78$ . Filled arrow indicates $x_{Z_{st}}$ . Open-faced arrow indicates $x_{T_{max}}$ . ....	56
Figure 5.3. Rates of reactions 5.1R, 5.2R, and 5.3R for (a) fuel/air $Z_{st} = 0.064$ , (b) $Z_{st} = 0.4$ , and (c) diluted-fuel/oxygen $Z_{st} = 0.78$ . Filled arrow indicates $x_{Z_{st}}$ . Open-faced arrow indicates $x_{T_{max}}$ . ....	58
Figure 5.4. Total heat release rate for (a) fuel/air $Z_{st} = 0.064$ , (b) $Z_{st} = 0.4$ , and (c) diluted-fuel/oxygen $Z_{st} = 0.78$ . Filled arrow indicates $x_{Z_{st}}$ . Open-faced arrow indicates $x_{T_{max}}$ . ....	60

Figure 5.5. Four zones of heat release for (a) fuel/air $Z_{st} = 0.064$ , (b) $Z_{st} = 0.4$ , and (c) diluted-fuel/oxygen $Z_{st} = 0.78$ . $Q_{ex(i)}$ represents the summation of the heat released by the exothermic reactions associated with Zone (i). $Q_{en(i)}$ represents the summation of the heat consumed by the endothermic reactions associated with Zone (i). .....	62
Figure 5.6. Heat release from reactions 5.1R and 5.2R for (a) fuel/air $Z_{st} = 0.064$ , (b) $Z_{st} = 0.4$ , and (c) diluted-fuel/oxygen $Z_{st} = 0.78$ . .....	64
Figure 5.7. Rates of $O_2$ destruction and production by reactions 5.4R and 5.5R for (a) fuel/air $Z_{st} = 0.064$ , (b) $Z_{st} = 0.4$ , and (c) diluted-fuel/oxygen $Z_{st} = 0.78$ . .....	65
Figure 5.8. Superposition of temperatures resulting from two displaced heat sources for (a) low $Z_{st}$ flame (b) high $Z_{st}$ flame. Filled arrow indicates $x_{Z_{st}}$ . .....	67
Figure 5.9. Comparison of temperature profiles from the detailed numerical model and that resulting from the superposition of temperatures based on three point source heat zones for (a) the low $Z_{st}$ (fuel/air) flame and (b) the high $Z_{st}$ (diluted-fuel/oxygen) flame. Filled arrow indicates $x_{Z_{st}}$ . .....	69
Figure 6.1. Computed temperature and species profiles for (a) Flame A (fuel/air, $Z_{st}=0.064$ ) and (b) Flame I (diluted-fuel/oxygen, $Z_{st}=0.78$ ). Arrow indicates the location of the stagnation point. Asterisk indicates the mole fraction of ethylene at 1600 K. ....	75
Figure 6.2. Concentration profiles of OH, O, H, $O_2$ , and $C_2H_2$ along with temperature in C/O ratio space for (a) Flame A (low $Z_{st}$ ) and (b) Flame I (high $Z_{st}$ ). The dashed lines indicate the region between $0.5 \leq C/O \leq 0.6$ . ....	77
Figure 6.3. Diagram showing all phenyl producing reactions in [137]. .....	79
Figure 6.4. Relative contribution of individual phenyl producing reactions to total phenyl production rate. ....	80
Figure 6.5. Graphical representation of dominant propargyl formation reactions. ....	80
Figure 6.6. Dominant pathways to benzene and phenyl at (a) $Z_{st} = 0.064$ and (b) $Z_{st} = 0.78$ . Note: * indicates an activated or energized species. ....	81
Figure 6.7. Natural log of the total acetylene concentration in the flame vs natural log of free-stream fuel mole fraction. The linear regression fitted to points from flames with similar scalar dissipation rates in the region of interest indicates that the total acetylene is proportional to the free-stream fuel concentration. ....	82
Figure 6.8. Mixture fraction in physical space showing the variation with increasing $Z_{st}$ . Changing $Z_{st}$ can result in different local mixture fraction gradients in the reaction region. ....	83
Figure 6.9. Contribution to total net acetylene production from selected reactions vs. $Z_{st}$ . ....	85
Figure 6.10. Contribution to total net acetylene destruction from selected reactions vs. $Z_{st}$ . ....	86

Figure 6.11. Natural log of total propargyl concentration in the flame vs natural log of free-stream fuel mole fraction.....	87
Figure 6.12. Contribution to total net propargyl production from selected reactions vs. $Z_{st}$ .....	89
Figure 6.13. Contribution to total net propargyl destruction from selected reactions vs. $Z_{st}$ .....	90
Figure 6.14. Rate profiles for reactions 6.8R and 6.12R, H mole fraction profile, and temperature profile in physical space for (a) Flame A, (b) Flame C, (c) Flame D, and (d) Flame I. ....	91
Figure 7.1. Flow diagram comparing conventional air-fired coal combustion with MEA absorption for CO <sub>2</sub> separation with an idealized oxy-coal combustion unit adapted from Buhre et al. [18]. ....	101
Figure 8.1. Schematic of horizontal 30 kWth combustor. ....	133
Figure 8.2. Schematic of experimental burner. ....	134
Figure 8.3. Continuous O <sub>2</sub> , NO and exhaust temperature measurements following ignition under air-fired conditions at 30 kWth. ....	138
Figure 8.4. SEM images of fly ash collected during steady-state operation of the laboratory-scale coal combustor at 30 kWth. ....	139
Figure 8.5. Nitric oxide measured in exhaust under air-fired conditions with 16 vol.% excess air as a function of thermal input. ....	142
Figure 8.6. Nitric oxide measured in exhaust vs. % SO swirl under air-fired conditions with 16 vol.% excess air. ....	143
Figure 8.7. Nitric oxide measured in exhaust vs. primary oxidizer stream velocity. ....	144
Figure 8.8. NO emissions vs. the global stoichiometric ratio, $\lambda$ , under air-fired conditions at 30 kWth. ....	145
Figure 8.9. NO emissions vs. % sawdust cofired under air-fired conditions. ....	147
Figure 8.10. Photographs of primary tube exit as seen through the burner ignition port showing (a) attached flame (b) detached or lifted flame. The bright yellow luminance observed near the PO exit in (a) is not observable in (b) because the flame has moved downstream out of the field of view. (Note: aperture and shutter speed settings were identical for both photographs.).....	147
Figure 8.11. Nitric oxide and carbon monoxide measured in exhaust vs. stoichiometric ratio under oxy-fuel conditions at 30 kWth with 30% O <sub>2</sub> and 70% CO <sub>2</sub> in the PO and SO streams. ....	150
Figure 8.12. Nitric oxide emissions vs. % SO swirl at 30 kWth.....	152
Figure 8.13. Nitric oxide emissions and maximum near burner temperature ( $T_{nb}$ ) (not corrected for radiative loss) vs. adiabatic flame temperature (lower abscissa) and vol.% O <sub>2</sub> in the SO stream (upper abscissa) .....	154

Figure 8.14. NO emissions vs. mass percentage of sawdust cofired with coal at a thermal input of 30 kW, 100% SO swirl, and 3 vol.% O <sub>2</sub> measured in the exhaust.....	156
Figure 8.15. NO emissions under oxy-fuel conditions while varying gas composition in the PO and SO streams at constant adiabatic flame temperature and 3% O <sub>2</sub> in the exhaust effluent.....	157
Figure 8.16. NO emission vs. thermal input and $\lambda_{PO}$ for non-swirling oxy-fuel flames at the same adiabatic flame temperature with 40 vol.% O <sub>2</sub> in the PO and 27 vol.% O <sub>2</sub> in the SO and 3 vol.% O <sub>2</sub> measured in the exhaust. ....	159



# 1 Introduction

While combustion can be considered the oldest technology of mankind, the complex processes involved in even a simple candle flame continue to intrigue and perplex modern scientists. Michael Faraday, one of the greatest scientists of the 19<sup>th</sup> century, introduced his first lecture on the chemical history of a candle by saying, “There is not a law under which any part of this universe is governed which does not come into play and is touched upon in these phenomena. There is no better, there is no more open door by which you can enter into the study of natural philosophy than by considering the physical phenomena of a candle.” [1]. Indeed combustion is a rich and challenging field of study involving fluid mechanics, transport, thermodynamics, chemical kinetics, radiation, and turbulence. And yet, for all of the physical complexities associated with studying combustion science, it could be argued that there is no simpler way to produce heat, light, and electricity than by the burning of a hydrocarbon fuel in air. As a consequence, the combustion of fossil fuels has been, and remains the dominant source of primary worldwide energy production.

Unfortunately, many of the by-products of fossil fuel combustion can be detrimental to the environment and human health if released into the atmosphere. Particulate matter (PM) such as soot, which forms during fuel-rich premixed combustion or in many conventional non-premixed combustion scenarios, has been linked to respiratory illnesses, cancer, and death. Nitric oxide (NO) and nitrogen dioxide (NO<sub>2</sub>), which can be formed from both the oxidation of molecular nitrogen (N<sub>2</sub>) in the combustion air and the oxidation of nitrogen found in most solid fuels, can lead to acid rain and photochemical smog, while nitrous oxide (N<sub>2</sub>O) is a greenhouse gas (GHG) capable of influencing the balance of heat

within the earth's atmosphere. A key feature of the pollutants mentioned above along with other common combustion pollutants such as sulfur dioxide (SO<sub>2</sub>), carbon monoxide (CO), and unburned hydrocarbons (UHCs) is that they are typically found in concentrations on the parts-per-million (PPM) scale and can be reduced or even eliminated in some cases without a crippling economic penalty by combustion modifications or post-combustion treatment of the exhaust gases. On the other hand, carbon dioxide (CO<sub>2</sub>), which is a greenhouse gas and a main product of fossil fuel combustion, cannot be avoided by combustion modifications and is expensive to capture from both a capital and operational cost perspective. Moreover, in April of 2009 the Environmental Protection Agency categorized carbon dioxide (CO<sub>2</sub>) along with five other key greenhouse gases as a danger to "the public health and welfare of current and future generations through climate change" [2].

Heightened awareness and concern among all facets of society regarding the environmental impacts of energy derived from fossil fuel combustion, especially the threat of global climate change due to increased CO<sub>2</sub> in the atmosphere, has elevated efforts among researchers and industry to further develop and use carbon-neutral or carbon-free energy sources such as biofuels, wind turbines, solar thermal, and solar photovoltaics. Nevertheless, in 2007 only 7% of the total energy supplied in the U.S. came from renewable sources, with 3.7% of this generated from biomass, 2.5% from hydroelectric, 0.35% each from geothermal and wind, and only 0.07% from solar voltaics and solar thermal combined [3]. Thus, even with the growing interest and support for renewable energy technologies analysts have concluded that global energy needs in the foreseeable future will continue to be met predominantly by fossil fuels [4, 5]. As such, there is a need to better address the combustion by-products and pollutants that have been regulated and those, such as carbon dioxide (CO<sub>2</sub>)

that may soon be regulated. One of the technologies with the potential to address both pollutant reduction and CO<sub>2</sub> capture is oxygen-enhanced combustion (OEC).

In general, oxygen-enhanced combustion refers to the use of an oxidizer stream containing a higher O<sub>2</sub> concentration than that in air (>21% vol.). Baukal [6] reported in 1998 that there are four common techniques for implementing OEC in industrial heating processes, namely: air enrichment, oxygen lancing, oxy/fuel (or oxy-fuel), and air-oxy/fuel. Air enrichment refers to the addition of oxygen to the combustion air prior to mixing the fuel with the oxidizer, oxygen lancing involves strategically placed ports inside the combustion chamber where oxygen is introduced, oxy/fuel refers to the use of pure oxygen as the oxidizer, and air-oxy/fuel is a hybrid of the three previous methods in which air and oxygen are injected separately through the burner.

From a historical perspective, oxygen's potential for improving the combustion process in steel production was recognized by Bessemer in 1855; however, the earliest record of oxygen usage in this process was not until 1931. By the 1960s and 70s the use of oxygen enhanced combustion in both ferrous and non-ferrous metallurgical industries was commonplace, while nearly all facets of the glass industry had implemented a form of OEC by the 1990s [6]. In the late 1980s OEC proved beneficial in waste incineration, and reports sponsored by the Department of Energy (DOE) in 1987 [7] and the Gas Research Institute in 1989 [8] indicated that the use of OEC would be increasingly important in the future.

In the processes mentioned above, the potential benefits of OEC over conventional air-fired combustion include [6]:

- increased thermal efficiency, processing rates, and productivity as the chemical energy released from the fuel is transferred at a higher rate to the raw materials;

- reduced flue gas volume (since some or all of the  $N_2$  has been removed from the system) leading to lower capital equipment costs for flue gas ductwork and flue gas cleanup equipment;
- reduced pollutant emissions since the combustion process can be modified to minimize pollutants in situ and lower flue gas volumes leading to higher pollutant concentrations making their capture more efficient;
- improved flame stability, turndown ratio, and ignition characteristics, as elevated  $O_2$  concentrations result in higher near-burner temperatures and enhanced kinetics; and
- greater fuel and material flexibility since low heating value fuels can be utilized and the extremely high processing temperatures required for certain materials can be achieved.

Although full commercial deployment of OEC has been largely limited to industrial heating processes for the production of materials, OEC technologies are being considered in transportation and electricity generation applications as well. For example, OEC has been investigated as a method to improve performance and reduce particulate emissions in gasoline and diesel engines [9-17] and oxy-fuel combustion with flue gas recycle (FGR) has been identified as an enabling technology for  $CO_2$  capture from coal-fired power plants while incorporating many of the benefits listed above [18]. One factor that may influence the economics when considering oxy-fuel combustion for post-flame  $CO_2$  capture, as opposed to exhaust scrubbing techniques (e.g. amine absorption), is the ability of oxy-fuel technology to reduce nitrogen oxide ( $NO_x$ ) levels in situ such that  $NO_x$  flue gas cleanup equipment can be greatly scaled back or completely eliminated resulting in capital and operational cost

savings. Laboratory and pilot-scale studies have demonstrated NO<sub>x</sub> reductions as high as 70% with oxy-fuel combustion; however, the mechanisms responsible for this reduction are not completely understood, making NO<sub>x</sub> formation in oxy-fuel combustion a relevant and timely area of study [19-21].

Another application for oxy-fuel combustion in conjunction with CO<sub>2</sub> capture involves the cofiring of biomass with coal, an approach that would remove CO<sub>2</sub> from the atmosphere. Cofiring studies performed under conventional air-fired conditions have identified economic and environmental benefits as well as many combustion related difficulties, which will be discussed later [22-25]. Because of the flexibility of an oxy-fuel system, it is believed that oxy-fuel combustion can be utilized to address many of the challenges associated with cofiring biomass and coal. Moreover, initiatives at the federal and state level in the United States are seeking to increase the production of energy from renewable sources [26]; and, in many instances the cofiring of biomass in coal fired power plants may be the lowest-cost and highest impact solution in the near-term to meeting the renewables requirements [27].

The potential for increased utilization of OEC has also led to numerous academic studies investigating the effects of OEC on flame characteristics at a fundamental level. For example, several studies have demonstrated that combining oxygen-enrichment with fuel dilution has an inhibitory effect on soot formation [28-38]. While there has been some debate in these studies over the controlling factors, the most recent experimental evidence suggests that fuel-dilution combined with oxygen-enrichment inhibits soot formation through the dramatic changes that occur in the relationship between the local temperature and local species concentrations (i.e. flame structure) [35, 36]. A model has been developed by Sunderland et al. [36] that describes how oxygen-enrichment and fuel dilution influence

the flame structure in the region conducive to soot particle inception in non-premixed flames. While this simple model is able to predict the effects of flame structure on soot inception, many simplifications were made. To advance this model and further the understanding of structural effects on soot formation, finite-rate reactions and the influence of flame structure on detailed chemistry must be considered. Furthermore, the presence of appreciable molecular oxygen at the location of maximum temperature has been observed numerically and experimentally in diluted-fuel/oxygen-enriched flames and this was considered to play an important role in soot suppression by Du and Axelbaum [30] and in flame stability by Chen and Axelbaum [39]. While these studies highlighted the benefits of appreciable oxygen at the location of peak temperature, the phenomenon has not been explained.

The above discussion has highlighted many of the benefits of OEC and introduced some of the fundamental and applied focus areas requiring attention. As the title suggests, the overarching goal of this work is to further the understanding of the effects of OEC at both a fundamental level and in relevant areas of application. Chapter 2 discusses the research objectives of this work in detail.

## 2 Research Objectives

In this work two specific aspects of oxygen-enhanced combustion are investigated: fuel-dilution and oxygen-enrichment in gaseous laminar non-premixed flames, and oxy-fuel combustion of coal and coal/biomass mixtures. Consequently, this work is divided into two parts. Part I addresses fundamental aspects related to the effects of fuel-dilution and oxygen-enrichment on soot formation and flame structure in gaseous laminar non-premixed flames having thermal inputs less than 1 kW. Part II investigates the effects of oxy-fuel combustion with simulated flue gas recycle on nitric oxide emissions in turbulent coal and coal/biomass cofired flames at thermal inputs ranging from 19 kW to 35 kW.

The dissertation is organized as follows: Part I, *Fundamental Non-premixed Gaseous Flame Studies* begins in Chapter 3 with background information on non-premixed flames, flame structure, and soot formation, and a review of the relevant literature. Chapters 4-6 then present the results of the fundamental flame studies performed. Part II, *Air-fired and Oxy-fuel Combustion of Coal and Coal/Biomass Mixtures* begins in Chapter 7 with background information on coal and biomass, a summary of the processes involved in the combustion of solid fuels, and an overview on the formation of nitrogen oxides with a review of the relevant oxy-fuel and biomass cofiring literature. Chapter 8 presents the experimental studies investigating the influence of oxy-fuel combustion and biomass cofiring on NO emissions. A summary of the work and recommendations is provided in Chapter 9.

## 2.1 Part I Objectives

Counterflow flame studies by Kennedy [40], Du et al. [41], Du and Axelbaum [30], and Lin and Faeth [42] have demonstrated the importance of residence time and finite-rate chemistry for soot formation in non-premixed flames. A model developed by Sunderland et al. [36], which describes the structural effects of oxygen-enrichment with fuel dilution on soot formation, does not account for these effects. One objective of this work was to demonstrate and evaluate the influence of finite-rate chemistry on soot formation in non-premixed laminar coflow flames of ethylene and to expand the model of Sunderland et al. to include these effects. Experimental data was also correlated with the updated model to determine empirical constants and evaluate the model's predictive capabilities.

In the work of Du and Axelbaum [30] and Chen and Axelbaum [39] the presence of oxygen at the location of peak temperature for flames having high levels of oxygen-enrichment and fuel dilution was identified and associated with inhibition of soot and improved flame stability, respectively. In subsequent work with these flames, Sun et al. [33] and Cheng et al. [43] verified the presence of appreciable  $O_2$  at the location of peak temperature experimentally using spontaneous Raman spectroscopy. Simplified flame models assuming infinitely fast chemistry, which inherently predict zero  $O_2$  at the location of peak temperature, correlate reasonably well with experimental measurements and detailed numerical modeling results for the fuel/air flame; however, in diluted-fuel/oxygen-enriched flames a more complex description is required. Thus, another objective of this work was to evaluate and explain the key sub-mechanisms responsible for the presence of appreciable oxygen at the location of peak temperature in diluted-fuel/oxygen-enriched flames.



As mentioned above, the increased presence of oxygen in the high temperature region for diluted-fuel/oxygen-enriched flames has been associated with the inhibition of soot formation. However, the effects of changing flame structure through oxygen-enrichment and fuel dilution on the detailed chemistry of soot precursor formation have not been evaluated. This is of particular importance when considering the existence of high temperature soot-free flames at long residence times (i.e. permanently blue flames). In such flames, simplified first-order in fuel kinetics may not capture important changes that occur in the soot precursor chemistry for diluted-fuel/oxygen-enriched flames. Thus, the final objective of Part I was to determine the dominant pathway to the soot precursor species benzene and phenyl, evaluate the concentrations and rates of key intermediates under conventional fuel/air conditions and when combining oxygen-enrichment with fuel dilution, and use this information to explain the phenomenon of permanently blue flames.

## 2.2 Part II Objectives

Under the anticipated carbon cap-and-trade legislation utilities providers emitting CO<sub>2</sub> in excess of predefined limits will be required to pay a monetary penalty by purchasing additional carbon credits. Thus, the economics of any carbon capture and storage scenario will depend upon the costs associated with CCS versus the price of carbon credits. If the cost margins are close, the viability of oxy-coal combustion as an enabling technology for CCS may depend upon its potential for reducing the emission of nitrogen oxides (NO<sub>x</sub>) such that post-combustion NO<sub>x</sub> cleanup equipment is deemed unnecessary. Both laboratory-scale experiments and pilot-scale demonstrations have shown that significant NO<sub>x</sub> reductions are possible due to the reduction of recycled NO<sub>x</sub> by hydrocarbon species, achieving in some cases up to 70% less NO<sub>x</sub> in the exhaust [18, 44-60]. Under oxy-fuel

conditions, a wide range of gas compositions can be set in the primary oxidizer (PO, or fuel carrier gas) and secondary oxidizer (SO) streams since the oxygen and inert (recycled flue gas) streams can be independently controlled. Thus, NO<sub>x</sub> emissions during oxy-fuel combustion could potentially be further reduced if an optimal set of PO and SO gas compositions exists. A key objective of Part II therefore, was to investigate the effect of varying the PO and SO gas compositions on NO emissions in a 30 kWth laboratory-scale unstaged combustor. Preliminary work involved characterizing NO emissions under air-fired conditions to develop a baseline while varying the thermal input, secondary swirl, the primary stream flow rate, and the system stoichiometric ratio (i.e. excess air).

The cofiring of biomass with coal has also been investigated as a means to reduce the net output of CO<sub>2</sub> from coal utility boilers and as a means to reduce NO<sub>x</sub> emissions. While a net reduction in CO<sub>2</sub> output per unit energy produced is essentially guaranteed when cofiring a sustainably produced/harvested biomass with coal (since the CO<sub>2</sub> released during biomass combustion is part of the active carbon cycle), lower NO<sub>x</sub> emissions appear to be achievable only under certain conditions [23, 24]. A second key objective of Part II was to evaluate the effects of cofiring biomass (sawdust) with coal on NO emissions under both air-fired and oxy-fuel conditions. At the time of this work, no cofiring studies considering nitric oxide emissions under oxy-fuel conditions were available in the literature; thus, this work will be the first of its kind.

**Part I**  
**Fundamental Non-Premixed Gaseous**  
**Flame Studies**

## 3 Background

### 3.1 Non-premixed Combustion of Gaseous Fuels

Most practical combustion systems are non-premixed. That is, the fuel and oxidizer remain separated and unreacted except in a thin reaction region where the fuel and oxidizer mix in nearly stoichiometric proportion. The reaction region acts as a sink for the reactant species and a source for product species and heat. As such, non-premixed combustion is characterized by steep temperature and species concentration gradients on both sides of the flame, which can introduce complexity when attempting to understand flame processes at a fundamental level. This complexity however, provides an opportunity to manipulate the flame in ways that are not possible in premixed systems.

For example, changing the free stream reactant concentrations by diluting the fuel with an inert and enriching the air with oxygen in a non-premixed flame can have a significant impact on the relationship between the local temperature and local species concentrations (i.e. flame structure). Moreover, the range of fuel and oxidizer free stream concentrations that will yield a robust flame at standard conditions for a variety of fuels spans an order of magnitude—making non-premixed flames highly flexible [39, 61, 62].

Much work has been done to understand and quantify the effects of combining oxygen-enrichment with fuel dilution on the structure of non-premixed flames. Significant insight can be gained through a simplified approach that assumes one-step, infinitely fast chemistry. Under these assumptions the flame structure is representative of equilibrium flow conditions [63]. Section 3.1.1 briefly introduces one formulation of this simplified approach and demonstrates the influence of fuel dilution and oxygen-enrichment on the equilibrium

flame structure. A more detailed description of the formulation used here is provided in Appendix A, while a highly rigorous discussion of this and other simplified formulations can be found in Law [63] or Williams [64].

### 3.1.1 Equilibrium Flame Structure

The governing equations for reacting flows can be greatly simplified under the following assumptions.

- steady-state
- mass diffusion occurs only due to concentration gradients
- viscous heating is negligible
- body forces are ignored
- radiation heat transfer is ignored
- diffusion coefficients equal for all species (i.e.  $D_{i,j}=D$ )
- unity Lewis number, i.e. equal thermal and mass diffusivities
- one-step chemistry, Fuel + Oxidizer  $\rightarrow$  Products

Further, by using conserved scalars or coupling functions the reaction terms (as detailed in Appendix A) can be eliminated resulting in a general form for the species and energy conservation equations given by

$$\nabla \cdot [\rho \mathbf{v} \beta - (\rho D) \nabla \beta] = 0 \quad (3.1)$$

where  $\rho$  is the density of the mixture,  $\mathbf{v}$  is the velocity of the bulk flow,  $D$  is the diffusion coefficient assumed equivalent for all species, and  $\beta$  is any conserved scalar that is unaffected by reaction in the flame. Under the one-step chemistry formulation used here, it is sufficient

to define conserved scalars for the stoichiometrically weighted fuel and oxygen mass fractions

$$\beta_{F,O_2} = \tilde{Y}_F - \tilde{Y}_{O_2}, \quad (3.1a)$$

the stoichiometrically weighted fuel mass fraction and stoichiometrically weighted non-dimensional temperature

$$\beta_F = \tilde{Y}_F + \tilde{T}, \quad (3.1b)$$

and the stoichiometrically weighted oxygen mass fraction and stoichiometrically weighted non-dimensional temperature

$$\beta_{O_2} = \tilde{Y}_{O_2} + \tilde{T}. \quad (3.1c)$$

In equations 3.1a-3.1c the stoichiometrically weighted mass fraction for species  $i$ ,  $Y_p$  is given by,

$$\tilde{Y}_i = \frac{1}{\sigma_{i,F}} \left( \frac{Y_i}{Y_{F,fu}} \right) \quad (3.1d)$$

where  $F$  designates the fuel species, the subscript  $fu$  indicates that the quantity is to be evaluated in the fuel free stream, and

$$\sigma_{i,F} = \frac{W_i(v_i'' - v_i')}{W_F(v_F'' - v_F')}. \quad (3.1e)$$

In Eq. 3.1e,  $W$  is the molecular weight, and  $v'$  and  $v''$  are the stoichiometric coefficients in the one-step reaction for the reactants and products, respectively. The stoichiometrically weighted non-dimensional temperature in Eqs. 3.1b and c is given by

$$\tilde{T} = \frac{c_p T}{Y_{i,F} q_{c,F}} \quad (3.1f)$$

where  $c_p$  is the specific heat of the mixture and

$$q_{c,F} = \frac{\sum_{k=1}^N h_k^0 W_k (v_k'' - v_k')}{W_F (v_F'' - v_F')} \quad (3.1g)$$

is the chemical heat release per unit mass of fuel reacted. In Eq. 3.1g,  $h_k^0$  is the heat of formation of species  $k$  and  $N$  is the number of species (i.e. fuel, oxygen, and products).

It is useful to consider structural changes in non-premixed flames independent of the flame's configuration or coordinate system. One approach that is commonly used involves transforming the equations from physical space to mixture fraction space. The mixture fraction,  $Z$ , is a conserved scalar and is defined as the local fraction of mass that originated from the fuel stream. For one-step chemistry

$$Z = \frac{\beta_{F,O_2} - (\beta_{F,O_2})_{ox}}{(\beta_{F,O_2})_{fu} - (\beta_{F,O_2})_{ox}} = \frac{\tilde{Y}_F - \tilde{Y}_{O_2} + \tilde{Y}_{O_2,ox}}{\tilde{Y}_{F,fu} + \tilde{Y}_{O_2,ox}} = \frac{\sigma_{O_2,F} Y_F - Y_{O_2} + Y_{O_2,ox}}{\sigma_{O_2,F} Y_{F,fu} + Y_{O_2,ox}} \quad (3.2)$$

where  $\sigma_{O_2,F}$  is defined as before and the subscript  $ox$  indicates that the quantity is to be evaluated in the oxidizer free stream. It can be seen in Eq. 3.2 that the mixture fraction has been written in terms of the stoichiometrically weighted fuel and oxidizer mass fractions that were defined previously. Thus, a simple algebraic solution for the species profiles in mixture fraction space can be obtained by rearranging Eq. 3.2. Moreover, under the unity Lewis number assumption, the mixture fraction can be written in terms of the stoichiometrically weighted species mass fraction and stoichiometrically weighted non-dimensional

temperature (see Appendix A in detail). Consequently, the temperature profile can be obtained in a similar fashion.

At the flame sheet the reactants are in stoichiometric proportion and the mixture fraction is the *stoichiometric mixture fraction*,  $Z_{st}$  given by

$$Z_{st} = \left(1 + \sigma_{O_2,F} Y_{F, fu} / Y_{O_2, ox}\right)^{-1} . \quad (3.3)$$

Thus, pure fuel burning in air represents a low  $Z_{st}$  flame while heavily diluted fuel burning in pure oxygen represents a high  $Z_{st}$  flame. If the free-stream temperatures,  $T_{fu}$  and  $T_{ox}$  are equal

$$Y_F = \left(Y_{F, fu} + Y_{O_2, ox} / \sigma_{O_2,F}\right) Z - Y_{O_2, ox} / \sigma_{O_2,F} \quad (3.4)$$

and

$$T = \frac{q_c}{c_p} \frac{Y_{O_2, ox}}{\sigma_{O_2,F}} (1 - Z) + T_{ox} \quad (3.5)$$

on the fuel side of the flame where  $Z > Z_{st}$  and  $Y_{O_2} = 0$ . On the oxidizer side of the flame, where  $Z < Z_{st}$  and  $Y_F = 0$ ,

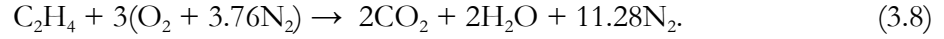
$$Y_{O_2} = -\left(\sigma_{O_2,F} Y_{F, fu} + Y_{O_2, ox}\right) Z + Y_{O_2, ox} \quad (3.6)$$

and

$$T = \frac{q_c}{c_p} Y_{F, fu} Z + T_{ox} . \quad (3.7)$$

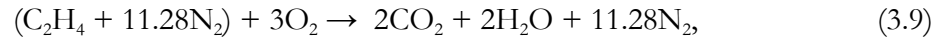


As an example of the effects of oxygen-enrichment with fuel dilution on non-premixed equilibrium flame structure, consider the global reaction of ethylene ( $C_2H_4$ ) with air represented by



Stoichiometry requires 3 moles of oxygen per mole of ethylene along with 11.28 moles of  $N_2$  since air is approx. 79 vol.%  $N_2$ . The free-stream mass fractions of fuel and oxygen for this flame are unity and 0.233, respectively, resulting in a stoichiometric mixture fraction of 0.064 and an adiabatic flame temperature of 2370 K.

If pure oxygen is placed in the oxidizer stream and the stoichiometric amount of  $N_2$  previously carried by the air is used to dilute the fuel stream i.e.,



the free-stream fuel and oxygen mass fractions are 0.08 and unity, respectively, resulting in a stoichiometric mixture fraction of 0.78, while the adiabatic flame temperature remains 2370 K. The impact of fuel-dilution and oxygen-enrichment on flame structure can be observed in Fig. 3.1 where the fuel and oxidizer concentration profiles and temperature profiles from Eqs. 3.4 through 3.7 are shown.

Note first that the concentration gradients in  $Z$  space are dictated by  $Z_{st}$  such that the fuel and oxidizer are transported to the flame sheet in stoichiometric proportions. This explains why the flame of Eq. 3.8 is close to the  $Z = 0$  boundary and the flame of Eq. 3.9 resides near the  $Z = 1$  boundary. For low  $Z_{st}$  greater demand for  $O_2$  forces the flame to reside close to the oxidizer free stream, while for high  $Z_{st}$  greater demand for fuel forces the flame to reside close to the fuel free stream. Consider also the region of high temperature where  $T/T_{ad} > 0.7$  designated by the shaded region. Comparing the fuel and oxygen

concentrations in this region for the low and high  $Z_{st}$  flames, it is apparent that more fuel is found in the high temperature region of the low  $Z_{st}$  flame while more oxygen is found in the high temperature region of the high  $Z_{st}$  flame. These structural changes have been identified as dominant factors leading to reduced soot formation at high  $Z_{st}$ , and furthering the fundamental understanding of these effects is a key component of this work. A brief introduction to soot is provided in Section 3.1.2 and a review of the relevant literature on the effects of flame structure on soot formation is provided in Section 3.1.3.

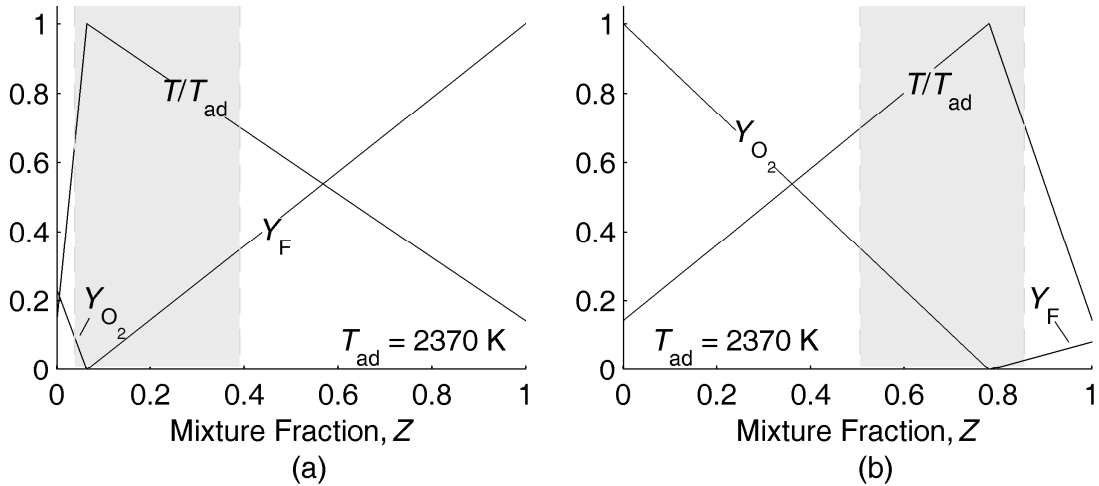


Figure 3.1. Illustration of equilibrium structure of (a) ethylene/air  $Z_{st} = 0.064$  and (b) diluted-ethylene/oxygen  $Z_{st} = 0.78$  flames at  $T_{ad} = 2370 \text{ K}$ . Filled area indicates the region of high temperature ( $T/T_{ad} \geq 0.7$ ).

### 3.1.2 Soot

Soot can be defined as the carbonaceous particulates that form during rich premixed hydrocarbon combustion or in non-premixed hydrocarbon combustion where sufficient time, temperature, and carbon containing species are available. Epidemiological studies have linked soot inhalation to death from lung cancer and cardiopulmonary disease [65-72]. The heightened health impact of particles formed via hydrocarbon combustion processes is due to their small size ( $< 2.5 \mu\text{m}$ ), which allows them to travel deep into the lungs where they are

quickly introduced into the blood stream. Also, they are associated with mutagenic and tumorigenic polycyclic aromatic hydrocarbons (PAH) [67-72]. Soot has been identified as a potential contributor to global climate change [73-77], and along with other particulate matter (PM), soot is a major contributor to reduced atmospheric visibility [78].

Palmer and Cullis [79] reported that soot contains at least 1% hydrogen by mass, resulting in an approximate empirical formula of  $C_8H$ . Transmission electron microscope (TEM) images of soot aggregates from a non-premixed flame indicate a fractal-like structure with primary particle sizes ranging from 100 to 500 Å and a fractal dimension of 1.82 [80, 81]. Rates of soot formation can be extremely high, with particles forming in less than 1 millisecond and growing to diameters of 500-1000 Å in less than 10 milliseconds [82].

While the formation processes are not completely understood and there has been debate regarding the dominant reaction pathways, it is generally accepted that in the combustion of aliphatic fuels the self-combination of propargyl is the dominant pathway leading to the first aromatic ring and that the hydrogen abstraction and acetylene addition (HACA) mechanism is involved in the growth of soot precursor species from benzene and phenyl to higher aromatics [83-91]. In this work emphasis is placed on the gas phase reactions leading to the formation of the first aromatic ring species, which lead to larger aromatics that are stable enough to combine and eventually nucleate forming incipient soot particles. For example, pyrene has been identified in molecular dynamics simulations as a species that is sufficiently stable and can survive long enough to evolve into soot nuclei [92]. The present understanding of the complex processes involved in soot formation has required a substantial amount of experimental and theoretical research, and reviews can be found in Haynes and Wagner [93], Bockhorn [94], Kennedy [95], Richter and Howard [85], and Hansen et al. [91].

### 3.1.3 Flame Structure and Soot Formation

One of the earliest studies of the effects of fuel and oxidizer dilution on soot formation, as determined by smoke point measurements, was performed by McLintock [96] who showed that soot formation is dependent upon diluent type, dilution conditions, and burner dimensions. The smoke point is typically defined as the flame height immediately prior to the flame emitting smoke (i.e. soot particles surviving oxidation downstream of the flame sheet). Thus, at the smoke point soot formation is exactly offset by soot oxidation. Glassman and Yaccarino [97] also used fuel dilution with various inert types and suggested that flame temperature and fuel structure are the most important factors determining a non-premixed flame's propensity to soot and that fuel concentration was of secondary importance.

The effects of temperature and fuel dilution on soot formation were isolated by Axelbaum and co-workers [41, 98-100] who showed that temperature effects dominate under heavily diluted fuel conditions while for moderate fuel dilution, where temperatures are only slightly reduced, dilution effects dominate. Axelbaum and co-workers also investigated the effects of preferential diffusion on soot formation by using several inert types with different diffusivities and showed that inert diffusion rates in the fuel rich region can influence local fuel and soot precursor concentrations thereby influencing soot formation [101].

Glassman [102] postulated that the soot formation region in fuel/air and diluted-fuel/air flames is bounded by the incipient particle formation isotherm and the stoichiometric flame temperature isotherm and that the size of this region controls the soot volume fraction. It was stated that this distance corresponds to the particle growth time

before soot particle oxidation occurs at the flame, and thus the thermal diffusivity of the fuel or fuel additives has a direct effect on the soot growth time. Glassman showed further that soot formation exhibits a logarithmic dependence on temperature and a linear dependence on dilution.

The effect of oxygen addition in the fuel stream was studied by Hura et al. [103, 104] and Sugiyama et al. [105], while Du et al. [106] studied both the effects of oxygen and carbon dioxide addition. The results of Du et al. [106] indicated that thermal, chemical, and dilution effects were significant when introducing CO<sub>2</sub> with the fuel. When introduced with the oxidizer both thermal and chemical effects were observed. Oxygen addition to propane was shown to suppress soot chemically at concentrations up to 30 vol.%. Above 40 vol.% oxygen addition to propane resulted in a rapid increase in soot formation kinetics. The effect of varying the oxygen concentration in the oxidizer was demonstrated to be primarily thermal. Liu et al. [107] performed a numerical study and concluded that soot suppression occurs with CO<sub>2</sub> addition to the fuel and oxidizer side due to the elevated production of the hydroxyl radical (OH) when CO<sub>2</sub> is attacked by H. Increased OH was shown to attack soot precursors thereby reducing the soot nucleation rate, and the chemical effect was observed to be more significant when CO<sub>2</sub> was added to the oxidizer.

Glassman and Yaccarino [108] studied the effect of increasing the O<sub>2</sub> concentration in the oxidizer stream on sooting heights for non-premixed coflow flames and found that increasing the O<sub>2</sub> concentration has two competing effects on soot formation. The first effect is an increase in fuel pyrolysis and soot formation rates due to elevated adiabatic flame temperatures, while the competing effect is an increased particle oxidation rate near the flame. Results suggested that increased fuel pyrolysis and soot formation rates dominate for

high levels of oxygen addition while increased oxidation rates dominate for low levels of oxygen addition.

By diluting the fuel with inert and using oxygen-enriched air Sugiyama [28], Du and Axelbaum [30], Lin and Faeth [29, 42, 109, 110], and Kang et al. [111] showed that soot could be eliminated in non-premixed flames of aliphatic fuels, even at high temperatures. Sugiyama, Lin and Faeth, and Kang et al. attributed this result to the direction of gas flow relative to the flame sheet. This argument can be understood by observing the spatial changes that occur in counterflow flames when increasing  $Z_{st}$ . Figure 3.2 provides a simple schematic of the fuel/air and diluted-fuel/oxygen flames in a counterflow configuration. Here it is observed that the fuel/air (i.e. low  $Z_{st}$ ) flame resides on the oxidizer side of the stagnation point, whereas the diluted-fuel/oxygen (i.e. high  $Z_{st}$ ) flame resides on the fuel side of the stagnation point. In both cases, soot formation occurs on the fuel side of the flame so that in the fuel/air case convection carries soot particles toward the fuel-rich region promoting soot growth whereas in the high  $Z_{st}$  flame convection carries the soot particles toward the oxygen rich region promoting soot oxidation.

Du and Axelbaum [30] attributed the soot inhibiting effects of increased  $Z_{st}$  to flame structure and considered hydrodynamic effects to be secondary. They showed further that for small amounts of fuel dilution and oxygen-enrichment soot is reduced primarily due to the lower fuel concentration, while for higher levels of fuel dilution and oxygen-enrichment the radical species OH and O shift toward the fuel side of the flame and appreciable  $O_2$  is present at the location of peak temperature resulting in a narrowing of the soot inception zone. The presence of  $O_2$  at the location of peak temperature for high  $Z_{st}$  flames was confirmed by Sun et al. [33] and Cheng et al. [43], who validated their numerical results by measuring temperature and  $O_2$  concentrations via spontaneous Raman spectroscopy.

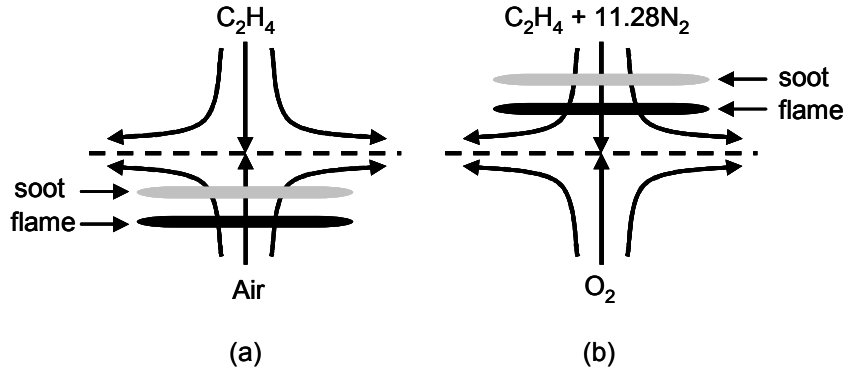


Figure 3.2. Schematic of counterflow flames at (a)  $Z_{st} = 0.064$  (ethylene/air) and (b)  $Z_{st} = 0.78$  (diluted-ethylene/oxygen)

Structural changes leading to accelerated consumption of soot and soot precursors at high  $Z_{st}$  were investigated by Chao et al. [32] and Liu et al. [112] using a simplified 3-step reaction scheme for fuel consumption, soot or precursor production, and soot consumption with high activation energy asymptotics. It was demonstrated that the soot precursor consumption reaction had a negligible effect on the soot process for conventional fuel/air flames but was significant for high  $Z_{st}$  flames. Moreover, soot precursor consumption in high  $Z_{st}$  flames was attributed primarily to structure and not hydrodynamics.

In further support of the work by Du and Axelbaum [113], non-premixed spherical microgravity experiments by Sunderland et al. [35] also showed that soot suppression occurs at high  $Z_{st}$  predominantly due to structural effects and that convection direction has a secondary influence on soot inception. Sunderland et al. [36] also demonstrated that the flame temperature increases linearly with  $Z_{st}$  for non-premixed flames at their sooting limits and attributed the linear relationship to the existence of a critical local temperature  $T_{cr}$  and a critical local carbon-to-oxygen ratio  $(C/O)_{cr}$  where soot formation is no longer favorable. A simple model was developed that correlated well with experimental data, but did not account for potentially important residence time effects or finite-rate chemistry. Kumfer et al. [37] also found that the sooting limit flame temperature increases linearly with  $Z_{st}$  for non-

premixed coflow flames and correlated the critical local C/O ratio for soot inception proposed by Sunderland et al. [36] with experimental measurements of polycyclic aromatic hydrocarbons (PAH).

In this dissertation, the work presented in Chapter 4 extends the model of Sunderland et al. to include the effects of residence time and finite-rate chemistry and correlates the updated model with experimental data. Chapter 5 contains a numerical study investigating the presence of appreciable oxygen at the location of maximum temperature in high  $Z_{st}$  flames. Part I concludes with Chapter 6, which contains another numerical study examining the effects of flame structure on the detailed chemistry leading to the formation of key soot precursor species.



# 4 Measuring and Modeling Soot Inception Limits in Laminar Diffusion Flames

## 4.1 Introduction

For a typical fuel/air diffusion flame, it is generally accepted that soot inception occurs as a consequence of fuel pyrolysis, which leads to the formation of polycyclic aromatic hydrocarbons (PAH) and soot particles. Given that the chemistry of soot inception is high-activation energy, soot inception will only occur if the local temperature and residence time are sufficiently high. The soot inception temperature, *i.e.* the temperature at which soot is first observed on the fuel side of the flame, has been measured in sooting diffusion flames [114-116]. Gomez *et al.* [114] measured the inception temperature along the centerline of the coflow flame for four different fuels and determined it to be approx. 1350 K, regardless of fuel type or level of dilution. Dobbins [117] proposed that the inception temperature can be predicted from an Arrhenius reaction equation, which describes the conversion of soot precursors to soot particles. Glassman [102] postulated that the distance between the incipient particle formation isotherm and the stoichiometric flame temperature isotherm controls the soot volume fraction. He further stated that this distance corresponds to the particle growth time before soot particle oxidation occurs at the flame, and thus the thermal diffusivity of the fuel or fuel additives has a direct effect on the soot growth time. Counterflow flame studies have also shown the importance of residence time on soot formation. For example, it has been observed that a sooting counterflow flame will become soot-free upon increasing the strain rate. The limiting strain rate that results in a soot-free flame has been measured by Kennedy [40], Du *et al.* [41] and Lin and Faeth [42].

The local gas composition is also an important criterion for soot formation in diffusion flames. In the work of Du *et al.* [106], it was demonstrated that fuel dilution reduces soot. This effect was separated from the effects of temperature by using different inert gases, while maintaining constant flame temperature. Furthermore, it has been demonstrated that fuel dilution and oxygen enrichment can lead to a net reduction in soot formation, even at high temperatures. For example a sooting fuel/air flame can be made blue (soot-free) by replacing air with oxygen and diluting the fuel while maintaining constant flame temperature [30]. As demonstrated in Chapter 2, the relative amounts of oxygen enrichment and fuel dilution can be quantified by the stoichiometric mixture fraction,  $Z_{st}$ . The influence of  $Z_{st}$  on soot inception has been the subject of many investigations [29, 36, 113, 118, 119]. Lin and Faeth [109] suggested that changes in  $Z_{st}$  affect soot formation through the variation in the velocity and direction of flow normal to the flame sheet, while Du and Axelbaum [113] and Sunderland *et al.* [36] have concluded that soot inception is affected by  $Z_{st}$  primarily because of its influence on the relationship between the local temperature and the local gas composition in the soot zone.

In this work emphasis is placed on soot *inception*, which is considered here to be the growth of gas-phase species culminating in the creation of a luminous soot particle. Phenomenon occurring after particle inception, such as particle transport and surface oxidation, will not be considered here. In previous studies, soot inception limits were measured as a function of  $Z_{st}$  in counterflow flames [41], spherical microgravity flames [36] and normal coflow flames [37]. In each of these studies, the flame temperature at the sooting limit was found to increase linearly with  $Z_{st}$  and this behavior was attributed to the variation in flame structure with  $Z_{st}$ . In other words, gas composition and its relationship to temperature plays a primary role in governing soot inception. In addition, a theory for

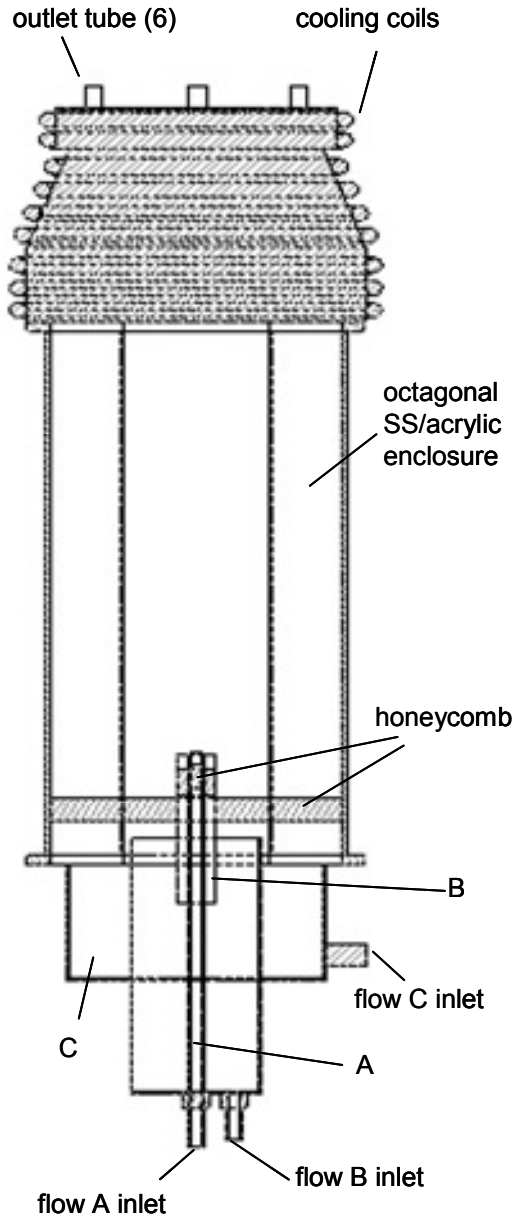
predicting the sooting limit data was evaluated, which assumes that soot inception can only occur when the local C/O ratio is equal to or above a critical value [36]. Values for the nonpremixed critical *local* C/O ratio were previously derived utilizing the normal coflow flame and, perhaps surprisingly, the sooting limit results agreed well with published results for the *global* C/O ratio for premixed flames for a variety of gaseous fuels [37]. However, these results were obtained with the assumption that the variation in residence time between flames had a secondary effect on the sooting limits.

The objective of this chapter is to expand the sooting limit model to include the effects of finite rate soot chemistry and the characteristic residence time. In order to better examine these effects, both normal and inverse coflow flames are utilized. Normal flames are created by injecting fuel into a surrounding oxidizer stream, while inverse flames are created by injecting oxidizer into a surrounding fuel stream. While soot formation in the normal coflow flame has been well characterized, soot formation in the inverse flame has received less attention [120-125]. In the inverse flame, soot particles form in the fuel-rich region on the outside of the stoichiometric flame surface and they are not directed into the oxidizer stream by convection. Thus, the inverse flame is valuable for studying early-stage soot formation since formation processes are well separated from oxidation processes [121]. More importantly for this work, the inverse flame has the added advantage that the flame height can be varied without varying the fuel flow rate, enabling one to separate effects from these parameters. Studies characterizing soot formation in the inverse flame were performed by Sidebotham and Glassman [120, 121], who utilized gas chromatography, and Makel and Kennedy [122], who utilized light scattering. Vander Wal [123], Blevins et al. [124], and Oh *et al.* [125] performed studies on the early stages of soot inception in the inverse flame, while

Kaplan and Kailasanath [126] employed numerical simulations to compare flow-field effects on soot formation in normal and inverse flames.

## 4.2 Experimental Methods

The experimental setup consists of a tri-axial coflow burner surrounded by an octagonal stainless steel chimney with three of the steel panels replaced by acrylic window for optical diagnostics as shown in Fig. 4.1. The inner, secondary, and tertiary tube diameters are 6.2 mm, 17 mm, and 120 mm, respectively. The third coannular flow is added to ensure that sufficient fuel is available within the chimney when operating in the inverse mode and to provide for an overventilated condition independent of the secondary stream velocity. The gas composition exiting the outer tube (tube C) and the intermediate tube (tube B) are kept identical at all times. The outer flow rate is kept small, while the exit velocity of the intermediate stream can be increased as needed. In this way, when operating in the inverse mode, the velocity of the fuel stream adjacent to the oxidizer stream can be varied without introducing significantly more fuel into the system, which would result in safety concerns associated with exhausting large amounts of unburned fuel. Honeycomb is used in all streams to produce uniform and stable flows. The fuel ( $C_2H_4$ ) and oxidizer mass fractions are controlled by dilution with nitrogen. Flow rates are measured with calibrated sonic nozzles. At the top of the chimney, the exhaust is forced through 6 outlet tubes and when operating in the inverse mode, any unburned fuel is immediately burned in room air with the aid of pilot flames.



Tube A, ID	Tube B, ID	Tube C, ID
6.2 mm	17 mm	120 mm

Figure 4.1. Schematic diagram of burner for normal and inverse coflow flames.

The sooting limit is defined as the flame condition that leads to the disappearance of visible soot luminosity at a given location as observed using a cathetometer in a dark room. In a previous study, the sooting limit as determined by soot luminosity was compared with the limit determined by the threshold of Rayleigh scattering of laser light from particles [41].

The sooting limits based on these two methods were found to be in good agreement, and in fact the visible soot luminosity method was found to be slightly more sensitive than the light scattering method. Thus, soot luminosity will be used to obtain the sooting limit. We observe the sooting limit at a fixed height of 8 mm, measured from the burner exit. The limit is obtained by varying the total amount of inert (nitrogen) at constant  $Z_{st}$  until yellow luminosity is first perceptible at the 8 mm height. That is, above this height there is yellow luminosity in the flame, but below this height there is no yellow luminosity at any radial position in the flame.



**Figure 4.2.** Photographs of (a) normal and (b) inverse sooting limit flames. The sooting limit is observed at a height of 8 mm from the burner tip.

The adiabatic flame temperature for each sooting limit flame is computed using the CEA chemical equilibrium code [127]. Photographs of both a normal and inverse flame near the sooting limit are shown in Fig. 4.2. It is noteworthy that the soot luminosity in the normal flame is yellow in color, while the soot appears orange in the inverse flame. This difference in emission may be attributed to differences in particle temperature.

The flame temperature is measured in selected limit flames using a bare Pt-6%Rh/Pt-30%Rh thermocouple constructed from 50  $\mu\text{m}$  wire. Corrections for radiative heat loss are made using the Nusselt number correlation for convective heat transfer to a spherical bead, with a measured diameter of 290  $\mu\text{m}$  and assuming a bead emissivity equal to 0.22. Thermocouple temperatures in excess of approx. 2100 K are not obtainable due to the limits of the Pt-6%Rh/Pt-30% wire. Measurements of the velocity field are taken using laser Doppler velocimetry (LDV). The flows are seeded with alumina particles manufactured by Alfa Aesar, which have a nominal size of 0.3  $\mu\text{m}$ .

### 4.3 Results and Discussion

For the first set of experiments, the flame height is held constant and the flow rate from the central tube is varied. In the second set, the fuel flow rate is held constant, resulting in a variable flame height (for the normal flame). The input parameters for all of the limit flames are summarized in Table 4.1, where  $V_{e,F}$  and  $V_{e,O}$  are the mean fuel and oxidizer exit velocities, which are determined by dividing the volumetric flow rate by the exit area, and  $Y_{F,0}$  and  $Y_{O,0}$  are the fuel and oxygen mass fractions at the burner outlet, respectively.

**Constant Flame Height** For this set of experiments, the flame height is maintained at  $16 \pm 1$  mm. When  $Z_{st}$  is varied in the normal flame configuration, a constant 16 mm flame height can only be obtained if the fuel stream flow rate is varied, since flame height is a function of both  $Z_{st}$  and fuel flow rate. For inverse flames, flame height is controlled by the oxidizer stream flow rate, and thus the fuel stream flow rate can be held constant for all stoichiometric mixture fractions. The flow rate of the oxidizer stream in the inverse flame is found to have no effect on soot inception in the region of interest for the flow rates considered in this study. Since the fuel flow rate can be held constant and the oxidizer flow

rate does not affect the sooting limit, only buoyancy should have an impact on residence time for the sooting limit data for the inverse flames.

**Table 4.1. Input parameters for sooting limit flames**

Normal Coflow					Inverse Coflow				
$Z_{st}$	$Y_{F, fu}$	$Y_{O_2, ox}$	$V_{e, fu}$	$V_{e, ox}$	$Z_{st}$	$Y_{F, fu}$	$Y_{O_2, ox}$	$V_{e, fu}$	$V_{e, ox}$
--	--	--	cm/s	cm/s	--	--	--	cm/s	cm/s
<b>Exp. #1 Constant Flame Height</b>									
0.20	0.259	0.222	11	17	0.20	0.259	0.222	11	45
0.25	0.215	0.245	14	17	0.25	0.215	0.245	11	42
0.30	0.185	0.272	18	17	0.30	0.185	0.272	11	38
0.35	0.163	0.301	21	17	0.35	0.163	0.301	11	34
0.40	0.148	0.338	24	17	0.40	0.148	0.338	11	31
0.45	0.138	0.387	28	17	0.45	0.136	0.379	11	29
0.50	0.133	0.454	31	17	0.50	0.125	0.429	11	24
0.55	0.129	0.541	37	17	0.55	0.118	0.495	11	18
0.60	0.126	0.648	47	17	0.60	0.111	0.568	11	17
0.65	0.126	0.799	48	17	0.65	0.105	0.668	11	14
<b>Exp. #2 Constant Mean Exit Velocity</b>									
0.17	0.314	0.218	43	43	0.24	0.220	0.244	30	30
0.21	0.255	0.238	43	43	0.32	0.179	0.288	30	30
0.24	0.232	0.249	43	43	0.39	0.150	0.330	30	30
0.30	0.195	0.288	43	43	0.42	0.150	0.364	30	30
0.36	0.168	0.324	43	43	0.45	0.145	0.404	30	30
0.42	0.154	0.377	43	43	0.47	0.140	0.422	30	30
0.46	0.145	0.428	43	43	0.51	0.134	0.480	30	30
0.55	0.139	0.587	43	43	0.56	0.128	0.553	30	30
0.59	0.133	0.647	43	43	0.61	0.125	0.680	30	30
					0.66	0.122	0.800	30	30
					0.73	0.110	1.000	30	30

Since the sooting limit is defined for a height of 8 mm, these flames may be described as *half blue* [37]. In Fig. 4.3, the adiabatic flame temperature corresponding to the half blue condition is plotted as a function of  $Z_{st}$ . In addition, the measured flame temperature at the flame half-height (8 mm) is plotted. The normal and inverse data are shown together for comparison. For both normal and inverse flames, the sooting limit flame temperature increases with  $Z_{st}$  by as much as 500 °C. This is the case for both flame-types



despite the fact that the direction of convection for the normal flame is opposite that of the inverse flame. The suppression of soot with increasing  $Z_{st}$  is consistent with results in counterflow flames [29, 118], spherical microgravity flames [36] and normal coflow flames [37]. The results further demonstrate the usefulness of oxygen-enhanced combustion in combination with fuel dilution as a tool for optimizing temperature while minimizing soot formation.

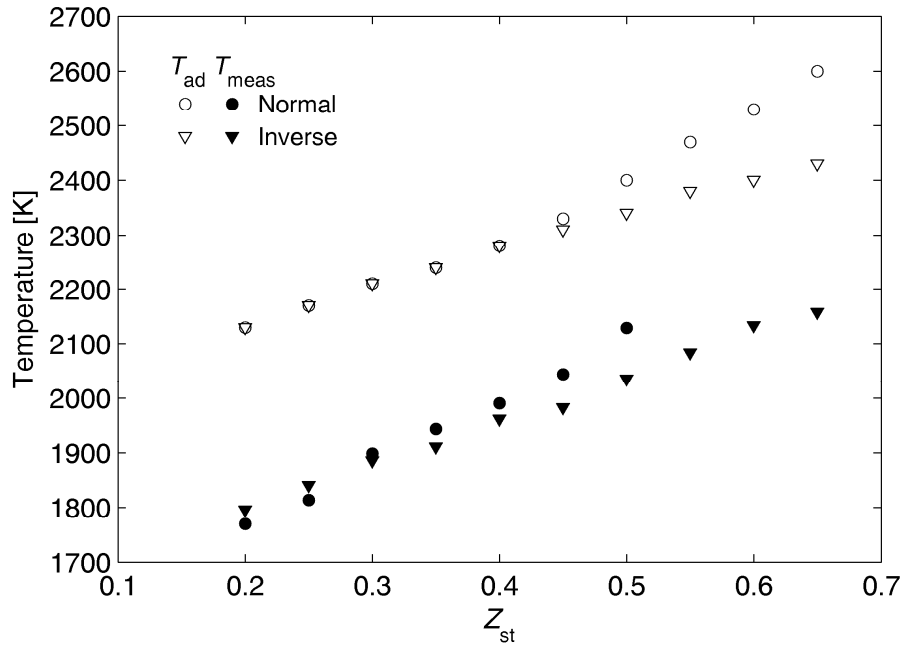


Figure 4.3. Sooting limit flame temperature vs stoichiometric mixture fraction for normal and inverse flames. Case 1: Constant flame height of 16 mm.

As demonstrated in Fig. 4.3, the limits for the normal and inverse flames are similar for  $0.2 < Z_{st} < 0.4$ . Beyond  $Z_{st} = 0.4$  the limits for the normal flames deviate from those of the inverse flame. As shown in Table 4.1, at  $Z_{st} = 0.20$  the mean fuel stream exit velocities for the normal and inverse flames are nearly identical, while for larger  $Z_{st}$  the differences increase by up to 300%. The increased fuel stream velocity in the normal flame may reduce the characteristic residence time for soot formation in coflow flames. Decreasing residence time results in a reduction of soot, as demonstrated by the aforementioned counterflow

studies [29, 41]. Thus, the deviation of the normal flame limit data from the inverse flame data may be a result of reduced residence time. The flow field and thus the residence time may be affected by both exit velocity and acceleration due to buoyancy. The influence of buoyancy can be assessed from the Richardson number,  $Ri$ , defined as

$$Ri = gL(T_f - T_0)/(T_0 V^2). \quad (4.1)$$

Since we are concerned with the effects of buoyancy on the soot inception limit, we choose  $L = 8$  mm (soot inception height) and  $V = V_{e,F}$ . The Richardson numbers for the extreme cases (low and high  $Z_{st}$ ) are given in Table 4.2. Indeed, for most of the flames in this study,  $Ri \gg 1$  indicating that the flow field is dominated by buoyancy. Thus, the exit velocity alone is insufficient to characterize the residence time for soot inception in these flames. The high- $Z_{st}$  normal flame, in which the  $Ri$  is on the order of unity, is an exception to this. In this case, the exit velocity is sufficiently high such that buoyancy effects are reduced and the residence time begins to scale with  $L/V$ .

In order to obtain a more accurate characterization of residence time, the vertical component of velocity in the region of soot inception was measured by LDV. These results are also summarized in Table 4.2. Using these data, the residence time,  $\tau$ , for soot inception is found by tracking a parcel of fuel from the burner exit to the location of soot inception, and is calculated from

$$\tau = \int_0^{8mm} 1/V(z) dz. \quad (4.2)$$

It is assumed that the vertical component of velocity increases linearly with height,  $z$ . Earlier measurements of the entire flow field taken in similar half-blue coflow flames [37] indicated that this is a good approximation. As can be seen from Table 4.2,

the residence time in the normal flame decreases dramatically as  $Z_{st}$  is increased, while  $\tau$  is nearly constant (within 6%) for the inverse flame over the entire span of  $Z_{st}$ . This is strong evidence that the differences between the normal and inverse sooting limits observed in Fig. 4.3 can be attributed to residence time.

**Table 4.2. Selected properties of sooting limit flames**

	$Z_{st}$	$V_e$	$V_{8mm}$	Ri	$\tau$
	--	cm/s	cm/s	--	ms
Normal	0.20	11	66	32	26.1
	0.65	48	100	2	11.3
Inverse	0.20	11	87	32	21.8
	0.65	11	80	40	23.0

### Constant Exit Velocity

Measurements of sooting limits were performed in a second set of experiments in which the mean exit velocities of the fuel and oxidizer streams are set equal and held constant as  $Z_{st}$  is varied. While this causes the flame length to vary, the sooting limit is still identified at a height of 8 mm from the burner lip throughout the experiments. The flow rates are kept large so that  $Ri = O(1)$  and the effects of buoyancy at a height of 8 mm are minimized. In this way, the residence time is held constant as  $Z_{st}$  is varied and velocity gradients normal to the flame surface are minimized. For the normal flames, the mean exit velocity is 43 cm/sec. For the inverse flames, a mean exit velocity of 43 cm/sec could not be attained without flame fluctuations; thus for these flames a mean exit velocity of 30 cm/sec is used. Since some of the flames in these experiments are quite tall, a 12.7 mm stainless steel tube is placed above the flame at a height of approx. 50 mm from the burner to quench and stabilize the top portion of the flame and minimize flame fluctuations. The flames were observed with and without the quenching tube to ensure that the tube caused no visible effect on the sooting limit. The sooting limit results for constant residence time are shown in Fig. 4.4.

In this case, the slope of the best-fit line through the data for the normal flame is nearly equal to that of the inverse flame. This implies that the effects of  $Z_{st}$  on soot inception are the same, regardless of the geometric differences, provided that the residence time is fixed. The intercept of the best-fit line is larger for the normal flame, and this is attributed to the overall shorter residence time associated with these flames.

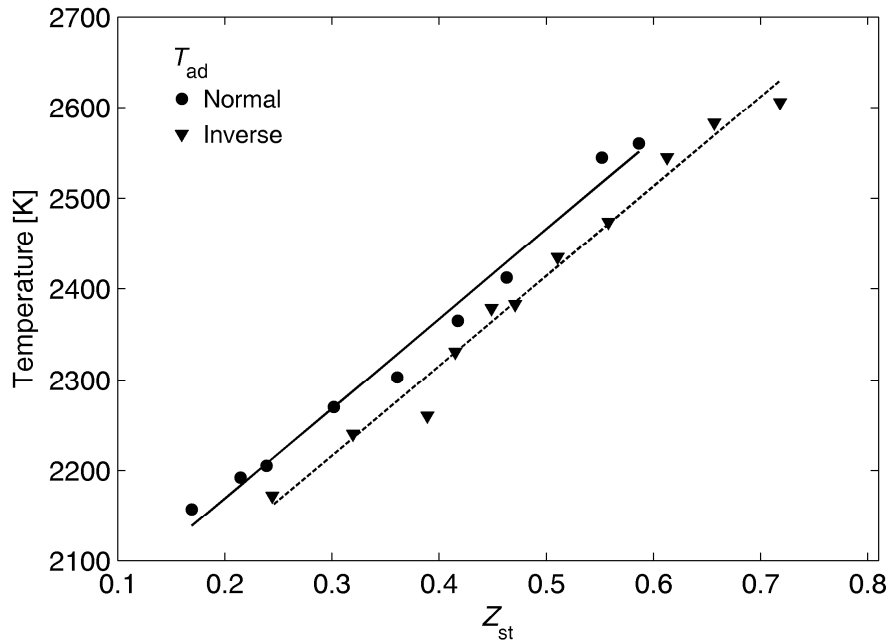


Figure 4.4. Sooting limit flame temperature vs stoichiometric mixture fraction for normal and inverse flames. Case 2: Constant gas exit velocity.

In the following section, we present a simple model for sooting limits that combines the residence time effects demonstrated above with the idea of a critical local C/O ratio, as proposed by Sunderland *et al.* [36].

### Modeling the Sooting Limit

The region conducive to soot inception in a nonpremixed flame can be considered bounded by two locations in the fuel side, one is at a low temperature, below which the chemistry of soot inception is too slow; the other is at a

higher temperature where the local gas composition is not favorable for soot inception due to the presence of oxygen-containing species. This concept of two boundaries has similarities to that proposed in the work of Glassman [102]. In that work it was assumed that the high temperature sooting limit boundary was coincident with the location of stoichiometric flame temperature.

For simplicity, we assume that the onset of soot can be described by a set of reactions that are overall first-order in fuel such that they can be represented by



The reaction rate coefficient,  $k$ , is assumed to be of Arrhenius form, and the change in soot mass fraction,  $Y_{\text{soot}}$ , due to soot formation is written as,

$$w = \frac{dY_{\text{soot}}}{dt} = A \cdot \exp\left(-\frac{E}{R \cdot T}\right) \cdot Y_{\text{fuel}} \quad (4.4)$$

where  $E$  is the activation energy for soot inception,  $R$  is the gas constant, and  $Y_{\text{fuel}}$  is the local fuel mass fraction. The local fuel mass fraction can be related to the local temperature by imposing the classical Burke-Schumann assumptions and utilizing coupling functions. Through this approach, the local soot formation rate can be written as a function of temperature only. Thus for any flame defined by the flame temperature,  $T_f$ , and  $Z_{st}$  we can write,

$$w = A \cdot \exp\left(-\frac{E}{RT}\right) \cdot \frac{(T_f - T)}{Z_{st}} \cdot \frac{c_p}{q_c} \quad (4.5)$$

where  $c_p$  denotes the constant gas specific heat and  $q_c$  the heat of combustion. Also note that for given freestream fuel and oxidizer concentrations,  $Z_{st}$  and  $T_f$  are uniquely defined.

We now identify  $T_{kin}$  as the temperature above which the kinetics are favorable for soot formation. More specifically, at the location of  $T_{kin}$  there is a barely detectable luminous quantity of soot, and this critical soot mass fraction is denoted as  $Y_{soot,c}$ . It is assumed that the time required to reach  $Y_{soot,c}$  is proportional to the characteristic residence time,  $\tau$ , and by considering the mean soot formation rate over the soot inception region,  $W = 1/L \int w \, dx$ , we can write the following,

$$Y_{soot,c} \propto \tau \cdot W. \quad (4.6)$$

By substituting Eq. 4.6 into Eq. 4.5, and lumping the constants together into a new constant,  $C_0$ , we obtain,

$$T_f = T_{kin} + \frac{Z_{st}}{C_0 \cdot \tau} \exp\left(\frac{E}{RT_{kin}}\right). \quad (4.7)$$

Thus for any flame defined by  $Z_{st}$ ,  $T_f$  and  $\tau$ ,  $T_{kin}$  can be predicted provided that  $C_0$  can be obtained for one set of conditions.

The boundary on the high temperature side of the soot formation zone corresponds to the location at which the local gas composition is no longer favorable for soot formation since sufficient oxygen-containing species exist. It has been proposed that soot formation is no longer favorable when the local C/O ratio is less than some critical value,  $(C/O)_{cr}$  [30]. Sunderland *et al.* [36] employed the Burke-Schumann approach and derived Eq. 4.8 below, which relates the local temperature to the local C/O ratio at the high temperature boundary,

$$T_f = T_0 + (T_{C/O} - T_0) \cdot \left[ 1 + Z_{st} \cdot \left( 2 \cdot \frac{m+n/4}{m} \cdot (C/O)_{cr} - 1 \right) \right] \quad (4.8)$$

where  $T_{C/O}$  is the local temperature at this soot formation boundary and  $(C/O)_{cr}$  is the critical carbon-to-oxygen ratio. In Eq. 4.8,  $m$  represents the number of carbon atoms and  $n$  the number of hydrogen atoms in fuel  $C_mH_n$ , and  $T_0$  denotes the inlet temperature.

Based on Eqs. 4.7 and 4.8 above, the sooting limit occurs when the low temperature boundary and the high temperature boundary converge, *i.e.*  $T_{C/O} = T_{kin}$ . For a flame at its sooting limit, a decrease in  $Z_{st}$ , or an increase in either residence time or flame temperature will result in the appearance of luminous soot. We define  $T_{lim}$  as the temperature at the location where soot is first observed in a limit flame such that at the sooting limit  $T_{lim} = T_{kin} = T_{C/O}$ .

To use the model the pre-exponential constant ( $C_0$ ) in Eq. 4.7 must first be determined. Once this is known,  $T_{kin}$  can be predicted for a given residence time and  $Z_{st}$ . The amount of inert in the freestreams must also be provided as this will affect the flame temperature. The pre-exponential factor  $C_0$  and  $T_{kin}$  in Eq. 4.7 can be obtained empirically. Since  $\tau$  and  $T_f$  were measured in the inverse flames of constant flame height, this data can be substituted into Eq. 4.7. The overall activation energy for soot inception is available in the literature. Du *et al.* measured an activation energy for ethylene of 31 kcal/mol [113]. Equation 4.7 can then be solved for  $C_0$  at each experimental data point by letting  $T_{kin}$  vary until the standard deviation of  $C_0$  is minimized. The best fit for the constant flame height, inverse flame data was obtained for  $C_0 = 780 \text{ K}^{-1}\text{s}^{-1}$  and  $T_{kin} = 1640 \text{ K}$ . Since these are limit flames, we can write  $T_{kin} = T_{lim}$  and thus we conclude that  $T_{lim} = 1640 \text{ K}$ .

Using a thermocouple, Gomez *et al.* [114] measured the inception temperature along the centerline of a heavily sooting laminar coflow flame and obtained a temperature of approx. 1350 K for a variety of fuels. This is in contrast to the work of Glassman *et al.* [128],

who studied heavily-diluted ethylene/air coflow flames where soot luminosity was no longer visible at the tip. They measured the temperature where luminosity last appeared and found it to be approx. 1600 K. Note that the measurements of soot inception temperature in these two studies were obtained using different criterion. Gomez *et al.* measured the centerline temperature where soot was first observed in sooting flames, which is consistent with our definition of  $T_{kin}$ , whereas Glassman *et al.* measured the temperature where soot appears in a flame at its sooting limit, or  $T_{lim}$ . The latter is more relevant to this work and the value of circa 1600 K fares well with our predicted value of 1640 K.

With  $T_{lim}$  known, Eq. 4.8 can now be solved for the critical C/O ratio at each experimental data point. Letting  $T_{C/O} = T_{lim} = 1640$  K, we obtain an average  $(C/O)_{cr}$  of 0.53 with a standard deviation of 0.005. The linear relationship between the flame temperature at the sooting limit and  $Z_{st}$  predicted by the model is shown together with the experimental data from the inverse flame in Fig. 4.5, and the model is a good representation of the data.

Interestingly, the value for  $(C/O)_{cr}$  is similar to, though slightly lower than, the global critical C/O ratio that is observed in ethylene premixed flames. Harris *et al.* [129] observed that for premixed flames, the critical C/O ratio varies from 0.55 to 0.64 in the temperature range of 1620-1840 K. The value of  $(C/O)_{cr}$  for ethylene obtained in this work is somewhat lower than the value obtained previously by this group in the study of normal coflow flames of constant flame height (0.53 compared to 0.60) [37]. This difference is likely due to the fact that the soot inception model of the previous work did not address the effects of variable residence time. The results in Fig. 4.3 demonstrate that the slope of the sooting limit line increases with  $Z_{st}$  for the normal flames at constant flame height. As discussed, residence time decreases for these flames and thus the higher  $Z_{st}$  flames are expected to have higher limit temperatures than they would if residence time were constant. The increase in slope



will in turn result in an overprediction of  $(C/O)_{cr}$  if Eq. 4.8 is directly fitted to this sooting limit data as it was in [37], and thus the value of  $(C/O)_{cr} = 0.6$  in [37] is believed to be an overprediction.

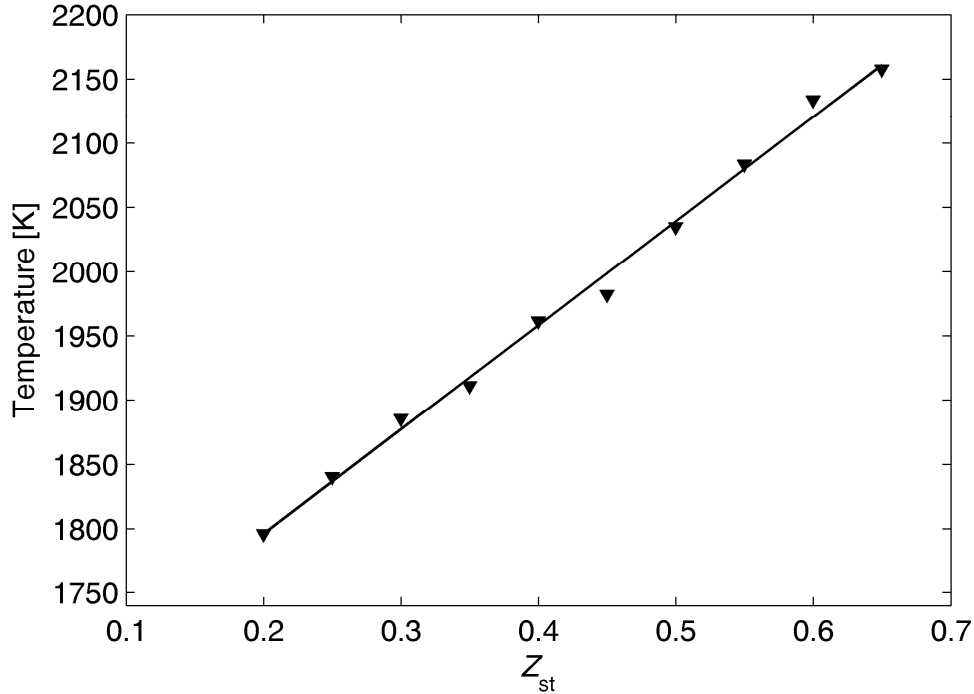


Figure 4.5. Comparison of measured inverse flame sooting limits and the model (line) obtained with  $E_a = 31$  kcal/mol;  $C_0 = 780$  K<sup>-1</sup> s<sup>-1</sup>,  $\tau = 22.4$  ms and  $(C/O)_{cr} = 0.53$ .

Plotting Eqs. 4.7 and 4.8 in  $Z_{st}$  space provides valuable insight into the effect of  $Z_{st}$  on soot inception. Both  $T_{kin}$  and  $T_{C/O}$  are plotted in Fig. 4.6 as functions of  $Z_{st}$  assuming a flame temperature of 2100 K and a residence time of 22 ms. The residence time was chosen to be similar to that of the inverse flame data in Table 4.2 but is for illustrative purposes only. To understand how to interpret Fig. 4.6, first consider the  $T_{kin}$  curve (solid line). This curve represents simple Arrhenius kinetics that are first order in fuel. The abscissa is the temperature on the fuel side of the flame and if we consider a given  $Z_{st}$  we see that soot will not form in the regions where temperature is low on the fuel side (e.g. below 1450 K at  $Z_{st} = 0.3$ ). That is, below the solid line even though there is a high concentration of fuel, the

kinetics are too slow to form soot in the available residence time. As we cross the solid line we move into a region where the temperature is sufficiently high to allow soot to form in the available time. The upper branch of the solid line represents a region very close to the peak temperature location where soot can not form because the fuel concentration is too low, approaching zero at the flame. Of course, multistep kinetics would alter the details of this description, but this simple description yields the critical features associated with flame structure.

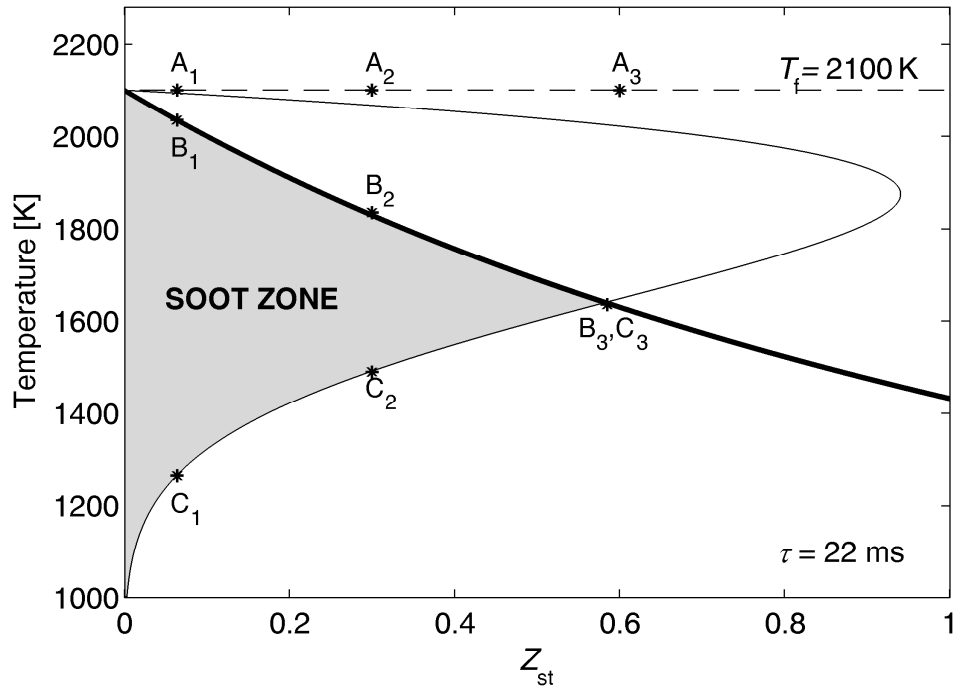


Figure 4.6. Representation of the collapse of the soot formation zone with increasing  $Z_{st}$ .

As we shall show below, the relevant branch on the  $T_{kin}$  curve is the lower branch, as the upper branch is not realizable in practice. Consider the dashed curve that represents  $T_{C/O}$  obtained from Eq. 4.8. Above  $T_{C/O}$ , soot cannot form because the C/O ratio is too low, *i.e.* there is too much oxygen available from oxygen-containing species relative to carbon from

carbon-containing species. Also, as can be shown from Eq. 4.8 the temperature at which this critical C/O ratio occurs decreases with  $Z_{st}$ .

This reduction of  $T_{C/O}$  with  $Z_{st}$  is critical to understanding why high  $Z_{st}$  flames can be made to be intrinsically soot free for any strain rate, *i.e.*, they can be “permanently” blue [42]. It can also be used to illustrate how, for a given residence time and flame temperature, a sooting limit can be achieved by increasing  $Z_{st}$ . To illustrate this, the results from the flame sheet model are plotted in mixture fraction space in Fig. 4.7. These figures correspond to the three flames considered in Fig. 4.6, which have identical flame temperatures and residence times but distinct stoichiometric mixture fractions. To begin this illustration, first consider Case 1 (as denoted by subscript 1) in Fig. 4.6, which represents a fuel/air flame with  $Z_{st} = 0.064$  and a flame temperature of approximately 2100 K.

Moving vertically from the x-axis to point  $C_1$  in Fig. 4.6 is equivalent to moving along the temperature curve from right to left in mixture fraction space in Fig. 4.7a. At  $C_1$  there is sufficient temperature, time, and fuel species for soot formation to occur on the fuel side of the flame where the local temperature is approximately 1250 K. At any temperature lower than  $C_1$  soot will not form because the chemistry is too slow. Moving vertically in Fig. 4.6 from  $C_1$  to  $B_1$ , we pass through the broad soot zone associated with the fuel/air flame, until we reach the location in the flame where sufficient oxygen containing species are available so that soot formation is no longer favored. At point  $B_1$  the soot zone ends because the local C/O ratio is equivalent to the critical C/O ratio. We note also that the high temperature soot zone boundary at  $B_1$  is not coincident with the peak temperature location at  $A_1$  although for low  $Z_{st}$  flames the two are relatively close. Thus, for low  $Z_{st}$  flames our results compare well with Glassman’s statement that soot particles begin forming at the nucleation boundary and are consumed at the location of stoichiometric flame

temperature[102]. As  $Z_{st}$  increases however, the high temperature soot zone boundary moves away from the stoichiometric flame temperature location, as will be shown next. It is also noteworthy that the finite distance between the peak temperature and the high temperature soot inception boundary predicted by the model indicates that a dead space should exist on the fuel side of the peak temperature where no soot can form as has been observed by Du [30].

Increasing  $Z_{st}$  to 0.3 while maintaining the same flame temperature and residence time, is Case 2 in Fig. 4.6. As we move up in temperature to point  $C_2$ , we notice that the low temperature boundary has moved to a higher temperature compared with  $C_1$  at  $Z_{st} = 0.064$ . The increased temperature necessary for the onset of soot can be explained by the lower fuel concentration at the  $Z$  location of  $C_2$ , as indicated in Fig. 4.7b. Moving vertically from  $C_2$  in Fig. 4.6 we note that the high temperature boundary at  $B_2$  is found at a lower temperature than that of the fuel/air case. This suggests that the effect of increasing  $Z_{st}$  results in oxidizing species moving farther into the fuel rich side of the peak temperature location where they are available to oxidize potential soot precursor species. Note that the peak temperatures of these two flames are the same; however, as seen in Figs. 4.7a and b, the location of peak temperature has shifted in mixture fraction space, as expected.

At  $Z_{st} = 0.6$ , we see from Fig. 4.6 that the low temperature boundary represented by  $C_3$  and the high temperature boundary represented by  $B_3$  have converged, indicating a sooting limit. If we first consider the low temperature boundary, which is governed by finite rate chemistry, there is sufficient fuel, temperature, and residence time for soot formation at  $C_3$ . However, by considering the boundary governed by the critical C/O ratio, we see that the increase in  $Z_{st}$  has moved oxygen-containing species farther into the fuel rich zone, thereby preventing soot formation at this location. We also note as before that the

magnitude of the peak temperature has not changed but the location of the peak temperature has shifted further in mixture fraction space as indicated by  $A_3$  in Fig. 4.7c.

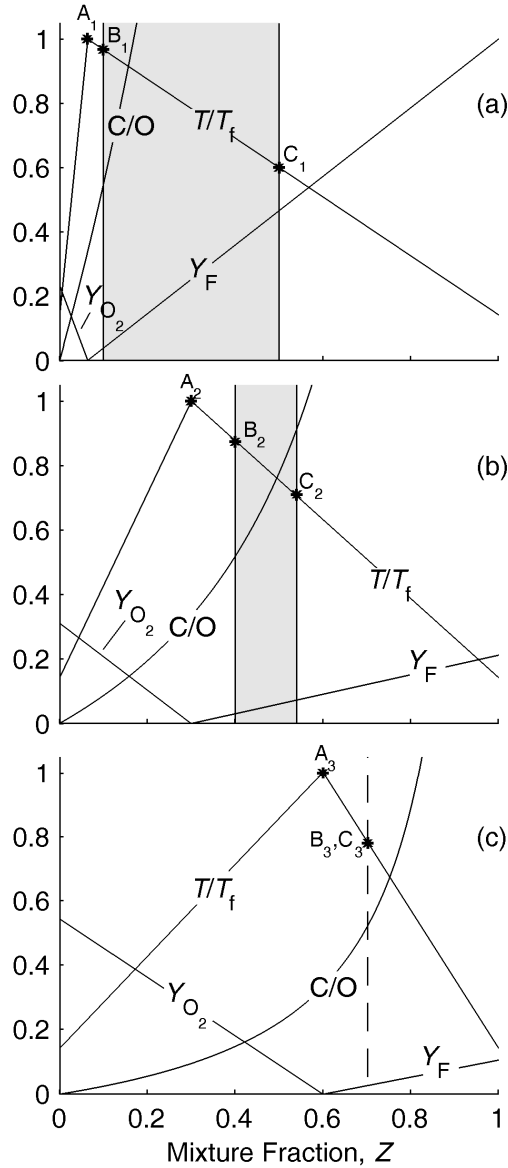


Figure 4.7. Flame sheet approximation results for Cases 1, 2, and 3 from Fig. 4.6 showing shrinking of soot formation zone due to convergence of low-temperature ( $T_{kin}$ ) and low C/O ratio (high-temperature  $T_{C/O}$ ) boundaries.

This approach to describing the dynamics of soot inception in nonpremixed flames can be used to understand the controlling mechanisms for the sooting limits at different values of  $Z_{st}$ . In Fig. 4.8 plots similar to Fig. 4.6 are shown for flames corresponding to the

inverse diffusion flames in Fig. 4.3. In Fig. 4.8a, a limit flame at  $Z_{st} = 0.2$  with a flame temperature of 1800 K is shown. For this flame temperature and residence time the model suggests that the sooting limit is controlled by flame temperature, residence time, and fuel dilution alone, with no supplemental effect from the critical C/O ratio boundary. This can be seen as the  $T_{kin}$  and  $T_{C/O}$  curves intersect slightly above the point where  $T_{kin}$  has reached its peak value of  $Z_{st}$ . That is, the model indicates that for a flame with a residence time of 0.022 s and a flame temperature of 1800 K the sooting limit is achieved at  $Z_{st} = 0.2$  because there is insufficient time, temperature, and fuel—not because of the availability of oxygen containing species as characterized by the  $T_{C/O}$  curve. This case is characteristic of the common case of a fuel/air or diluted-fuel/air flame. In Fig. 4.8b the model predicts a sooting limit at  $Z_{st} = 0.25$  for a flame temperature of 1840 K. At this temperature and residence time the  $T_{kin}$  and  $T_{C/O}$  curves intersect below the point where  $T_{kin}$  has reached its peak value of  $Z_{st}$  suggesting that the boundary associated with oxygen-containing species (the critical C/O boundary) begins to affect sooting limits when  $Z_{st} > 0.2$ .

In Fig. 4.8c the model predicts a sooting limit at  $Z_{st} = 0.4$  for a flame temperature of 1960 K. Unlike the case in Fig. 4.8a, now the  $T_{C/O}$  curve does not intersect the  $T_{kin}$  curve until well below the point where  $T_{kin}$  reaches its peak value of  $Z_{st}$ . In other words, the soot region is being substantially narrowed due to the critical C/O boundary. Figure 4.8d demonstrates the dramatic effect of the critical C/O ratio boundary when the flame temperature is 2150 K at  $Z_{st} = 0.65$ . The  $T_{kin}$  curve clearly extends beyond the realizable value of stoichiometric mixture fraction, suggesting that if the soot zone were considered to be strictly governed by pyrolysis then one would conclude that a sooting limit cannot exist for this flame temperature and residence time. On the contrary, a sooting limit is easily obtained for this flame because of the effect of the critical C/O ratio boundary. These results dramatically

illustrate that flame structure governs soot inception in high temperature oxygen-enhanced/diluted-fuel (*i.e.* high  $Z_{st}$ ) flames.

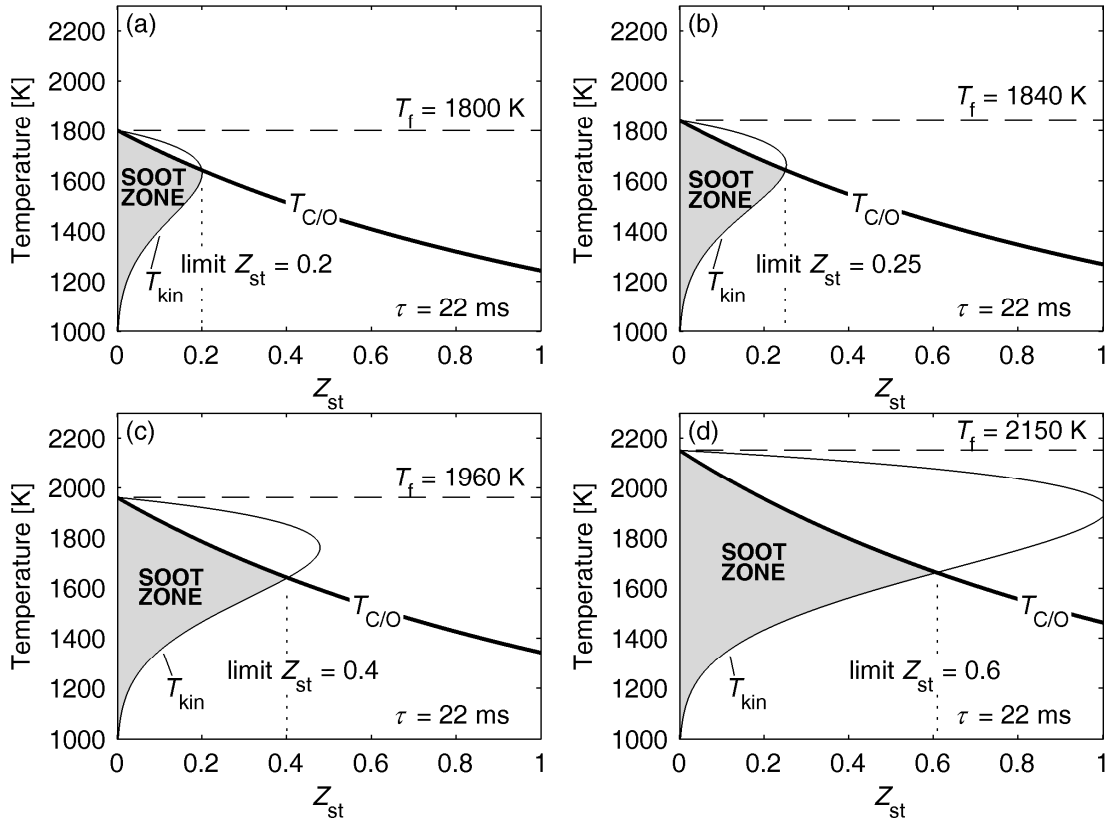


Figure 4.8. Representation of the sooting zones of four flames with varying flame temperatures.

## 4.4 Conclusions

A simple theory for predicting soot inception limits in nonpremixed flames has been presented that takes into account temperature, residence time, and gas composition. This model is an extension of previous soot inception models for diffusion flames in that it is applicable to high  $Z_{st}$  combustion. This model is particularly useful for demonstrating how oxyfuel combustion may lead to reduced soot formation without a compromise in flame temperature. By increasing the stoichiometric mixture fraction via the combination of oxygen enrichment and fuel dilution, soot formation is reduced and thus the sooting limit

occurs at a higher temperature. This is found to occur in both normal and inverse flames. The sooting limit inception temperature is influenced by residence time, and when the effects of residence time are removed it is clear that increasing  $Z_{st}$  affects both the normal and the inverse flames equally, indicating that flame configuration does not have a strong effect on the sooting limit. As demonstrated by the model, the effect of increasing  $Z_{st}$  is to move the two boundaries of the soot formation zone towards each other. We find that the analysis made by Glassman [102], that the soot formation region is bounded by the isotherms corresponding to the incipient particle formation temperature and the stoichiometric flame temperature, to be a good approximation for flames of very low  $Z_{st}$ , *e.g.* the typical fuel/air flame. The proposed sooting limit model reveals, however, that the high temperature soot boundary can be moved well into the fuel side of the peak temperature for flames with higher  $Z_{st}$ . We find that oxygen enrichment begins to affect soot inception limits when  $Z_{st} > 0.2$ . Following the work of Sunderland *et al.* [36], the high temperature soot boundary is described as the location where the local C/O ratio is equal to a critical value. The results of this work suggest that  $(C/O)_{cr} = 0.53$  for the case of ethylene. It is demonstrated that the soot inception temperature is not a unique quantity, but rather is dependent upon residence time and  $Z_{st}$ . Finally, after comparing various measurements of soot inception temperature found in the literature, we find that there is an important distinction to be made between a soot inception temperature that is measured at the low temperature boundary of a large soot formation zone ( $T_{kin}$ ), and an inception temperature measured at the sooting limit, where the soot zone can be considered infinitely thin ( $T_{lim}$ ).



# 5 Structural Changes in OEC Resulting in the Presence of Appreciable Oxygen at the Location of Maximum Temperature

## 5.1 Introduction

When utilizing oxygen-enhanced combustion in non-premixed systems the concentrations of the free-stream fuel and oxidizer can have a dramatic impact on the flame structure, i.e. the relationship between local temperature and local species concentrations. When oxygen-enrichment is combined with fuel-dilution such that a constant amount of inert is present at the flame, the adiabatic flame temperature is unchanged. Nonetheless, the flame structure is changed dramatically. The extent of oxygen-enrichment and fuel dilution can be quantified by the stoichiometric mixture fraction,  $Z_{st}$ , given by

$$Z_{st} = \left(1 + \sigma_{O_2,F} Y_{F, fu} / Y_{O_2, ox}\right)^{-1} \quad (5.1)$$

where  $\sigma_{O_2,F}$  and  $Y_{ij}$  are defined as in Chapter 3. While examining the effects of flame structure on soot formation, Du and Axelbaum [30] showed that increasing the stoichiometric mixture fraction in ethylene flames can result in a nearly two order of magnitude increase in the concentration of molecular oxygen at the location of maximum temperature ( $x_{T_{max}}$ ), with molar concentrations of  $O_2$  reaching 8 vol.%. This phenomenon is referred to here as *appreciable molecular oxygen at the location of maximum temperature* and has been subsequently observed both numerically and experimentally by Sun et al. [33] in acetylene flames and Cheng et al. [43] in methane flames. Experimental results suggest that

characteristics of the OEC-process are quite sensitive to changes in the concentration of molecular oxygen at the location of maximum temperature.

With regards to flame strength, Du and Axelbaum [61], Chen and Axelbaum [39], and Kitajima et al. [62] showed experimentally that increasing  $Z_{st}$  results in a higher strain rate and scalar dissipation rate at extinction for non-premixed counterflow flames. At high  $Z_{st}$  extinction scalar dissipation rates 20-40 times greater than for fuel-air flames can be obtained even when the equilibrium flame temperatures are the same. To understand their results Du and Axelbaum and Chen and Axelbaum simulated the flames using a counterflow flame code and proposed that the availability of oxygen in the high temperature region due to increased  $Z_{st}$  accelerates the chain branching reaction  $H + O_2 = OH + O$  resulting in improved flame strength. Furthermore, Chen and Axelbaum [39] found that at high  $Z_{st}$  the flames are able to resist extinction at lower temperatures because at high  $Z_{st}$  the location of radical production and  $x_{T_{max}}$  are coincident, which allows the branching reaction to “make most efficient use” of the high temperature zone. To the contrary, in fuel-air flames the radical production zone is found at a lower temperature on the oxidizer side of  $x_{T_{max}}$ .

The increased presence of oxygen and oxidizing species in the region of high temperature for high  $Z_{st}$  flames can also influence soot inception by affecting both the rate of soot precursor oxidation and the relative location of precursor oxidation to precursor formation as discussed in Chapter 4. Sunderland et al. [36] proposed a theory suggesting that in order for soot to form in a non-premixed flame the local temperature and local carbon-to-oxygen ratio (C/O) must be above threshold values and the work in Chapter 4 expanded this theory to include the effects of finite-rate chemistry and residence time and developed a simple model that describes the region conducive to soot inception as being confined

between two boundaries: a low temperature boundary that is governed by finite-rate chemistry and can be manipulated by changing the fuel concentration, flame temperature, or characteristic residence time, and a high temperature boundary that is related to the presence of oxygen and oxidizing species and is characterized by the local C/O ratio as described in Sunderland et al. [36].

The above findings indicate that high  $Z_{st}$  dramatically affects flame properties, and that one of the primary reasons for this is that high  $Z_{st}$  flames have appreciable molecular oxygen at the location of maximum temperature. While the existence of appreciable molecular oxygen has been observed both numerically and experimentally [30, 33, 43], no explanation has been given in the literature for this phenomenon. The purpose of this work is to develop such an explanation by using a counterflow flame code with detailed chemistry in order to distinguish the key sub-mechanisms responsible for the existence of appreciable  $O_2$  at  $x_{T_{max}}$ . Results obtained in this study will further our fundamental understanding of the effect of oxygen-enhancement and fuel-dilution (i.e. increasing  $Z_{st}$ ) on flame structure.

## 5.2 Numerical

The counterflow flame code employed here was originally developed by Kee et al. [130] for premixed opposed-flow flames and was later modified for adiabatic non-premixed combustion by Lutz et al. [131]. Chemical reaction rates, transport properties, and thermodynamic properties are evaluated by the Chemkin software package. The detailed kinetic mechanism used here consists of 101 species and 544 reactions and was proposed by Wang and Frenklach [132] and modified by Appel et al. [133]. The mechanism is publicly available, and therefore, is not included in the appendix.

The accuracy of a mechanism similar to that used here was demonstrated by Sun et al. [33] at low and high  $Z_{st}$  by comparing numerical results with temperature and species profiles obtained via spontaneous Raman spectroscopy. The larger mechanism used here was validated by modeling the flame conditions of Sun et al. and verifying that temperature and species profiles were replicated.

The computational grid was initialized with 21 grid points and the fuel and oxidizer stream inlet boundaries were spaced 2 cm apart. Adaptive grid refinement was utilized resulting in approx. 105 grid points on average at convergence. The fuel and oxidizer stream exit velocities were held constant at 80 cm/s for all flames resulting in a strain-rate,  $a$ , of  $62 \text{ s}^{-1}$  for the fuel-air case (Flame A),  $61 \text{ s}^{-1}$  for the  $Z_{st} = 0.4$  case (Flame B), and  $68 \text{ s}^{-1}$  for the  $Z_{st} = 0.78$  case (Flame C). The strain rates were determined by fitting a straight line to the computed velocity profile upstream of the thermal mixing layer on the oxidizer side for Flames A and B, and on the fuel side for Flame C. Chen and Axelbaum [39] reported numerically determined extinction strain rates greater than  $2400 \text{ s}^{-1}$  for ethylene counterflow flames at  $T_{ad} = 2370 \text{ K}$ , thus the flames considered in this study are far from extinction. The square of the gradient in mixture fraction  $(dZ/dx)^2$ , which is proportional to the scalar dissipation rate, was also calculated at the location of stoichiometry for all flames. The values were found to be  $0.45 \text{ cm}^{-2}$ ,  $5.76 \text{ cm}^{-2}$ , and  $4.12 \text{ cm}^{-2}$  for Flames A, B, and C, respectively. To ensure that the higher scalar dissipation rates of Flames B and C were not responsible for the increasing concentrations of  $\text{O}_2$  at  $x_{T_{max}}$ , Flames B and C were generated a second time (labeled Flames B' and C') with fuel and oxidizer exit velocities of 15 cm/s resulting in strain rates of approx.  $8 \text{ s}^{-1}$  and mixture fraction gradients much closer to that of Flame A. It was observed that the peak temperature shift was more pronounced in Flames B' and C' resulting in an even higher concentration of  $\text{O}_2$  at the location of maximum temperature.

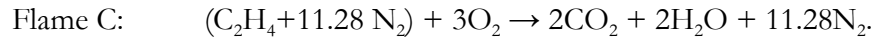
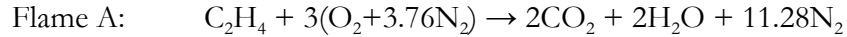
Thus, leakage is not responsible for the presence of appreciable  $O_2$  at  $x_{T_{\max}}$  in high  $Z_{st}$  flames. Rather, this phenomenon is a result of changes in flame structure. The relevant flame parameters are provided in Table 5.1 for reference.

**Table 5.1. Flame Parameters**

Flame	$X_{F, \text{fu}}$	$X_{O_2, \text{ox}}$	$a$	$(dZ/dx)^2$	$O_2$ at $x_{T_{\max}}$
--	--	--	(s <sup>-1</sup> )	(cm <sup>-2</sup> )	(vol.%)
A	1.0	0.21	62	0.45	0.34
B	0.16	0.33	61	5.76	0.93
C	0.08	1.0	68	4.12	8.18
B'	0.16	0.33	8	1.02	1.39
C'	0.08	1.0	9	0.76	8.22

### 5.3 Preliminary analysis: comparing the detailed chemistry with the flame sheet approximation

Significant insight can be gained by comparing the basic structure of low and high  $Z_{st}$  flames obtained with detailed chemistry and with the traditional flame sheet approximation. For example, it is instructive to compare the case of ethylene burning in air with that of heavily-diluted ethylene burning in pure oxygen represented by the global reactions:



In Flame C the stoichiometric amount of  $N_2$  is the same as that found in air except the  $N_2$  is placed in the fuel stream. In this way the adiabatic flame temperature is unaffected [30]; however, the flame structure changes dramatically as demonstrated in Fig. 5.1 below. The abscissa in Fig. 5.1 is the mixture fraction,  $Z$ , defined as the local fraction of mass that originated from the fuel stream. Thus,  $Z = 0$  is the oxidizer boundary and  $Z = 1$  is the fuel boundary.

In Fig. 5.1, results from the flame sheet approximation are given by the solid lines while the dashed lines represent numerical results similar to those of Du and Axelbaum [30] for flames at strain rates away from their extinction strain rates. We note first that for the conventional fuel-air flame shown in Fig. 5.1a the numerical results agree with the flame sheet approximation in that molecular oxygen is depleted at the location of maximum temperature,  $x_{T_{\max}}$ , which is coincident with the location of stoichiometric composition for the global reaction,  $x_{Z_{st}}$ . The consistency of this result with the flame sheet approximation under fuel-air conditions may lead one to believe that  $O_2$  will be depleted at the  $x_{T_{\max}}$  for OEC as well. However, this is not the case, as demonstrated in Fig. 5.1b where we see that the concentration of molecular oxygen at  $x_{T_{\max}}$  has increased to 8 vol.% for the high  $Z_{st}$  flame.

Clearly, for high  $Z_{st}$  flames the location of oxygen depletion is not coincident with  $x_{T_{\max}}$  because the location of maximum temperature has shifted toward the oxidizer side of  $x_{Z_{st}}$ . From this preliminary analysis, there are two key questions to consider when explaining the presence of appreciable molecular oxygen at  $x_{T_{\max}}$ :

- (1) Molecular oxygen is depleted at  $x_{Z_{st}}$  for low and high  $Z_{st}$  flames; however, are the controlling mechanisms for molecular oxygen depletion the same at low and high  $Z_{st}$ ?
- (2) Why does  $x_{T_{\max}}$  shift toward the oxidizer side of  $x_{Z_{st}}$  for high  $Z_{st}$  flames?

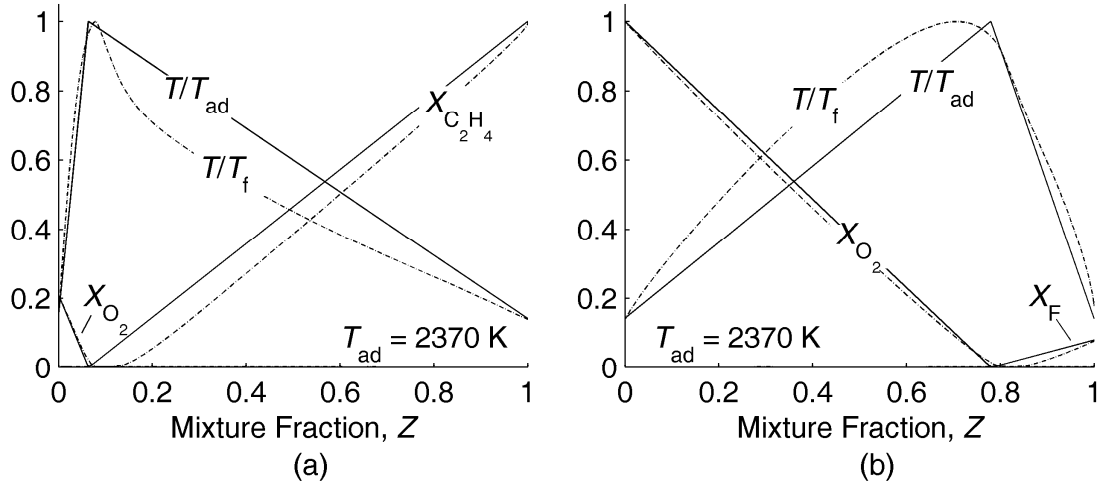


Figure 5.1. Flame sheet approximation (solid) and numerical solution (dash-dot) for (a) ethylene/air ( $Z_{st} = 0.064$ ) and (b) diluted-ethylene/oxygen ( $Z_{st} = 0.78$ ).

## 5.4 Results and Discussion

### 5.4.1 Characterizing oxygen depletion

To explain the presence of appreciable molecular oxygen at  $x_{T_{max}}$  for high  $Z_{st}$  flames, first we analyze the process of molecular oxygen depletion. Specifically we evaluate

- (i) the characteristics of the location where  $O_2$  is depleted;
- (ii) the reaction(s) responsible for  $O_2$  consumption in both low and high  $Z_{st}$  flames.

Figures 5.2a-c present profiles of the  $O_2$  mole fraction for Flames A-C and corresponding profiles of the net rate of molecular oxygen consumption and the rate of the reaction



In this figure  $x_{Z_{st}}$  is indicated by the filled arrow and  $x_{T_{max}}$  is indicated by the open-faced arrow. From this figure it is clear that 5.1R is the dominant reaction responsible for  $O_2$  consumption for flames of any  $Z_{st}$ . We note that for all flames, the location of maximum net

consumption of molecular oxygen is only slightly to the fuel side (right) of  $x_{Z_{st}}$  and that the concentration of  $O_2$  at each of these locations is almost identical for the three flames.

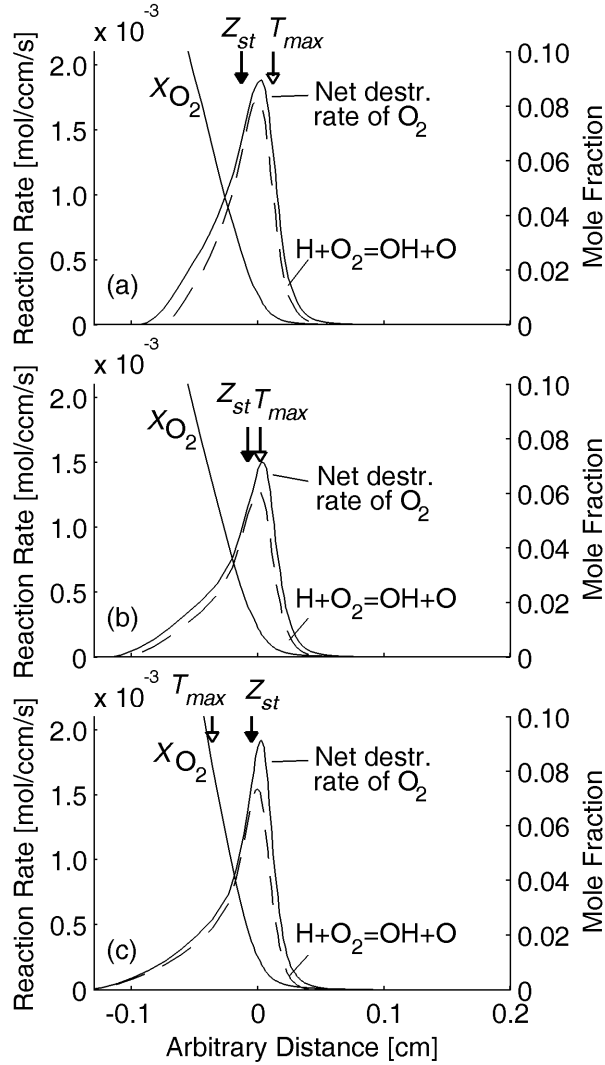


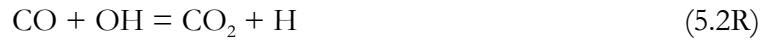
Figure 5.2. Oxygen mole fraction and net rate of oxygen consumption for flames at (a)  $Z_{st} = 0.064$ , (b)  $Z_{st} = 0.4$ , and (c)  $Z_{st} = 0.78$ . Filled arrow indicates  $x_{Z_{st}}$ . Open-faced arrow indicates  $x_{T_{max}}$ .

For example, the  $O_2$  mole fraction at the location of maximum  $O_2$  consumption is  $1.13 \times 10^{-2}$  in the fuel-air flame,  $1.06 \times 10^{-2}$  in the  $Z_{st} = 0.4$  flame, and  $1.21 \times 10^{-2}$  in the  $Z_{st} = 0.78$  flame. Moreover, one could consider the location where the rate of 5.1R reaches its maximum to be the characteristic location of  $O_2$  depletion, independent of  $Z_{st}$ , since the rate of  $O_2$  consumption diminishes rapidly and in a similar fashion for all flames beyond this



location on the fuel side. As mentioned previously, the location of oxygen depletion differs significantly from  $x_{T_{\max}}$  for high  $Z_{\text{st}}$  flames because  $x_{T_{\max}}$  has shifted toward the oxidizer side of  $x_{Z_{\text{st}}}$ . Because of this shift, Fig. 5.2 demonstrates that the concentration of  $\text{O}_2$  at  $x_{T_{\max}}$  increases from 0.3 vol.% for Flame A to 8 vol.% for Flame C.

The location of molecular oxygen depletion, or equivalently,  $x_{Z_{\text{st}}}$ , can also be identified with the location of product formation (i.e.,  $\text{CO}_2$  and  $\text{H}_2\text{O}$ ). Figure 5.3 shows the net rate of 5.1R with the rates of reactions



and



for Flames A-C. The relative locations where 5.1R-5.3R occur and the basic trends of the distributions are similar for all three flames.

Noting that 5.1R requires H radicals and both 5.2R and 5.3R produce H radicals, it can be seen that in the region where molecular oxygen is depleted, a “balancing” is observed between the oxygen consuming reaction ( $\text{H} + \text{O}_2 = \text{OH} + \text{O}$ ) and the reactions that produce H radicals. In this sense, we can talk about a kinetic coupling between H and OH radicals and moreover between 5.1R-5.3R, which confines the location of molecular oxygen depletion to the location of stoichiometry for flames of any  $Z_{\text{st}}$ . Thus, we conclude that the mechanisms responsible for  $\text{O}_2$  depletion are unaffected by changes in  $Z_{\text{st}}$ , and the presence of appreciable molecular oxygen at the location of maximum temperature is a result of the shift in maximum temperature relative to the location of  $\text{O}_2$  depletion at high  $Z_{\text{st}}$ .

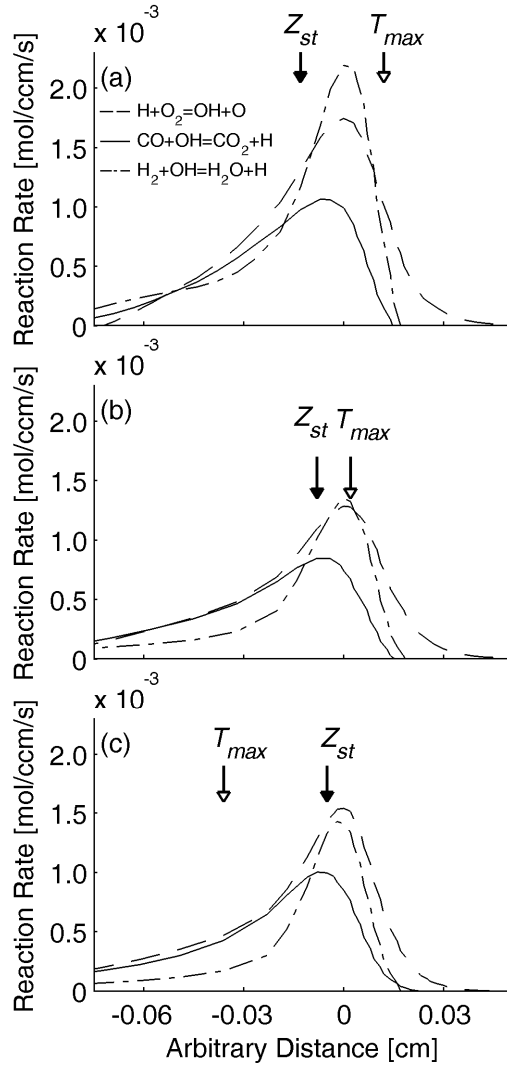


Figure 5.3. Rates of reactions 5.1R, 5.2R, and 5.3R for (a) fuel/air  $Z_{st} = 0.064$ , (b)  $Z_{st} = 0.4$ , and (c) diluted-fuel/oxygen  $Z_{st} = 0.78$ . Filled arrow indicates  $x_{Z_{st}}$ . Open-faced arrow indicates  $x_{T_{max}}$ .

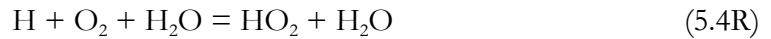
### 5.4.2 Maximum temperature shift at high $Z_{st}$

Next we investigate the shifting of  $x_{T_{max}}$  relative to the location of  $O_2$  depletion at high  $Z_{st}$ . Early investigations on the structure of non-premixed flames revealed distinct heat release “zones” within the reaction region. Pandya and Weinberg [134] and Pandya and Srivastava [135] observed two small valleys in the heat release profile on either side of the maximum heat release, suggesting a reaction region with three distinct zones. Bilger [136]

proposed that the reaction region in hydrocarbon diffusion flames could be described by a double-zone structure consisting of an endothermic pyrolysis zone and an exothermic zone at the location of stoichiometry. In a more recent study, Sun et al. [33] distinguished the following three reaction zones in ethylene flames:

1. A zone of pyrolysis with a net conversion of  $C_2H_4$  to  $C_2H_2$
2. A primary oxidation zone characterized by acetylene oxidation and CO formation
3. A secondary oxidation zone characterized by  $CO_2$  and  $H_2O$  formation via 5.2R and 5.3R, respectively.

With respect to the total heat release rate profile Sun et al. also noted that three distinct zones could be identified and associated the secondary exothermic heat release peak with 5.2R and 5.3R and the reactions



and



In our flames we also see three heat release zones in the profile of the total heat release rate as demonstrated in Fig. 5.4. We also point out that in the low  $Z_{st}$  flame of Fig. 5.4a the location of peak temperature, indicated by the open faced arrow, is coincident with the peak heat release location, while in the high  $Z_{st}$  flame the location of peak temperature has shifted to the oxidizer side (left) of the peak heat release location.

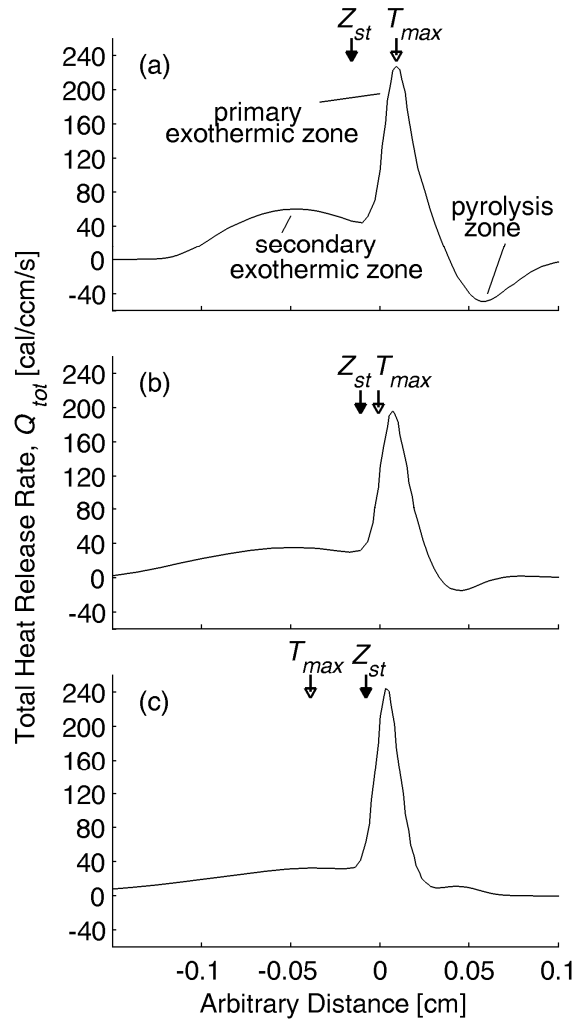


Figure 5.4. Total heat release rate for (a) fuel/air  $Z_{st} = 0.064$ , (b)  $Z_{st} = 0.4$ , and (c) diluted-fuel/oxygen  $Z_{st} = 0.78$ . Filled arrow indicates  $x_{Z_{st}}$ . Open-faced arrow indicates  $x_{T_{max}}$ .

Figure 5.5 demonstrates that it is actually possible to identify four overlapping, but distinct zones with respect to heat release. The reactions responsible for the majority of the heat release in each zone are provided in Table 5.2, and were selected such that the overall shape of the total heat release profile was maintained and approx. 65% of the total integrated heat release was captured.

In Fig. 5.5 each curve represents the combined heat release in each zone from the reactions listed in Table 5.2, e.g.  $Q_{ex1}$  is the exothermic heat release from the dominant

reactions identified in Zone 1. From right to left in Fig. 5.5, we distinguish the four zones as the

1. endothermic pyrolysis zone
2. high heat intensity zone
3. moderate heat intensity zone
4. low heat intensity zone.

For low  $Z_{st}$  flames the pyrolysis zone (Zone 1) is overall endothermic; however, as  $Z_{st}$  increases the endothermicity of the pyrolysis zone decreases until it eventually becomes overall exothermic as demonstrated by the pyrolysis zone in Fig. 5.4c. Just as exothermic reactions may contribute significantly in the pyrolysis zone, significant endothermic reactions are found in the high heat intensity zone (Zone 2) and moderate heat intensity zone (Zone 3) (see Table 5.2 in detail).

As in Sun et al. [33], we note that the dominant reactions in the endothermic pyrolysis zone involve the decomposition of ethylene and the vinyl radical in the formation of acetylene, while the reactions dominating the high heat intensity zone involve the oxidation of acetylene, the methyl radical, and CH by O. The moderate heat intensity zone is characterized by the formation of  $\text{CO}_2$  and  $\text{H}_2\text{O}$  via CO and  $\text{H}_2$  oxidation by OH and the consumption of  $\text{O}_2$  by H radicals. Recognizing that 5.1R is endothermic while 5.2R and 5.3R produce substantial heat, it appears that the kinetic coupling discussed previously is further intensified by the interplay of the exo- and endothermic reactions in Zone 3. Furthermore, Fig. 5.6 demonstrates that the endothermicity of 5.1R and the exothermicity of 5.2R nearly mirror each other. Finally, the broad low heat intensity zone (Zone 4) is characterized by 5.4R and 5.5R.

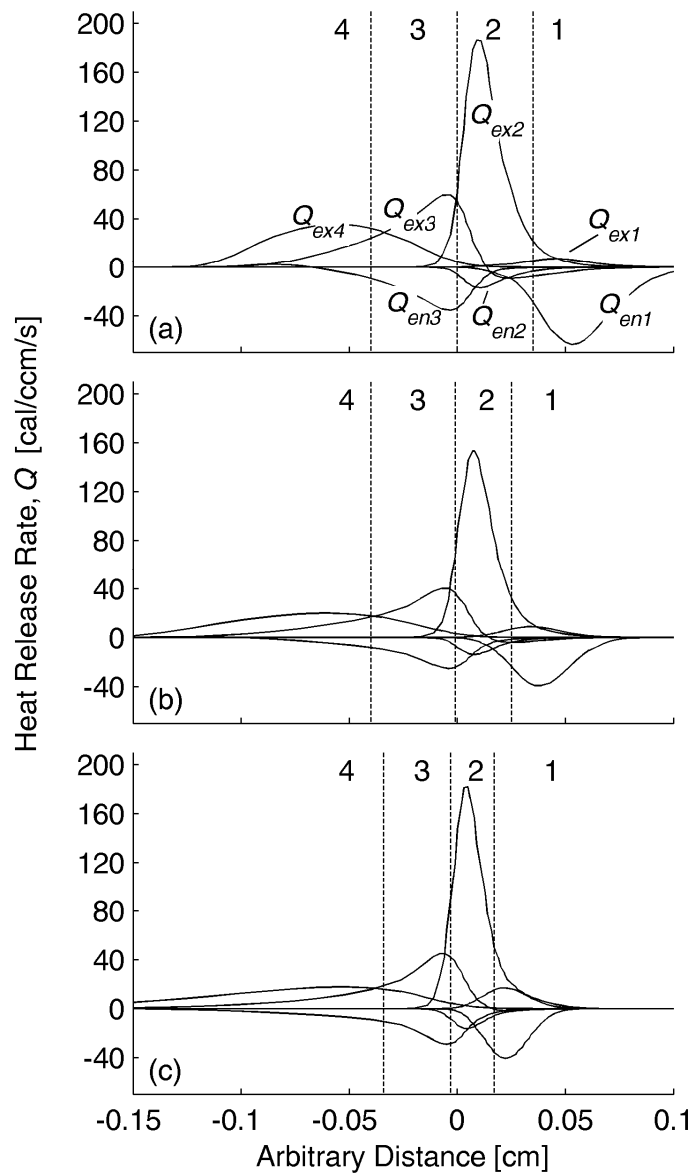


Figure 5.5. Four zones of heat release for (a) fuel/air  $Z_{st} = 0.064$ , (b)  $Z_{st} = 0.4$ , and (c) diluted-fuel/oxygen  $Z_{st} = 0.78$ .  $Q_{ex(i)}$  represents the summation of the heat released by the exothermic reactions associated with Zone (i).  $Q_{en(i)}$  represents the summation of the heat consumed by the endothermic reactions associated with Zone (i).

**Table 5.2. Dominant reactions in four different heat zones.**

<b>Exothermic Reactions</b>			
	$Q_{\max} \geq 20$ (cal/ccm/s)	$10 \leq Q_{\max} < 20$ (cal/ccm/s)	$5 \leq Q_{\max} < 10$ (cal/ccm/s)
Zone 1			$C_2H_3+H(+M)=C_2H_2+H_2(+M)$
Zone 2	$C_2H_2+O=CH_2+CO$	$C+O_2=CO+O$	$CH_2O+OH=HCO+H_2O$
	$CH+H_2O=CH_2O+H$	$HCCO+H=CH_2^*+CO$	$CH_2O+H=HCO+H_2$
		$C_2H_2+O=HCCO+H$	$HCO+H=CO+H_2$
		$C+OH=CO+H$	$CH_2^*+CO_2=CH_2O+CO$
		$CH_3+O=CH_2O+H$	$CH+CO_2=HCO+CO$
			$HCCO+O=H+CO+CO$
			$CH_2+OH=CH_2O+H$
			$C_2H+O_2=HCO+CO$
			$CH+H=C+H_2$
		$CH_3+H(+M)=CH_4(+M)$	
Zone 3	$CO+OH=CO_2+H$	$H+OH(+M)=H_2O(+M)$	
	$H_2+OH=H_2O+H$		
Zone 4		$H+O_2+H_2O=HO_2+H_2O$	$HO_2+OH=O_2+H_2O$
			$HO_2+H=OH+OH$
			$H+O_2+N_2=HO_2+N_2$
			$OH+OH=O+H_2O$
<b>Endothermic Reactions</b>			
	$ Q_{\min}  \geq 20$ (cal/ccm/s)	$10 \leq  Q_{\min}  < 20$	$5 \leq  Q_{\min}  < 10$
Zone 1	$C_2H_3(+M)=C_2H_2+H(+M)$		$C_2H_4+H=C_2H_3+H_2$
Zone 2		$HCO(+M)=H+CO(+M)$	
Zone 3	$H+O_2=OH+O$	$OH+OH=H_2O+O$	

**Note:** the asterisk denotes an energized molecule

This fourth zone plays an important role in the phenomenon of appreciable molecular oxygen being present at the location maximum temperature in high  $Z_{st}$  flames because it is displaced from the location of  $O_2$  depletion and contributes substantially to the secondary peak in the total heat release rate (Fig. 5.4). As noted previously, the exothermic contribution from 5.2R to the total heat release rate profile is counteracted by the endothermic heat release from 5.1R. This amplifies the observed exothermic contribution from 5.4R and 5.5R and displaces the secondary exothermic zone peak farther from the location of  $O_2$  depletion. We also point out that the production of  $H_2O$  in Zone 4 differs

from that of Zone 3 in that the intermediate step (5.4R) forming  $\text{HO}_2$  in Zone 4 requires a third body and is inversely dependent on temperature. Moreover, while oxygen is consumed in the formation of  $\text{HO}_2$ , it is produced when  $\text{HO}_2$  forms  $\text{H}_2\text{O}$  in 5.5R such that the net  $\text{O}_2$  depletion rate in Zone 4 by 5.4R and 5.5R, shown in Fig. 5.7, is an order of magnitude less than the peak  $\text{O}_2$  depletion rate via the reaction  $\text{H} + \text{O}_2 = \text{OH} + \text{O}$  (compare Fig. 5.2).

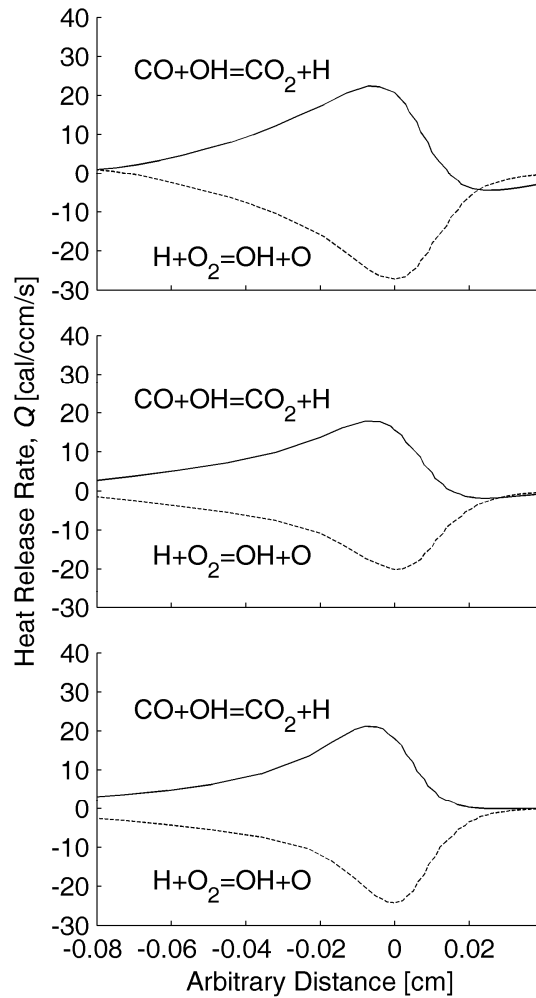


Figure 5.6. Heat release from reactions 5.1R and 5.2R for (a) fuel/air  $Z_{\text{st}} = 0.064$ , (b)  $Z_{\text{st}} = 0.4$ , and (c) diluted-fuel/oxygen  $Z_{\text{st}} = 0.78$ .



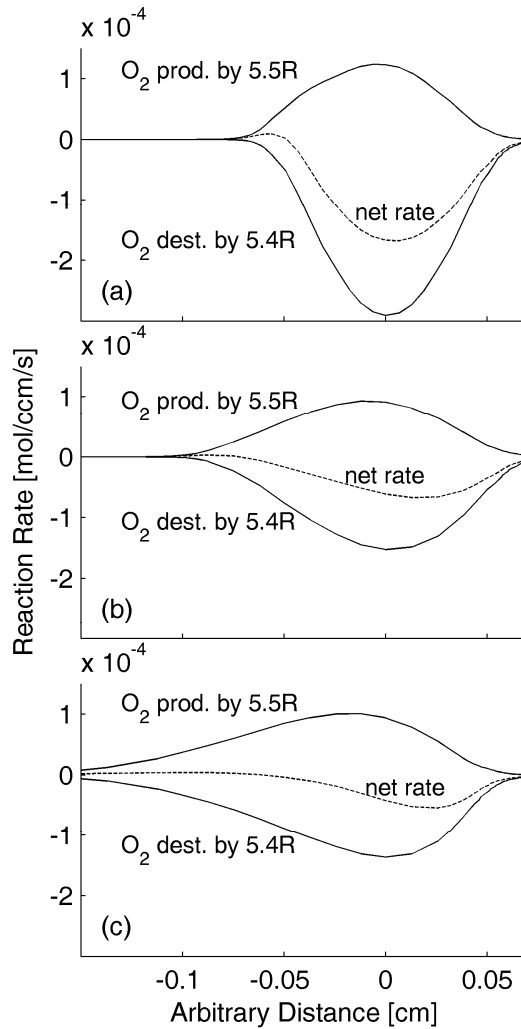


Figure 5.7. Rates of  $O_2$  destruction and production by reactions 5.4R and 5.5R for (a) fuel/air  $Z_{st} = 0.064$ , (b)  $Z_{st} = 0.4$ , and (c) diluted-fuel/oxygen  $Z_{st} = 0.78$ .

Figure 5.7 also shows that 5.4R and 5.5R are broadened at high  $Z_{st}$  and that the peak rate of 5.4R is reduced by a factor of approx. 3 when comparing Flame A to Flame C. Comparing the temperatures and the H,  $O_2$ , and  $H_2O$  concentrations in this zone for Flames A and C, we note that the broadening of 5.4R and 5.5R is due to the higher  $O_2$  concentration, while the reduced peak rate of reaction 5.4R is predominantly due to the increased temperature observed in this zone for Flame C because of the temperature shift. Even though the lower peak rate of 5.4R at high  $Z_{st}$  reduces the amplitude of the exothermic

heat release in this zone, the broadening of 5.4R and 5.5R result in exothermic heat release at locations farther displaced from the location of O<sub>2</sub> depletion. As will be demonstrated below, the separation of the location of O<sub>2</sub> depletion and this secondary heat release zone contribute to the shifting of the location of maximum temperature.

To explain the shifting of the maximum temperature relative to the location of O<sub>2</sub> depletion at high  $Z_{st}$  a method of superposition was used to evaluate the effective increase in temperature (enthalpy) that would result from displaced point sources of heat in a diffusion controlled system. For simplicity, we perform a simple qualitative analysis for both low and high  $Z_{st}$  flames to demonstrate the effect of two displaced heat release points. These points represent the primary exothermic zone where acetylene (as a product of ethylene decomposition) is oxidized and the secondary exothermic zone where the heat release from 5.2R-5.5R combines to form the secondary heat release maximum. In Fig. 5.8 the vertical dashed lines represent the point sources of heat release. The lightweight solid lines represent the temperature profiles,  $\theta_1$  or  $\theta_2$ , which would result if only the primary heat source or secondary heat source existed, respectively. The superposition of the two independent temperature profiles,  $\theta_3$ , is represented by the bold curve and the approximate location of stoichiometry is given by the filled arrow. We note immediately in Fig. 5.8b that the shifting of  $x_{T_{max}}$  toward the oxidizer side of  $x_{Z_{st}}$  which results in the presence of appreciable O<sub>2</sub> at  $x_{T_{max}}$  for the high  $Z_{st}$  flame, is captured in this simple demonstration. Note also that for the low  $Z_{st}$  fuel-air flame of Fig. 5.8a  $x_{T_{max}}$  and  $x_{Z_{st}}$  are nearly coincident, as expected.

The shifting of  $x_{T_{max}}$  towards the oxidizer side of  $x_{Z_{st}}$  can be explained by considering how the magnitude of the independent temperature profile slopes change in Fig. 5.8 when going from low to high  $Z_{st}$ . Beginning with the low  $Z_{st}$  flame of Fig. 5.8a and

moving from left to right we see that  $\theta_3$  increases with a constant slope until the location of the heat source responsible for  $\theta_2$  is reached. At this point, the slope of  $\theta_3$  is reduced because  $\theta_2$  is decreasing; however,  $\theta_3$  continues to increase because the magnitude of the positive slope associated with  $\theta_1$  is greater than the magnitude of the negative slope associated with  $\theta_2$ . Upon reaching the location of the heat source responsible for  $\theta_1$ , the  $\theta_3$  curve decreases linearly since both  $\theta_1$  and  $\theta_2$  decrease after this point.

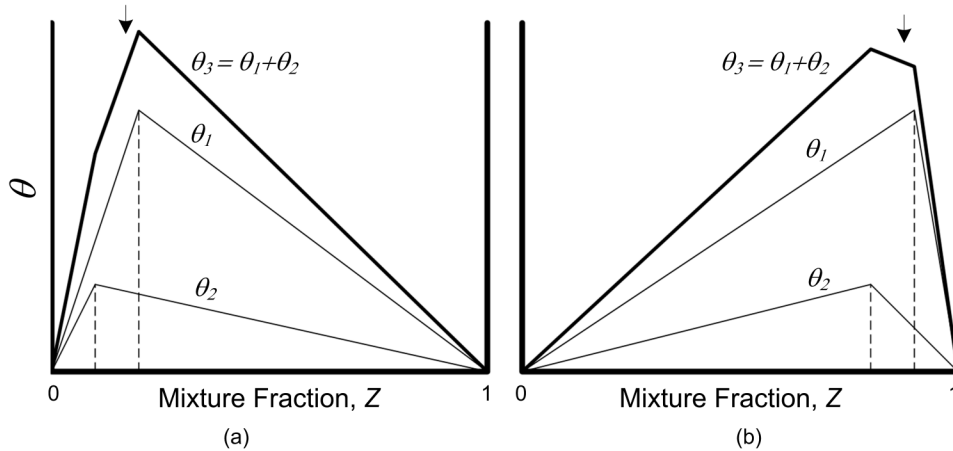


**Figure 5.8. Superposition of temperatures resulting from two displaced heat sources for (a) low  $Z_{st}$  flame (b) high  $Z_{st}$  flame. Filled arrow indicates  $x_{Z_{st}}$ .**

For the high  $Z_{st}$  flame of Fig. 5.8b, moving left to right we see that  $\theta_3$  again increases linearly until we reach the location of the heat source responsible for  $\theta_2$ ; however, rather than continuing to increase after this point with a reduced slope as in the low  $Z_{st}$  flame,  $\theta_3$  begins to decrease. This occurs because the heat release region is closer to the  $Z = 1$  boundary, which causes the magnitude of the negative slope associated with  $\theta_2$  to be greater than the positive slope associated with  $\theta_1$ . Thus, at high  $Z_{st}$  the exothermic contribution from reactions 5.2R-5.5R at a location displaced from the location of oxygen depletion can be considered responsible for the shifting of the maximum temperature relative to the location of global stoichiometry.

A more thorough analysis can be performed by obtaining values for the three heat source zones by integrating the total heat release profile of Fig. 5.4 numerically within each reaction zone. The heat sources are placed at the location in mixture fraction space where the local heat release extremum occurs for the respective reaction zone. For Flame A the fuel pyrolysis zone has a local minimum while for Flame C the fuel pyrolysis zone actually has a small local maximum. In the primary and secondary oxidation zones local maxima occur for all flames. As above, the final temperature distribution is obtained from the superposition of the independent temperature distributions resulting from the point heat sources and the results are shown in Fig. 5.9.

In Fig. 5.9 the dashed curve ( $T_{num}$ ) represents the temperature profile from the numerical results plotted in mixture fraction space. The total heat release distribution,  $Q_{tot}$ , is also included as a reference.  $\theta_{pyr}$  is the temperature distribution that would result if only the heat release from the fuel pyrolysis zone were considered,  $\theta_{pri}$  is the temperature that would result if only the exothermic heat release from the primary oxidation zone were considered, and  $\theta_{sec}$  is the resulting temperature if only the exothermic heat release from the secondary oxidation zone were considered. The bold line ( $T_{sup}$ ) represents the superposition of these temperatures. The location of  $Z_{st}$  is indicated by the filled arrow.

We first note in Fig. 5.9 how well this simple three step empirical correlation captures the temperature profile produced by the flame code. By including the endothermic zone as a third heat source in the low  $Z_{st}$  fuel-air flame (Fig. 5.9a) we see how the endothermic reactions result in a narrowing of the high temperature region in mixture fraction space. In Fig. 5.9b we again demonstrate how the location of maximum temperature shifts to the oxidizer side of  $x_{Z_{st}}$ . Furthermore, we note that the pyrolysis zone has a

negligible effect on the temperature profile and the region of high temperature is broadened in mixture fraction space for the high  $Z_{st}$  flame due to the secondary exothermic zone.

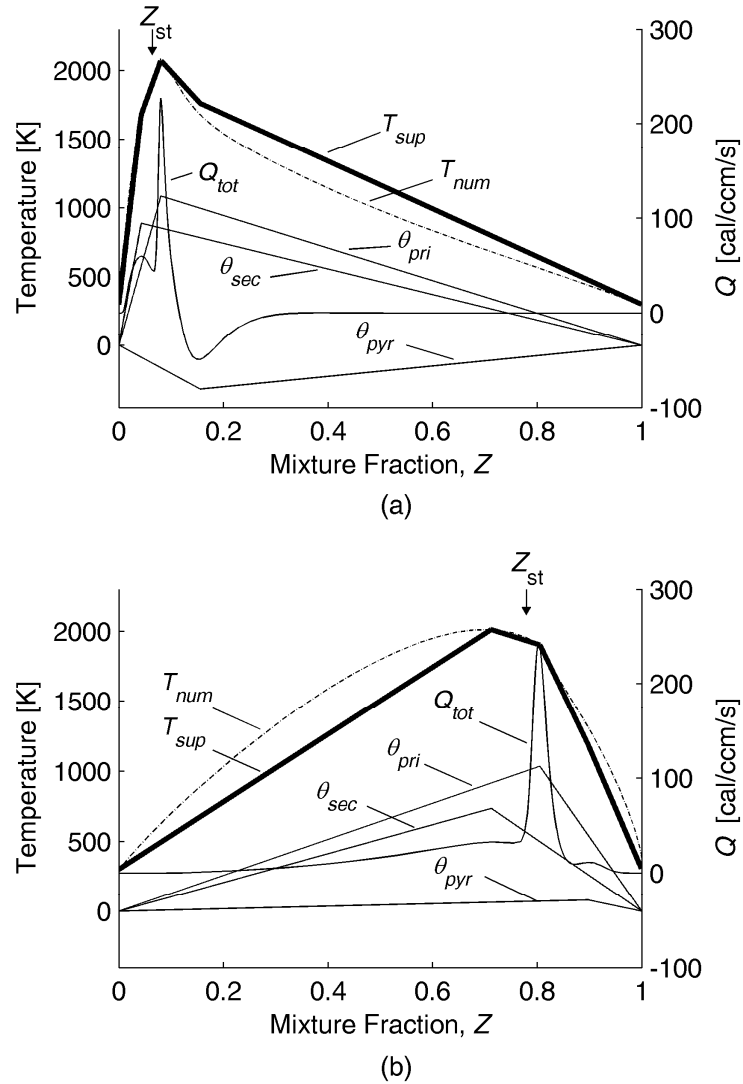


Figure 5.9. Comparison of temperature profiles from the detailed numerical model and that resulting from the superposition of temperatures based on three point source heat zones for (a) the low  $Z_{st}$  (fuel/air) flame and (b) the high  $Z_{st}$  (diluted-fuel/oxygen) flame. Filled arrow indicates  $x_{Z_{st}}$ .

## 5.5 Conclusions

The presence of appreciable molecular oxygen at the location of maximum temperature in oxygen-enhanced combustion of ethylene was analyzed computationally using a detailed kinetic mechanism. Based on this analysis, it was found that:

- 1) The characteristic location of molecular oxygen depletion is nearly coincident with the location of stoichiometry, which can be characterized by the location of maximum  $\text{CO}_2$  or  $\text{H}_2\text{O}$  production for both conventional and oxygen-enhanced combustion.
- 2) Molecular oxygen consumption is dominated by H radical attack for both conventional and oxygen-enhanced combustion, and an apparent kinetic and thermal coupling was observed between this endothermic reaction and the exothermic reactions producing  $\text{CO}_2$ ,  $\text{H}_2\text{O}$ , and H radicals.
- 3) Four heat zones can be distinguished within the reaction region, namely a pyrolysis zone that is endothermic at low  $Z_{\text{st}}$  and is slightly exothermic at high  $Z_{\text{st}}$ , a high heat intensity zone where acetylene is oxidized by O, a moderate heat intensity zone where the majority of  $\text{CO}_2$  and  $\text{H}_2\text{O}$  are formed, and a low heat intensity zone that broadens and extends farther into the oxygen rich region at high  $Z_{\text{st}}$  due to the increased  $\text{O}_2$  concentrations.
- 4) The presence of appreciable molecular oxygen at the location of maximum temperature for high  $Z_{\text{st}}$  flames is due to a shifting of the location of maximum temperature relative to the location of molecular oxygen depletion. This shifting occurs at high  $Z_{\text{st}}$  due to

- i. finite-rate reactions that release heat at a location displaced toward the oxidizer side of the location of stoichiometry,  $O_2$  depletion, or maximum heat release and contribute substantially to a secondary peak in the total heat release rate profile
- ii. the relative location of the heat release region with respect to the  $Z = 0$  and  $Z = 1$  boundaries in mixture fraction space.

Finally, the shifting of the location of maximum temperature was explained by considering the superposition of the temperature profiles that would result from two displaced heat sources.

# 6 Structural Effects on Soot Precursor Kinetics Resulting in Soot-Free Flames

## 6.1 Introduction

As discussed in previous chapters, for non-premixed flames the free-stream fuel and oxidizer concentrations can dramatically impact the flame structure and soot formation characteristics; and, the extent of oxygen-enhancement and fuel-dilution can be quantified by the stoichiometric mixture fraction,  $Z_{st}$ . Lin and Faeth [42] demonstrated that at sufficiently high  $Z_{st}$  “permanently blue” counterflow flames (i.e. flames in which soot formation does not occur even at strain rates approaching zero) could be obtained and concluded, as did Sugiyama [28], that the soot inhibiting effect of oxygen-enrichment and fuel-dilution was due to hydrodynamics. As discussed in Chapters 3 and 4 however, experiments in which the influence of convection direction was minimized or eliminated indicate that flame structure is the primary factor influencing soot formation in permanently blue flames with convection direction playing a secondary role. Theoretical studies by Chao et al. [32] and Liu et al. [112] using a simplified three-step reaction scheme and high activation energy asymptotics reached a similar conclusion.

While the evidence discussed up to this point indicates structural changes in high  $Z_{st}$  flames are responsible for the permanently blue flame phenomenon, a detailed investigation has not been done showing how structure affects the formation and destruction of key species leading to soot. This work uses a counterflow flame code with detailed chemistry to examine the dominant chemical pathways leading to the formation of phenyl and benzene and investigates, in detail, the rates of acetylene and propargyl production and destruction



for a set of nine ethylene flames ranging from low  $Z_{st}$  (fuel burning in air) to high  $Z_{st}$  (diluted-fuel burning in oxygen). The main objective of this work is to demonstrate and explain how altering flame structure by increasing  $Z_{st}$  leads to changes in the soot formation pathway and, consequently, soot-free flames.

## 6.2 Numerical

The counterflow flame code employed here was described in Chapter 5. Chemical reaction rates, transport properties, and thermodynamic properties are evaluated by the Chemkin software package as before. The chemical mechanism used in this study combines the latest release from Wang et al. [137] with chemistry up to pyrene from Wang and Frenklach [132] and Appel et al. [133]. The mechanism contains 143 species and 938 reactions and, as this mechanism is a hybrid of two publicly available mechanisms, is included in Appendix B for reference. The accuracy of this mechanism was confirmed according to the method described in Chapter 5.

The computational grid was initialized with 21 grid points and the fuel and oxidizer stream inlet boundaries were spaced 2 cm apart. Adaptive grid refinement parameters were adjusted to ensure the attainment of converged solutions. Flame parameters are provided in Table 6.1 and the strain rates were determined as described in Law [63]. The square of the gradient in mixture fraction  $(dZ/dx)^2$ , which is proportional to the scalar dissipation rate, was calculated at the location of stoichiometry for all flames. The mixture fraction,  $Z$ , is defined as the local fraction of mass that originated from the fuel stream and for one-step chemistry can be written as

$$Z = \frac{\sigma_{O_2,F} Y_F - Y_{O_2} + Y_{O_2,ox}}{\sigma_{O_2,F} Y_{F,fu} + Y_{O_2,ox}} \quad (6.1)$$

where  $Y_i$  and  $\sigma$  are defined as before in Chapter 3. A more general expression based on the local mass fractions of carbon, hydrogen, and oxygen atoms is given by

$$Z = \frac{\frac{Y_H - Y_{H,ox}}{nW_H} + \frac{Y_C - Y_{C,ox}}{mW_C} + \frac{Y_{O,ox} - Y_O}{(m+n/4)W_O}}{\frac{Y_{H,fu} - Y_{H,ox}}{nW_H} + \frac{Y_{C,fu} - Y_{C,ox}}{mW_C} + \frac{Y_{O,ox} - Y_{O,fu}}{(m+n/4)W_O}} \quad (6.2)$$

where  $m$  and  $n$  represent the number of carbon and hydrogen atoms, respectively, in the fuel  $C_mH_n$  [138, 139]. Thus, the mixture fraction provides an indication of the level of mixing at a given location in the flame while the gradient of the mixture fraction is an indicator of the rate of mixing.

**Table 6.1. Flame parameters**

Flame	$Z_{st}$	$X_{F,fu}$	$X_{O_2,ox}$	$a$	$(dZ/dx)^2$ at $Z_{st}$
	--	--	--	(s <sup>-1</sup> )	(cm <sup>-2</sup> )
A	0.06	1.00	0.21	8.7	0.08
B	0.10	0.64	0.22	8.9	0.17
C	0.20	0.32	0.25	8.9	0.45
D	0.30	0.21	0.28	9.2	0.78
E	0.40	0.16	0.33	9.4	0.98
F	0.50	0.13	0.40	9.6	1.12
G	0.60	0.11	0.51	9.8	1.08
H	0.70	0.10	0.70	9.7	0.98
I	0.78	0.08	1.00	9.8	0.75

## 6.3 Results and Discussion

To illustrate the effects of increasing  $Z_{st}$  on flame structure, consider first the temperature, and species profiles of the fuel/air ( $Z_{st} = 0.064$ ) and diluted-fuel/oxygen ( $Z_{st} = 0.78$ ) flames shown in Figs. 6.1a and b, respectively. Note the location of each flame relative to the stagnation point, the oxygen mole fraction at the location of peak temperature, and the fuel mole fraction at 1600 K in the two flames. The selection of 1600 K is justified by the results of Glassman and coworkers who measured a temperature of 1600 K in heavily diluted ethylene/air coflow flames at the location where soot was no longer visible in the tip

[128] and the work of Sunderland et al. [36] and Kumfer et al. [37, 38] who observed a correlation between a local temperature near 1600 K and soot-free conditions when varying

$Z_{st}$ .

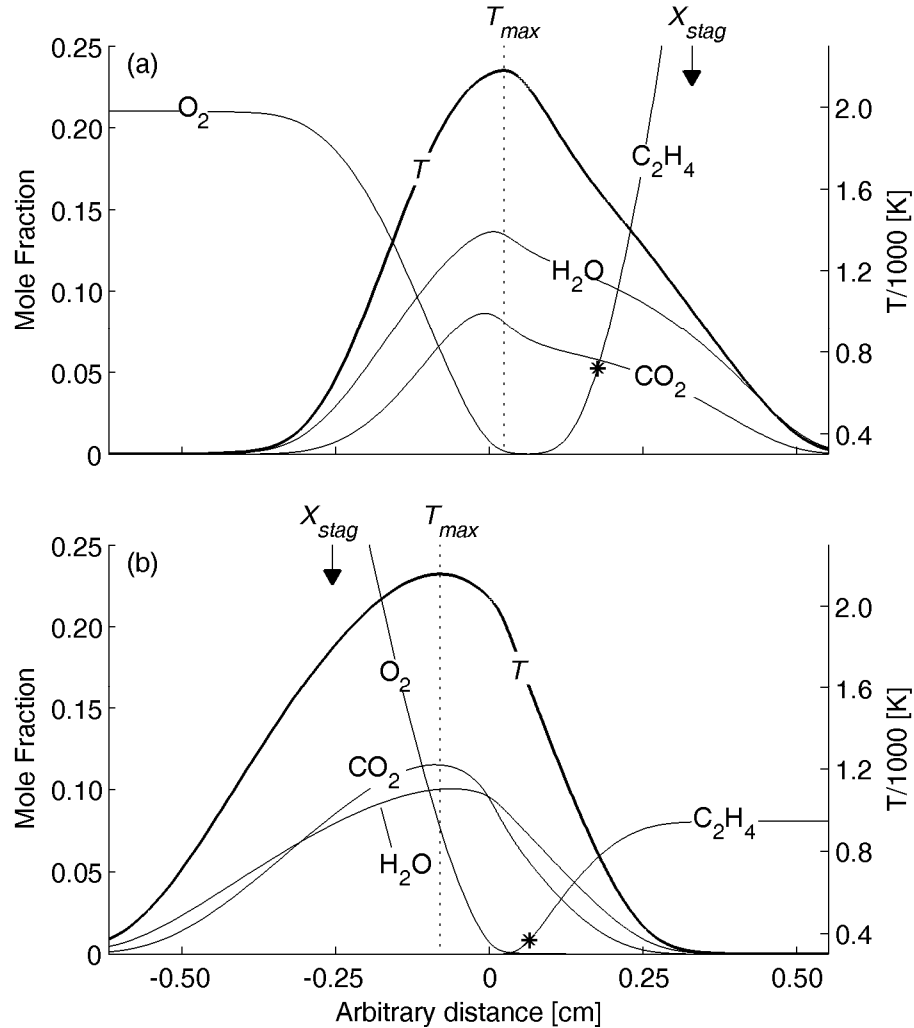


Figure 6.1. Computed temperature and species profiles for (a) Flame A (fuel/air,  $Z_{st}=0.064$ ) and (b) Flame I (diluted-fuel/oxygen,  $Z_{st}=0.78$ ). Arrow indicates the location of the stagnation point. Asterisk indicates the mole fraction of ethylene at 1600 K.

In Fig. 6.1a it can be seen that the fuel/air flame is located on the oxidizer side of the stagnation point, the oxygen is nearly depleted at the location of peak temperature, and the mole fraction of ethylene at 1600 K (indicated by the asterisk) is approx. 0.05. In contrast,

the results in Fig. 1b demonstrate that the high  $Z_{st}$  flame resides on the fuel side of the stagnation point, more than 5 vol.% oxygen is found at the location of peak temperature, and the mole fraction of ethylene at 1600 K is approx. 0.01. Clearly, the relationship between the local temperature and local fuel and oxygen species concentrations is significantly different in these two flames.

In Fig. 6.2 the mole fraction profiles of the hydroxyl radical (OH), H, O, O<sub>2</sub>, and acetylene are plotted along with temperature profiles for Flame A and Flame I. In this figure the abscissa is the local carbon-to-oxygen ratio (C/O) given by

$$C/O = \frac{1}{2} \frac{m Y_{F, fu} W_{O_2}}{Y_{O_2, ox} W_F} \frac{Z}{(1-Z)}. \quad (6.3)$$

Du and Axelbaum [30] first discussed the local C/O ratio as a potentially important parameter for characterizing a non-premixed flame's propensity to soot. Sunderland et al. [36] and Kumfer et al. [37], as well as the results presented in Chapter 4, showed a correlation between soot-free conditions in ethylene flames and a local C/O ratio of 0.5-0.6 at a local temperature of ca. 1600 K. It was suggested that for high  $Z_{st}$  flames in the region where the local C/O ratio was 0.5-0.6, the increased presence of oxidizing species may inhibit soot formation. Thus, it is instructive to consider the structure of low and high  $Z_{st}$  flames in C/O ratio space. Comparing Figs. 6.2a and b it is observed that in C/O ratio space the location and shape of the radical profiles is similar for low and high  $Z_{st}$  flames and it is apparent that the region associated with a local C/O ratio in the range of 0.5-0.6 can be identified with the edge of the O<sub>2</sub> concentration profile and the edge of the radical pool. Note also that the location of the peak OH and O concentrations is fixed near the location where the local C/O ratio is in stoichiometric proportion (based on the global reaction of ethylene with oxygen). This was discussed in Chapter 5, and is due to the coupling of the

chain branching reaction  $\text{H} + \text{O}_2 = \text{OH} + \text{O}$  to  $\text{CO}_2$  and  $\text{H}_2\text{O}$  production via  $\text{CO} + \text{OH} = \text{CO}_2 + \text{H}$  and  $\text{H}_2 + \text{OH} = \text{H}_2\text{O} + \text{H}$  [140]. More specifically, the chain branching reaction requires heat and H radicals to produce OH and O, while the dominant  $\text{CO}_2$  and  $\text{H}_2\text{O}$  formation reactions supply heat and H radicals and require hydroxyl radicals.

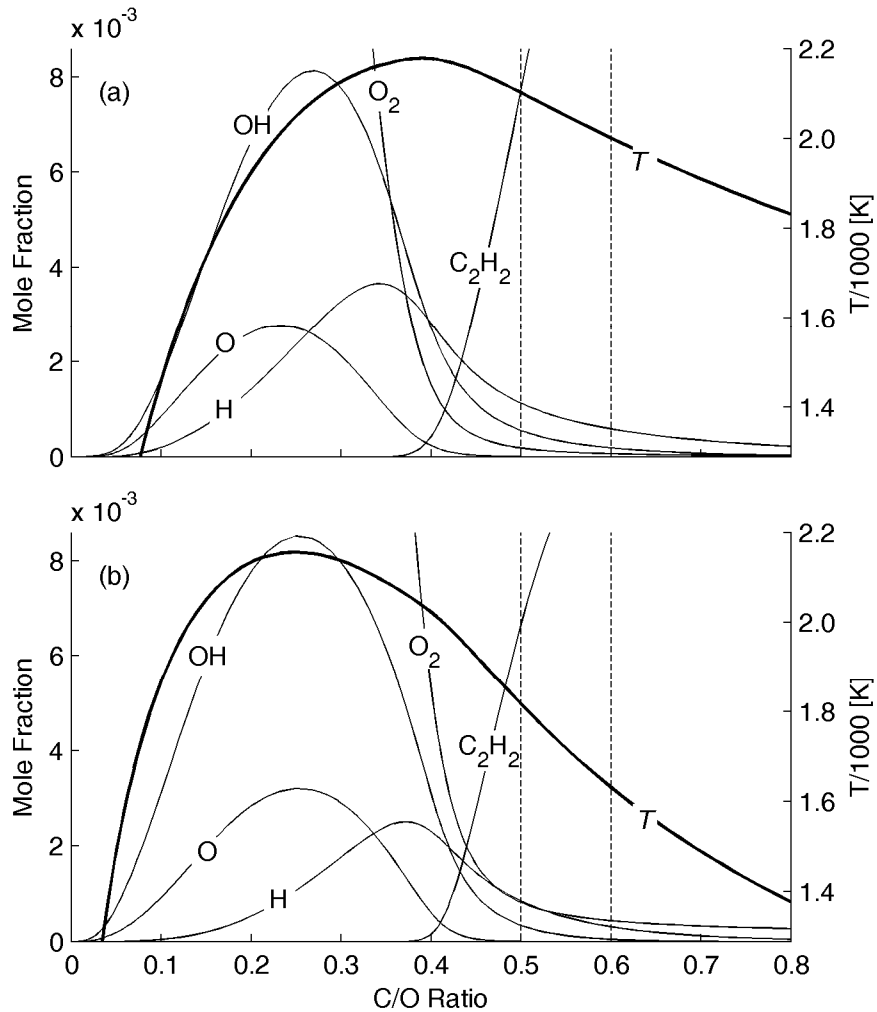


Figure 6.2. Concentration profiles of OH, O, H,  $\text{O}_2$ , and  $\text{C}_2\text{H}_2$  along with temperature in C/O ratio space for (a) Flame A (low  $Z_{st}$ ) and (b) Flame I (high  $Z_{st}$ ). The dashed lines indicate the region between  $0.5 \leq \text{C/O} \leq 0.6$ .

Next, consider the temperature and acetylene concentration profiles in Figs. 6.2a and b and assume for simplicity that the local temperature and local acetylene concentration is sufficient to characterize the flame's propensity to soot. At  $\text{C/O} = 0.5$  the concentration of

acetylene is similar in Flame A and Flame I; however, the temperatures at this location differ by more than 200 K even though the peak temperatures and adiabatic flame temperatures are the same. Moreover, in the region between  $C/O = 0.5$  and  $C/O = 0.8$  the temperature drops off more rapidly in Flame I compared to Flame A. Thus, even with similar acetylene concentrations at  $C/O \approx 0.5$  one might expect reduced soot or no soot in Flame I due to the lower temperatures inhibiting the high activation energy kinetics of soot formation. Nevertheless, this simple example does not explain the existence of permanently blue flames since based on this argument soot could still form at these temperatures in Flame I given sufficient residence time. Clearly, a more thorough analysis of the changes that occur in the key soot precursor reaction steps at high  $Z_{st}$  is required to understand the permanently blue flame phenomenon.

As it is well accepted that the formation of the first aromatic ring is an important step in the path to soot formation for aliphatic fuels [91, 141], this investigation begins by evaluating the effects of structure on the detailed chemistry leading to the formation of benzene and phenyl. The dominant pathways to benzene and phenyl in both the fuel/air (low  $Z_{st}$ ) and diluted-fuel/oxygen (high  $Z_{st}$ ) flames were determined based on a reverse pathway analysis, which can be explained by the following illustration.

Based on the chemical mechanism used here, eight reactions contribute to the net formation of phenyl ( $C_6H_5$ ) as shown in Fig. 6.3. To determine the contribution from each reaction to the total phenyl produced, the net reaction rate profiles were integrated for each reaction over the entire domain. Because some reactions produce phenyl in one region of the flame and consume phenyl in another region of the flame, only the net positive contribution is considered in this analysis. In this way, spatial variations in the net direction of each reaction that may result in some reactions being neglected or considered of less

importance can be accounted for. Once the rates have been integrated, the sum of these quantities represents the total rate of phenyl produced via all contributing reactions in the flame. The relative contribution from each reaction was then determined based on the ratio of the integrated individual quantities to the sum.

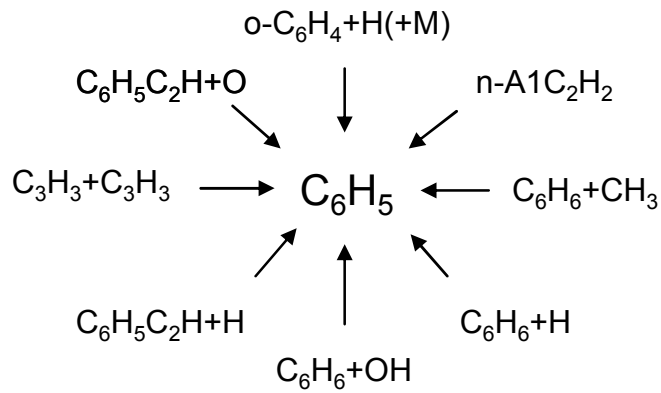


Figure 6.3. Diagram showing all phenyl producing reactions in [137].

In Fig. 6.4, the relative contributions from phenyl producing reactions are shown in a pie chart. For this analysis, and for other species evaluated, reactions producing less than 2.5% of the total have been neglected. Consistent with recent literature, it is clear from Fig. 6.4 that propargyl ( $\text{C}_3\text{H}_3$ ) self-combination is the dominant reaction leading to phenyl [91]. Continuing in reverse order and performing this same analysis with propargyl substituted for phenyl yields the dominant propargyl producing reactions as shown in Fig. 6.5. This reverse pathway analysis was utilized to evaluate the dominant pathways to benzene and phenyl at both low and high  $Z_{st}$ , and a graphical representation of the results is provided in Figs. 6.6a and b. Though not shown in the figure, the analysis was considered complete when the primary production reaction of the analyzed species was fuel decomposition.

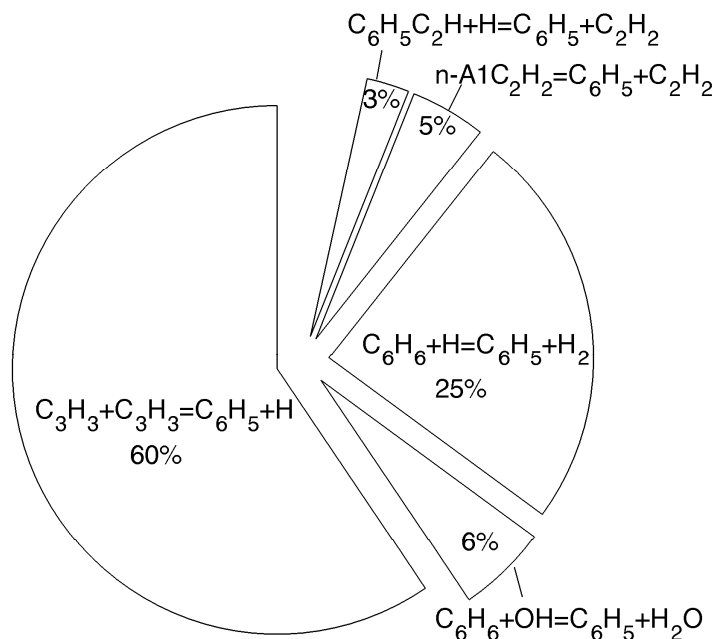


Figure 6.4. Relative contribution of individual phenyl producing reactions to total phenyl production rate.

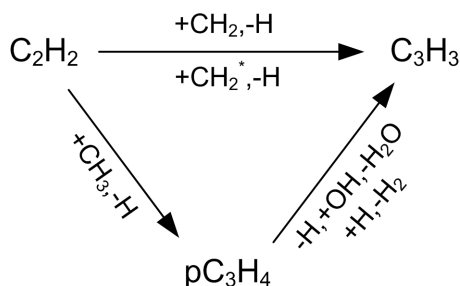


Figure 6.5. Graphical representation of dominant propargyl formation reactions.

The weight of the arrows in Fig. 6.6 indicates the relative net integrated contribution for a given reaction. Most importantly, it is apparent that in the low  $Z_{st}$  fuel/air flame two dominant routes exist for propargyl formation from acetylene; however, in the high  $Z_{st}$  diluted-fuel/oxygen flame a reaction in the pathway through propyne ( $pC_3H_4$ ) is reversed in all regions of the flame, and in fact, becomes the dominant route for propargyl destruction. As will be presented in detail below, this is a key point in understanding how the flame structure in high  $Z_{st}$  flames leads to soot-free conditions at high temperature. In the



following discussion an analysis is presented of the changes that occur in the acetylene and propargyl concentrations and the dominant acetylene and propargyl formation and destruction reactions, which lead to the observed changes in the soot formation pathway at high  $Z_{st}$ .

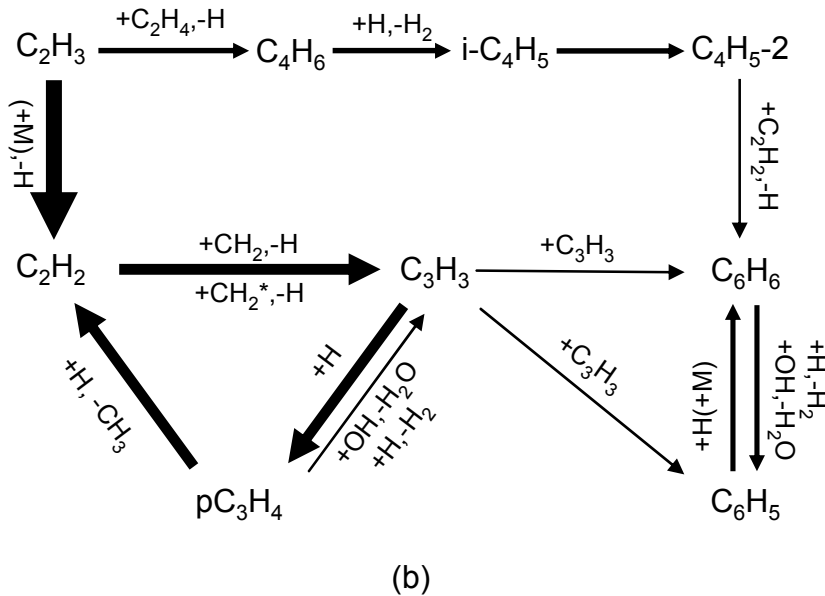
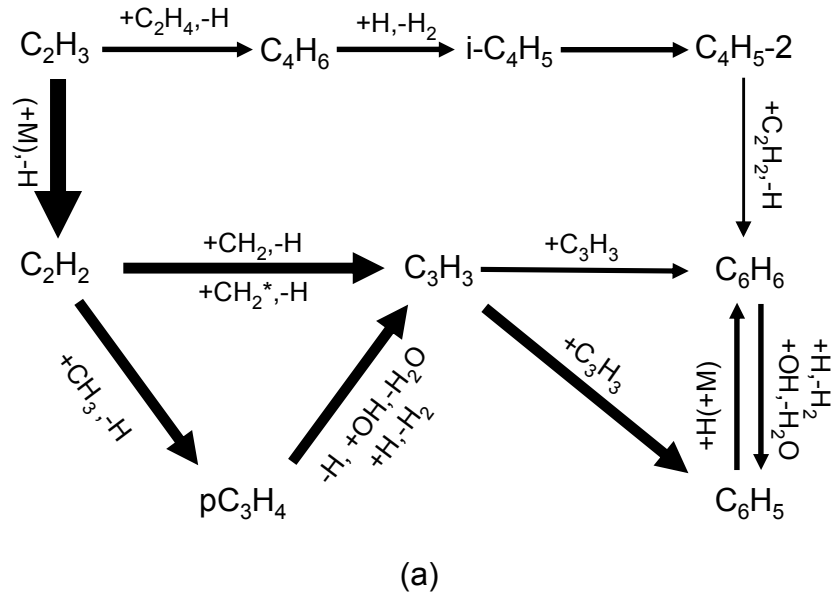


Figure 6.6. Dominant pathways to benzene and phenyl at (a)  $Z_{st} = 0.064$  and (b)  $Z_{st} = 0.78$ . Note: \* indicates an activated or energized species.

### Acetylene Chemistry

Recognizing that acetylene is an important species in both the formation and growth of aromatics, the effects of increasing  $Z_{st}$  on the integrated amount of acetylene and the rates of the dominant acetylene production and destruction reactions are first evaluated. A qualitative functional dependence is sought between the total acetylene concentration in the flame and the free-stream ethylene concentration in the form of  $C_2H_{2,tot} = \int [C_2H_2] dx = BX_{F, fu}^b$  where  $x$  is the coordinate normal to the flame and the integration is performed along the stagnation streamline,  $B$  is an arbitrary constant, and  $b = 1$  if the total amount of acetylene in the flame is linearly dependent on the free-stream fuel concentration. To determine  $b$ , the natural log of the total amount of acetylene in the flame is plotted against the natural log of the free-stream fuel concentration in Fig. 6.7.

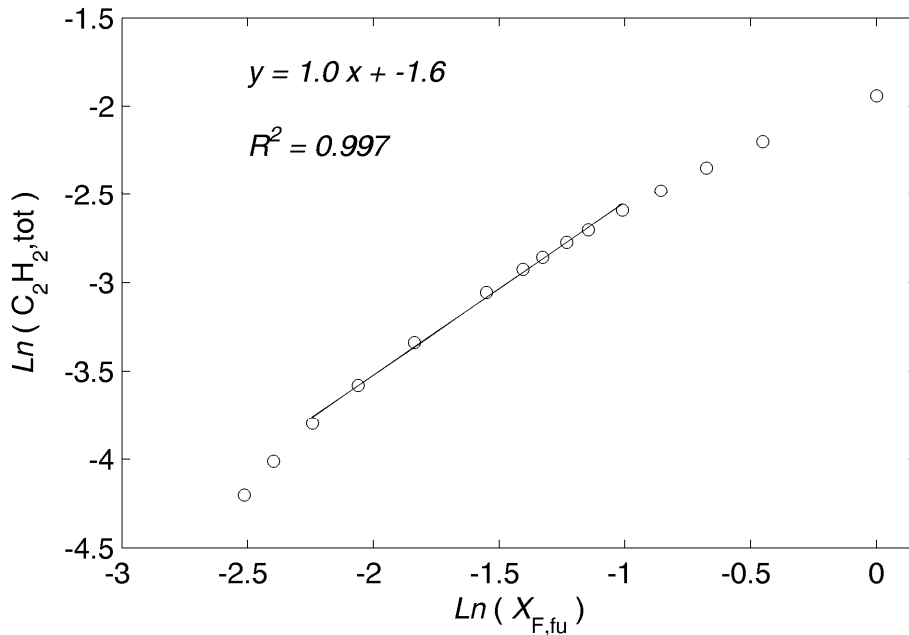


Figure 6.7. Natural log of the total acetylene concentration in the flame vs natural log of free-stream fuel mole fraction. The linear regression fitted to points from flames with similar scalar dissipation rates in the region of interest indicates that the total acetylene is proportional to the free-stream fuel concentration.

Note that additional flame results, not included in Table 6.1, were computed in the range of  $Z_{st} = 0.1$  to 0.3 for this figure. The qualitative functional dependence sought here is only considered valuable for flames having similar scalar dissipation rates at the location of peak acetylene production. When considering a plot of the mixture fraction in physical space as shown in Fig. 6.8, it can be seen that for low and high  $Z_{st}$  flames the local mixture fraction gradient, which is proportional to the scalar dissipation rate, in the reaction region (i.e. the region near stoichiometry) can vary significantly. Note also that in Table 6.1 it was observed that the scalar dissipation rate at the location of stoichiometry is a strong function of  $Z_{st}$  in the range of  $0.064 < Z_{st} < 0.3$ , while the changes are moderate for  $0.3 < Z_{st} < 0.78$ . However, at the location of peak acetylene production, which is displaced toward the fuel side of the location of stoichiometry, it was observed that the scalar dissipation rate remained nearly constant for flames between  $0.2 \leq Z_{st} \leq 0.6$ . Thus, in this range of  $Z_{st}$  the apparent order of acetylene with respect to the free-stream fuel concentration may be determined.

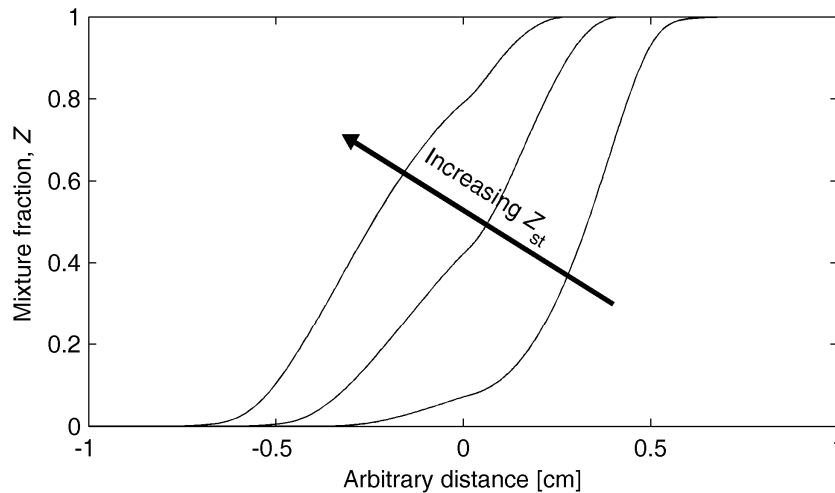
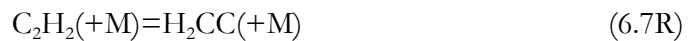


Figure 6.8. Mixture fraction in physical space showing the variation with increasing  $Z_{st}$ . Changing  $Z_{st}$  can result in different local mixture fraction gradients in the reaction region.

Ignoring the two points on the far left and the four points on the far right in Fig. 6.7 (since these results are from flames with different scalar dissipation rates at the location of peak acetylene production) a linear fit to the remaining nine points yields a slope of unity with a coefficient of determination of 0.997; thus,  $b = 1.0$  and the total amount of acetylene in the flame is proportional to the free-stream fuel concentration for the conditions investigated here when  $0.2 \leq Z_{st} \leq 0.6$ . In the following discussion, changes in the individual acetylene reactions as a function of  $Z_{st}$  are considered.

In the mechanism used in this study there are 80 reactions involving acetylene chemistry; however, the net rate of acetylene production can be adequately represented (within 5%) at low, moderate, and high  $Z_{st}$  by the 11 reactions below.



To determine the relative contribution of each of these reactions to the total net production and destruction of acetylene, the net rate profiles of each reaction were integrated and the ratio of the individual rate components to the sum of all components from each rate was calculated as described previously. As shown in Fig. 6.9, in the low  $Z_{st}$  fuel-air flame 6.1R contributes approx. 80% of the total net acetylene production with the remaining 20% produced by 6.7R and 6.11R.

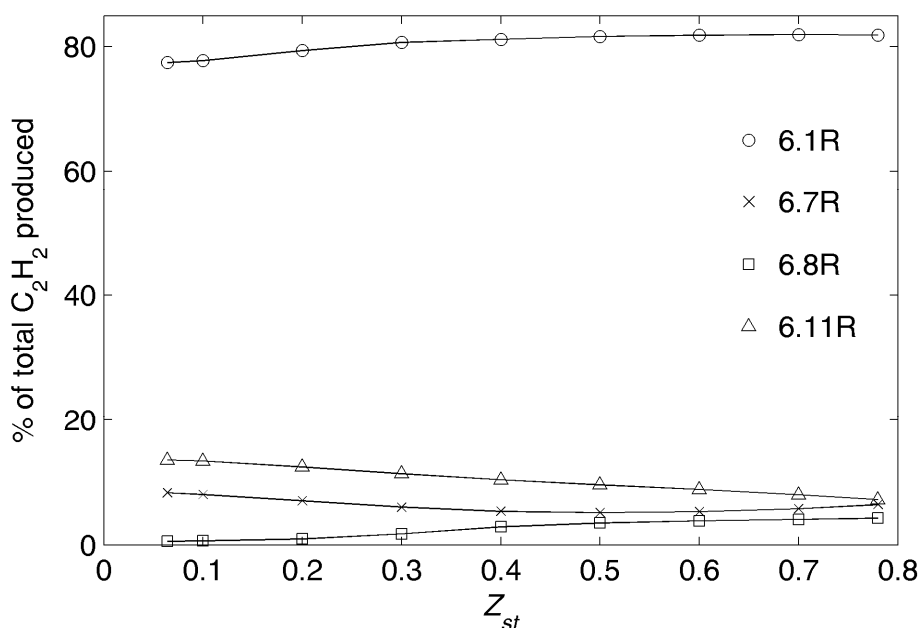


Figure 6.9. Contribution to total net acetylene production from selected reactions vs.  $Z_{st}$ .

More dramatic changes are observed in the relative contributions of the dominant acetylene destruction reactions when changing  $Z_{st}$ , as shown in Fig. 6.10. Specifically, the dominant oxidation routes for acetylene, which include 6.2R-6.4R, combine to account for approx. 50% of the total net acetylene destroyed in the fuel/air flame, while at high  $Z_{st}$ , 6.2R-6.4R account for more than 80% of the total net acetylene destruction. Thus, at high  $Z_{st}$  more acetylene is consumed by oxidation than at low  $Z_{st}$  resulting in less acetylene available for subsequent PAH and soot growth via the HACA mechanism. Also, given that soot

nucleation and surface growth is often linked to the gas-phase through a first-order dependency on acetylene, as in Leung et al. [142], soot models for OEC may have to be updated since the results in Fig. 6.10 indicate that the acetylene destruction chemistry changes at high  $Z_{st}$ .

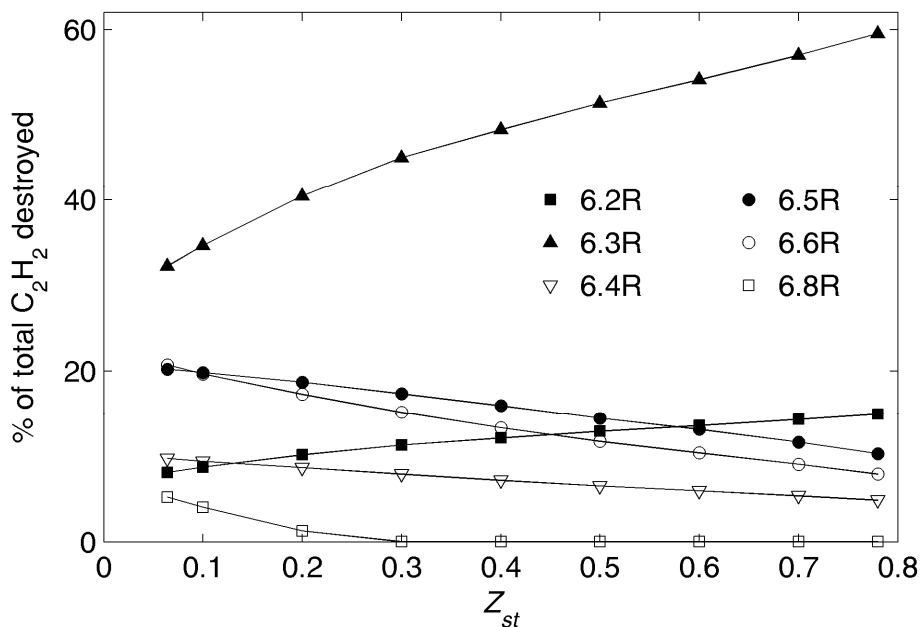


Figure 6.10. Contribution to total net acetylene destruction from selected reactions vs.  $Z_{st}$ .

### Propargyl Chemistry

It is generally accepted that for aliphatic fuels the self-combination of the resonantly-stabilized propargyl radical is the dominant source of the first aromatic ring and is therefore the rate-limiting step for soot formation [83-91]. Thus, it seems plausible that the existence of permanently blue ethylene flames may be related to the effects of increasing  $Z_{st}$  on either reactions forming propargyl or the self-combination reaction itself.

A qualitative functional relationship similar to that considered above for acetylene is sought for propargyl. In Fig. 6.11 the natural log of the total propargyl in the flame is plotted

versus the natural log of the free-stream fuel concentration. Unfortunately, the scalar dissipation rate at the location of peak propargyl formation is a relatively strong function of  $Z_{st}$  making this analysis controvertible. Nevertheless, neglecting the differences in scalar dissipation rate the results suggest that the total amount of propargyl in the flame is greater than would be anticipated based on a linear dependence on the free-stream fuel concentration for  $0.064 \leq Z_{st} \leq 0.2$ , while for  $Z_{st} > 0.4$  the total propargyl scales with the square of the free-stream fuel mole fraction. This being the case, a change in the free-stream fuel concentration yields a larger reduction in the total propargyl in a high  $Z_{st}$  flame resulting in less benzene and phenyl formation via propargyl self-combination.

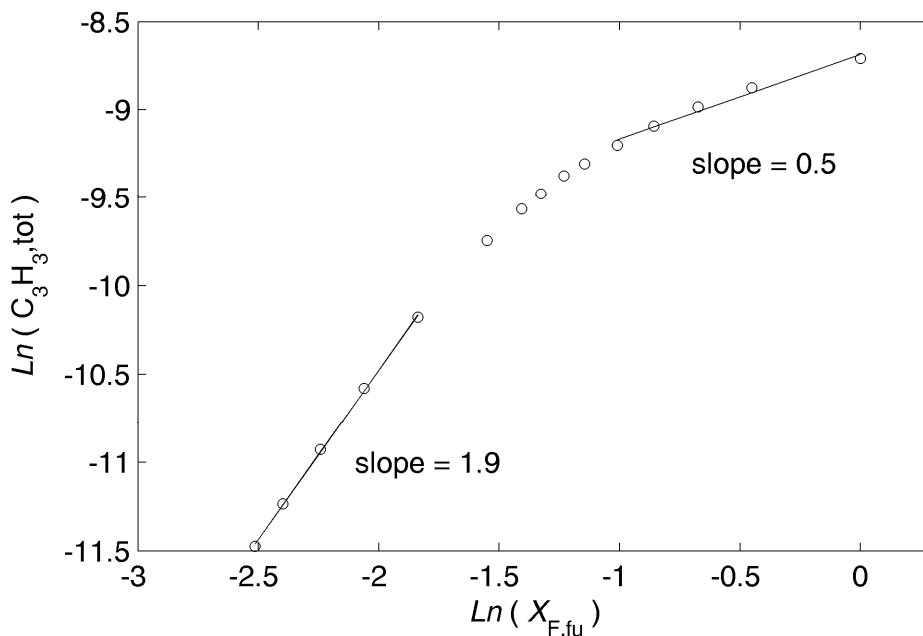
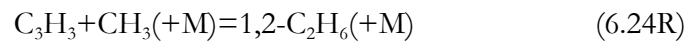


**Figure 6.11.** Natural log of total propargyl concentration in the flame vs natural log of free-stream fuel mole fraction.

Next, the effects of increasing  $Z_{st}$  on the dominant propargyl formation and destruction reactions are considered. The mechanism used in this study includes 36 reactions involving propargyl and nearly all reactions are needed to accurately describe the net rate

profile. For brevity, only the reactions that combine to account for approx. 80% of the total propargyl production and destruction are listed below. Note that 6.9R and 6.10R from above also belong to this list.



In Fig. 6.12 the relative contributions of selected reactions to the total net propargyl formation are plotted as a function of  $Z_{st}$ . Here significant changes in the contributions from 6.9R and 6.12R are observed, with smaller changes occurring for 6.10R, 6.13R, and 6.14R. In fact, in the fuel/air flame 6.12R is responsible for more than 30% of the propargyl formed,



but produces no propargyl at  $Z_{st} = 0.3$  and beyond. Note also that OH is active in propargyl formation, not destruction.

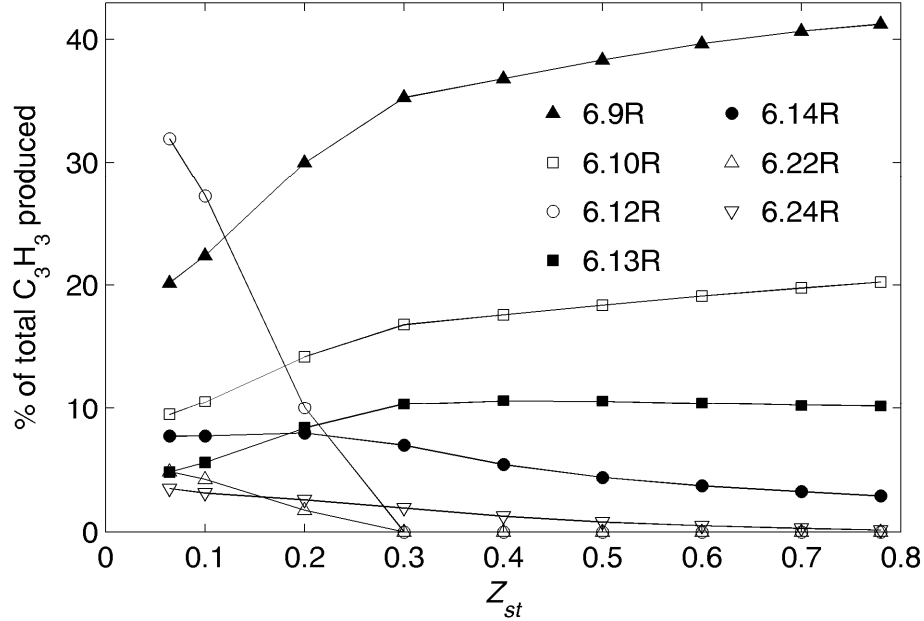


Figure 6.12. Contribution to total net propargyl production from selected reactions vs.  $Z_{st}$ .

Next consider the contributions from selected reactions to the total destruction of propargyl as a function of  $Z_{st}$  shown in Fig. 6.13. In the fuel/air flame 40% of the total propargyl destroyed forms phenyl through 6.18R with nearly 20% forming benzene via 6.19R. At high  $Z_{st}$  these pathways are virtually eliminated. Note also that the percentage of propargyl destroyed by O is unaffected when increasing  $Z_{st}$ . There is a dramatic change in the percentage of propargyl destroyed by 6.12R at high  $Z_{st}$ , rising to approx. 75% of the total propargyl destruction in the  $Z_{st} = 0.78$  flame. As shown previously in Figs. 6.9 and 6.10, 6.8R demonstrated a similar phenomenon resulting in propyne destruction (and thus acetylene formation) rather than propyne formation for  $Z_{st} > 0.3$ . The following analysis seeks to determine why these changes in the forward and reverse rates occur for 6.8R and 6.12R with increasing  $Z_{st}$ .

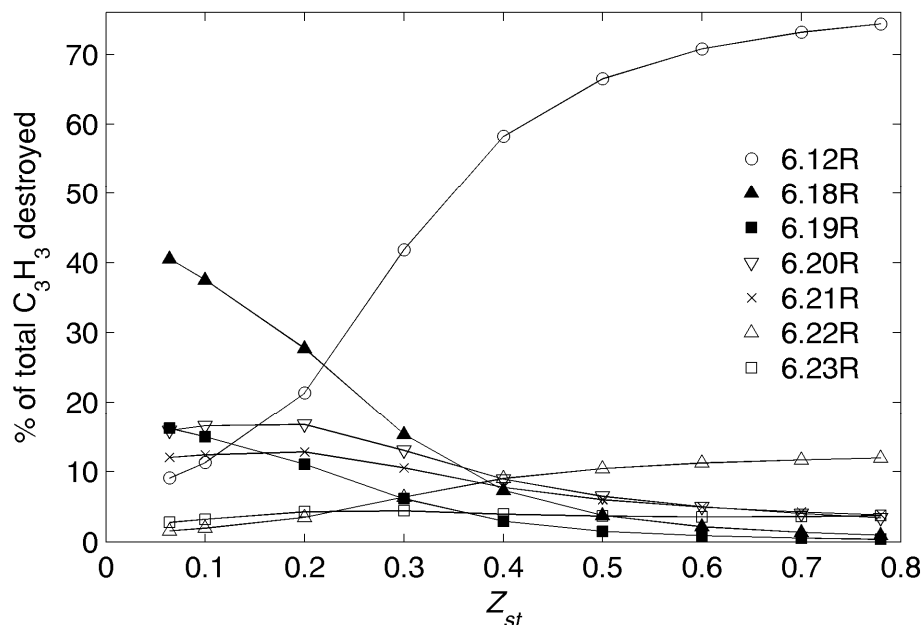


Figure 6.13. Contribution to total net propargyl destruction from selected reactions vs.  $Z_{st}$ .

Two important factors influence the net direction of 6.8R and 6.12R in low and high  $Z_{st}$  flames. The first factor to consider is that H is produced in both 6.8R and 6.12R, and if sufficient H is available locally the reverse of these reactions will be preferred, even at high temperature. The second factor to consider is that 6.8R and 6.12R are endothermic reactions (i.e., the equilibrium constants ( $K_c$ ) increase with temperature). Thus, if the flame structure is altered such that the temperature in the reaction region of 6.8R and 6.12R is lowered,  $K_c$  will be reduced resulting in an increase in the reverse rate constant ( $k_{rev}$ ) relative to the forward rate constant ( $k_{for}$ ). As shown in Fig. 6.14a, in the fuel/air flame a location exists on the fuel side of stoichiometry where the local temperature is high (ca. 2000 K) but sufficient H is available to drive 6.8R and 6.12R from net propyne and propargyl production to net destruction. In the  $Z_{st} = 0.2$  flame of Fig. 6.14b, which would still be producing soot based on the results of Du and Axelbaum [30] and Lin and Faeth [109], there are three important observations: 1) a small region on the

fuel side (right) of the peak rates of 6.8R and 6.12R exists where the temperature is low and the reverse rates are preferred, 2) the peak net rates of 6.8R and 6.12R near 1800 K have been reduced by a factor of approx. 4, and 3) just as in the fuel/air flame the reverse rates of 6.8R and 6.12R dominate in the region of high H concentration and high temperature.

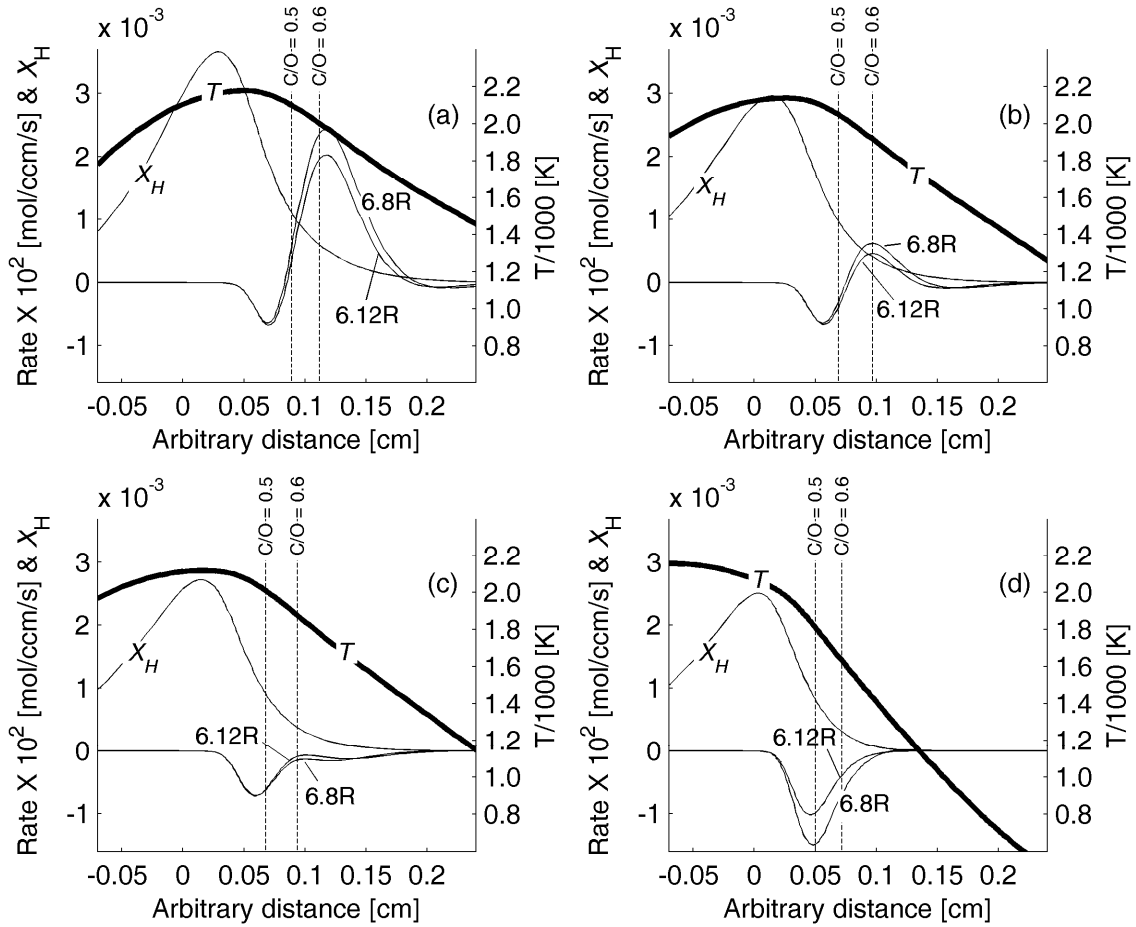


Figure 6.14. Rate profiles for reactions 6.8R and 6.12R, H mole fraction profile, and temperature profile in physical space for (a) Flame A, (b) Flame C, (c) Flame D, and (d) Flame I.

In Fig. 6.14c it is observed that in the  $Z_{st} = 0.3$  flame, which is approaching the permanently blue flame conditions observed by Du and Axelbaum [30] and Lin and Faeth [29], that the two regions of net propyne and propargyl destruction by 6.8R and 6.12R can still be distinguished; however a region of net propyne and propargyl production through 6.8R and 6.12R no longer exists. In the high  $Z_{st}$  flame shown in Fig. 6.14d, which is well

beyond the conditions required to achieve a permanently blue flame, the two regions of propyne and propargyl destruction by 6.8R and 6.12R are indistinguishable and the rates are amplified as the region of low temperature has merged with the edge of the H radical profile. Thus, at high  $Z_{st}$  the two factors that influence the preferred direction of 6.8R and 6.12R (low temperature and ample H concentration) combine to drive the propargyl formed through 6.9R and 6.14R back to propyne and subsequently back to acetylene thereby significantly reducing the opportunity for benzene and phenyl formation by propargyl self-combination.

## 6.4 Conclusions

The phenomenon of high  $Z_{st}$  soot-free non-premixed flames at strain rates approaching zero (a.k.a. permanently blue flames) has been attributed to the effects of hydrodynamics by Lin and Faeth [29, 42, 109] and flame structure by Du and Axelbaum [30]. Experiments performed with spherical flames in microgravity by Sunderland et al. [34-36], in which the effects of hydrodynamics and structure could be isolated, have confirmed that structure is primarily responsible for soot suppression at high  $Z_{st}$  with hydrodynamics having a secondary effect. In this work a counterflow flame code with detailed chemistry was used to understand the effects of flame structure, as described by  $Z_{st}$ , on the chemistry of soot precursors leading to the permanently blue flame phenomenon. The dominant pathway leading to the formation of the first aromatic ring (i.e. benzene and phenyl) was evaluated at low and high  $Z_{st}$  and significant changes were observed in the production and destruction characteristics of species critical to soot formation and growth, namely acetylene and propargyl.

When increasing  $Z_{st}$  the total amount of acetylene in the flame is proportional to the free-stream ethylene concentration for flames with similar scalar dissipation rates in the region of acetylene production. Negligible changes are observed in the relative contributions of the dominant acetylene formation reactions with increasing  $Z_{st}$ ; however, the percentage of acetylene destroyed by direct oxidation reactions with O and OH increases from about 50% to more than 80% for the diluted-fuel/oxygen flame when compared with the fuel/air flame. Thus, at high  $Z_{st}$  a greater percentage of the acetylene destruction in the flame is due to oxidation.

In the fuel/air flame two dominant propargyl formation routes are observed—one direct route via the reaction of acetylene with methylene (and activated methylene) and a second via H abstraction from propyne, which is predominantly formed from acetylene reacting with the methyl radical. As  $Z_{st}$  is increased, propargyl formation through propyne is eliminated and this route becomes the dominant propargyl destruction route. The net direction of the dominant acetylene→propyne and propyne→propargyl reactions can be influenced by the local H concentration and the local temperature. At low  $Z_{st}$  these reactions proceed in the direction of soot formation until a sufficiently high H concentration in the high temperature region promotes the reverse rates. As  $Z_{st}$  increases the flame structure changes resulting in lower temperatures and more H in the pyrolysis zone, which promotes the reverse reactions of the acetylene→propyne and propyne→propargyl pathway. Thus, at high  $Z_{st}$  the formation of the first aromatic ring via propargyl self-combination is severely limited because a key pathway that dominated propargyl production at low  $Z_{st}$  has been reversed resulting in rapid propargyl destruction.

**Part II**  
**Air-Fired and Oxy-Fuel Combustion of**  
**Coal and Coal/Biomass Mixtures**

## 7 Background

The fundamental studies presented in Part I of this dissertation demonstrated that for non-premixed flames the free-stream fuel and oxidizer concentrations can dramatically influence flame structure and soot formation. These studies were partially driven by the potential for wide-scale deployment of oxy-fuel combustion in coal-fired power plants (*oxy-coal combustion*) as an enabling tool for carbon capture and sequestration (CCS), and a need to understand the influence of the fuel and oxidizer compositions on flame characteristics. Oxy-fuel combustion is one configuration of oxygen-enhanced combustion involving the use of an oxygen stream mixed with externally recycled flue gases (RFG) as the oxidizer. Because the fuel, oxygen, and RFG can be controlled independently, the fuel and oxidizer stream compositions can be altered in a manner somewhat similar to the gaseous flames studied in Part I of this work. A key objective of Part II therefore, is to investigate the effects of varying the compositions of the coal carrier gas stream (primary oxidizer stream) and the concentric or secondary oxidizer stream on nitric oxide (NO) emissions during oxy-coal combustion. Other objectives include parameterizing the laboratory-scale combustor utilized in this study under air-fired conditions and examining the effect of cofiring biomass with coal on NO emissions under both air-fired and oxy-fuel conditions. The sections that follow provide background and supporting information on coal, biomass, the combustion of solid fuels, and the formation of nitrogen oxides during coal and biomass combustion. For more detailed information on the combustion of solid fuels the reader is referred to [64, 143-145]. For more information on biomass combustion and cofiring the reader is referred to

Van Loo and Koppejan [25]. A review of NO<sub>x</sub> formation during the combustion of solid fuels can be found in Glarborg et al. [146].

## 7.1 Coal

### 7.1.1 Coal Formation and Characterization

Coal is a solid, brittle, combustible sedimentary rock containing both organic and inorganic components. Its formation is believed to have occurred as a result of temperature and pressure acting on the remains of fallen plants buried beneath the earth's surface over the course of 200-300 million years. From an elemental perspective, coal contains varying amounts of carbon, hydrogen, nitrogen, oxygen, and sulfur along with trace amounts of other species and mineral matter [147, 148]. Coal can be classified as lignite, subbituminous, bituminous, and anthracite, with lignite more closely resembling the original plant matter and anthracite more closely resembling graphite. The coal *rank* increases from lignite to anthracite and is determined based on the coal's calorific value (for low rank coals) and its fixed carbon content (for high rank coals) [148].

### 7.1.2 Coal Usage and Resources

In 2006 coal accounted for nearly 50% of electricity production and 27% of total energy production worldwide. From 1980 to 2007 worldwide coal production increased almost 70% from 4.2 billion short tons to 7.1 billion short tons and is projected to increase 1.7% per year until 2030 as China, India, and other developing nations rely heavily upon coal as an affordable and reliable fuel [4]. While coal is found on every continent, the largest coal reserves that have been identified are in the United States, the former Soviet Union, and China—with 29% of the world's reserves found in the U.S., 19% in the former Soviet Union and 14% in China [149]. A comparison based on 2007 data indicated that cost of usable



energy generated by coal was \$6 per MWhr (\$1.78 per million BTU (MMBtu)), while oil and natural gas costs were \$25 per MWhr (\$7.40/MMBtu) and \$24 per MWhr (\$7.10/MMBtu), respectively. Moreover, analysts project that the cost of energy from coal will remain below \$7 per MWhr (\$2.00/MMBtu) in 2007 dollars through 2030 if no penalty for carbon dioxide emissions is imposed [150]. Finally, an interdisciplinary study from MIT on the future of coal, published in 2007, concluded that energy production from coal would continue to increase while renewable energy sources are being developed because a) coal is inexpensive, b) coal is abundant in many regions of the world making it a secure energy source, and c) existing renewable energy technologies cannot support current worldwide demand and will remain so for an extremely long time [5].

### **7.1.3 Coal and Global Climate Change**

Unfortunately, the combustion of coal produces more CO<sub>2</sub> per unit energy than any other fuel. This, along with its abundant use makes CO<sub>2</sub> emissions from coal-fired power plants a major contributor to the rising atmospheric CO<sub>2</sub> levels that have been linked to the melting of polar ice caps, the thawing of permafrost, and global climate change in general. In an effort to mitigate anthropogenic CO<sub>2</sub> emissions, particularly from coal fired power stations, the Department of Energy initiated a carbon sequestration program in 1997 that continues to promote and sponsor the development of carbon capture and sequestration (CCS) technologies. In the MIT interdisciplinary study previously mentioned it was concluded that “CCS is the critical enabling technology that [will] reduce CO<sub>2</sub> emissions significantly while also allowing coal to meet the world’s pressing energy needs” [5].

One of the most promising CO<sub>2</sub> storage scenarios utilizes underground geologic formations such as deep saline aquifers, oil and gas fields, and unmineable coal seams. In the

mid-1990s Statoil, a Norwegian petroleum company, began successfully injecting 1 million metric tons of CO<sub>2</sub> each year into a deep saline aquifer below the North Sea [151]. Since October of 2000, 13 million metric tons of CO<sub>2</sub> have been transferred through a 205 mile pipeline from a gasification company in North Dakota for sequestration in an oil field in Saskatchewan, Canada [152]. And, beginning in 2004 a third sequestration project began in Algeria with the goal of sequestering 17 million metric tons of CO<sub>2</sub> in a gas reservoir over its lifetime at an average rate of 1.2 million metric tons per year [153]. While these projects have been successful and show promise, sequestration rates and quantities will need to increase substantially for CCS to mitigate CO<sub>2</sub> emissions from large coal-fired power plants, which individually produce approx. 8 million metric tons of CO<sub>2</sub> annually. Fortunately, estimates of the worldwide geologic sequestration capacity are large, suggesting that storage sites will not be the limiting factor for the geologic CO<sub>2</sub> storage scenario for several hundred years [154].

Under conventional air-fired coal combustion the exhaust gases typically consists of more than 80 vol.% N<sub>2</sub>. However, because high pressures (ca. 1500 psia) are required for geologic sequestration, a relatively pure stream of CO<sub>2</sub> is desirable to avoid wasting energy compressing N<sub>2</sub>. Moreover, separating CO<sub>2</sub> from the other combustion products also drastically reduces the volumetric requirements for CO<sub>2</sub> storage. For post-combustion CO<sub>2</sub> capture from existing coal-fired utility boilers, this separation process can be accomplished by scrubbing the CO<sub>2</sub> from the nitrogen rich exhaust, or by separating the oxygen and nitrogen in air prior to combustion and burning the fuel in a mixture of oxygen and recycled flue gases (i.e. oxy-fuel combustion). The most commonly discussed and commercially proven scrubbing process is chemical absorption using monoethanolamine (MEA); however, other methods have been considered such as those using a microporous membrane with a solvent, cryogenic fractionation, and adsorption using molecular sieves [155, 156]. While

both the MEA scrubbing and oxy-fuel technologies are considered viable and are being pursued at the research and pilot-scale, several techno-economic studies have indicated a preference for oxy-fuel combustion [18, 157]. A brief discussion of the potential benefits of oxy-fuel combustion over the MEA absorption process is included in the next section.

It should also be noted that for new coal burning utility plants pre-combustion CO<sub>2</sub> capture is possible in an Integrated Gasification Combined Cycle (IGCC). In an IGCC plant equipped for CO<sub>2</sub> capture the coal is first converted into gaseous components or syngas (CO and H<sub>2</sub>). Following the addition of water, the syngas then undergoes a water-gas shift to convert CO and H<sub>2</sub>O to CO<sub>2</sub> and H<sub>2</sub>. The CO<sub>2</sub> is then captured from the emerging stream and the hydrogen combusted to drive a gas turbine. The combined cycle refers to the use of a heat recovery steam generator (HRSG), which drives a steam turbine. In addition, direct chemical looping in which metal oxides are used as an oxygen carrier and the oxidation and reduction reactions proceed in separate chambers has been proposed as a potential retrofit technology. Because IGCC is not applicable as a retrofit to the existing fleet of coal-fired boilers and direct chemical looping with coal is not yet a proven technology at the commercial scale, they will not be discussed in detail here.

#### **7.1.4 Oxy-Coal Combustion for CCS**

Oxy-coal combustion with flue gas recycle is an enabling technology for CCS as it can lead to flue gas CO<sub>2</sub> concentrations greater than 90 vol.%. A flow diagram comparing conventional air-fired combustion equipped with an MEA absorption unit for CO<sub>2</sub> separation and an idealized oxy-coal system is provided in Fig. 7.1. For oxy-coal combustion the amount of flue gas recycled to the burner (i.e. recycle ratio) defines the oxygen concentrations and is variable, leading to enhanced flexibility for burner optimization as

demonstrated by Liu and Okazaki [158] and discussed by Varagani et al. [159]. While both the MEA absorption and oxy-coal scenarios involve parasitic loads that will reduce plant efficiency, oxy-coal combustion may be preferred over MEA absorption if the combustion process can be designed to recover a portion of the lost efficiency [160] and if lower nitrogen oxide (NO<sub>x</sub>) sulfur oxide (SO<sub>x</sub>) emissions can be achieved resulting in the elimination or scaling back of post-combustion NO<sub>x</sub> and SO<sub>x</sub> cleanup equipment [161]. Lu and coworkers [157] concluded that electricity costs relative to current sub-critical pulverized coal generation would increase by 79% using MEA absorption technology and by 60% using oxy-fuel combustion technology.

Demonstrations of oxy-fuel combustion at the pilot-scale (30 MW and larger) have successfully achieved flue gas CO<sub>2</sub> concentrations of 95 vol.% while reducing NO<sub>x</sub> concentrations below detectable limits [60, 162]. The greatest additional costs associated with the oxy-fuel CCS system result from the air-separation unit (ASU) needed to produce a stream of oxygen and the CO<sub>2</sub> compression and purification unit (CPU). In addition to the cost estimates of Lu and coworkers [157], estimates in a 2005 report from the Intergovernmental Panel on Climate Change (IPCC) suggested oxy-fuel CCS technology could increase consumer energy costs from 50 to 100%; however, cost-saving technological advancements in combustion efficiency, air separation, and CO<sub>2</sub> capture are anticipated [18, 163].

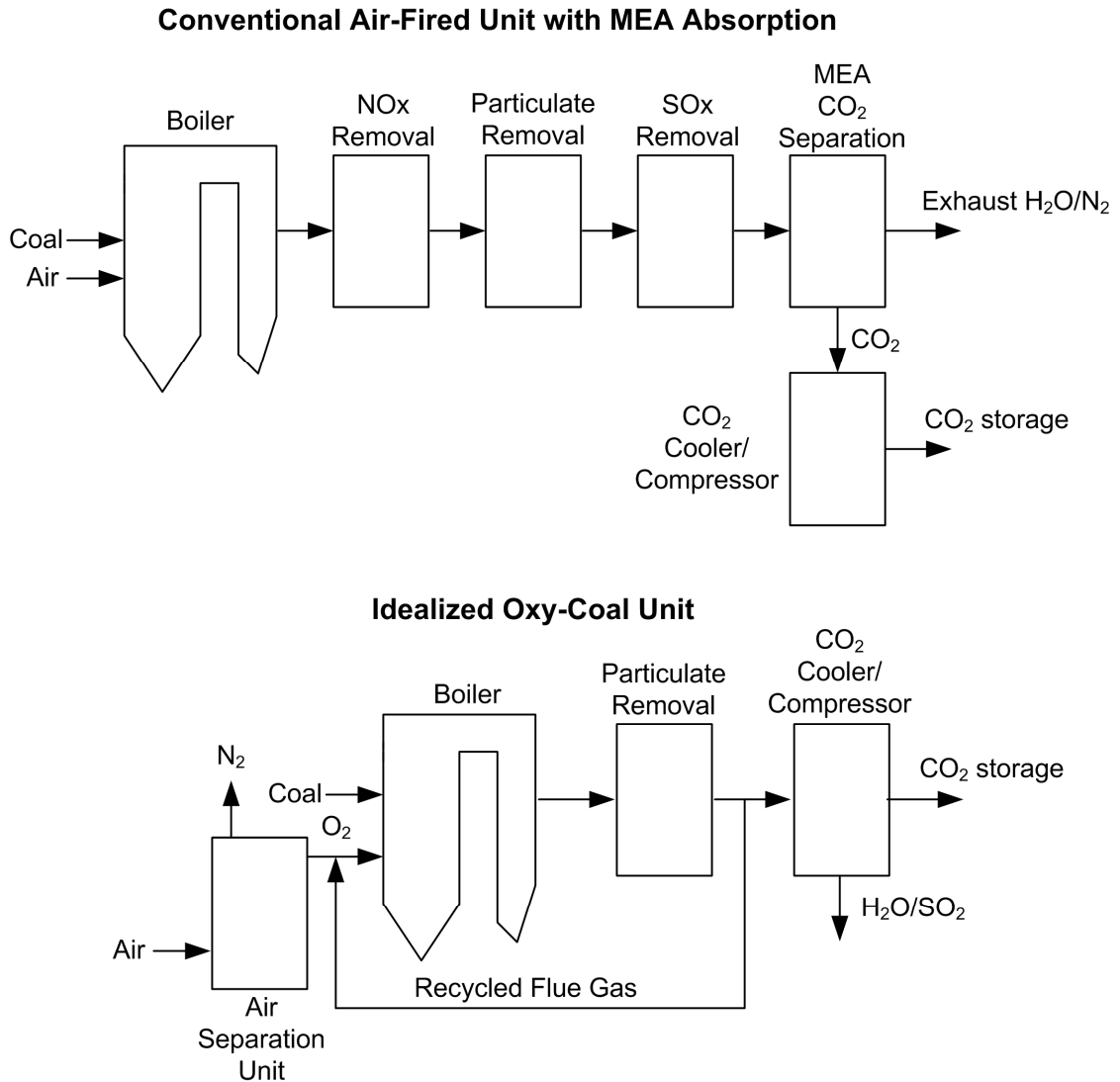


**Figure 7.1. Flow diagram comparing conventional air-fired coal combustion with MEA absorption for CO<sub>2</sub> separation with an idealized oxy-coal combustion unit adapted from Buhre et al. [18].**

In the literature review by Buhre et al. [18], four key areas of research were identified that need to be addressed to develop a better fundamental understanding of the differences between air-fired and oxy-fuel combustion, namely:

- Heat transfer performance and the effects of oxygen feed concentration and the amount of CO<sub>2</sub> recycled;

- Gas cleaning required (note that the flow diagram in Fig. 7.1 was idealized and excluded NO<sub>x</sub> and SO<sub>x</sub> gas cleanup equipment);
- Economic assessments identifying the cost of electricity and the cost of CO<sub>2</sub> avoided; and
- Combustion characteristics including ignition, burn-out, and emissions.

The work performed here addresses issues associated with the fourth research area identified by Buhre et al. by investigating the effects of oxy-coal combustion on the formation of nitric oxide and comparing the results with baseline air-fired data. Although not specifically targeted, some information on ignition and burnout was obtained. Background information on the processes involved in the combustion of solid fuels, including ignition and burnout, will be presented in Section 7.3, while a summary of nitrogen oxide formation during coal combustion and a review of the literature investigating NO<sub>x</sub> formation under oxy-coal conditions will be presented in Section 7.4.

## 7.2 Biomass

In the broadest sense, biomass includes any material that was derived directly or indirectly from living or recently living organisms [25]. Humans have long relied upon the combustion of biomass in many varieties for heat and light; however biomass currently plays a relatively insignificant role in electricity production globally and domestically. Nevertheless, in recent years both developing and developed countries have come to recognize the potential political, economic, and environmental benefits of increased biomass utilization in the utilities sector. Political benefits include energy security by reducing dependence on foreign oil and gas, economic benefits may come in the form of job creation, and environmental benefits include zero net CO<sub>2</sub> emissions, reduced acid rain, and

improvements to soil [25]. Economic modeling by Robinson et al. [164] indicated that cofiring biomass with coal for electricity generation could be competitive for reducing nitrogen oxides and sulfur oxides at fuel prices under \$15 per ton, while, depending on forthcoming CO<sub>2</sub> legislation, cofiring could reduce CO<sub>2</sub> emissions in the U.S. utilities sector by 100 million tons per year. Moreover, it was noted that renewable cofiring technology can be deployed at full-scale within 2-3 years [164].

Technically, the combustion of biomass can only be considered a renewable energy technology when accomplished in a sustainable manner. Thus, traditional methods of biomass utilization for non-commercial heating and cooking cannot be considered renewable. When biomass is harvested and utilized for energy in a sustainable manner the term “modern biomass” is often applied. In spite of this distinction, many of the statistics compiled by energy analysts overestimate the contribution of biomass to the worldwide renewable energy figures by including, for example, the use of trees for fuel in a non-sustainable way [165]. An important requirement for sustainable biomass usage is that significantly more energy be extracted from the biomass fuels than is consumed in fossil fuel energy resources during its cultivation and processing. Hughes [166] reports that the fossil fuel energy consumed during these activities is typically equivalent to less than 5% of the biomass energy content.

### **7.2.1 Biomass Resources**

The Biomass Research and Development Technical Advisory Committee (BRDTAC) that was formed under the Biomass R&D Act of 2000 set the following goals to be achieved in the U.S. by the year 2030: biomass will supply 1) 5% of power, 2) 20% of transportation fuels, and 3) 25% of chemicals. Such an undertaking will require a nearly

fivefold increase over the current biomass consumption in these sectors and is equivalent to displacing nearly 1/3<sup>rd</sup> of the U.S. transportation demands from petroleum [167, 168]. More recently, the U.S. Department of Agriculture (USDA) and the Department of Energy (DOE) concluded in a 2005 feasibility study that the 900 million dry metric tons of biomass required to meet the BRDTAC goals could be produced and utilized domestically while continuing to meet food, feed, and export demands [167]. According to this study, a major contribution to the total fuel feedstock can come from wood that must be cleared from both public and private lands to promote healthy forests. In August of 2000 the U.S. Forest Service developed the Nation Fire Plan in response to an unprecedented wildland fire season. They reported that 67 million acres of national forests across the country are at moderate to high risk for catastrophic destruction by wildfire. Utilization of just half of the reported wood resources could result in more than 7,000 MW of power generation annually, which would double the current contribution of biomass to electricity production in the U.S. [169]. Additionally, three new U.S. Department of Energy sponsored bioenergy resource centers were announced in 2007 that will focus on energy specific crops such as poplar and switchgrass as well as the development of cellulosic ethanol [170]. A summary of many of the biomass fuel resources potentially relevant to combustion are listed in Table 7.1.

**Table 7.1. Potential biomass resources adapted from [24, 25]**

Agriculture residues	Corn stover, wheat and barley straw, sugarcane bagasse, cotton gin
Forestry residues	Branches, treetops, whole trees from early thinnings, prunings
Lumber industry residues	Bark, sawdust
Food industry residues	Olive cakes and pits, rice husks, oat husks, nut shells
Energy crops	Switchgrass, miscanthus, poplar, willow, microalgae
Waste	Cattle manure, sewage sludge, demolition wood, railroad ties



### 7.2.2 Oxy-Coal/Biomass Cofiring

Another proposed application for oxy-fuel combustion in conjunction with CCS that would not only reduce CO<sub>2</sub> emissions, but would actually remove CO<sub>2</sub> from the atmosphere and reduce fossil fuel consumption involves the cofiring of biomass with fossil fuels. In the proposed scenario, biomass that has removed CO<sub>2</sub> from the atmosphere via photosynthesis, is cofired with coal in a CCS equipped plant. Because the CO<sub>2</sub> released by the biomass during combustion is part of the active carbon cycle, and assuming that nearly all of the CO<sub>2</sub> in the flue gases will be captured, this cofired CCS equipped power plant becomes a carbon sink instead of carbon-neutral. Under the proposed CO<sub>2</sub> cap-and-trade policy those emitting CO<sub>2</sub> into the atmosphere beyond predetermined levels will be required to pay a monetary penalty (i.e. purchase carbon credits). This means a coal/biomass cofired CCS equipped power plant could supplement power production and distribution revenue with carbon-credit sales. While a substantial amount of work has been done to identify the benefits and challenges associated with the cofiring of biomass and coal in conventional air-fired boilers, to date this author is aware of only a few studies in the literature investigating the cofiring of biomass with coal under oxy-fuel conditions.

Many of the potential challenges associated with biomass cofiring under air-fired conditions have been discussed by Sami et al. [24] and in detail by Van Loo and Koppejan [25], and include fuel feeding, boiler efficiency losses, slagging, fouling, corrosion, flame stability, burnout, and pollutant formation. As the focus of this work is in NO<sub>x</sub> formation, only a brief discussion of the other issues is included here.

Biomass fuel processing and feeding can be difficult as conventional coal milling and delivery equipment is not designed for fibrous low-density materials. Low level cofiring has

been performed successfully using the existing fuel processing equipment, but has been limited to less than 5% biomass (on a thermal basis). When separate biomass feeding systems have been utilized the thermal contribution from biomass has been as high as 40% [164].

Boiler efficiencies can suffer when cofiring if the biomass moisture content is excessive. In some of the literature reviewed by Robinson et al. [164] efficiency reductions of 0.5% per 10 wt.% biomass cofired have been reported, while others reported no efficiency reductions and even higher efficiencies when cofiring biomass with less moisture content than the coal.

Slagging can result when the ash that collects on the furnace walls or near burner surfaces is at temperatures near or above its melting point. The viscous liquid minerals in the ash may collect resulting in flow field changes or blockages, or they may creep downward along the furnace walls over time due to gravity. Fouling refers to the build up mineral species that condense on heat transfer surfaces and can influence plant efficiency. It has been observed that the higher sodium and potassium concentrations in certain forms of biomass can aggravate both slagging and fouling problems as these alkaline metals lower the melting point of ash. Moreover, biomass combustion deposits can be denser and more difficult to remove. In addition, cofiring biomass fuels with high chlorine content can accelerate surface corrosion due to the presence of hydrochloric acid. At present, literature discussing the combined effects of oxy-fuel combustion and biomass cofiring on slagging, fouling, and corrosion could not be found.

With respect to ignition and flame stability, which will be discussed in Section 7.3.5, biomass cofiring can delay ignition resulting in lifted flames and increased NO<sub>x</sub> formation.

Burnout can be influenced by the reactivity of the biomass and was shown to be improved when cofiring feedlot waste [171]. The reactivity can be greater in biomass fuels relative to coal if the biomass is highly porous. Under both air-fired and oxy-fuel conditions, Arias et al. [172] examined the effect of cofiring Eucalyptus with coals of differing rank on ignition and burnout in an entrained flow reactor. It was demonstrated that biomass addition can reduce the ignition temperature of the blend under air-fired conditions and that this effect can be amplified under oxy-fuel conditions with oxygen concentrations greater than 30 vol.%. The lowering of the ignition temperature when cofiring was attributed to the higher reactivity of the biomass when compared to the coals used. Char burnout was unchanged when cofiring under air-fired conditions, while under oxy-fuel conditions with 35 vol.% oxygen an increase in char burnout, though small, was observed. These small differences in char burnout were attributed to changes in the temperature distribution within the reactor resulting from the different reactivities of the various coals and biomass.

Cofiring biomass may also influence the formation of nitrogen oxides in ways other than by reducing flame stability. Many biomass fuels contain significantly less fuel bound nitrogen than coal, and all else being equal, could result in less NO<sub>x</sub> production when cofired with coal. In addition, much of the nitrogen contained in biomass may be converted to ammonia (NH<sub>3</sub>), which can reduce NO<sub>x</sub> in situ [173, 174]. As the effect of biomass cofiring on NO<sub>x</sub> formation is one focus of this work, additional discussion on the chemistry of NO<sub>x</sub> formation and the potential influence of biomass will be provided in Section 7.4. At the present time, no literature has been found investigating the combined effects of biomass cofiring and oxy-fuel combustion on NO<sub>x</sub> formation. Thus, the oxy-fuel cofiring work presented in Chapter 8 is the first of its kind.

## **7.3 Physical Processes of Solid Fuel Combustion**

The burning of a solid fuel in a gaseous oxidizer is a more complex process than the combustion of a fuel and oxidizer that are both initially in the gas phase. When considering the combustion of small solid particles as in this work, there are four key stages involved: heating and drying, devolatilization, volatiles oxidation, and char oxidation. These four stages are summarized below. A discussion of flame stability and ignition is also included.

### **7.3.1 Heating and Drying**

The moisture content of solid fuels varies depending upon the fuel type and the conditions under which the fuel was obtained, transported, and stored. On a wet basis (w.b.) coal may inherently contain 1 to 40 wt.% moisture. For solid biomass fuels, the moisture content can vary even more dramatically reaching 60 to 70 wt.% on a wet basis (w.b.). In a pulverized fuel (PF) boiler the heating and drying process typically begins before the fuel enters the combustion chamber while it is being transported by preheated air to the burner. If the moisture content of the fuel is too high upon entering the combustion chamber the ignition process can be negatively affected resulting in poor boiler performance and even flame extinction since the remaining water will influence devolatilization and ignition.

### **7.3.2 Devolatilization**

Devolatilization, or the release of organic and mineral volatile matter contained in a solid fuel, occurs as a result of both pyrolysis and gasification. Pyrolysis is the thermal decomposition of the fuel in the absence of an externally supplied oxidizer, whereas gasification implies thermal decomposition in the presence of an externally supplied oxidizer [175-177]. Solid fuels may contain small amounts of volatiles as in the case of anthracite coal (0-10 wt.%, dry basis (d.b.)) or large amounts of volatiles as in the case of woodchips and

woody biomass (70-86 wt.% d.b.). Low volatile fuels are not typically used in pulverized fuel (PF) combustion due to ignition difficulties.

When a coal or solid biomass particle enters the combustion chamber it is rapidly heated and devolatilization begins. The organic (non-mineral) volatiles released from coal and biomass can vary in composition from molecular hydrogen to small hydrocarbons and heavy tars, while the devolatilization of oxygen-rich biomass fuels can also release significant amounts of CO and CO<sub>2</sub> [24]. The rate of devolatilization is dependent upon the heat flux to the particle surface by radiation and diffusion, particle size, thermal properties of the particle, and thermal effects within the particle. For pulverized coal (PC) and small biomass particles, devolatilization typically occurs within the first 10-15% of the particle's lifetime after entering the combustion chamber. The material remaining after all volatiles have been released is commonly referred to as char, and contains carbon and various minerals.

Because the complex physical-chemical processes by which volatiles are released and subsequently burned are critical in determining flame characteristics, including flame stability, ignition, and pollutant formation, coal devolatilization has been studied and reviewed extensively [178-185]. In addition, several studies have been conducted on the devolatilization of biomass fuels due to increased interest in direct firing and cofiring of biomass with coal [186-195].

### **7.3.3 Volatiles Oxidation**

During the devolatilization of a single coal particle, experimental observations have indicated that volatiles can exit the particle and burn as tiny non-premixed jet flames or they can exit more uniformly resulting in a non-premixed flame that envelopes the particle and prevents oxygen from reaching the particle surface such that heterogeneous char oxidation

cannot proceed simultaneously [182, 183]. The large number of species and the complexity of a detailed kinetic mechanism including all possible elementary steps for volatiles oxidation have led researchers to develop simplified approaches to describe the combustion of volatiles [196]. One approach, referred to as *local equilibrium*, assumes that when local temperatures are sufficiently high the volatiles and the oxidizing gas will be in thermodynamic equilibrium locally. Under these conditions the volatiles are consumed close to the particle surface immediately after being released such that the rate of combustion is limited by the rate of devolatilization or pyrolysis [147]. Based on a knowledge of the elemental composition of the volatiles and the heat of devolatilization this method has been adequate to predict local temperatures, gas compositions, and char consumption times [196].

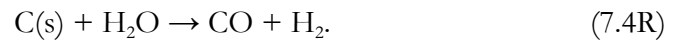
Another useful approach that does not require the equilibrium assumption and provides some indication of volatiles combustion rates utilizes global reactions. In this approach the global rates for the oxidation (or partial oxidation) of various hydrocarbon species representative of the volatiles are correlated leading to a global rate expression for a “pseudomolecule”,  $C_nH_m$ , having a carbon to hydrogen ratio ( $n/m$ ) determined by an analysis of the coal [196].

While these simplified models describing volatiles oxidation have proven useful in some applications (e.g. burnout), when attempting to understand near burner phenomena relating to ignition and flame stability or the formation of pollutants such as NO<sub>x</sub> and SO<sub>x</sub> a more detailed description of volatiles chemistry may be required.

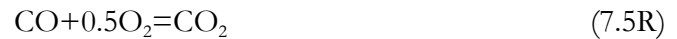
### **7.3.4 Char Oxidation**

Char oxidation is a heterogeneous process as it involves reactions between gaseous oxidizing species and the solid char. Reactions can occur at the particle surface or within the

particle's porous structure. When the particle temperature is high, the heterogeneous reactions are fast enough to consume the oxygen at the outer surface of the particle such that the rates are limited by the diffusion of the oxidizing species through the boundary layer, in which case the system can be understood through transport phenomena alone. At moderate particle temperatures, sufficient time is available for oxygen to diffuse deeper into the particle pores resulting in simultaneous reactions at the surface and within the particle's porous structure. Thus, at moderate temperatures the process is limited by the reaction kinetics and the diffusion of oxygen within the particle. When the particle temperature is sufficiently low, oxygen is able to diffuse into the particle uniformly resulting in reactions that occur through the entire particle volume and are kinetically limited [147]. The semi-global reactions commonly used to describe char oxidation include the heterogeneous irreversible reactions



where (s) indicates a solid species, and the homogeneous reversible reactions



and



### 7.3.5 Ignition and Flame Stability

For wall-fired PF combustion, flame stability refers to ignition occurring within a reasonable distance from the burner face. Lifted or detached flames are considered unsafe due to the increased risk of flame extinction and the potential for a dust explosion [197]. The ignition of coal and small biomass particles can be a homogeneous or a heterogeneous process depending upon volatile content, fixed carbon, composition, particle size, and heat and mass transport. Following their release, volatiles will ignite spontaneously close to the parent particle if the local temperature and mixing are sufficient; however, when local temperatures are too low the mixture of volatiles and oxidizer can ignite at large distances from the parent particle [147]. As mentioned previously for a single particle, if the volatiles evolve uniformly and enshroud the particle with a flame, oxygen is prevented from reaching the particle surface and heterogeneous ignition will not occur. If the volatile combustion is incomplete, or volatiles are released intermittently or as jets, then homo- and heterogeneous combustion can proceed in parallel, provided other requirements are met [24]. Heterogeneous ignition of char can be predicted by the Semenov model [147, 198], or by more modern thermal explosion theories [199], which are based on the principle that ignition will occur if the rate of heat release from chemical reaction is greater than the rate of heat loss such that “thermal runaway” results.

Ignition characteristics can be influenced under oxy-fuel conditions. Molina *et al.* [200] found that higher local gas mixture heat capacities resulting from the increased presence of CO<sub>2</sub> in oxy-fuel systems can inhibit particle ignition and reduce volatile diffusivity by up to 20% when compared with N<sub>2</sub> dominated mixtures, while Kiga *et al.* [48] studied the combustion of coal dust clouds in microgravity using CO<sub>2</sub>, N<sub>2</sub>, and Ar as diluents



and demonstrated that the flame speed is lower in environments with high CO<sub>2</sub> concentrations due to the increased heat capacity of the gas mixture.

As conditions promoting robust ignition characteristics are critical to ensuring the safe and efficient operation of pulverized fuel systems, numerous studies have investigated these characteristics through flame stability measurements. The earliest work on flame stability in coal combustion examined the importance of hydrodynamic effects under conventional air-fired conditions. Beer and Chigier [201, 202] and Wolanski and Wojcicki [203] considered hydrodynamic effects such as swirl, burner geometry, and the presence of a bluff-body. Syred and Beer [204] reviewed the effects of swirl on combustion characteristics and Beer and Chigier were the first to reference the use of a divergent extension to the burner, commonly referred to as the quarl, which produced a “high intensity, compact flame with the flame front within the divergent nozzle even at low degrees of swirl.” The pioneering work of Beer and subsequent studies by Lockwood and Mahmud [205] have identified the residence time of coal particles in the internal recirculation zone (IRZ) as the key parameter governing pulverized coal flame stability. Long particle residence times in the IRZ ensures the availability of hot volatile combustion products that promote early char ignition [205]. Experiments by Truelove and Holcombe [206] used coals of various volatile content and also identified burner aerodynamics as the most important parameter governing flame stability.

Flame stability challenges due to hydrodynamic effects may arise if oxy-fuel technology is to be retrofitted to existing air-fired burners. For example, studies suggest that 30% by volume O<sub>2</sub> is required under oxy-fuel conditions to achieve similar boiler temperature profiles and heat transfer characteristics to air-fired combustion. Because the total flow of O<sub>2</sub> is more or less a fixed quantity (for stoichiometric and pollutant formation

purposes) a reduction in the total volumetric flow through the burner occurs for oxy-fuel systems. Since the volumetric flow through the primary stream must be maintained for fuel entrainment and delivery, flow in the secondary stream must be reduced. In a burner that utilizes secondary swirl, a reduction in flow rate can impact flame shape and stability. Recognizing the importance of flame shape as it relates to ignition and flame stability, the International Flame Research Foundation (IFRF) has developed a classification system to identify flame shapes in swirl burners. A Type-0 flame utilizes a small amount or no swirl and is characterized by a long jet-flame stabilized at the fuel injector or downstream with some amount of external recirculation. Type-2 flames are generated when a high level of swirl induces an IRZ resulting in a short high intensity flame that ignites very close to the fuel injector. A Type-1 flame is a combination of Type-0 and Type-2 characteristics and includes some level of fuel-jet penetration through the IRZ [207].

Khare *et al.* [208] recently examined the effects of oxy-fuel combustion on ignition and flame stability retrofitted to existing conventional air-fired swirl burners. The oxy-fuel system was configured such that the furnace heat transfer matched that of the conventional air-fired system and the flames were identified as Type 0. In addition to delayed ignition and flame speed reduction due to the higher heat capacity of CO<sub>2</sub>, Khare *et al.* showed that flame shape and flame type were influenced by aerodynamic effects and that flame type could potentially change from Type-2 to Type-0 in a retrofitted oxy-fuel system due to the reduction in total volumetric flow rate and the associated reduced swirl. Thus, maintaining a Type-2 flame in a retrofitted system may require burner modifications.

Flame ignition and stability characteristics may also be affected when cofiring biomass with coal. Although biomass fuels and coal follow a similar sequence of devolatilization and combustion, their moisture and volatile contents, compositions, and

heating values can be significantly different [24]. Biomass typically contains a higher percentage of volatiles than coal and begins pyrolysis at lower temperatures, which could enhance flame stability; however, biomass particles often contain more inherent moisture and are difficult to reduce in size leading to increased heating times and delayed ignition [209-213]. In addition, biomass particles may follow different trajectories and interact differently with the turbulent flow field (i.e. turbulence modulation) because of their lower densities and potentially different shapes and sizes [213].

## 7.4 Nitrogen Oxides

The formation of nitrogen oxides (NO<sub>x</sub>), including nitric oxide (NO), nitrogen dioxide (NO<sub>2</sub>), and nitrous oxide (N<sub>2</sub>O) in combustion processes has been the subject of extensive research for more than 30 years. Consequently, an exhaustive review of all the potentially relevant literature on NO<sub>x</sub> formation is not within the scope of this work. The adverse effects of NO<sub>x</sub> in the atmosphere are well known and include the formation of acid rain and photochemical smog and global climate change due to the greenhouse effect of N<sub>2</sub>O. The sections that follow present a brief overview of the important chemical mechanisms in NO<sub>x</sub> formation during coal combustion and a summary of recent NO<sub>x</sub> studies examining the effects of oxy-coal combustion as well as the effects of biomass cofiring under air-fired conditions.

### 7.4.1 Thermal NO<sub>x</sub>

Thermal NO<sub>x</sub> refers to the oxidation of molecular nitrogen (N<sub>2</sub>) as described by the extended Zeldovich mechanism





Typically, this mechanism does not contribute significantly to NO<sub>x</sub> production until temperatures exceed 1800 K due to the nitrogen triple bond; however, if high concentrations of NO are present due to other mechanisms or if N<sub>2</sub> has been removed, as in oxy-fuel combustion, the reverse of reaction 7.7R can contribute significantly to NO destruction [146, 214, 215].

### 7.4.2 Prompt NO<sub>x</sub>

The prompt NO<sub>x</sub> pathway, proposed by Fenimore, begins with the attack of the CH radical on the N<sub>2</sub> triple bond and can result in the formation of NO<sub>x</sub> through intermediate amines or cyano compounds within time scales that are short compared to the high activation energy kinetics of the thermal mechanism [145, 216]. The dominant route for NO<sub>x</sub> formation via the prompt mechanism is dependent on local stoichiometry and can involve numerous elementary reaction steps. For fuels such as coal, which may inherently contain up to 2 wt.% nitrogen, the contribution of the prompt mechanism to the total NO<sub>x</sub> emissions is usually insignificant, thus it is not discussed in detail here [196]. Additional details on the prompt mechanism can be found in [217] and [145].

### 7.4.3 Fuel NO<sub>x</sub>

Fuel NO<sub>x</sub> refers to the oxidation of nitrogen bound to the fuel, i.e. *fuel-N*. In coal, the fuel-N is contained in both the volatiles and the char (i.e. *volatiles-N* and *char-N*), and depending on the coal rank and the local temperature, may evolve as hydrogen cyanide (HCN), soot bound nitrogen, or to a lesser extent ammonia (NH<sub>3</sub>) [218]. As discussed in

[145], HCN and NH<sub>3</sub> may then react with radicals forming intermediate amines, which lead to atomic nitrogen, and subsequently NO. Pershing and Wendt [219] demonstrated that fuel nitrogen oxidation was the primary source of NO (>75%) during unstaged coal combustion, with volatile-N conversion to NO dominating over char-N conversion. Pohl and Sarofim [220] concluded that the relative contributions of volatiles-N and char-N to the total fuel-N conversion are strongly dependent upon near burner temperature, residence time, and stoichiometry. Consequently, many low-NO<sub>x</sub> coal combustion systems have been designed to control these characteristics.

#### 7.4.4 Conventional NO<sub>x</sub> Reduction Strategies

Common thermal NO<sub>x</sub> reduction methods involve reducing the combustion temperatures to prevent the dissociation of N<sub>2</sub>. The combustion temperature can be reduced by injecting water, recirculating flue gases, or if some or all of the combustion air is preheated, by reducing the preheat temperature. Injecting water reduces the temperature by absorbing energy during a phase transition from liquid to vapor. Flue gas recirculation decreases temperature by increasing the amount of inert relative to the stoichiometric amount of oxygen and its effectiveness is determined by the amount and initial temperature of the gases added, as well as the relative contribution of thermal NO<sub>x</sub> to the total NO<sub>x</sub> emissions. Recycling flue gases can also reduce NO<sub>x</sub> in the recycled flue gas to N<sub>2</sub> and O<sub>2</sub> via reactions with hydrocarbons and hydrocarbon intermediates, so-called NO<sub>x</sub> *reburning*, which is an inherent characteristic of oxy-fuel technology discussed in Section 7.4.5.

Another method to reduce NO<sub>x</sub> emissions involves oxidizer staging, which is accomplished by operating some or all burners with insufficient oxidizer and supplying the remaining air to complete the combustion at a location downstream. The goal of oxidizer

staging is to create a reducing environment where the NO<sub>x</sub> that was produced in the high temperature near-burner region can react with hydrocarbon species leading to N<sub>2</sub>. The oxidizer deficiency in the near burner region defines the depth of staging, and for wall-fired boilers typically 80% of the total combustion air is introduced through the burner. Deeper staging (i.e. less air introduced through the burner) can result in flame instability [161, 221].

Fuel reburn or fuel-staging is a NO<sub>x</sub> reduction technique that involves introducing a portion of the fuel downstream of the primary combustion zone to create a fuel-rich reburn zone [222]. In the reburn zone NO<sub>x</sub> reacts with hydrocarbon volatiles released from the reburn fuel and is reduced to N<sub>2</sub> by reactions similar to those described by the Fenimore mechanism. Combustors utilizing coal reburn have demonstrated NO<sub>x</sub> reductions as high as 60%.

The emission of nitrogen oxides can also be reduced by post-combustion gas treatment methods such as selective non-catalytic reduction (SNCR) or selective catalytic reduction (SCR). Selective non-catalytic reduction involves injecting ammonia or urea into the combustion exhaust when it is between 1100 K and 1400 K to reduce NO<sub>x</sub> to molecular nitrogen. Under ideal conditions with perfect mixing, sufficient time, and the proper temperature SNCR can theoretically reduce NO<sub>x</sub> by nearly 90%. In practice however, these conditions are not achievable due to temperature gradients, injection constraints, and less than ideal mixing resulting in more modest reductions in the range of 20-30%. Selective catalytic reduction is similar to SNCR in that ammonia or urea is often used as the reducing agent, but differs by using a catalyst to reduce the temperature required to activate the NO reducing reactions. Large reductions in NO<sub>x</sub> emissions with SCR have been demonstrated at full-scale (70-95%), but capital and operational costs are restrictive.

### 7.4.5 Oxy-Fuel Combustion for NO<sub>x</sub> Reduction

The potential to lower NO<sub>x</sub> emissions under oxy-fuel combustion conditions was demonstrated as early as 1985 by Weller et al. [223]. Several subsequent studies at the laboratory and pilot scale have been conducted demonstrating that NO<sub>x</sub> emissions can decrease by as much as 70% when compared to conventional air-fired combustion [18, 44-60]. Early works reported that the main effects resulting in lower NO<sub>x</sub> emissions under oxy-fuel conditions with flue gas recycle were: 1) enhanced NO<sub>x</sub> reduction by char due to higher CO concentrations, 2) the reduction of recycled NO<sub>x</sub> to N<sub>2</sub> by hydrocarbons as it passes through the flame zone, and 3) interactions between fuel-N released during fuel pyrolysis resulting in decreased NO<sub>x</sub> formation [47]. Okazaki and Ando [47] investigated the relative contributions of these mechanisms using an electrically heated entrained-flow reactor containing a flat premixed methane (CH<sub>4</sub>) flame doped with NH<sub>3</sub> to simulate coal volatiles and anthracite to simulate char. It was concluded that the reduction of recycled NO<sub>x</sub> to N<sub>2</sub> through chemical reactions with the hydrocarbon containing volatile species represents the dominant mechanism by which NO<sub>x</sub> emissions are lowered during oxy-fuel combustion. Reviewing the work of [47], Mackrory [21] identified three features of the study that may have led to results inconsistent with practical systems, namely:

- 1) CH<sub>4</sub> and NH<sub>3</sub> may not sufficiently represent the numerous volatile species associated with coal combustion, and CH<sub>4</sub> could have amplified the NO<sub>x</sub> reburning effect and prompt NO<sub>x</sub> mechanism [224]. Moreover, HCN, not NH<sub>3</sub>, is typically considered the dominant nitrogen containing species.

- 2) Premixing of CH<sub>4</sub> and NH<sub>3</sub> may have prevented the potentially important effects of variable local stoichiometry due to imperfect mixing and the time-temperature dependent release of volatiles.
- 3) Char interactions may have been underrepresented as the active surface area of anthracite is considered to be less than that of industrial char.

Hu et al. [225] studied the effects of oxygen concentration (20, 50, 80, 100 vol.%), temperature (1123-1573 K), and fuel equivalence ratio ( $\phi = 0.4-1.6$ ) on NO<sub>x</sub> emissions under both O<sub>2</sub>/N<sub>2</sub> and O<sub>2</sub>/CO<sub>2</sub> environments in an electrically heated furnace using high volatility coal (48 wt.% d.b.) at mass flow rates up to 180 g/hr. Measurements were compared on a concentration (ppm) basis and in terms of the NO<sub>x</sub> emissions index (mg-N/g-Coal-fed). Emissions under the O<sub>2</sub>/CO<sub>2</sub> conditions were observed to be lower than those measured in the O<sub>2</sub>/N<sub>2</sub> environment for all oxygen concentrations (<100%), and this was attributed to the absence of thermal NO<sub>x</sub> and/or interactions between NO, CO, and char. At 1273 K the NO<sub>x</sub> emissions index showed some dependence on the oxygen concentration under the O<sub>2</sub>/N<sub>2</sub> environment, but limited dependence under the O<sub>2</sub>/CO<sub>2</sub> environment except at 20 vol.% O<sub>2</sub>. The maximum NO<sub>x</sub> emissions index was observed under an O<sub>2</sub>/N<sub>2</sub> environment at 50 vol.% O<sub>2</sub>, and NO<sub>x</sub> emissions returned to levels comparable to the air-fired data at 100 vol.% O<sub>2</sub>. Peak NO<sub>x</sub> in the O<sub>2</sub>/CO<sub>2</sub> environment was also observed at 50 vol.% O<sub>2</sub>. Peak NO<sub>x</sub> at 50 vol.% O<sub>2</sub> with N<sub>2</sub> was explained based on the high concentrations of both O<sub>2</sub> and N<sub>2</sub> promoting thermal NO<sub>x</sub>; however, peak NO<sub>x</sub> at 50 vol.% O<sub>2</sub> in CO<sub>2</sub> was not explained. During single coal particle burning experiments Timothy et al. [226] observed that particle temperatures increased from 2000 K in air to 2750 K in pure oxygen for lignite coal, and from 2300 K in air to 3100 K in pure oxygen for



bituminous coal. In addition, the observable volatile “flame” times were reduced from 6-12 ms in air to 2-4 ms in pure oxygen and char burnout was reduced from 80 ms in air to 10 ms in pure oxygen. Thus, the results observed Hu et al. [225] at elevated oxygen concentrations may be related to particle temperature and combustion times. Increasing the furnace temperature in [225] was observed to have a more significant effect on NO<sub>x</sub> emissions at lower equivalence ratios, with peak NO<sub>x</sub> increasing by 50-70% for the O<sub>2</sub>/N<sub>2</sub> cases and 30-50% for the O<sub>2</sub>/CO<sub>2</sub> cases, while for a fuel equivalence ratio  $\phi > 1.4$  the differences were not as pronounced. Earlier work by Pershing and Wendt [219] using Western Kentucky and Colorado coals with volatile contents of 37.9 wt.% d.b. and 40.2 wt.% d.b., respectively, and using variable preheat with an oxidizer mixture of argon, nitrogen, and recycled flue gases to control temperature, concluded that the effect of temperature on fuel-NO<sub>x</sub> formation was insignificant in the range of approx. 2150-2480 K at 15 vol.% excess air. A comparison of [219, 225] suggests that the temperature dependence may be influenced by the coal volatility, the concentration of CO<sub>2</sub>, or that small-scale furnace results may not capture important interactions relevant to practical systems.

Using the same experimental setup, Hu et al. [50] investigated the effects of oxygen concentration, temperature, and fuel equivalence ratio on the reduction of simulated recycled NO<sub>x</sub>. Increasing the fuel equivalence ratio was observed to enhance the reduction of recycled NO<sub>x</sub> (i.e. improve reduction efficiency), while increasing the oxygen concentration had the reverse effect. Varying temperature did not have an obvious effect. The improved NO<sub>x</sub> reduction at high equivalence ratio was explained by the increased availability of CH fragments, unburnt char, and CO, species that would preferentially be oxidized under fuel-lean conditions. Reduced reduction efficiencies at higher oxygen concentrations were explained by rapid consumption of CH fragments early in the flame. The negligible changes

observed when increasing temperature were attributed to the competing effects of rapid volatile release resulting in higher concentration of reducing species and accelerated NO<sub>x</sub> kinetics.

Liu and Okazaki [158] used an entrained flow reactor similar to that described above [47] and proposed a unique scenario using both recycled flue gas and recycled heat to maintain combustion at low oxygen concentrations to further reduce NO<sub>x</sub> formation. It was observed that with 40% heat recycle the oxygen concentration could be reduced to 15 vol.% while maintaining combustion intensity and reducing NO<sub>x</sub> emissions to one seventh of conventional air-fired combustion.

Mackrory and Tree [20] used a laminar unheated multi-fuel flow reactor to investigate the various mechanisms contributing to NO<sub>x</sub> reduction for a variety of coals under staged oxy-fuel conditions with approx. 80% of the stoichiometric oxidizer introduced at the burner. A premixed natural gas flame was used to sustain coal combustion at coal feed rates ranging from 0.6-0.9 kg/hr and it was determined that the methane flame did not interfere with the coal processes. In addition to experiments, the system was modeled as a plug flow reactor to elucidate detailed information about the influence of oxy-fuel conditions on NO<sub>x</sub> chemistry. Lower NO<sub>x</sub> emissions and faster NO<sub>x</sub> destruction were observed under oxy-fuel conditions when compared to air-firing, and this was attributed partially to the higher observed CO and NO concentrations. Higher CO concentrations were attributed primarily to thermal dissociation of CO<sub>2</sub> at temperatures greater than 1500 K, while the contribution from gasification of char by CO<sub>2</sub> was deemed secondary.

Croiset and Thambimuthu [227] reported NO<sub>x</sub> emissions under air-fired and oxy-fuel conditions in 0.21 MW facility while varying the oxygen concentration (28, 35, 42 vol.%)

with no flue gas recycle and dry flue gas recycle (i.e. wet recycle = H<sub>2</sub>O not removed, dry recycle = H<sub>2</sub>O condensed out). Emissions from oxy-fuel flames were always lower than those measured while air-firing, even when the oxygen concentration was 42 vol.%. Flame temperatures and NO<sub>x</sub> emissions were observed to increase with increasing oxygen concentrations and minimum NO<sub>x</sub> emissions were observed with 28 vol.% O<sub>2</sub>. Dry flue gas recycle resulted in a 40-50% reduction in NO<sub>x</sub> emissions when compared to no recycle.

Liu et al. [228, 229] performed oxy-coal experiments in a 20 kWth down-fired combustor using a UK bituminous coal. Axial temperature profiles were measured and found to be similar to air-firing when the oxidizer contained 30 vol.% O<sub>2</sub> and 70 vol.% CO<sub>2</sub>, although it was noted that approx. 10% of the total flow under oxy-fuel conditions was air entrained during coal feeding. During unstaged combustion a burner stoichiometric ratio of 1.2, fuel-N conversion to NO was lowered by 20% under oxy-fuel conditions with no recycle when compared to air-firing. This was attributed to the higher NO and CO concentrations in the vicinity of the particle under oxy-fuel conditions (i.e. the total volumetric flow is reduced under oxy-fuel conditions) leading to the reduction of NO by CO and the reduction of NO on the char surface. Experiments under staged conditions at two different levels (570 mm and 880 mm downstream of the burner) were also performed and the difference between air-fired and 30/70 oxy-fuel NO conversion diminished as the oxidizer was shifted to the closer down stream port, but remained significant as the oxidizer was shifted to the far downstream port. Reduction of recycled NO<sub>x</sub> was shown to improve under oxy-fuel conditions when compared to air-firing and with oxidizer staging. Recycling NO<sub>x</sub> through the staging (i.e. overfire) ports was less effective at reducing NO<sub>x</sub> compared to recycling NO<sub>x</sub> through the burner.

Andersson et al. [215] measured NO (NO<sub>2</sub> was not reported) under air-fired and oxy-fuel conditions at 100 kW with predried German lignite at flame temperatures near 1600 K. The system was operated with and without air infiltration. A model was also developed using both simplified and detailed NO chemistry. Under oxy-fuel conditions NO emissions on a mass per unit energy basis were reduced 70-75% compared to air-firing. Air infiltration was shown to have no effect indicating that the thermal and prompt NO<sub>x</sub> mechanisms were not important at this temperature. The simple model was shown to adequately describe the basic features of NO formation and destruction and it was concluded that lower NO emissions under oxy-fuel conditions were due to more rapid destruction of formed and recycled NO. Additional modeling indicated that NO destruction may actually be improved at very high temperatures under oxy-fuel conditions by the reverse Zeldovich mechanism when near-zero levels of molecular nitrogen are present. This concept was discussed further by Normann et al. [214].

#### **7.4.6 Biomass Cofiring for NO<sub>x</sub> Reduction**

The cofiring of biomass with coal has been recognized as one of the most promising technologies to mitigate CO<sub>2</sub> emissions from the utilities sector in the near-term [27]. As with oxy-fuel combustion, the economics of biomass cofiring can be improved by its ability to reduce NO<sub>x</sub> emissions, especially when biomass fuel prices are high [164]. Most biomass fuels contain less nitrogen than coal; however, cofiring does not always lead to significant reductions in NO<sub>x</sub> emissions, and in some cases may result in higher NO<sub>x</sub>. The ability to reduce NO<sub>x</sub> emissions when cofiring is dependent on several parameters beyond the biomass fuel's nitrogen content, including: particle size and shape, moisture content, volatile content, calorific value, burner hydrodynamics, delivery method and location, staging

conditions, coal characteristics, and potentially several others. The effects of cofiring on NO<sub>x</sub> emissions under oxy-fuel conditions is a relatively new area of research for which published results are not yet available. A brief discussion of the relevant air-fired cofiring studies reviewed by Sami et al. [24] follows indicating the potential for mixed results.

Regland et al. [230] and Aerts et al. [231] cofired switchgrass with coal in a 50 MW pf boiler and observed a 20% reduction in NO<sub>x</sub> emissions when approx. 25% of the thermal input was provided by the switchgrass. This result was attributed to the lower nitrogen content of switchgrass.

Siegel et al. [232] cofired straw and cereal in a 500 kW PF combustor under different fuel injection schemes. When biomass was introduced through a central tube and coal was injected through a larger diameter coannular tube, NO<sub>x</sub> emissions began to decrease relative to coal only firing (through the coannular tube) at thermal cofiring percentages above 20%, with a reduction of approx. 35% when cofiring 60% straw and cereal. Cofiring the coal and biomass together through the larger coannular tube also resulted in reduced NO<sub>x</sub> above 25% biomass (relative to coal only in the coannular tube), but the change was not as significant. When the coal was introduced through the central tube with the biomass exiting from the larger coannular tube the NO<sub>x</sub> emissions increased. It is also important to point out that the standard coal-air configuration (coal exiting the central tube) produced the least amount of NO<sub>x</sub>. That is, all cofiring scenarios produced more NO<sub>x</sub> than coal burning alone when introduced through the central tube.

Brouwer et al. [233] cofired wood waste in a down-fired pulverized fuel furnace under both unstaged and staged conditions. The wood waste was introduced directly with the coal and as a reburn fuel downstream in a fuel-staging scenario. Results showed that

cofiring biomass directly with no air-staging reduced NO<sub>x</sub> emissions by 17% when biomass provided 50% of the thermal input. Under air-staged conditions NO<sub>x</sub> emissions were not reduced until more than 50% biomass was cofired. Using the wood waste as a reburn fuel resulted in a 60% reduction in NO<sub>x</sub> at an optimal reburn stoichiometry of 0.85.

The literature reviewed by Sami et al. [24] also indicates that fuel-N released from biomass may be mostly converted to NH radicals, including ammonia (NH<sub>3</sub>), which can act as a NO<sub>x</sub> reducing agent provided the local temperature is appropriate [173, 174]. Werther et al. [234] notes that the high alkaline content of some biomass fuels can deactivate the catalyst used in SCR.

## 7.5 Summary

This chapter has provided background information on coal and biomass and has summarized important concepts in the combustion of solid fuels. The relevant NO<sub>x</sub> formation mechanisms were introduced and literature pertaining to NO<sub>x</sub> reduction under oxy-fuel conditions as well as NO<sub>x</sub> formation during biomass cofiring was reviewed. Many issues remain unresolved with respect to the potential for NO<sub>x</sub> reduction in both scenarios. Chapter 8 presents a systematic experimental evaluation of NO emissions from a 30 kWth laboratory-scale combustor under a variety of air-fired and oxy-fuel conditions with the goal of increasing the current understanding of the effects of oxy-fuel combustion as well as biomass cofiring on NO<sub>x</sub> formation.

# 8 Nitric Oxide Emissions from Coal and Coal/Biomass Combustion Under Air-Fired and Oxy-Fuel Conditions

## 8.1 Introduction

One of the most pressing environmental challenges facing our world is the threat of climate change due to the presence of excess greenhouse gases, mainly carbon dioxide ( $\text{CO}_2$ ), in the atmosphere. As a major contributor to global  $\text{CO}_2$  emissions coal-fired power plants are receiving enormous attention. One of the proposed methods to reduce  $\text{CO}_2$  emissions from coal power plants involves capturing the  $\text{CO}_2$  present in the exhaust gases for long-term geologic storage, for enhanced oil recovery (EOR), or enhanced coal bed methane (ECBM) production. Under conventional air-fired conditions the concentration of  $\text{CO}_2$  in the exhaust gases is relatively low (10-20%) due to the presence of  $\text{N}_2$  from air. As discussed previously, at such low concentrations  $\text{CO}_2$  capture requires post-combustion separation processes that require a significant amount of energy with no potential benefit to the combustion process. However, oxy-coal combustion can produce exhaust gas  $\text{CO}_2$  concentrations of up to 95% [235] enabling capture by more direct methods while potentially improving combustion efficiency and reducing pollutant emissions.

Oxy-coal combustion involves replacing the oxidizer air with a combination of oxygen ( $\geq 95$  vol.%  $\text{O}_2$ ) and recycled flue gas (RFG). Since proposed as a means to produce  $\text{CO}_2$  for enhanced oil recovery [236], many laboratory-scale, pilot-scale, and computational studies investigating the design and operational issues of oxy-coal combustion have been performed and a review of the work prior to 2005 is available in Buhre et al. [18]. Increased

energy costs are anticipated in an oxy-coal CCS equipped power plant due in large part to the parasitic load of the air separation unit (ASU) and the CO<sub>2</sub> compression and purification unit (CPU). Nevertheless, oxy-fuel combustion results in a reduced flue gas volume enabling higher boiler thermal efficiencies and has demonstrated the potential to reduce NO<sub>x</sub> emissions by as much as 60-75% and SO<sub>x</sub> emissions by as much as 27%, suggesting post combustion treatment equipment can be scaled back, improving the benefit-to-cost ratio [157, 161].

A common low NO<sub>x</sub> strategy for pulverized coal boilers is oxidizer staging. For wall-fired units a burner is typically configured with two separate gas streams that supply insufficient air for complete combustion: a primary oxidizer (PO) in which the coal particles are entrained and a secondary oxidizer (SO) that surrounds the PO and usually exits through swirl vanes to aid in flame stabilization and mixing. A third flow (overfire air or oxidizer) can be introduced some distance downstream to consume the remaining fuel (usually char) under fuel-lean conditions. This strategy results in a reducing region between the burner and the overfire oxidizer where NO<sub>x</sub> can be converted to molecular nitrogen. The effectiveness of staged combustion can be influenced by the level of oxidizer deficiency in the burner (i.e. the depth of staging), the flame stand-off distance, and the near burner temperature, which can influence the stand-off distance and the rate of coal devolatilization. Less air is desirable in the near burner region for NO<sub>x</sub> formation suggesting deeper staging would result in lower NO<sub>x</sub> emissions; however, less air reduces near burner temperatures leading to greater flame stand-off distances and potential instabilities, late coal devolatilization, and reduced boiler efficiencies and char burnout [161, 220]. Increased stand-off distances can result in SO air entrainment and higher NO<sub>x</sub> emissions [237], while delayed or slower devolatilization can



result in more nitrogen remaining in the char where it can be converted to NO<sub>x</sub> after overfire oxidizer is introduced [220].

Considering these limitations, it has been recognized that oxy-fuel combustion provides opportunities for further reductions in NO<sub>x</sub> emissions since molecular nitrogen has largely been removed from the system, some NO<sub>x</sub> will be recycled through the flame region where it will have additional opportunities to be reduced to N<sub>2</sub> [44-47], and independent control of oxygen and RFG concentrations enables a decoupling of temperature and stoichiometry in the near burner and post-flame regions [20, 21, 159, 237-239]. A few of the key references are discussed below, while a more detailed review can be found in Chapter 7.

Early oxy-coal studies [44-47] identified three pathways for NO<sub>x</sub> reduction in oxy-fuel combustion, namely: i) high CO<sub>2</sub> concentrations, either due to gasification of char ( $\text{char} + \text{CO}_2 \rightarrow 2\text{CO}$ ) or thermal dissociation, may lead to more CO available to reduce NO<sub>x</sub> to N<sub>2</sub> via the reaction  $\text{NO} + \text{CO} = 0.5\text{N}_2 + \text{CO}_2$ , which can be catalyzed at the char surface ii) recycled NO<sub>x</sub> may interact with nitrogen species released during devolatilization (volatiles-N), and iii) recycled NO<sub>x</sub> may be reduced to N<sub>2</sub> by hydrocarbon volatiles when passing through the flame zone. Okazaki and Ando [47] investigated the relative influence of these mechanisms by simulating the effects of volatiles with CH<sub>4</sub> and NH<sub>3</sub> and char with anthracite in separate experiments. It was concluded that increased CO<sub>2</sub> concentrations contributed to less than 10% of the observed NO<sub>x</sub> reduction, while reactions between recycled NO<sub>x</sub> and volatiles-N and recycled NO<sub>x</sub> and hydrocarbon species in the flame accounted for 10-50% and 50-80% of the observed reduction, respectively.

The influence of oxygen concentration ( $\geq 20$  vol.%), as enabled by independent control of oxygen and RFG, was demonstrated by Hu et al. [50, 225] at variable

temperatures and equivalence ratios in an electrically heated furnace. Emissions of NO<sub>x</sub> on a mass basis were shown to be only slightly dependent on oxygen concentrations  $\geq 50$  vol.%, and were comparable to results obtained in air when pure oxygen was used. Liu and Okazaki [158] proposed a novel oxy-fuel scenario in which the oxygen concentration was reduced relative to air ( $< 21$  vol.%) and combustion was sustained by recycling heat as well as flue gases. It was demonstrated that reducing the oxygen concentration to 15 vol.% while recycling 40% of the heat could reduce NO<sub>x</sub> emissions by a factor of seven.

In a larger more practical system, Chatel-Pelage et al. [161, 221] indicated that higher temperatures in the fuel-rich near burner region induced by high oxygen concentrations can increase the rate of NO reduction to N<sub>2</sub> as well as the rate of volatile nitrogen species to N<sub>2</sub> relative to NO. The results of Mackrory et al. [239] appeared to support this phenomenon. Higher oxygen concentrations have also been utilized to promote shorter flame standoff distances resulting in less SO entrainment and lower NO<sub>x</sub> [237] as well as deeper staging without the limitations encountered under air-firing [240]. In addition, Andersson et al. [215] and Normann et al. [214] investigated the reduction of NO<sub>x</sub> at high temperature in oxy-fuel combustion and showed that NO<sub>x</sub> destruction by the Zeldovich mechanism is possible.

In addition to oxy-fuel combustion for CO<sub>2</sub> mitigation and lower NO<sub>x</sub> emissions, increased utilization of biomass in both direct and cofiring scenarios is another viable technology receiving increased attention as utilities providers strive to meet regional and statewide renewable energy standards. When combined with CCS the cofiring of biomass fuels can result in a net decrease in atmospheric CO<sub>2</sub>. Many studies have examined the effects of cofiring biomass with fossil fuels under conventional air-fired conditions and reviews can be found in Werther et al. [234] and Sami et al. [24]. Based on the current literature, biomass cofiring under oxy-fuel conditions is a nascent area of study with

enormous potential. For example, air-fired studies by Brouwer et al. [233] reported a 17% reduction in NO<sub>x</sub> when 50% wood (on a thermal basis) containing 0.2 wt.% nitrogen was cofired with coal containing 1.6 wt.% nitrogen during unstaged combustion. While these results are promising, the reduction in NO was not proportional to the reduced amount of fuel bound nitrogen in the system. Moreover, insignificant changes were observed when wood was cofired directly with coal in a staged low-NO<sub>x</sub> system until 70% wood was cofired on a thermal basis. Based on these results it was suggested that reductions in NO<sub>x</sub> emissions when cofiring may not scale with the reduction in fuel bound nitrogen since rapid biomass volatile release can result in increased near burner temperatures leading to enhanced *thermal* NO<sub>x</sub>. However, under oxy-fuel conditions N<sub>2</sub> is removed from the oxidizer streams and, all else being equal, NO<sub>x</sub> formation should scale with the fuel-N present in the system leading to reduced NO<sub>x</sub> when cofiring with a biomass having a lower nitrogen content. Furthermore, higher local temperatures induced by rapid biomass devolatilization could result in reduced NO<sub>x</sub> formation due to the rate and residence time effects discussed by Mackrory [20], or NO<sub>x</sub> destruction via the Zeldovich mechanism, as suggested by Andersson et al. [215] and Normann et al. [214] above. Sami et al. [24] also noted that the increased fuel loading required to maintain the same thermal input when cofiring, due to the lower heating value of biomass, may alter the flame position resulting in flame instabilities and higher NO<sub>x</sub>. Nevertheless, under oxy-fuel conditions the gas compositions can be changed to improve flame stability when cofiring as discussed in [237].

Recognizing the potential for improvements in NO<sub>x</sub> reduction under oxy-fuel conditions and when cofiring biomass, this work explores a range of oxy-fuel and cofiring conditions to quantify their effects on NO concentrations in the exhaust gas using no overfire oxidizer and CO<sub>2</sub>. Baseline conventional air-fired results are first obtained and the

effects of thermal input, secondary swirl, primary stream flow rate, excess air, and biomass cofiring are demonstrated. Nitric oxide emissions are then examined under oxy-fuel conditions while varying excess air, secondary swirl, adiabatic flame temperature, and while cofiring sawdust. Finally, the effects of changing both the PO and SO gas compositions on NO production at constant adiabatic flame temperature are investigated.

## 8.2 Experimental

Experiments were conducted under both air-fired and oxy-fuel conditions in a cylindrical, horizontally-fired 30 kWth combustor. A schematic of the combustor is shown in Fig. 8.1. Pulverized coal and sawdust were fed to the combustor using separate volumetric screw feeders (K-Tron and Schenk AccuRate, respectively) and were entrained with the primary oxidizer (PO) stream using a Fox Valve Venturi eductor. Gas flows were controlled using calibrated rotameters. Compressed air was supplied by the building facilities and was dried and filtered prior to being metered and sent to the burner. Under oxy-fuel conditions flue gases were not recycled; rather, industrial grade O<sub>2</sub> and CO<sub>2</sub> were metered independently and mixed before entering the burner. The refractory lined combustion chamber was sealed and the eductor was contained within an enclosure to prevent air infiltration. Though not considered in this study, air infiltration can be simulated using a separate stream of air or bottled N<sub>2</sub>. The exhaust outlet was configured with the building exhaust system using an adjustable baffle such that the combustor was maintained at a slight negative pressure (ca. 10 Pa). The visible flame was largely contained within the first section of the combustor (14 cm ID) and the second section (37 cm ID) provided sufficient residence time for burnout of larger char particles and for the gas composition to become uniform.

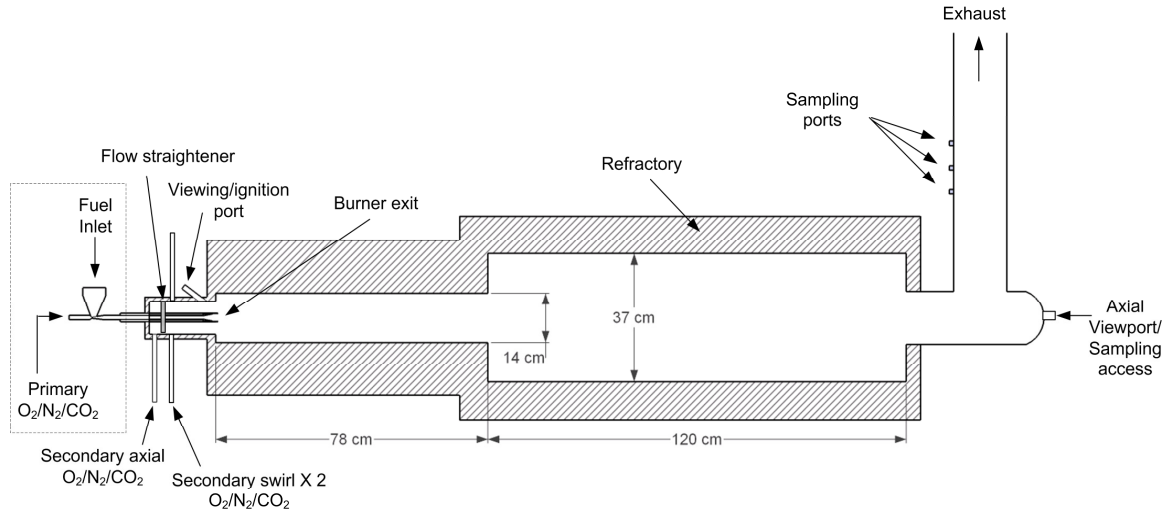


**Figure 8.1. Schematic of horizontal 30 kWth combustor.**

The burner was constructed in-house and is depicted schematically in Fig. 8.2. The coal delivery tube (PO tube) exits the eductor with an inner diameter of 1.1 cm such that under standard operating conditions the velocity is high enough to prevent particle settling. Approximately 3 cm prior to entering the combustion chamber the PO tube diverges gradually to 2.3 cm to reduce the PO exit velocity. The diverging nozzle was custom built and includes small openings around the outer edge to allow the use of methane gas for lighting purposes only (i.e. all flames were stabilized without the aid of a pilot gas). The outer walls of the burner are lined with 1.2 cm of refractory resulting in a secondary oxidizer (SO) tube I.D. of 9.5 cm. The SO stream can be introduced axially or through tangential ports to induce a swirling secondary flow. Brass wool and stainless steel honeycomb fill the space between the inlet of the axial SO and the tangential SO to straighten the axial flow. Both the SO axial and tangential flows can be controlled independently enabling variable swirl. Neither the PO nor SO flows were preheated.

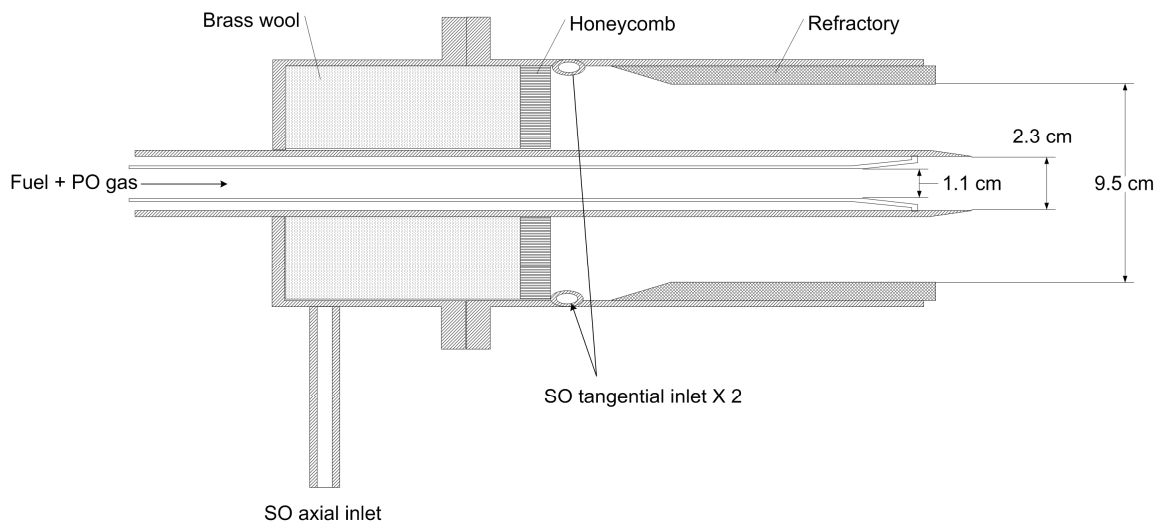


**Figure 8.2. Schematic of experimental burner.**

Exhaust gas samples were extracted 250 cm downstream of the burner exit at a rate of 200 ccm using an uncooled ceramic 2 cm I.D. probe and were dried and diluted by a dilution probe (Thermo Electron, Inc.). Pershing and Wendt [219] reported no differences in NO measurements when using a water-cooled stainless steel probe, a cooled quartz probe, or an uncooled quartz probe, but noted that the measurements were taken after the exhaust had cooled below 800 K and at least 0.5 vol.% O<sub>2</sub> was present in the sample. In this work the exhaust temperature at the sampling location was also below 800 K and at least 0.5 vol.% O<sub>2</sub> was present. The concentrations of CO and NO were monitored using a continuous emissions monitoring system (CEM) (Thermo Electron, Inc.). Nitrogen oxide concentrations were measured using a chemiluminescence analyzer (Thermo Electron, model 42i) and CO concentrations were measured using gas filter correlation (Thermo Electron, model 48i). To prevent ash accumulation in the probe the CEM was set to purge approx. every 15 minutes. The purge results in a significant pressure increase inside the dilution probe, which interfered with the continuous operation of a pressure sensitive O<sub>2</sub> sensor (Maxtec Inc., model MAX-250). Consequently, a separate exhaust slip stream was

extracted, dried, filtered, and passed through the oxygen sensor. Prior to each run all gas analyzers were calibrated.

Under oxy-fuel conditions a correction was required to account for changes in the operation of the Thermo Electron Inc. dilution probe when the exhaust gases were predominantly CO<sub>2</sub>. In the dilution probe, the gas sample is diluted after passing through a critical orifice with a constant pressure drop in which the flow is choked. From compressible flow theory, assuming ideal gas behavior and isentropic flow the mass flow rate for choked flow is given by

$$\dot{m} = \rho_0 \left( \frac{2}{\gamma + 1} \right)^{\frac{1}{2} \left( \frac{\gamma + 1}{\gamma - 1} \right)} \sqrt{\gamma R T_0} A \quad (8.1)$$

where  $\rho_0$  and  $T_0$  are the density and temperature of the fluid, respectively, at the stagnation conditions,  $\gamma$  is the ratio of specific heats,  $R$  is the universal gas constant divided by the species or mixture molecular weight, and  $A$  is the cross sectional area of the throat where the flow is choked. When air or predominantly N<sub>2</sub> is the working fluid the dilution probe is setup for a volumetric dilution ratio of 100:1. Under oxy-fuel conditions the CO<sub>2</sub> concentration in the flue gas is greater than 90 vol.% leading to a significant change in the molecular weight and  $\gamma$  of the sample, and consequently a change in the dilution ratio. The new dilution ratio is given by

$$100 : \frac{\left( \frac{2}{\gamma_{act} + 1} \right)^{\frac{1}{2} \left( \frac{\gamma_{act} + 1}{\gamma_{act} - 1} \right)} \sqrt{\gamma_{act} W_{air}}}{\left( \frac{2}{\gamma_{air} + 1} \right)^{\frac{1}{2} \left( \frac{\gamma_{air} + 1}{\gamma_{air} - 1} \right)} \sqrt{\gamma_{air} W_{act}}} \quad (8.2)$$

where the subscript *act* refers to the properties of the actual gas being sampled. Other works have reported inconsistencies with chemiluminescence NOx analyzers under oxy-fuel

conditions due to the increased presence of CO<sub>2</sub> molecules *quenching* the reaction of NO with ozone resulting in an underprediction of NO concentrations; however, this phenomenon was not observed in this study as the dilution ratio of the sample was sufficient to prevent quenching (greater than 100:1) before entering the NO<sub>x</sub> analyzer.

In order to compare NO and CO measurements from flames at different operating conditions (e.g. different excess air, air-fired vs. oxy-fuel) the measured concentrations must be normalized. Unless otherwise specified, NO and CO concentrations will be reported on a mass per unit energy basis (ng/J). The normalization is performed by first computing the product of the corrected NO or CO concentration (as described above) and molar flow of dry products in the exhaust assuming complete combustion. This value is then divided by the thermal input and species molecular weight.

$$NO \frac{ng}{J} = \frac{NO [ppm] \times Molar \ Flow \ of \ Dry \ Exhaust [kmol / s]}{W_{NO} \times Th. \ Input [W] \times 10^6} \quad (8.3)$$

Here,  $W_{NO}$  is the molecular weight of nitric oxide. In several of the figures below, the right ordinate has been converted to units of pounds per million Btu (lb/MMBtu) as these units are commonly used by the Environmental Protection Agency when specifying the allowable NO emission limits.

The exhaust gas temperature at the gas sampling location was measured with a sheathed 1.6 mm diameter type-K thermocouple. For select flames the maximum temperature in the near burner region ( $T_{nb}$ ) was measured with an unsheathed type-K thermocouple having a bead diameter of 750 microns. No radiation corrections were made. To obtain the maximum near burner temperature, the thermocouple was inserted through the viewing/ignition port shown in Fig. 8.1. The bead was moved in 1 cm increments until a peak temperature was observed. The process was repeated three times to confirm the same



peak temperature within 20 K at the same location. When the flame was significantly detached the near burner temperature was not indicative of the flame temperature.

Subbituminous Powder River Basin (PRB) coal provided by a local power plant and waste sawdust obtained from a local sawmill were utilized as fuels this study. Proximate, ultimate, and sieve analyses were performed for both the coal and sawdust and the results are provided in Table 8.1. As obtained from the sawmill, the sawdust contained 21 wt.% moisture, which led to feeding difficulties. The moisture content was reduced to 16 wt.% by spreading the sawdust out on a large tarp under the sun for approx. 6 hours. Prior to combustion, the sawdust was also sieved through a 20 mesh screen. Measurements of the moisture content of both the coal and sawdust were taken daily prior to each set of experiments using a HI-Res TGA (TA Instruments Inc.). The average moisture content in the coal was approx. 20 wt.%.

The combustor standard operating procedure (SOP) is included in Appendix C. Following ignition of the coal flame, the length of time required to reach steady-state NO readings was dependent on the thermal input. At 20 kWth a steady-state gas composition, as indicated by the CO and NO concentrations, could be achieved within 45-60 minutes, while at 30 kWth steady conditions required approx. 80 minutes as shown in Fig. 8.3 (CO was not included in the figure due to excessive noise). Furthermore, at steady state conditions with 3 vol.% O<sub>2</sub> in the exhaust CO levels were below the gas analyzer's detectable limits (0.04 ppm) under both air-fired and oxy-fuel conditions. Fly ash particles were viewed by scanning electron microscopy (SEM) and the images are shown in Fig. 8.4. Loss-on-ignition for the fly ash was determined to be less than 1%.

**Table 8.1. Fuel properties**

	PRB Coal	Sawdust
<b>HHV MJ/kg (DAF)</b>	29.70	20.20
<b>Proximate Analysis</b>	<b>wt.% (dry)</b>	<b>wt.% (dry)</b>
Ash	7.50	0.59
Volatile Matter	43.36	84.52
Fixed Carbon	49.13	14.89
<b>Ultimate Analysis</b>	<b>wt.% (dry)</b>	<b>wt.% (dry)</b>
Carbon	69.51	49.28
Hydrogen	4.61	5.79
Oxygen	17.02	44.14
Nitrogen	0.97	0.15
Sulfur	0.40	0.05
<b>Sieve Analysis</b>	<b>wt.% retained</b>	<b>wt.% retained</b>
20 Mesh	--	0.0
30 Mesh	<0.1	2.3
50 Mesh	<0.1	36.3
100 Mesh	1.9-3.2	81.3
200 Mesh	18-29	94.7

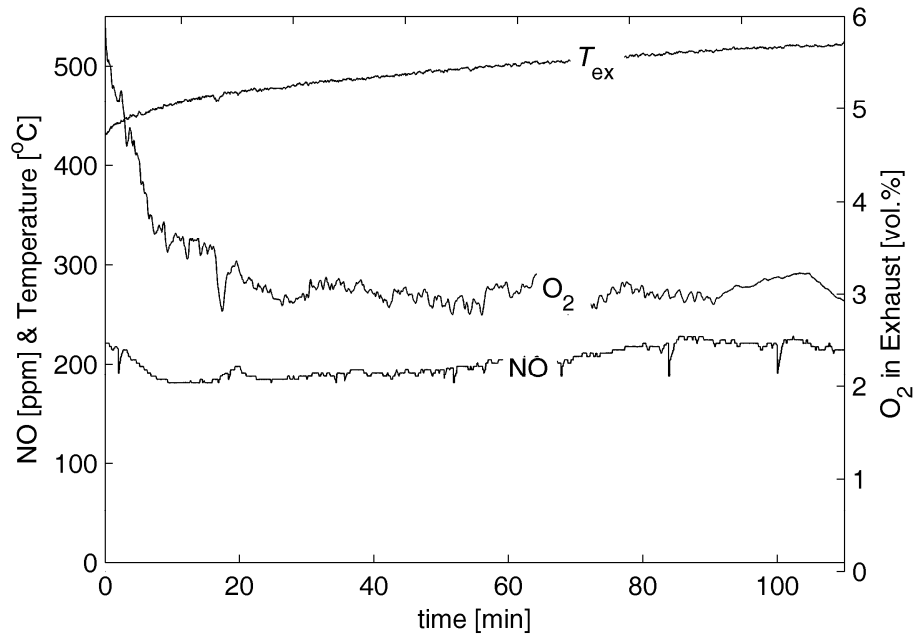


**Figure 8.3. Continuous O<sub>2</sub>, NO and exhaust temperature measurements following ignition under air-fired conditions at 30 kWth.**

A summary of the range of experimental conditions considered in this study is provided in Table 8.2. When possible, conditions were revisited multiple times and on different days to demonstrate repeatability and to evaluate the experimental uncertainty for the NO measurements. Conventional air-fired conditions were first evaluated and the effects of thermal input, secondary swirl, primary stream flow rate, excess air, and sawdust cofiring on NO levels are reported. Except for conditions demonstrating the influence of excess air, all other air-fired and oxy-fuel experiments were performed such that the combined flow from the PO and SO streams resulted in 3 vol.% O<sub>2</sub> in the stack (i.e. no overfire oxidizer was utilized).

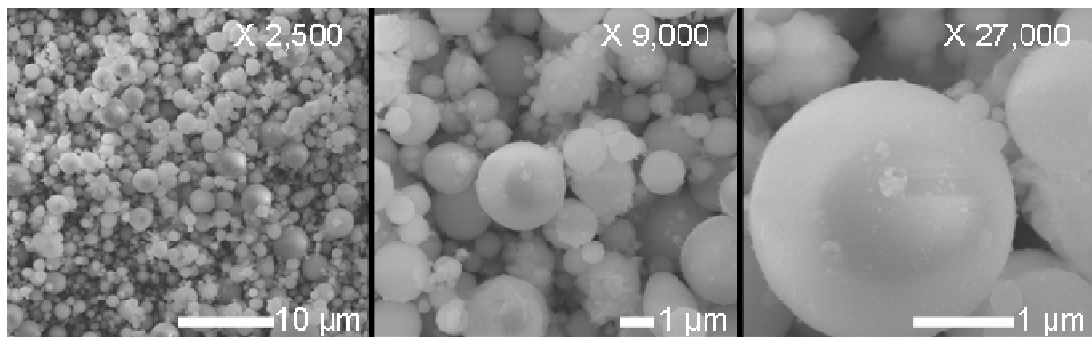


Figure 8.4. SEM images of fly ash collected during steady-state operation of the laboratory-scale coal combustor at 30 kWth.

**Table 8.2. Summary of experimental operating conditions**

$\dot{m}_{\text{coal}}$ (kg/hr)	$\dot{m}_{\text{bio}}$ (kg/hr)	Th. Input (kW)	PO O <sub>2</sub> vol.%	$Q_{\text{PO}}$ (m <sup>3</sup> /hr)	SO O <sub>2</sub> vol.%	$Q_{\text{SO}}$ (m <sup>3</sup> /hr)	SO Swirl %
<b>Air-Fired</b>							
1.8-4.9	0-2.1	19-30	air	4.2-7.7	air	17-30	0-100
<b>Oxy-Fuel</b>							
3.3-5.7	0-2.1	25-35	0-50	4.2-5.3	24-38	13-21	0-100

As discussed previously, it has been observed that the temperature profile and heat transfer characteristics of the oxy-coal and coal-air flame are similar when air is replaced with

a mixture of 30 vol.% O<sub>2</sub> and 70 vol.% CO<sub>2</sub>. Under these conditions, the effects of excess O<sub>2</sub>, secondary swirl, and biomass cofiring on NO emissions were investigated, as in the air-fired studies. The effect of adiabatic flame temperature on NO emissions was also investigated with a 30/70 mix of O<sub>2</sub> and CO<sub>2</sub> in the PO stream while varying the oxygen concentration in the SO stream. Finally, the effect of varying the both the PO and SO stream gas compositions at constant adiabatic flame temperature on NO emissions was examined.

## 8.3 Results and Discussion

### 8.3.1 Air-fired Conditions

The effect of increasing the thermal input on NO emissions under air-fired conditions with 16 vol.% excess air is shown in Fig. 8.5. Excess air is defined as the percentage of air introduced into the system beyond that required by stoichiometry, i.e.  $(\dot{m}_{air}/\dot{m}_{air,st}-1) \times 100\%$ . In all cases shown in Fig. 8.3 the primary stream flow rate was held constant at 5.3 m<sup>3</sup>/hr resulting in a variable primary stream stoichiometric ratio,  $\lambda_{PO}$ , defined as

$$\lambda_{PO} = \frac{\dot{m}_{air,PO}}{\dot{m}_{air,st}} = \frac{\dot{m}_{O_2,PO}}{\dot{m}_{O_2,st}} \quad (8.4)$$

where  $\dot{m}$  is the mass flow rate, the subscript *st* refers to the conditions required to meet stoichiometry, and the subscript *PO* refers to the flow issuing from the primary oxidizer stream. For the range of thermal inputs considered here the primary stream stoichiometric ratio,  $\lambda_{PO}$ , varies from 0.28 at 19 kW to 0.18 at 30 kW. The maximum temperature in the near burner region at 19, 25, and 30 kWth was measured to be  $1450 \pm 20$  K for the swirling

flames and  $1000 \pm 20$  K for the non-swirling flames. In addition, the swirling flames appeared brighter and more intense when observed through the ignition port. The higher temperature measured for the swirling flame may have been due to enhanced mixing, recirculation of hot products that could increase the flame intensity, or Nusselt number effects. As mentioned previously, radiation corrections were not made.

In Fig. 8.5 results from flames having a non-swirling secondary stream are shown with open-faced symbols and results for flames in which all SO air was introduced tangentially (i.e. 100% SO swirl) are shown with closed-face symbols. For flames with a non-swirling secondary the NO emissions were initially reduced when increasing power and a minimum of 121 ng/J was observed at a thermal input of 25 kW. Upon increasing the thermal input above 25 kW, the NO emissions increased reaching ca. 150 ng/J at a thermal input of 30 kW. For flames with a swirling secondary stream, the NO emissions were on average approx. 30% lower when compared to the non-swirling flames up to a thermal input of 25 kW. Above 25 kW the NO emissions from flames with 100% SO swirl remained relatively constant with increased thermal input. There is a 40% reduction at 30 kW when compared to the non-swirling flame. The higher NO measured in the lower thermal input swirling flames correlated with an observable change in the appearance of the flame as seen through the axial view port. At 19 kW the flame appeared to be pushed toward one side of the combustor. It was concluded that at 19 kW the secondary oxidizer flow required to supply 16 vol.% excess air was insufficient to produce a symmetrical swirling flame, while at 22 kW and above a symmetrical flame was observed.

Recognizing the impact of swirl on NO emissions, the effect of variable swirl was investigated at thermal inputs of 19, 25, and 30 kW with 16 vol.% excess air. The results are shown in Fig. 8.6 below. For all three thermal inputs conditions were observed that resulted

in increased NO emissions, with a maximum amount of NO produced when the swirl was reduced to 20-25% of the total SO flow. As discussed above, at a thermal input of 19 kW 100% SO swirl was insufficient to produce a symmetrical swirling flame, thus a small reduction in swirl exacerbated the asymmetry and higher NO was observed. At a thermal input of 25 kW NO emissions were relatively unaffected until the swirl was reduced to 50% of SO flow, at which point asymmetry was observed.

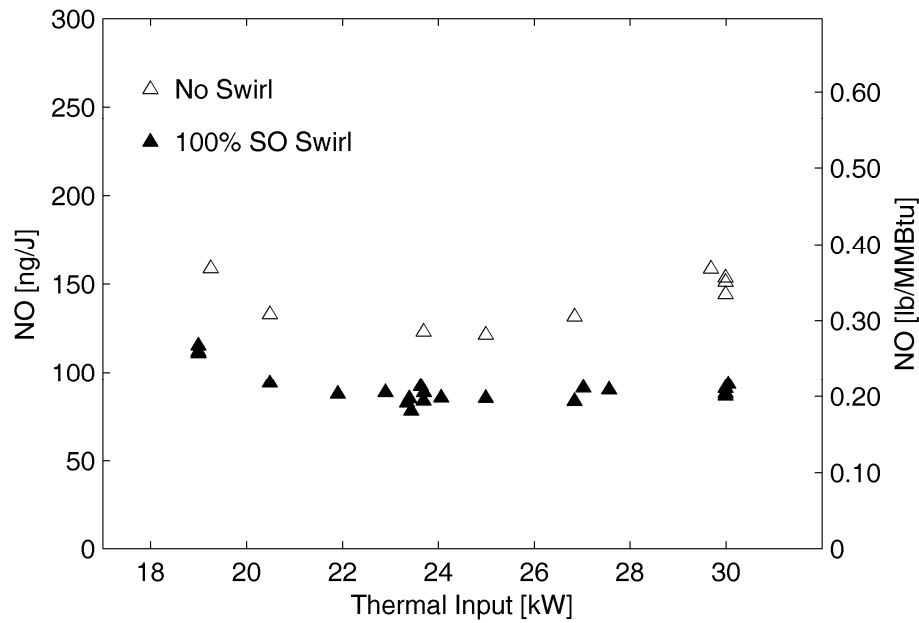


Figure 8.5. Nitric oxide measured in exhaust under air-fired conditions with 16 vol.% excess air as a function of thermal input.  $\Delta$  No SO swirl;  $\blacktriangle$  100% SO swirl

At a thermal input of 30 kW the NO emissions remained constant until the swirl was reduced to 20-25% of the SO flow. The abrupt increase in NO emissions observed under these conditions was correlated with another distinct change in the appearance of the flame. In addition to appearing asymmetric, the interaction of the swirl and axial flow produced a periodic fluctuation of the flame location. After further reducing the swirl, the flame appearance improved and the NO emissions were reduced.

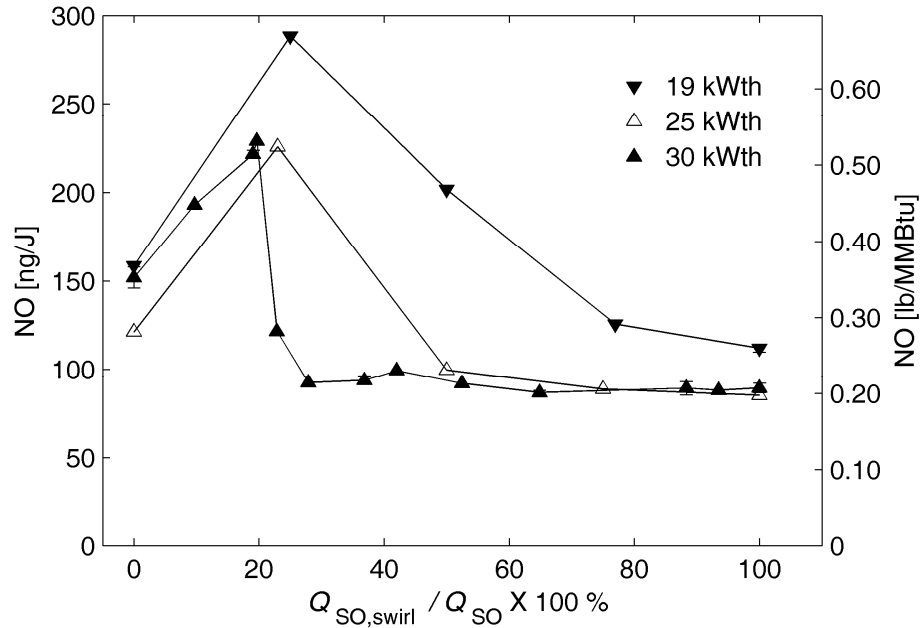


Figure 8.6. Nitric oxide measured in exhaust vs. % SO swirl under air-fired conditions with 16 vol.% excess air. ▼ 19 kWth; △ 25 kWth; ▲ 30 kWth

In Fig. 8.7 the effect of varying the PO flow rate on NO emissions is demonstrated for flames with both a non-swirling and swirling secondary stream at a thermal input of 30 kW. For the non-swirling flames the NO emissions increase linearly with the PO flow rate, while moderate changes are observed for the flames with 100% SO swirl. Increasing the PO flow rate at constant thermal input can influence the NO emissions in three ways, namely: 1) increased mixing rates as characterized by the PO Reynolds number, 2) increased local stoichiometric ratios, and 3) flame detachment resulting in SO air entrainment.

Noting that increasing the PO flow rate did not result in significant increases in NO emissions for flames with 100% SO swirl, it can be concluded that the rate of PO mixing and the local stoichiometric ratio PO are not primary factors influencing NO formation in these flames. At higher PO flow rates or higher local stoichiometric ratios a more dramatic effect may be observed. Considering also that the NO emissions for the swirling and non-swirling flames with a PO flow rate of 4.2 m<sup>3</sup>/hr were the same and that the lack of swirl can

reduce flame stability, the linear increase in NO emissions for the non-swirling flames when increasing the PO flow rate was attributed to flame detachment resulting in SO air entrainment. Entrainment can increase NO production by allowing more air into the high temperature core of the flame creating premixed conditions much closer to stoichiometry.

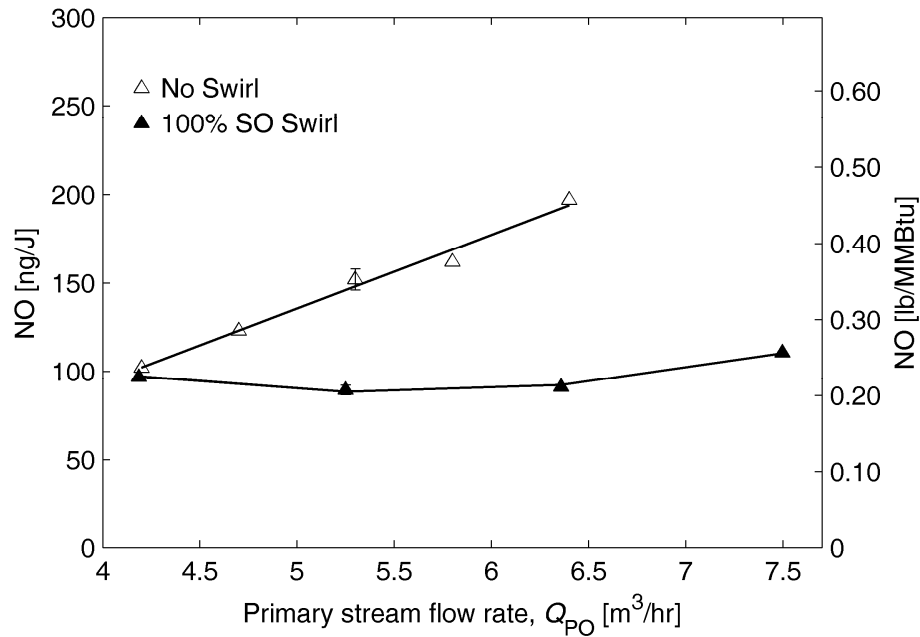


Figure 8.7. Nitric oxide measured in exhaust vs. primary oxidizer stream velocity.  $\Delta$  No SO swirl;  $\blacktriangle$  100% SO swirl

The effect of varying the excess air, as quantified by the global stoichiometric ratio, on NO emissions under swirling and non-swirling conditions at  $30 \text{ kW}_{th}$  is shown in Fig. 8.8. The *global* stoichiometric ratio,  $\lambda$ , is calculated as in Eq. 8.4 with the numerator replaced by the mass flow of air in both the primary and secondary streams. Results from Pershing and Wendt [219] are also included in this figure only for reference, as both their primary and secondary flows were preheated, their coal contained more nitrogen, and the hydrodynamics of their combustor were notably different from the conditions of this study. To accommodate the data of Pershing and Wendt the ordinate in Fig. 8.8 was changed to the concentration of NO in parts per million (PPM) based on the products of stoichiometric



combustion. This quantity was determined by calculating the molar flow of NO in each case, multiplying by  $10^6$ , and dividing by the molar flow of dry products assuming no excess air.

In Fig. 8.8 it can be seen that the NO emissions from the non-swirling flames of this study are approx. 18% lower than the results of Pershing and Wendt but follow a similar trend when varying the global stoichiometric ratio. In addition, it was observed that increasing the global stoichiometric ratio had a more pronounced affect on NO emissions for the non-swirling flames when compared to the swirling flames. This difference can be attributed to the slight detachment observed in the non-swirling flames, which resulted in entrainment of SO air, and the increased length of the non-swirling flames that led to more combustion taking place downstream where the fuel and oxidizer were well mixed and excess air was available for NO formation.

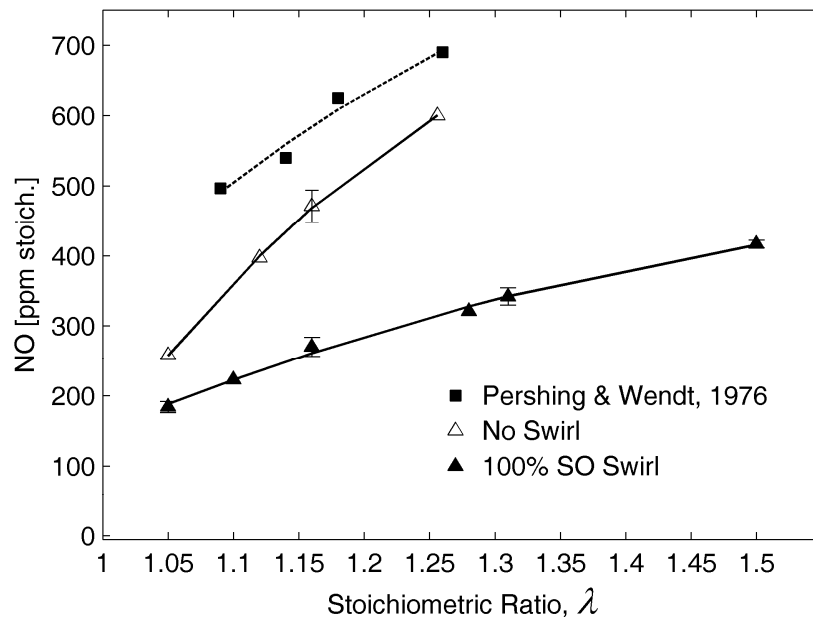


Figure 8.8. NO emissions vs. the global stoichiometric ratio,  $\lambda$ , under air-fired conditions at 30 kWth. ■ Pershing and Wendt, 1976; △ No SO swirl; ▲ 100% SO swirl

The effect of cofiring sawdust on NO emissions is shown in Fig. 8.9. In the 19 kWth flames, detachment was observed that became progressively worse as the percentage of sawdust cofired was increased and may have been a consequence of one or more of the following factors: the lower swirl associated with the 19 kWth flames, the larger average size of the sawdust particles, and the reduced amount of ultrafine coal particles available at higher sawdust percentages. Robinson and coworkers [241] noted that biomass devolatilization times can be longer than coal due to “intra-particle temperature gradients in the relatively large biomass particles”. The appearance of the near burner region when cofiring 20 wt.% sawdust at 19 kWth was similar to that of the non-swirling coal-air flames, appearing slightly dimmer and less intense than the coal-air flame with a maximum temperature 450 K cooler. However, cofiring 30 wt.% sawdust or more at 19 kWth led to a dark near burner region as shown in Fig. 8.10 and a maximum near burner temperature nearly 900 K cooler than the swirling coal-air flame. Consequently, increasing the amount of sawdust likely led to SO air entrainment and higher NO emissions.

When cofiring sawdust at a thermal input of 30 kW the flame remained attached; however it can be seen in Fig. 8.9 that the NO emissions were not reduced even though the nitrogen content of the sawdust was 0.15 wt.% compared with the 0.97 wt.% nitrogen content in the coal. Measurements of the maximum temperature in the near burner region indicated a reduction of approx. 100 K when going from 100% coal to cofiring 40 wt.% sawdust, which would influence the rate of volatile release. Observations from the axial view port also indicated that as the percentage of sawdust cofired was increased, the central core of the swirling flame became brighter. The higher volatile content of the sawdust could have elevated the local temperature resulting in this visible change, or the larger sawdust particle size and reduced near burner temperature may have resulted in delayed volatile release and a

higher local stoichiometric ratio. In either scenario, NO production from both coal bound nitrogen and sawdust bound nitrogen could be enhanced when increasing the percentage of sawdust cofired, resulting in no change in the NO emissions per unit energy.

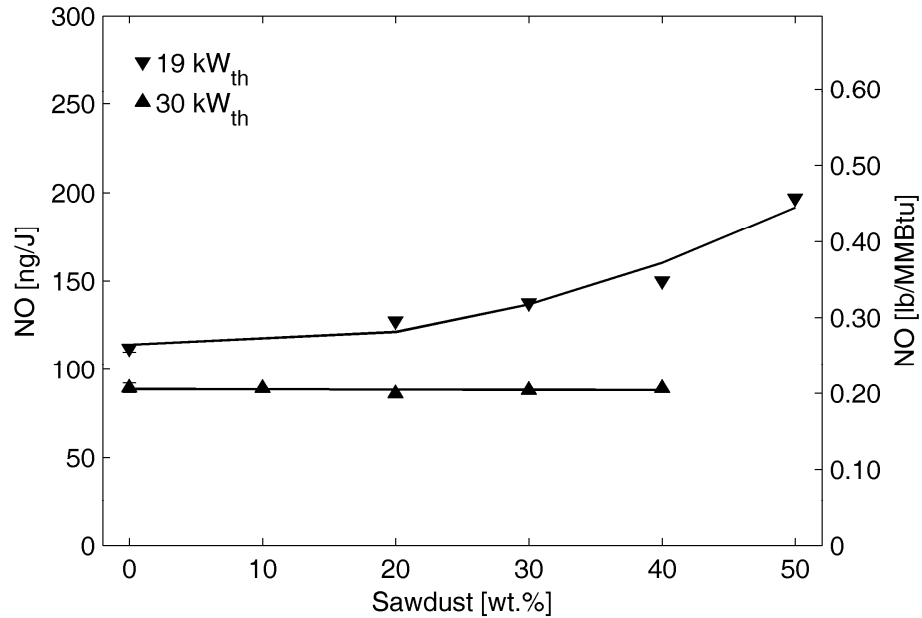


Figure 8.9. NO emissions vs. % sawdust under air-fired conditions and 100% SO swirl at ▼ 19 kW<sub>th</sub> and ▲ 30 kW<sub>th</sub>

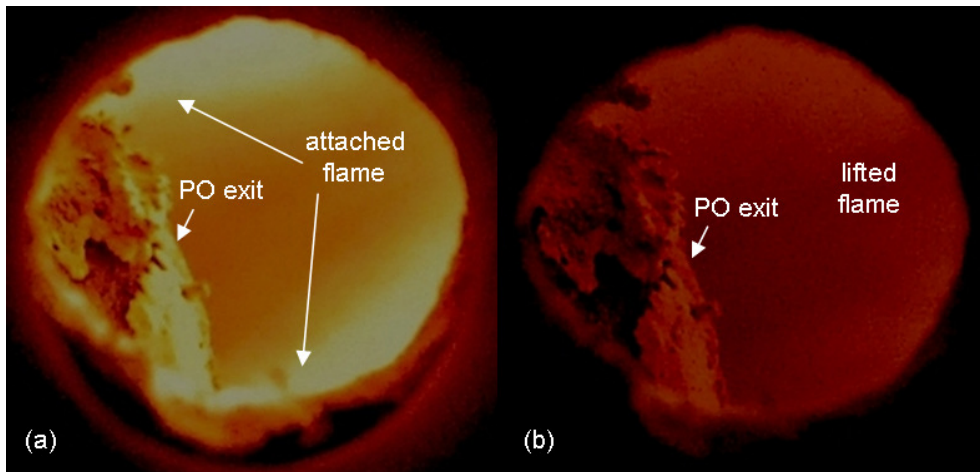


Figure 8.10. Photographs of primary tube exit as seen through the burner ignition port showing (a) attached flame (b) detached or lifted flame. The bright yellow luminance observed near the PO exit in (a) is not observable in (b) because the flame has moved downstream out of the field of view. (Note: aperture and shutter speed settings were identical for both photographs.)

### 8.3.2 Summary of Air-fired Results

The effects of thermal input, secondary oxidizer swirl, primary oxidizer flow rate, excess air, and sawdust cofiring on NO emissions under air-fired conditions were investigated systematically to parameterize the experimental system and to develop a baseline for comparison when considering oxy-fuel conditions in the next section. The following key results will aid in interpreting the oxy-fuel results:

- 1) Increasing thermal input did not dramatically effect NO emissions for flames with 100% SO swirl unless visible hydrodynamic differences were observed.
- 2) Decreasing swirl can increase NO emissions dramatically when interactions between the swirling flow and the axial flow create unsteady behavior. For this burner, unsteady behavior was observed when the SO swirl was reduced to approx. 20-25% of the total SO flow.
- 3) Increased PO flow rates resulting in variable mixing rates ( $Re \sim 4,000-8,000$ ) and stoichiometric ratios ( $\lambda_{PO} \sim 0.14-0.26$ ) did not influence NO emissions for flames with 100% SO swirl. NO emissions from non-swirling flames increased linearly with increasing PO flow rate, likely due to SO air entrainment.
- 4) Increasing the global stoichiometric ratio had a more pronounced effect on NO emissions for non-swirling flames. Results from Pershing and Wendt [219] were found to be approx. 18% higher than the non-swirling results of this study, but appeared to follow a similar trend.
- 5) Sawdust cofiring reduced flame stability and increased NO emissions significantly when cofiring more than 20 wt.% sawdust at a total thermal input of 19 kW.

Cofiring sawdust up to 40 wt.% at 30 kWth resulted in no observable changes to NO emissions, though the maximum near burner temperature was reduced.

### 8.3.3 Oxy-fuel Conditions

As discussed previously, the temperature characteristics of the oxy-coal flame resemble air-fired conditions when the oxidizer air is replaced with a mixture of 30 vol.% O<sub>2</sub> and 70 vol.% CO<sub>2</sub> largely due to the higher specific heat of the triatomic CO<sub>2</sub> molecule. As a consequence, the volumetric flow through the burner is reduced by approx. 30% under these conditions when compared to the air-fired scenario, if the same amount of excess oxygen is supplied. If the amount of oxygen measured in the exhaust gases is to be matched with the air-fired case, as in this study, the volumetric flow through the burner is reduced even more. Thus, if an air-fired burner is to be utilized without modifications for oxy-fuel combustion the burner hydrodynamics will be affected, which can ultimately influence flame attachment and pollutant formation [208]. The oxy-fuel results presented below first examine the effects of excess oxygen, swirl, adiabatic flame temperature, and sawdust cofiring on NO emissions under oxy-fuel conditions with a 30/70 volumetric mix of O<sub>2</sub> and CO<sub>2</sub> in the PO and SO streams. The effects of varying the PO and SO gas compositions on NO emissions are then considered at 30 kWth.

The effect of excess oxygen, as quantified by the global stoichiometric ratio, on NO and CO emissions is shown in Fig. 8.11 for flames at 30 kWth with 100% SO swirl. The flames were produced with a PO volumetric flow rate of 5.3 m<sup>3</sup>/hr in order to match the PO flow rate utilized for the majority of the air-fired cases. Consequently, the volumetric flow rate in the SO under these conditions was reduced by 38% when compared to the volumetric flow rate of the air-fired case at 30 kWth, but was similar to the volumetric flow

rate of the 19 kWth air-fired case (ca. 18 m<sup>3</sup>/hr). Under these conditions the oxy-fuel flame appeared asymmetric much like the 19 kWth air-fired flame. That is, the flame appeared to be pushed toward one side of the combustor. When decreasing the global stoichiometric ratio the NO emissions were only moderately reduced. It can be seen in Fig. 8.11 however, that the CO emitted was below the detectable limit of the gas analyzer until the stoichiometric ratio was reduced below 1.07 (i.e. 7 vol.% excess O<sub>2</sub>). At a stoichiometric ratio of 1.05 the CO increased to approx. 20 ng/J, at a stoichiometric ratio of 1.035 the CO rose to 40 ng/J, and at a stoichiometric ratio of 1.02 the CO exceeded 250 ng/J. A comparable experiment was attempted under air-fired conditions; however, the CO readings were unsteady during those runs.

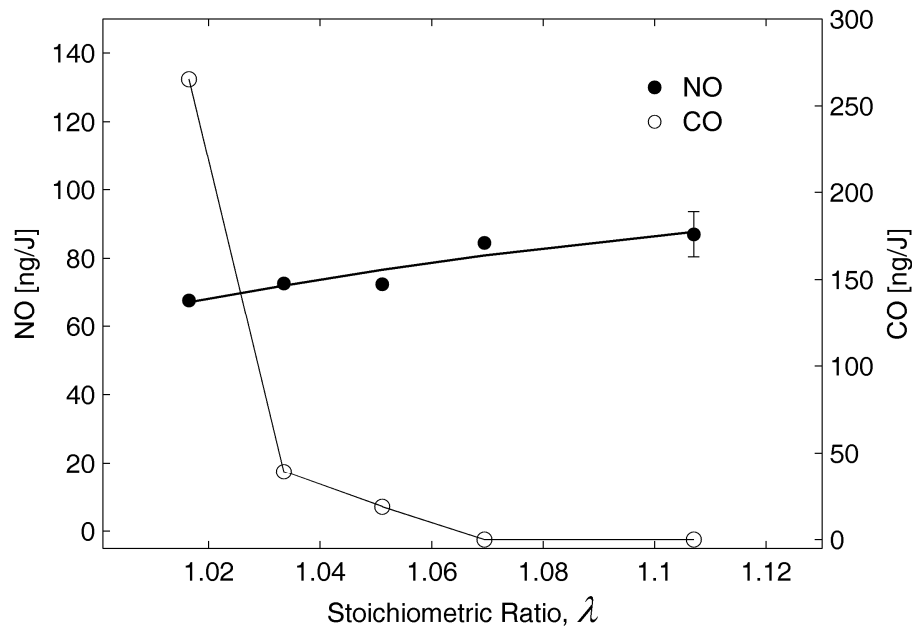


Figure 8.11. Nitric oxide and carbon monoxide measured in exhaust vs. stoichiometric ratio under oxy-fuel conditions at 30 kWth with 30% O<sub>2</sub> and 70% CO<sub>2</sub> in the PO and SO streams.

Assuming that air-fired combustion would have produced more CO than the oxy-fuel case at a comparable global stoichiometric ratio, the lack of detectable CO production at a global stoichiometric ratio of 1.07 and the relatively low amount of CO produced at  $\lambda = 1.05$  is an important result when considering the both the production of oxygen and the

capture of carbon dioxide. Specifically, if less excess oxygen is required for complete combustion under oxy-fuel conditions then the amount of oxygen supplied by the air separation unit (ASU) can be reduced resulting in capital and operational cost savings. Furthermore, when preparing the exhaust for sequestration less excess oxygen in the combustor means less oxygen will have to be removed and/or processed in the compression and purification unit (CPU).

The data in Fig. 8.12 demonstrate the effect of varying the amount of SO swirl under oxy-fuel conditions at 30 kWth with a 30/70 volumetric mixture of O<sub>2</sub> and CO<sub>2</sub> in the PO and SO streams and 3 vol.% oxygen measured in the stack (i.e. ~10 vol.% excess oxygen). Experiments were performed at two different PO volumetric flow rates (low PO 4.2 m<sup>3</sup>/hr and high PO 5.3 m<sup>3</sup>/hr), and the air-fired data at a thermal input of 30 kW designated by the closed-faced triangles is included for reference. For the high PO oxy-fuel case, designated by the closed-face circles, it can be seen that the NO produced at 100% SO swirl was similar to that produced by the air-fired flame at 30 kWth with the same PO flow rate.

Upon reducing the SO swirl the NO immediately increased reaching a maximum of approx. 275 ng/J when the swirl was 20-25% of the total SO flow and returning to a value comparable to the 30 kW air-fired case when no SO swirl was utilized. Thus, even though the molecular nitrogen has been completely removed from the system in the oxy-fuel case, presumably eliminating production of NO via the thermal mechanism, the NO was unchanged when compared to the air-fired flame at 100% and 0% SO swirl. A similar result was observed by Mackrory et al. [239] in a laminar methane piloted system when running under unstaged conditions.

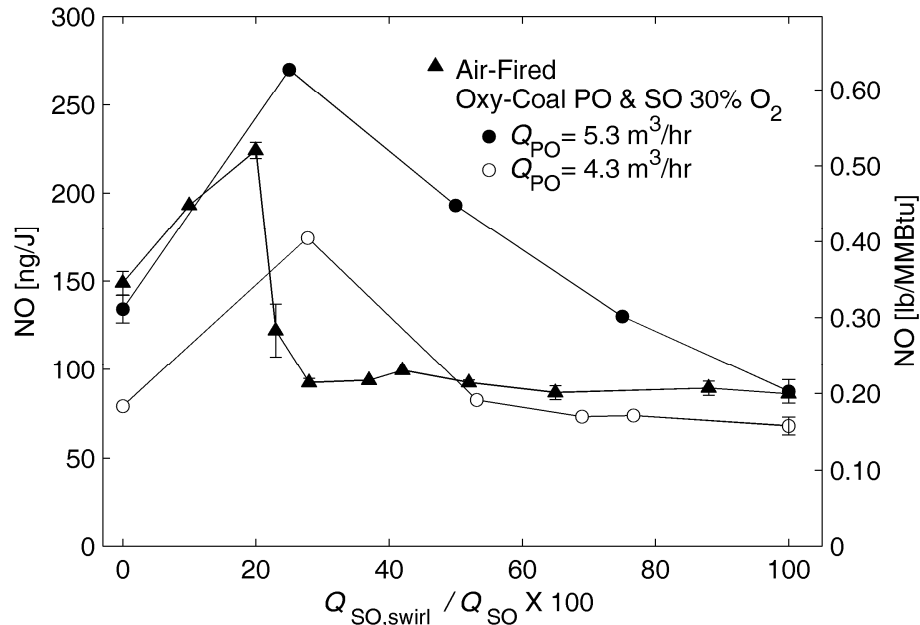


Figure 8.12. Nitric oxide emissions vs. % SO swirl at 30 kWth. ▲ air-fired; oxy-coal, 30% O<sub>2</sub>, 70% CO<sub>2</sub> in PO and SO ● Q<sub>PO</sub> = 5.3 m<sup>3</sup>/hr; ○ Q<sub>PO</sub> = 4.2 m<sup>3</sup>/hr

The low PO flow oxy-fuel flame with a 30/70 volumetric mixture of O<sub>2</sub> and CO<sub>2</sub> in the PO and SO streams, designated by the open-faced circles, was then considered in order to increase the relative amount of flow in the SO thereby improving the symmetry of the flame at 100% SO swirl. Under air-fired conditions it was previously observed in Fig. 8.7 that reducing the PO flow rate to 4.2 m<sup>3</sup>/hr had an insignificant effect on NO emissions with 100% SO swirl. Here it can be seen that when the swirl is sufficient to produce a symmetrical flame under oxy-fuel conditions with 100% SO swirl, the NO measured in the exhaust is reduced by 20% when compared to the air-fired case. Liu et al. [228] also observed a 20% reduction in NO emissions in a 20 kWth down-fired combustor under unstaged oxy-fuel conditions when compared to air-firing. Assuming that the production of NO via the thermal mechanism was eliminated under oxy-fuel conditions, these results and those of [228] were reasonable when considering the work of Pershing and Wendt [219, 242] who demonstrated that the thermal component of the NO formed in coal combustion



accounts for 20-25% of the total NO produced. Additionally, if local temperatures are sufficiently high ( $>2100$  K) Andersson et al. [215] and Normann et al. [214] showed that NO may be destroyed via the thermal mechanism during oxy-fuel combustion; however, it is unlikely that this mechanism played a role in this investigation given that temperatures greater than 2100 K were not achieved. Upon decreasing the amount of SO swirl in the low PO flow oxy-fuel case, the NO emissions remained relatively constant until the swirl flow was reduced to less than 50% of the total SO flow and, similar to all previous results, a maximum amount of NO was produced when the swirl flow was approx. 25% of the total SO flow. Also, similar to the air-fired case with a PO volumetric flow of  $4.2 \text{ m}^3/\text{hr}$ , the NO emissions at 100% and 0% swirl are comparable.

The effect of varying the adiabatic flame temperature by changing the concentration of oxygen in the SO stream with a 30/70 volumetric mixture of  $\text{O}_2$  and  $\text{CO}_2$  in the PO stream on NO emissions is shown in Fig. 8.13 designated by the closed-face circles. The flames were produced with a PO volumetric flow of  $5.3 \text{ m}^3/\text{hr}$ , no SO swirl, and sufficient SO flow to yield 3 vol.% oxygen in the exhaust. The adiabatic flame temperature was calculated using the lower heating value (LHV) of the PRB coal assuming complete combustion, considering excess oxygen as inert, and assuming the products are  $\text{CO}_2$  and  $\text{H}_2\text{O}(\text{g})$  only (no dissociation). The maximum temperature in the near burner region was also measured for each flame and is designated by the open-faced circles. As can be seen along the upper abscissa, the SO oxygen concentration was varied from 27 vol.% to 39 vol.%. With 39 vol.% oxygen in the SO stream the non-swirling flame remained slightly detached from the burner similar to the non-swirling air-fired flames as indicated by a comparison of the measured maximum near burner temperatures. Upon decreasing the adiabatic flame temperature by reducing the concentration of oxygen in the SO, the brightness of the near

burner region observed through the burner ignition port was reduced indicative of the lower temperatures that were measured and suggesting that the flame became slightly more detached.

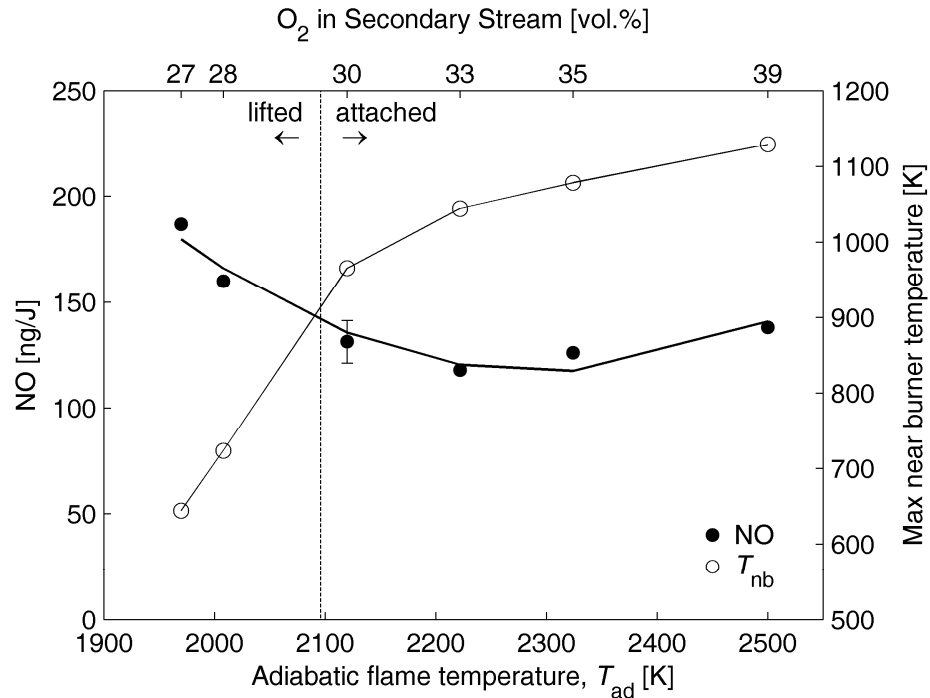


Figure 8.13. Nitric oxide emissions and maximum near burner temperature ( $T_{nb}$ ) (not corrected for radiative loss) vs. adiabatic flame temperature (lower abscissa) and vol.%  $O_2$  in the SO stream (upper abscissa)

A minimum amount of NO was produced at an adiabatic flame temperature of 2220 K with 33 vol.% oxygen in the SO. When the adiabatic flame temperature was decreased below 2100 K the flame was completely detached and the near burner region appeared dark as demonstrated by the photograph in Fig. 8.10b. The temperature measurements and increasing NO emissions also suggest that a transition occurred near this condition. The modest changes observed for the flames with adiabatic flame temperatures greater than 2100 K can be substantiated by the results of Pershing Wendt [219] who demonstrated that the fuel NOx mechanism is relatively insensitive to temperature changes for a variety of coals over the range of temperatures considered here. Conversely, Hu et al. [225] observed a

significant increase in NO<sub>x</sub> emissions with increasing temperature in an electrically heated furnace under oxy-fuel conditions. Nevertheless, these results may be a further indication that heated furnace results should be applied to practical systems with caution.

In Figure 8.14 the effect of cofiring sawdust on NO emissions under oxy-fuel conditions is presented along with the 30 kWth air-fired data discussed previously. The air-fired data is designated by the closed-faced triangles and the oxy-fuel flames produced with a swirling SO stream and a PO flow rate of 4.2 m<sup>3</sup>/hr are designated by the closed-faced circles. As observed for the air-fired flames, cofiring sawdust under these specific oxy-fuel conditions also had no effect on the production of NO. Moreover, these results provide additional evidence in support of the 20% reduction in NO emissions achieved under oxy-fuel conditions discussed previously. Assuming as before, that the thermal NO mechanism makes no contribution to NO production under oxy-fuel conditions, cofiring increased amounts of sawdust had no effect on the amount of NO produced because either more coal bound nitrogen is converted, sawdust bound nitrogen is converted to NO more efficiently than coal nitrogen, or some combination of both effects exists. The effect of elevated local temperatures, due to the higher volatile content of the sawdust, leading to increased thermal NO under air-fired conditions as previously discussed would not contribute here.

The effect of varying the PO and SO gas compositions under oxy-fuel conditions at a thermal input of 30 kW and constant adiabatic flame temperature with 3 vol.% oxygen measured in the stack is shown in Fig. 8.15. The adiabatic flame temperatures were maintained when reducing the PO oxygen concentration by increasing the oxygen concentration in the SO and were calculated as described previously. Results for high PO flow flames with a non-swirling SO are designated by the open-faced circles, while results for high PO flow flames with 100% SO swirl are designated by the closed-faced circles. Low PO

flow flames with 100% SO swirl are designated by the closed-face diamonds. For all three cases the amount of NO produced behaves non-monotonically as a function of the oxygen concentration in the PO stream. Minimum NO emissions were observed in the high PO flow non-swirling flame at 30 vol.% oxygen in the PO stream. For both the low and high PO flow swirling flames the minimum NO emissions were observed when the PO oxygen concentration was 20 vol.%, although the difference between the data at 20 and 30 vol.% is within the experimental uncertainty.

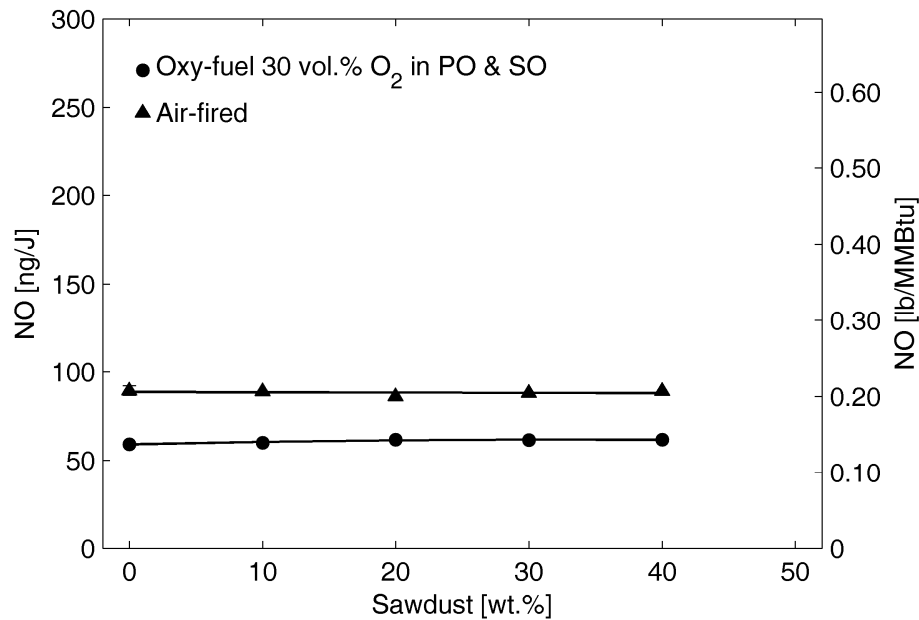


Figure 8.14. NO emissions vs. mass percentage of sawdust cofired with coal at a thermal input of 30 kW, 100% SO swirl, and 3 vol.% O<sub>2</sub> measured in the exhaust. ▲ Air-fired; ● Oxy-fuel with 30 vol.% O<sub>2</sub> in the PO and SO stream and a PO volumetric flow rate of 4.2 m<sup>3</sup>/hr

For the high PO flow flames with no SO swirl, the NO emissions were on average approx. 25% greater than the NO emissions from the swirling flames with the same PO flow rate when the PO oxygen concentration was 30 vol.% or less. When the PO oxygen concentration was increased to 40 vol.% the NO produced in these two cases was similar. Moreover, it was observed that at 40 vol.% O<sub>2</sub> in the PO stream the non-swirling flame was firmly attached to the burner in a similar fashion to the swirling flame. This result suggests

further that the enhanced stability of the swirling flame plays a dominant role in preventing SO stream entrainment and elevated NO emissions [237].

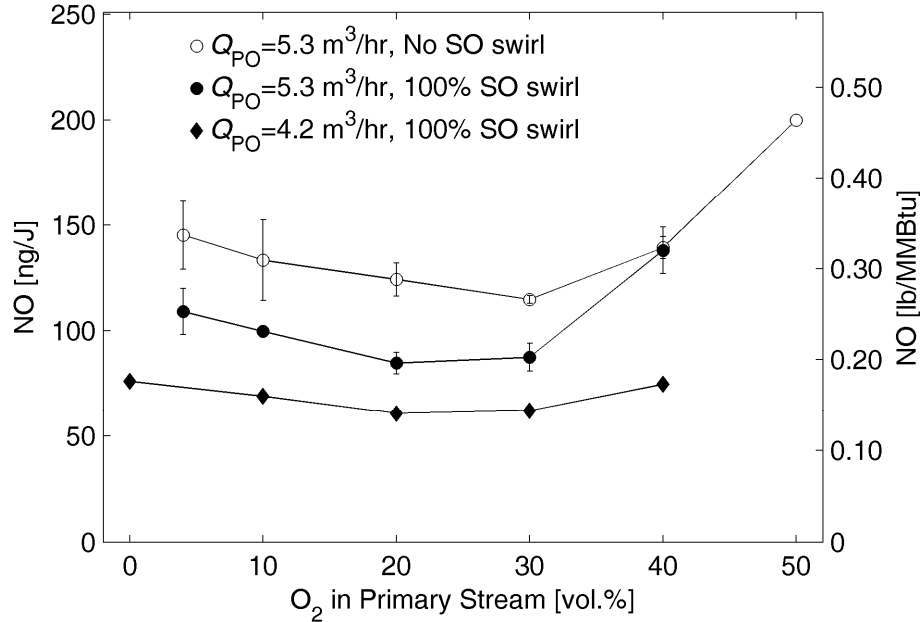


Figure 8.15. NO emissions under oxy-fuel conditions while varying gas composition in the PO and SO streams at constant adiabatic flame temperature and 3% O<sub>2</sub> in the exhaust effluent. ○ Q<sub>PO</sub> = 5.3 m<sup>3</sup>/hr, No SO swirl; ● Q<sub>PO</sub> = 5.3 m<sup>3</sup>/hr, 100% SO swirl; ◆ Q<sub>PO</sub> = 4.2 m<sup>3</sup>/hr, 100% SO swirl.

In the high PO flow non-swirling flame, the increasing NO observed when the oxygen concentration was reduced below 30 vol.% was attributed to slight flame detachment and SO entrainment, but delayed devolatilization resulting in more nitrogen remaining in the char for NO production in well-mixed regions downstream could have also contributed [220]. The latter effect may have been responsible for the increased NO emissions in the low and high PO flow swirling flame when decreasing the oxygen concentration below 20 vol.% as well, given that the maximum near burner temperatures decreased from 1400 K – 1500 K at 30 vol.% oxygen in the PO to 950 K – 1050 K at 4 vol.% oxygen in the PO.

As mentioned previously, at oxygen concentrations greater than 30 vol.% both the non-swirling and swirling high PO flow flames were firmly attached to the burner; thus, increased NO emissions at higher oxygen concentrations in the PO for these flames were

attributed to the local stoichiometric ratio,  $\lambda_{\text{PO}}$ , exceeding some critical value. Since NO emissions from the air-fired experiments did not exhibit a strong dependence on the stoichiometric ratio in the PO, and NO emissions in the low PO flow swirling flame with 40 vol.% oxygen in the PO did not increase substantially when compared to the emissions observed at 20 and 30 vol.% O<sub>2</sub> in the PO, this point requires further analysis.

Returning to the air-fired experiments with 100% SO swirl and variable PO flow rate,  $\lambda_{\text{PO}}$  ranged from 0.14 to 0.26 with minimal changes in NO emissions observed. For the low flow rate oxy-fuel flame with 40 vol.% oxygen in the PO  $\lambda_{\text{PO}}$  was 0.27, which is near the upper bound of the conditions considered in the air-fired experiments, a small increase in NO was observed. However, for the high PO flow oxy-fuel flame with 40 vol.% O<sub>2</sub> in the PO  $\lambda_{\text{PO}}$  was 0.34, which may be at or above a critical value. To provide additional evidence for this hypothesis NO emissions from four additional flames were measured. First, a coal-air flame was produced at a thermal input of 22 kW with a swirling secondary and a PO flow rate of 7.7 m<sup>3</sup>/hr resulting in a stoichiometric ratio in the PO of 0.34. Under these conditions the NO emissions increased approx. 100 ng/J when compared to the coal-air flame produced with a PO flow rate of 5.3 m<sup>3</sup>/hr. Three additional non-swirling oxy-coal low PO flow flames at the same adiabatic flame temperature were also generated with 40 vol.% O<sub>2</sub> in the PO stream at thermal inputs of 25, 33, and 35 kW, and sufficient excess oxygen to yield 3 vol.% O<sub>2</sub> in the exhaust. The NO measured in the exhaust for these three flames along with the non-swirling 30 kWth flame with 40 vol.% O<sub>2</sub> in the PO from Fig. 8.15 are shown in Fig. 8.16.

While the influence of enhanced mixing in the high PO flow rate coal-air flame may play an important role in the increased NO emissions, the influence of the stoichiometric ratio in the PO in the apparent *critical value region* was isolated in Fig. 8.16. It can be seen that

NO emissions were 30% higher in the 25 kWth flame having a stoichiometric ratio in the PO stream of 0.42 when compared to the 30 kWth flame having a stoichiometric ratio in the PO of 0.34. Upon increasing the thermal input to 33 kW, which reduced  $\lambda_{PO}$  to 0.31, the NO emissions dropped only 7%. Finally, at thermal input of 35 kW and a stoichiometric ratio in the PO of 0.29, the NO emissions were unchanged.

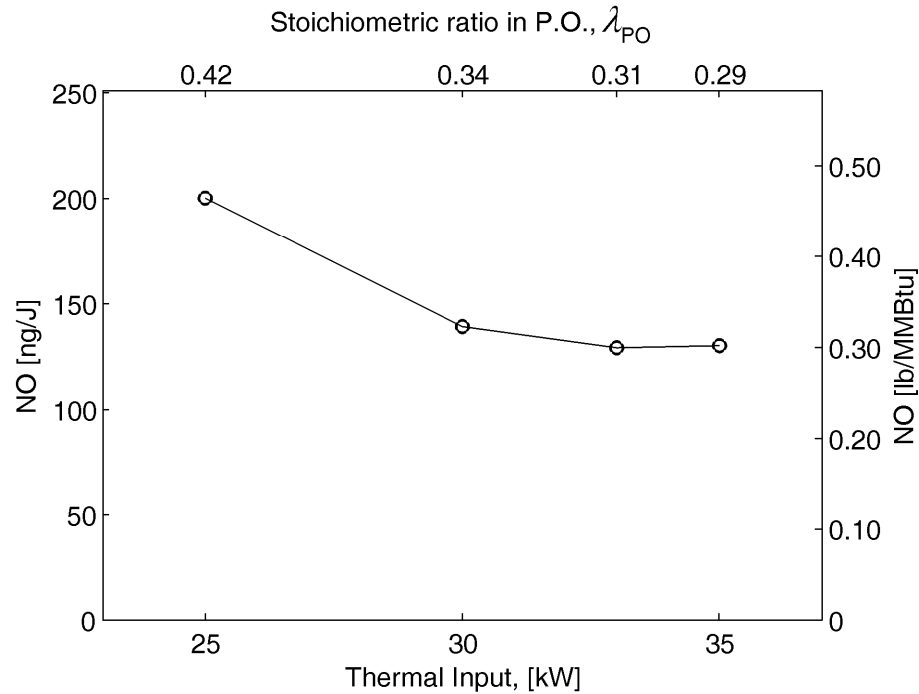


Figure 8.16. NO emission vs. thermal input and  $\lambda_{PO}$  for non-swirling oxy-fuel flames at the same adiabatic flame temperature with 40 vol.%  $O_2$  in the PO and 27 vol.%  $O_2$  in the SO and 3 vol.%  $O_2$  measured in the exhaust.

## 8.4 Conclusions

Measurements of NO concentrations in the exhaust gas during unstaged coal and coal/sawdust combustion in an unpiloted laboratory-scale 30 kWth combustor under a variety of air-fired and oxy-fuel conditions were performed. The effects of thermal input, secondary oxidizer swirl, primary oxidizer flow rate, excess air, and sawdust cofiring on NO emissions were first demonstrated under air-fired conditions. The effects of excess oxygen, swirl, adiabatic flame temperature, sawdust cofiring, and primary and secondary stream gas

composition were then demonstrated under oxy-fuel conditions and the following conclusions can be made:

- 1) In the system used here, which was not designed for low-NO<sub>x</sub> combustion (i.e. no burner optimization, no staged combustion), baseline NO emissions under air-fired conditions were approx. 86 ng/J (0.2 lb/MMBtu) with a swirling secondary flow and 130 ng/J (0.3 lb/MMBtu) without a swirling secondary flow. Typical power plants burning high-volatility bituminous coals utilizing low NO<sub>x</sub> burners and/or staged combustion emit 130-215 ng/J (0.3-0.5 lb/MMBtu) of NO<sub>x</sub>, and it is typically assumed that NO constitutes >95% of the total NO<sub>x</sub> [161].
- 2) In this burner, the primary influence of secondary swirl on NO emissions appears to be through flame stabilization. Moreover, interactions between the tangential swirling flow and the axial flow at reduced swirl (20-25% of total SO flow) resulted in poor hydrodynamics, unsteady detached flames, and increased NO emissions.
- 3) When operating under swirling oxy-fuel conditions in which the oxidizer air was replaced with a mixture of 30 vol.% O<sub>2</sub> and 70 vol.% CO<sub>2</sub> and the primary oxidizer stream volumetric flow rate was equivalent to the baseline air-fired scenario, NO emissions were not reduced relative to the baseline air-fired case. By maintaining the PO volumetric flow rate, as would likely be required under a retrofit scenario for existing utility boilers, the SO flow rate was reduced by 38% resulting in poor swirl hydrodynamics and unsteady flames. Reducing the PO volumetric flow rate by 20% was sufficient to produce a steady swirling flame under the 30/70 oxy-fuel conditions and a 20% reduction in NO emissions was observed similar to the work of Liu et al. [228]. Such a reduction in PO flow rate is not likely an option for current



boilers given that a minimum velocity of 17 m/s is required to keep the pulverized coal in suspension and the expense of coal delivery tube replacement is enormous. However, the ability to increase the angle of adjustable swirl vanes may have also been sufficient to resolve the hydrodynamic issues.

- 4) Cofiring sawdust having 84% less fuel-N on a mass basis (50% less fuel-N on a thermal basis) than the PRB coal used here in a marginally stable flame further reduced flame stability and increased NO formation. When cofiring this same sawdust under stable flame conditions up to 40 wt.% sawdust (33% thermal) NO emissions were not reduced under air-fired or oxy-fuel conditions (i.e. more fuel-N was converted to NO). Sami et al. [24] indicated that NO<sub>x</sub> emissions may not scale with the reduction in fuel-N when cofiring biomass due to the higher volatile content of biomass, which could increase local temperature resulting in elevated thermal NO<sub>x</sub>. However, comparing the air-fired and oxy-fuel results here, and assuming that the thermal NO<sub>x</sub> mechanism could be neglected under oxy-fuel conditions since molecular nitrogen had been removed from the system, these results suggest that other mechanisms may be important when considering cofiring for NO<sub>x</sub> reduction.
- 5) Under oxy-fuel conditions the excess oxygen was reduced below 7 vol.% (16 vol.% excess is common when air-firing) before CO concentrations could be detected. The ability to reduce the amount of excess oxygen while still achieving complete combustion under oxy-fuel conditions can result in energy savings in both the air separation unit (ASU) and the compression and purification unit (CPU) used to process the exhaust gases for sequestration.

- 6) Increasing the adiabatic flame temperature under oxy-fuel conditions by changing the oxygen concentration in the SO stream with a 30 vol.%/70 vol.% mixture of O<sub>2</sub> and CO<sub>2</sub> in the PO stream resulted in negligible changes in NO emissions when the flame remained attached to the burner. These results indicate that the fuel NO mechanism may not be strongly dependent on temperature. Reducing the adiabatic flame temperature below ca. 2100 K resulted in a detached flame as observed visually and via near burner thermocouple measurements. As in previous cases, flame detachment resulted in higher NO emissions. Since increasing the oxygen concentration in the PO will also increase the stoichiometric ratio in the high temperature core of the flame, this technique may be valuable for improving flame stability without increasing NO formation.
- 7) Varying the PO and SO gas compositions at constant adiabatic flame temperature (i.e. low O<sub>2</sub> in PO with high O<sub>2</sub> in SO, high O<sub>2</sub> in PO with low O<sub>2</sub> in SO) resulted in non-monotonic NO emissions as a function of the PO stream oxygen concentration. Minimum NO emissions were observed when the PO oxygen concentration was between 20 and 30 vol.%. Low oxygen concentrations in the PO reduced the maximum near burner flame temperature and presumably caused delayed devolatilization resulting in higher NO. At high oxygen concentrations in the PO a critical stoichiometric ratio was identified at which NO emissions increased sharply. Thus, if elevated oxygen concentrations are to be utilized in the PO stream for flame stability the stoichiometric ratio in the PO must be kept below a critical value, which is most likely coal dependent.

# 9 Summary and Recommendations

The work presented in this dissertation examined two aspects of oxygen-enhanced combustion and was divided into two parts. Part I, *Fundamental Non-Premixed Gaseous Flame Studies*, examined the effects of fuel-dilution and oxygen-enrichment on flame structure and soot formation in ethylene flames. Part II, *Air-Fired and Oxy-Fuel Combustion of Coal and Coal/Biomass Mixtures*, investigated the emission of nitric oxide (NO) from a 30 kWth unstaged combustor while burning coal and coal/biomass mixtures in air and when air was replaced by a mixture of oxygen and carbon dioxide (i.e. oxy-fuel combustion). A summary of the major findings and recommendations for future work follow.

## 9.1 Part I Summary

The main objective of Part I was to enhance the understanding of the structural changes that occur in high  $Z_{st}$  non-premixed flames leading to the inhibition of soot formation. This objective was pursued both experimentally and numerically. The following list summarizes the work performed and major conclusions.

- Non-premixed coflow flame experiments performed under normal and inverse conditions were able to isolate the effects of residence time, flame structure, and flame configuration on soot formation. Contrary to previous findings, the effect of increasing  $Z_{st}$  on soot formation was shown to be similar in normal and inverse coflow flames, provided the effect of residence time was removed.
- An extension to the soot inception model proposed by Sunderland et al. [36] was presented, which accounts for residence time and finite-rate chemistry effects

through a global one-step reaction scheme for soot inception. The region conducive to soot formation in non-premixed flames of ethylene was shown to be bounded on the fuel side of stoichiometry by two isotherms. The high temperature boundary was associated with the location where the local atomic carbon-to-oxygen (C/O) ratio was 0.53 and the local temperature was 1640 K. The low temperature boundary was associated with the location where insufficient temperature, time, and fuel species were available for soot formation. Soot-free flames at high  $Z_{st}$  were attributed to the convergence of these boundaries.

- A numerical investigation using detailed chemistry was performed to understand the key sub-mechanisms responsible for the presence of appreciable molecular oxygen at the location of maximum temperature in high  $Z_{st}$  non-premixed flames.
- The characteristics of the primary mechanism responsible for oxygen consumption were shown to be independent of  $Z_{st}$ . A *double* coupling (kinetic and thermal) was observed between the primary oxygen consumption reaction and the dominant  $\text{CO}_2$ ,  $\text{H}_2\text{O}$ , and heat producing reactions, which constrains the location of oxygen depletion to the location of global stoichiometry.
- The presence of appreciable oxygen at the location of maximum temperature for high  $Z_{st}$  flames was shown to be a consequence of a shifting of the location of maximum temperature toward the oxygen side of the location where  $\text{O}_2$  is consumed.

- The shifting of the location of maximum temperature was attributed to exothermic reactions displaced from the location of oxygen depletion and the location of the heat release profile relative to the fuel and oxidizer free-streams in mixture fraction space.
- A second numerical study investigated the effects of flame structure on the detailed kinetics of soot precursor formation and destruction to better understand the existence of soot-free high  $Z_{st}$  flames.
- A unique approach termed *reverse pathway analysis* was developed and utilized to determine the dominant chemical pathway leading to soot precursor formation.
- Based on the mechanism used here, one of the dominant chemical pathways leading to a key soot precursor species was shown to reverse directions at sufficiently high  $Z_{st}$  due to changes in flame structure. Consequently, increasing  $Z_{st}$  was shown to eliminate a primary pathway to soot and open up a new pathway for soot precursor oxidation leading to soot-free flames.

## 9.2 Part I Recommendations

The counterflow flame results of Du and Axelbaum [30] and Lin and Faeth [42], as well as spherical flame experiments conducted in microgravity by Sunderland et al. [36] indicate that soot-free flames can be obtained at residence times approaching infinity relative to typical flame time scales, even at high temperature. Recent inverse coflow flame experiments, not included in this work, suggest that soot-free flames may not be attainable in this configuration. Preliminary computational analysis indicates that this phenomenon may be a result of preferential diffusion of the H radical in the upper portion of the flame. Additional work is needed to confirm and explain these results.

The shifting of the peak temperature toward the oxygen side of global stoichiometry, which is responsible for the presence of appreciable oxygen at the location of maximum temperature in high  $Z_{st}$  flames, was explained only qualitatively. A more rigorous approach should be pursued by developing a simplified four-step reaction scheme, representative of the four observed heat release zones, and demonstrating the temperature shift at high  $Z_{st}$  via high activation energy asymptotics.

The numerical study investigating the detailed chemistry associated with high  $Z_{st}$  soot-free flames was conducted with only one fuel and one detailed mechanism. It is believed that the soot formation pathway for other aliphatic fuels such as ethane and propane may exhibit similar behavior leading to soot-free conditions at high  $Z_{st}$ . In addition, the soot pathway reversal should be investigated using additional chemical mechanisms having potentially different reactions and rate parameters to determine if the results presented here were mechanism dependent.

### 9.3 Part II Summary

The main objectives of Part II were to investigate the effects of oxy-fuel combustion and biomass cofiring on the emissions of nitric oxide (NO) relative to air-fired combustion of coal. A summary of the work performed and key findings are listed below.

- A 30 kWth coal combustor was designed and constructed and several technical issues relating to fuel delivery and carbon dioxide delivery (for simulating flue gas recycle) were overcome.
- Nitric oxide emissions under baseline air-fired unstaged conditions from the laboratory combustor with a swirling secondary oxidizer stream were near the low end of the average emissions produced by industrial utility boilers equipped

with low-NO<sub>x</sub> burners and/or running under staged combustion conditions. Air-firing with no secondary swirl resulted in NO emissions near the upper end of the average. At steady state, CO emissions were below the detectable limits for all cases when 3 vol.% O<sub>2</sub> was present in the exhaust.

- Under air-fired conditions the effects of thermal input, secondary swirl, excess air, primary oxidizer stream flow rate, and biomass (sawdust) cofiring on NO emissions were investigated. Varying the thermal input, primary stream flow rate, and excess air had a greater impact on NO emissions in non-swirling flames. At 30 kW<sub>th</sub> reducing the SO swirl did not affect NO emissions until the swirl was reduced to 20-25% of the total SO flow, at which point NO emissions rose sharply. Cofiring sawdust with less fuel-N on both a mass and thermal basis did not reduce NO emissions.
- Under the baseline oxy-fuel conditions in which the oxidizer air was replaced with a mixture of 30 vol.% O<sub>2</sub> and 70 vol.% CO<sub>2</sub>, the effects of excess oxygen, secondary swirl, and sawdust cofiring on NO emissions were investigated. When the primary stream flow rate was matched to that of the air-fired flame, the SO volumetric flow rate had to be reduced more than 30% to maintain 3 vol.% oxygen in the exhaust. Consequently, the SO swirl was insufficient to produce a symmetric flame and NO emissions were not reduced relative to air-firing, even though molecular nitrogen had been removed from the system. Upon reducing the primary stream flow rate and increasing the SO swirl, NO emissions were reduced by 20%. In this system CO remained below the gas analyzer's detectable limits until the excess oxygen was reduced below 7 vol.%. The ability to achieve complete combustion at low excess oxygen during oxy-fuel conditions has

important implications with respect to the requirements for the air separation unit and the CO<sub>2</sub> compression and purification unit. Reducing the SO swirl to 20% of the total SO flow also increased the NO emissions in the baseline oxy-fuel case, similar to the result observed during air-firing. Also similar to air-firing, cofiring sawdust did not reduce NO emissions.

- The effect of temperature on NO emissions was investigated by varying the oxygen concentration in the SO stream while maintaining the baseline oxy-fuel concentrations in the PO. Increasing the temperature beyond the oxy-fuel baseline did not result in significantly more NO, although at lower temperatures the flames became detached and NO emissions increased due to SO entrainment. Increased oxygen concentrations in the SO may be a valuable strategy to maintain flame stability under deeper staging.
- The effect of varying the oxygen concentrations in the PO and SO streams on NO emissions was investigated while maintaining constant adiabatic flame temperature and 3 vol.% O<sub>2</sub> in the exhaust. Non-monotonic behavior was observed and the results indicated that the primary influence of a swirling SO stream on NO emissions in this system is through flame stabilization. The results also indicated that increased oxygen concentrations in the PO can improve flame stability without increasing NO emissions provided the local stoichiometric ratio is maintained below some critical value.



## 9.4 Part II Recommendations

A number of modifications to the existing system are desirable. In addition, many highly valuable air-fired and oxy-fuel studies can be performed with this combustor as it stands, or after incorporating the modifications. The recommendations are listed below.

### 9.4.1 System Modifications

- Adding gas and temperature sampling ports from the near burner region incrementally along the length of the combustor would enable valuable measurements showing the evolution of NO and other species as well as the changes in the axial temperature profile under different air-fired and oxy-fuel conditions. In addition, the extent of flame detachment could be ascertained.
- Water cooling the combustor walls would decrease the time required to reach steady state and would prevent slagging. Cooling should also be added to the vertical stainless exhaust given that the sampling temperature approaches 800 K after several hours of operation under the current conditions. It was also observed that the laboratory HVAC system was insufficient to maintain a comfortable temperature. Thus, cooling would improve the comfort of operators.
- Visual observations as well as CFD modeling have indicated that flow and particles were being recirculated well into the burner head when operating with high swirl. It has been presumed that this is due to the relatively large diameter provided for the secondary swirling flow, which results in low axial velocities. Following CFD modeling to determine the optimal diameter, the burner head should be modified to eliminate this recirculation by reducing the

diameter of the SO flow inlet. A quarl should also be modeled for optimization and added to the burner at this same time.

- The primary stream exit velocity in this system was significantly lower than that observed in practical systems. This aided in flame stability, but may reduce the relevance of the results. The PO exit velocity can be increased without increasing the thermal input by reducing the diameter of the primary stream tube.
- Adjustable swirl vanes in the secondary stream should be added to enable higher tangential velocities when operating under oxy-fuel conditions.
- Overfire oxidizer ports should be added to enable staged combustion experiments.
- Carbon dioxide and sulfur oxide gas analyzers should be installed. A more robust oxygen sensor that is not pressure sensitive should also be installed if possible.

#### **9.4.2 Future Work**

- It is believed that the relatively low NO emissions observed in this unstaged combustor when compared to full-scale utility boilers were related to this system's excellent flame attachment resulting in flames that more closely resembled non-premixed combustion rather than partially-premixed combustion. This phenomenon should be explored to determine the relevance of results obtained with this system.
- Pulverized coal samples were obtained from a local power plant by sampling from a coal delivery pipe downstream of a mill. It is believed that the sampling method led to a bias in the particle size distribution toward smaller particles.

Though not specifically studied, it was observed on several occasions that samples having a larger fraction of smaller coal particles ( $< 74$  microns) led to improved flame stability and lower NO emissions. These effects could be quantified by preparing coal samples in binned size ranges via sieving.

- Cofiring sawdust having a lower nitrogen content than coal did not lower NO emissions. This was attributed to the larger sawdust particle sizes leading to delayed volatile release from both the coal and sawdust particles. This would leave more nitrogen in the char to form NO downstream where mixing has occurred. Experiments should be conducted with sawdust samples having a smaller average particle diameter to confirm this hypothesis. Sawdust samples should be prepared and cofired below 50 mesh, 80 mesh, 100 mesh, and 200 mesh to demonstrate the effect of particle size.
- In this study only one coal type and one biomass type were utilized. Future studies should investigate emissions using coals of different rank and chemical composition as well as the cofiring of a variety of biomass fuels such as switchgrass, miscanthus, algae, and wheat straw.
- The efficiency of particle capture techniques for fly ash under oxy-fuel combustion may be influenced by both the reduced volumetric flow of flue gases and changes in the particle size distribution. Cofiring biomass may also influence the particle size distribution. The effects of oxy-fuel combustion and biomass cofiring on the sub-micron particle size distribution should be quantified.
- Fly ash from coal utility boilers is often used in Portland cement and in many other applications. At the present time, fly ash produced from biomass is not

typically accepted for use. Moreover, oxy-fuel combustion may influence fly ash characteristics. The effects of oxy-fuel combustion and biomass cofiring on the characteristics and composition of the bottom ash and fly ash should be quantified. Studies could be conducted in conjunction with the structural engineering department to evaluate any differences between Portland cement produced with fly ash produced under various combustion scenarios.

- Higher oxygen concentrations in oxy-fuel combustion may lead to higher particle temperatures, which could influence slagging and fouling characteristics. When cofiring biomass fuels that contain more sodium and potassium than coal the ash melting temperature can be reduced leading to slagging problems. Biomass fuels may also contain high chlorine, which can accelerate boiler tube corrosion. Thus, the effects of oxy-fuel combustion and biomass cofiring on slagging, fouling, and corrosion should be quantified.
- Finally, following system modifications all experiments should be performed under staged and unstaged conditions.

# Appendix A

## Flame Equilibrium Formulation

In the flame equilibrium approach utilized here the following simplifications to the governing equations for a reacting flow are employed:

- steady-state
- mass diffusion occurs only due to concentration gradients
- viscous heating is negligible
- body forces are ignored
- radiation heat transfer is ignored
- diffusion coefficients equal for all species (i.e.  $D_{ij}=D$ )
- unity Lewis number,  $Le = k/(\rho c_p D) = 1$
- one-step chemistry, Fuel + Oxidizer  $\rightarrow$  Products

Under these simplifying assumptions the species conservation equation reduces to

$$\nabla \cdot [\rho \mathbf{v} Y_i - (\rho D) \nabla Y_i] = W_i (v_i'' - v_i') \omega \quad (\text{A.1})$$

where the subscript  $i$  refers to  $i$ th species,  $\rho$  is the density of the mixture,  $Y$  is the mass fraction,  $\mathbf{v}$  is the velocity of the bulk flow,  $D$  is the diffusion coefficient assumed constant and equivalent for all species,  $W$  is the molecular weight,  $v'$  and  $v''$  are the stoichiometric coefficients in the one-step reaction for the reactants and products, respectively, and  $\omega$  is the species independent reaction rate given by

$$\omega = \frac{w_i}{W_i(v_i'' - v_i')} \quad (\text{A.2})$$

where  $w_i$  is the reaction rate of species  $i$ . The energy equation is similarly reduced to

$$\nabla \cdot [\rho \mathbf{v} h^s - (\rho D) \nabla h^s] = - \sum_{i=1}^N h_i^o W_i (v_i'' - v_i') \omega \quad (\text{A.3})$$

where  $h^s$  is the sensible enthalpy,  $h_i^o$  is the enthalpy of formation of species  $i$ , and  $N$  is the number of species. Noting the similarity of the L.H.S. of Eqs. 1 and 3 and using the common abbreviation for the operation performed on  $Y_i$  and  $h^s$ ,  $L(\cdot) = \nabla \cdot [\rho \mathbf{v}(\cdot) - (\rho D) \nabla(\cdot)]$ , Eqs. 1 and 3 can be written as

$$L(Y_i) = W_i (v_i'' - v_i') \omega \quad (\text{A.1a})$$

and

$$L(h^s) = - \sum_{i=1}^N h_i^o W_i (v_i'' - v_i') \omega. \quad (\text{A.3a})$$

From the theory of linear ODEs the principle of superposition states that the linear combination of two or more unique solutions to an ODE is also a valid and unique solution. Thus, any combination of the individual species profiles represents a valid solution to Eq. 1 and any combination of species profiles with the profile of sensible enthalpy represents a valid solution to Eq. 3. The goal of any such combination is to eliminate the reaction term on the R.H.S. of the species and energy equations. When this goal is achieved, the combined quantity is referred to as a *conserved scalar* or *coupling function* because it is unaffected by chemical reactions in the flow and therefore removes the coupling between the species and energy equations.

Appropriate conserved scalars can be formulated by first defining a stoichiometrically weighted mass fraction for species  $i$  with respect to the fuel as

$$\tilde{Y}_i = \frac{1}{\sigma_{i,F}} \left( \frac{Y_i}{Y_{F,fu}} \right) \quad (\text{A.4})$$

where the subscript  $F$  refers to the fuel species,  $fu$  indicates that the quantity is to be evaluated in the fuel free stream, and

$$\sigma_{i,F} = \frac{W_i(v_i'' - v_i')}{W_F(v_F'' - v_F')} \quad (\text{A.5})$$

is the stoichiometric mass ratio of species  $i$  to the fuel. A stoichiometrically weighted non-dimensional enthalpy or temperature is then defined as

$$\tilde{h}_s = \frac{h_s}{Y_{i,F} q_{c,F}} = \tilde{T} = \frac{c_p T}{Y_{i,F} q_{c,F}} \quad (\text{A.6})$$

where  $q_{c,F}$  is the chemical heat release per unit mass of fuel reacted defined as

$$q_{c,F} = \frac{\sum_{k=1}^N h_k^o W_k (v_k'' - v_k')}{W_F (v_F'' - v_F')} \quad (\text{A.7})$$

Considering the one-step reaction Fuel + Oxygen  $\rightarrow$  Products, a suitable conserved scalar for Eq. 1,  $\beta_{F,O_2}$ , can be defined as  $\beta_{F,O_2} = \tilde{Y}_F - \tilde{Y}_{O_2}$ . For Eq. 3, two appropriate conserved scalars are  $\beta_F = \tilde{h}_s + \tilde{Y}_F$  and  $\beta_{O_2} = \tilde{h}_s + \tilde{Y}_{O_2}$ . Substituting these conserved scalars into Eqs. 1a and 3a yields

$$L(\beta_{F,O_2}) = 0, \quad (\text{A.1b})$$

$$L(\beta_F) = 0, \quad (\text{A.3b})$$

and

$$L(\beta_{O_2}) = 0. \quad (\text{A.3c})$$

While the solutions of Eqs. 1b, 3b, and 3c would yield useful results in physical space for a chosen flame configuration and coordinate system, it is desirable to develop a more general formulation that provides results as a function of a variable that is independent of flame configuration (i.e. counterflow, coflow, spherical). One such variable is the mixture fraction,  $Z$ , defined as the local fraction of mass that originated from the fuel stream. By considering Eqs. 1b, 3b, and 3c in  $Z$  space, a solution to these ODEs can be developed purely on the basis of the principle of superposition without formal integration.

In terms of the conserved scalar  $\beta_{F,O_2}$  the mixture fraction can be written for one-step chemistry as

$$Z = \frac{\beta_{F,O_2} - (\beta_{F,O_2})_{ox}}{(\beta_{F,O_2})_{fu} - (\beta_{F,O_2})_{ox}} = \frac{\tilde{Y}_F - \tilde{Y}_{O_2} + \tilde{Y}_{O_2,ox}}{\tilde{Y}_{F,fu} + \tilde{Y}_{O_2,ox}} = \frac{\sigma_{O_2,F} Y_F - Y_{O_2} + Y_{O_2,ox}}{\sigma_{O_2,F} Y_{F,fu} + Y_{O_2,ox}} \quad (\text{A.8})$$

where the subscripts  $fu$  and  $ox$  indicate that the quantity is to be evaluated in the fuel free stream and oxidizer free stream, respectively. Thus, by definition  $Z = 0$  in the oxidizer free stream and  $Z = 1$  in the fuel free stream. Because  $Z$  is linearly related to  $\beta_{F,O_2}$ , the principle of superposition requires that  $Z$  also be a solution to Eq. 1. Solving Eq. 8 for  $\beta_{F,O_2}$  yields

$$\beta_{F,O_2} = Z((\beta_{F,O_2})_{fu} - (\beta_{F,O_2})_{ox}) + (\beta_{F,O_2})_{ox}. \quad (\text{A.9})$$

Thus,

$$\tilde{Y}_F - \tilde{Y}_{O_2} = (\tilde{Y}_{F,fu} + \tilde{Y}_{O_2,ox})Z - \tilde{Y}_{O_2,ox}. \quad (\text{A.9a})$$



To solve for the fuel and oxidizer profiles in  $Z$  space it is now necessary to apply the flame sheet assumption. At the location of stoichiometric composition the flame sheet assumption requires complete consumption of the reactants (i.e.  $\tilde{Y}_F = \tilde{Y}_{O_2} = 0$ ). Thus, the stoichiometric mixture fraction,  $Z_{st}$ , can be written

$$Z_{st} = \frac{\tilde{Y}_{O_2,ox}}{\tilde{Y}_{F,fu} + \tilde{Y}_{O_2,ox}} = \left(1 + \sigma_{O_2,F} Y_{F,fu} / Y_{O_2,ox}\right)^{-1}. \quad (\text{A.10})$$

Note here that  $Z_{st}$  is a useful parameter in describing the extent of free stream fuel dilution and oxygen-enrichment given that  $Z_{st}$  is close to zero for pure fuel burning in air and close to unity for heavily-diluted fuel burning in pure oxygen. Since reactants are consumed at  $Z=Z_{st}$ , the fuel mass fraction on the fuel side of stoichiometry is described by

$$\tilde{Y}_F = (\tilde{Y}_{F,fu} + \tilde{Y}_{O_2,ox})Z - \tilde{Y}_{O_2,ox} \quad (\text{A.11})$$

while the oxygen mass fraction on the oxidizer side of stoichiometry is describe by

$$\tilde{Y}_{O_2} = -(\tilde{Y}_{F,fu} + \tilde{Y}_{O_2,ox})Z + \tilde{Y}_{O_2,ox}. \quad (\text{A.12})$$

Moreover, with the unity Lewis number assumption linear relationships between the mixture fraction and  $\beta_F$  and  $\beta_{O_2}$  can also be written as

$$Z = \frac{\beta_F - \tilde{h}_{s,ox}}{\beta_{F,fu} - \tilde{h}_{s,ox}} = \frac{\beta_{O_2} - \beta_{O_2,ox}}{\tilde{h}_{s,fu} - \beta_{O_2,ox}} \quad (\text{A.13})$$

yielding

$$\tilde{h}_s = \tilde{T} = (\beta_{F,fu} - \tilde{h}_{s,ox})Z + \tilde{h}_{s,ox} \quad (\text{A.14})$$

on the oxidizer side of stoichiometry and

$$\tilde{h}_s = \tilde{T} = (\tilde{h}_{s, fu} - \beta_{O_2, ox})Z + \beta_{O_2, ox} \quad (\text{A.15})$$

on the fuel side of stoichiometry. At the location of stoichiometry  $Z = Z_{st}$  and the adiabatic flame temperature is given by

$$\tilde{h}_{s, ad} = \tilde{T}_{ad} = \frac{\beta_{F, fu} - \tilde{h}_{s, ox}}{1 + \sigma_{O_2, F} \tilde{Y}_{F, fu} / \tilde{Y}_{O_2, ox}} + \tilde{h}_{s, ox}. \quad (\text{A.16})$$

Note that as previously indicated, the species and temperature profiles in mixture fraction space have been computed without formally solving the simplified linear ODEs.

# Appendix B

## Reaction Mechanism Used in Chapter 6

Chemistry from naphthalene to pyrene from Appel et al. [133] appended to USC Mech Version II [137].

Reactions Considered	k=A T <sup>b</sup> exp(-E/RT)				
	A	b	E (cal/mol)		
1 H+O2=O+OH	2.64E+16	-7.00E-01	1.70E+04		
2 O+H2=H+OH	4.59E+04	2.70E+00	6.26E+03		
3 OH+H2=H+H2O	1.73E+08	1.50E+00	3.43E+03		
4 OH+OH=O+H2O	3.97E+04	2.40E+00	-2.11E+03		
5 H+H+M=H2+M	1.78E+18	-1.00E+00	0.00E+00		
Enhanced by	H2	H2O	CO2	AR	
	0.00E+00	0.00E+00	0.00E+00	6.30E-01	
6 H+H+H2=H2+H2	9.00E+16	-6.00E-01	0.00E+00		
7 H+H+H2O=H2+H2O	5.62E+19	-1.20E+00	0.00E+00		
8 H+H+CO2=H2+CO2	5.50E+20	-2.00E+00	0.00E+00		
9 H+OH+M=H2O+M	4.40E+22	-2.00E+00	0.00E+00		
Enhanced by	H2	H2O	CO	CO2	AR
	2.00E+00	6.30E+00	1.75E+00	3.60E+00	3.80E-01
		9.43E+18	-1.00E+00	0.00E+00	
10 O+H+M=OH+M	H2	H2O	CO	CO2	AR
Enhanced by	2.00E+00	1.20E+01	1.75E+00	3.60E+00	7.00E-01
		1.20E+17	-1.00E+00	0.00E+00	
11 O+O+M=O2+M	H2	H2O	CO	CO2	AR
Enhanced by	2.40E+00	1.54E+01	1.75E+00	3.60E+00	8.30E-01
		5.12E+12	4.00E-01	0.00E+00	
		0.00E+00	6.33E+19	-1.40E+00	
		5.00E-01	1.00E-30	1.00E+30	
12 H+O2(+M)=HO2(+M)	O2	H2O	CO	CO2	AR
Low pressure limit	8.50E-01	1.19E+01	1.09E+00	2.18E+00	4.00E-01
TROE centering		5.92E+05	2.40E+00	5.35E+04	
Enhanced by		1.11E+14	-4.00E-01	0.00E+00	
		0.00E+00	2.01E+17	-5.84E-01	
		7.35E-01	9.40E+01	1.76E+03	
13 H2+O2=HO2+H	H2	H2O	CO	CO2	AR
14 OH+OH(+M)=H2O2(+M)	2.00E+00	6.00E+00	1.75E+00	3.60E+00	7.00E-01
Low pressure limit		3.97E+12	0.00E+00	6.71E+02	
TROE centering		7.48E+13	0.00E+00	2.95E+02	
Enhanced by		4.00E+13	0.00E+00	0.00E+00	
		1.30E+11	0.00E+00	-1.63E+03	
15 HO2+H=O+H2O		3.66E+14	0.00E+00	1.20E+04	
16 HO2+H=OH+OH		1.41E+18	-1.80E+00	6.00E+01	
17 HO2+O=OH+O2		1.12E+85	-2.23E+01	2.69E+04	
18 HO2+HO2=O2+H2O2		5.37E+70	-1.67E+01	3.29E+04	
Declared duplicate reaction		2.51E+12	2.00E+00	4.00E+04	
19 HO2+HO2=O2+H2O2		1.00E+136	-4.00E+01	3.48E+04	
Declared duplicate reaction		6.05E+06	2.00E+00	5.20E+03	
20 OH+HO2=H2O+O2		2.41E+13	0.00E+00	3.97E+03	
Declared duplicate reaction		9.63E+06	2.00E+00	3.97E+03	
21 OH+HO2=H2O+O2		2.00E+12	0.00E+00	4.27E+02	
Declared duplicate reaction		2.67E+41	-7.00E+00	3.76E+04	
22 OH+HO2=H2O+O2		1.36E+10	0.00E+00	2.38E+03	
Declared duplicate reaction					
23 OH+HO2=H2O+O2					
Declared duplicate reaction					
24 H2O2+H=HO2+H2					
25 H2O2+H=OH+H2O					
26 H2O2+O=OH+HO2					
27 H2O2+OH=HO2+H2O					
Declared duplicate reaction					
28 H2O2+OH=HO2+H2O					
Declared duplicate reaction					
29 H2O2+OH=HO2+H2O					
Declared duplicate reaction					
30 CO+O(+M)=CO2(+M)					

Low pressure limit		0.00E+00	1.17E+24	-2.79E+00	
Enhanced by	H2	H2O	CO	CO2	AR
	2.00E+00	1.20E+01	1.75E+00	3.60E+00	7.00E-01
31 CO+OH=CO2+H		7.05E+04	2.10E+00	-3.56E+02	
Declared duplicate reaction					
32 CO+OH=CO2+H		5.76E+12	-7.00E-01	3.32E+02	
Declared duplicate reaction					
33 CO+O2=CO2+O		1.12E+12	0.00E+00	4.77E+04	
34 CO+HO2=CO2+OH		1.57E+05	2.20E+00	1.79E+04	
35 HCO+H=CO+H2		1.20E+14	0.00E+00	0.00E+00	
36 HCO+O=CO+OH		3.00E+13	0.00E+00	0.00E+00	
37 HCO+O=CO2+H		3.00E+13	0.00E+00	0.00E+00	
38 HCO+OH=CO+H2O		3.02E+13	0.00E+00	0.00E+00	
39 HCO+M=CO+H+M		1.87E+17	-1.00E+00	1.70E+04	
Enhanced by	H2	H2O	CO	CO2	
	2.00E+00	0.00E+00	1.75E+00	3.60E+00	
40 HCO+H2O=CO+H+H2O		2.24E+18	-1.00E+00	1.70E+04	
41 HCO+O2=CO+HO2		1.20E+10	8.00E-01	-7.27E+02	
42 CO+H2(+M)=CH2O(+M)		4.30E+07	1.50E+00	7.96E+04	
Low pressure limit		0.00E+00	5.07E+27	-3.42E+00	
TROE centering		9.32E-01	1.97E+02	1.54E+03	
Enhanced by	H2	H2O	CH4	CO	CO2
	2.00E+00	6.00E+00	2.00E+00	1.50E+00	2.00E+00
	C2H6	AR			
	3.00E+00	7.00E-01			
43 C+OH=CO+H		5.00E+13	0.00E+00	0.00E+00	
44 C+O2=CO+O		5.80E+13	0.00E+00	5.76E+02	
45 CH+H=C+H2		1.10E+14	0.00E+00	0.00E+00	
46 CH+O=CO+H		5.70E+13	0.00E+00	0.00E+00	
47 CH+OH=HCO+H		3.00E+13	0.00E+00	0.00E+00	
48 CH+H2=CH2+H		1.11E+08	1.80E+00	1.67E+03	
49 CH+H2O=CH2O+H		5.71E+12	0.00E+00	-7.55E+02	
50 CH+O2=HCO+O		3.30E+13	0.00E+00	0.00E+00	
51 CH+CO(+M)=HCCO(+M)		5.00E+13	0.00E+00	0.00E+00	
Low pressure limit		0.00E+00	2.69E+28	-3.74E+00	
TROE centering		5.76E-01	2.37E+02	1.65E+03	
Enhanced by	H2	H2O	CH4	CO	CO2
	2.00E+00	6.00E+00	2.00E+00	1.50E+00	2.00E+00
	C2H6	AR			
	3.00E+00	7.00E-01			
52 CH+CO2=HCO+CO		3.40E+12	0.00E+00	6.90E+02	
53 HCO+H(+M)=CH2O(+M)		1.09E+12	5.00E-01	-2.60E+02	
Low pressure limit		0.00E+00	1.35E+24	-2.57E+00	
TROE centering		7.82E-01	2.71E+02	2.76E+03	
Enhanced by	H2	H2O	CH4	CO	CO2
	2.00E+00	6.00E+00	2.00E+00	1.50E+00	2.00E+00
	C2H6	AR			
	3.00E+00	7.00E-01			
54 CH2+H(+M)=CH3(+M)		2.50E+16	-8.00E-01	0.00E+00	
Low pressure limit		0.00E+00	3.20E+27	-3.14E+00	
TROE centering		6.80E-01	7.80E+01	2.00E+03	
Enhanced by	H2	H2O	CH4	CO	CO2
	2.00E+00	6.00E+00	2.00E+00	1.50E+00	2.00E+00
	C2H6	AR			
	3.00E+00	7.00E-01			
55 CH2+O=HCO+H		8.00E+13	0.00E+00	0.00E+00	
56 CH2+OH=CH2O+H		2.00E+13	0.00E+00	0.00E+00	
57 CH2+OH=CH+H2O		1.13E+07	2.00E+00	3.00E+03	
58 CH2+H2=H+CH3		5.00E+05	2.00E+00	7.23E+03	
59 CH2+O2=HCO+OH		1.06E+13	0.00E+00	1.50E+03	
60 CH2+O2=CO2+H+H		2.64E+12	0.00E+00	1.50E+03	
61 CH2+HO2=CH2O+OH		2.00E+13	0.00E+00	0.00E+00	
62 CH2+C=C2H+H		5.00E+13	0.00E+00	0.00E+00	
63 CH2+CO(+M)=CH2CO(+M)		8.10E+11	5.00E-01	4.51E+03	
Low pressure limit		0.00E+00	2.69E+33	-5.11E+00	
TROE centering		5.91E-01	2.75E+02	1.23E+03	
Enhanced by	H2	H2O	CH4	CO	CO2
	2.00E+00	6.00E+00	2.00E+00	1.50E+00	2.00E+00

	C2H6	AR			
	3.00E+00	7.00E-01			
64	CH2+CH=C2H2+H	4.00E+13	0.00E+00	0.00E+00	
65	CH2+CH2=C2H2+H2	3.20E+13	0.00E+00	0.00E+00	
66	CH2*+N2=CH2+N2	1.50E+13	0.00E+00	6.00E+02	
67	CH2*+AR=CH2+AR	9.00E+12	0.00E+00	6.00E+02	
68	CH2*+H=CH+H2	3.00E+13	0.00E+00	0.00E+00	
69	CH2*+O=CO+H2	1.50E+13	0.00E+00	0.00E+00	
70	CH2*+O=HCO+H	1.50E+13	0.00E+00	0.00E+00	
71	CH2*+OH=CH2O+H	3.00E+13	0.00E+00	0.00E+00	
72	CH2*+H2=CH3+H	7.00E+13	0.00E+00	0.00E+00	
73	CH2*+O2=H+OH+CO	2.80E+13	0.00E+00	0.00E+00	
74	CH2*+O2=CO+H2O	1.20E+13	0.00E+00	0.00E+00	
75	CH2*+H2O(+M)=CH3OH(+M)	2.00E+13	0.00E+00	0.00E+00	
	Low pressure limit	0.00E+00	2.70E+38	-6.30E+00	
	TROE centering	1.51E-01	1.34E+02	2.38E+03	
	Enhanced by	H2	H2O	CH4	CO
	2.00E+00	6.00E+00	2.00E+00	1.50E+00	2.00E+00
	C2H6				
	3.00E+00				
76	CH2*+H2O=CH2+H2O	3.00E+13	0.00E+00	0.00E+00	
77	CH2*+CO=CH2+CO	9.00E+12	0.00E+00	0.00E+00	
78	CH2*+CO2=CH2+CO2	7.00E+12	0.00E+00	0.00E+00	
79	CH2*+CO2=CH2O+CO	1.40E+13	0.00E+00	0.00E+00	
80	CH2O+H(+M)=CH2OH(+M)	5.40E+11	5.00E-01	3.60E+03	
	Low pressure limit	0.00E+00	1.27E+32	-4.82E+00	
	TROE centering	7.19E-01	1.03E+02	1.29E+03	
	Enhanced by	H2	H2O	CH4	CO
	2.00E+00	6.00E+00	2.00E+00	1.50E+00	2.00E+00
	C2H6				
	3.00E+00				
81	CH2O+H(+M)=CH3O(+M)	5.40E+11	5.00E-01	2.60E+03	
	Low pressure limit	0.00E+00	2.20E+30	-4.80E+00	
	TROE centering	7.58E-01	9.40E+01	1.56E+03	
	Enhanced by	H2	H2O	CH4	CO
	2.00E+00	6.00E+00	2.00E+00	1.50E+00	2.00E+00
	C2H6				
	3.00E+00				
82	CH2O+H=HCO+H2	2.30E+10	1.10E+00	3.28E+03	
83	CH2O+O=HCO+OH	3.90E+13	0.00E+00	3.54E+03	
84	CH2O+OH=HCO+H2O	3.43E+09	1.20E+00	-4.47E+02	
85	CH2O+O2=HCO+HO2	1.00E+14	0.00E+00	4.00E+04	
86	CH2O+HO2=HCO+H2O2	1.00E+12	0.00E+00	8.00E+03	
87	CH2O+CH=CH2CO+H	9.46E+13	0.00E+00	-5.15E+02	
88	CH3+H(+M)=CH4(+M)	1.27E+16	-6.00E-01	3.83E+02	
	Low pressure limit	0.00E+00	2.48E+33	-4.76E+00	
	TROE centering	7.83E-01	7.40E+01	2.94E+03	
	Enhanced by	H2	H2O	CH4	CO
	2.00E+00	6.00E+00	2.00E+00	1.50E+00	2.00E+00
	C2H6	AR			
	3.00E+00	7.00E-01			
89	CH3+O=CH2O+H	8.43E+13	0.00E+00	0.00E+00	
90	CH3+OH(+M)=CH3OH(+M)	6.30E+13	0.00E+00	0.00E+00	
	Low pressure limit	0.00E+00	2.70E+38	-6.30E+00	
	TROE centering	2.11E-01	8.35E+01	5.40E+03	
	Enhanced by	H2	H2O	CH4	CO
	2.00E+00	6.00E+00	2.00E+00	1.50E+00	2.00E+00
	C2H6				
	3.00E+00				
91	CH3+OH=CH2+H2O	5.60E+07	1.60E+00	5.42E+03	
92	CH3+OH=CH2*+H2O	2.50E+13	0.00E+00	0.00E+00	
93	CH3+O2=O+CH3O	3.08E+13	0.00E+00	2.88E+04	
94	CH3+O2=OH+CH2O	3.60E+10	0.00E+00	8.94E+03	
95	CH3+HO2=CH4+O2	1.00E+12	0.00E+00	0.00E+00	
96	CH3+HO2=CH3O+OH	1.34E+13	0.00E+00	0.00E+00	
97	CH3+H2O2=CH4+HO2	2.45E+04	2.50E+00	5.18E+03	
98	CH3+C=C2H2+H	5.00E+13	0.00E+00	0.00E+00	
99	CH3+CH=C2H3+H	3.00E+13	0.00E+00	0.00E+00	

100	CH3+HCO=CH4+CO	8.48E+12	0.00E+00	0.00E+00	
101	CH3+CH2O=CH4+HCO	3.32E+03	2.80E+00	5.86E+03	
102	CH3+CH2=C2H4+H	4.00E+13	0.00E+00	0.00E+00	
103	CH3+CH2*=C2H4+H	1.20E+13	0.00E+00	-5.70E+02	
104	CH3+CH3(+M)=C2H6(+M)	2.12E+16	-1.00E+00	6.20E+02	
	Low pressure limit	0.00E+00	1.77E+50	-9.67E+00	
	TROE centering	5.33E-01	1.51E+02	1.04E+03	
	Enhanced by	H2	H2O	CH4	CO
		2.00E+00	6.00E+00	2.00E+00	1.50E+00
		C2H6	AR		CO2
		3.00E+00	7.00E-01		2.00E+00
105	CH3+CH3=H+C2H5	4.99E+12	1.00E-01	1.06E+04	
106	CH3+HCCO=C2H4+CO	5.00E+13	0.00E+00	0.00E+00	
107	CH3+C2H=C3H3+H	2.41E+13	0.00E+00	0.00E+00	
108	CH3O+H(+M)=CH3OH(+M)	5.00E+13	0.00E+00	0.00E+00	
	Low pressure limit	0.00E+00	8.60E+28	-4.00E+00	
	TROE centering	8.90E-01	1.44E+02	2.84E+03	
	Enhanced by	H2	H2O	CH4	CO
		2.00E+00	6.00E+00	2.00E+00	1.50E+00
		C2H6			CO2
		3.00E+00			2.00E+00
109	CH3O+H=CH2OH+H	3.40E+06	1.60E+00	0.00E+00	
110	CH3O+H=CH2O+H2	2.00E+13	0.00E+00	0.00E+00	
111	CH3O+H=CH3+OH	3.20E+13	0.00E+00	0.00E+00	
112	CH3O+H=CH2*+H2O	1.60E+13	0.00E+00	0.00E+00	
113	CH3O+O=CH2O+OH	1.00E+13	0.00E+00	0.00E+00	
114	CH3O+OH=CH2O+H2O	5.00E+12	0.00E+00	0.00E+00	
115	CH3O+O2=CH2O+HO2	4.28E-13	7.60E+00	-3.53E+03	
116	CH2OH+H(+M)=CH3OH(+M)	1.80E+13	0.00E+00	0.00E+00	
	Low pressure limit	0.00E+00	3.00E+31	-4.80E+00	
	TROE centering	7.68E-01	3.38E+02	1.81E+03	
	Enhanced by	H2	H2O	CH4	CO
		2.00E+00	6.00E+00	2.00E+00	1.50E+00
		C2H6			CO2
		3.00E+00			2.00E+00
117	CH2OH+H=CH2O+H2	2.00E+13	0.00E+00	0.00E+00	
118	CH2OH+H=CH3+OH	1.20E+13	0.00E+00	0.00E+00	
119	CH2OH+H=CH2*+H2O	6.00E+12	0.00E+00	0.00E+00	
120	CH2OH+O=CH2O+OH	1.00E+13	0.00E+00	0.00E+00	
121	CH2OH+OH=CH2O+H2O	5.00E+12	0.00E+00	0.00E+00	
122	CH2OH+O2=CH2O+HO2	1.80E+13	0.00E+00	9.00E+02	
123	CH4+H=CH3+H2	6.60E+08	1.60E+00	1.08E+04	
124	CH4+O=CH3+OH	1.02E+09	1.50E+00	8.60E+03	
125	CH4+OH=CH3+H2O	1.00E+08	1.60E+00	3.12E+03	
126	CH4+CH=C2H4+H	6.00E+13	0.00E+00	0.00E+00	
127	CH4+CH2=CH3+CH3	2.46E+06	2.00E+00	8.27E+03	
128	CH4+CH2*=CH3+CH3	1.60E+13	0.00E+00	-5.70E+02	
129	CH4+C2H=C2H2+CH3	1.81E+12	0.00E+00	5.00E+02	
130	CH3OH+H=CH2OH+H2	1.70E+07	2.10E+00	4.87E+03	
131	CH3OH+H=CH3O+H2	4.20E+06	2.10E+00	4.87E+03	
132	CH3OH+O=CH2OH+OH	3.88E+05	2.50E+00	3.10E+03	
133	CH3OH+O=CH3O+OH	1.30E+05	2.50E+00	5.00E+03	
134	CH3OH+OH=CH2OH+H2O	1.44E+06	2.00E+00	-8.40E+02	
135	CH3OH+OH=CH3O+H2O	6.30E+06	2.00E+00	1.50E+03	
136	CH3OH+CH3=CH2OH+CH4	3.00E+07	1.50E+00	9.94E+03	
137	CH3OH+CH3=CH3O+CH4	1.00E+07	1.50E+00	9.94E+03	
138	C2H+H(+M)=C2H2(+M)	1.00E+17	-1.00E+00	0.00E+00	
	Low pressure limit	0.00E+00	3.75E+33	-4.80E+00	
	TROE centering	6.46E-01	1.32E+02	1.32E+03	
	Enhanced by	H2	H2O	CH4	CO
		2.00E+00	6.00E+00	2.00E+00	1.50E+00
		C2H6	AR		CO2
		3.00E+00	7.00E-01		2.00E+00
139	C2H+O=CH+CO	5.00E+13	0.00E+00	0.00E+00	
140	C2H+OH=H+HCCO	2.00E+13	0.00E+00	0.00E+00	
141	C2H+O2=HCO+CO	5.00E+13	0.00E+00	1.50E+03	
142	C2H+H2=H+C2H2	4.90E+05	2.50E+00	5.60E+02	
143	C2O+H=CH+CO	5.00E+13	0.00E+00	0.00E+00	

144	$C_2O+O=CO+CO$	5.00E+13	0.00E+00	0.00E+00		
145	$C_2O+OH=CO+CO+H$	2.00E+13	0.00E+00	0.00E+00		
146	$C_2O+O_2=CO+CO+O$	2.00E+13	0.00E+00	0.00E+00		
147	$HCCO+H=CH_2^*+CO$	1.00E+14	0.00E+00	0.00E+00		
148	$HCCO+O=H+CO+CO$	1.00E+14	0.00E+00	0.00E+00		
149	$HCCO+O_2=OH+2CO$	1.60E+12	0.00E+00	8.54E+02		
150	$HCCO+CH=C_2H_2+CO$	5.00E+13	0.00E+00	0.00E+00		
151	$HCCO+CH_2=C_2H_3+CO$	3.00E+13	0.00E+00	0.00E+00		
152	$HCCO+HCCO=C_2H_2+CO+CO$	1.00E+13	0.00E+00	0.00E+00		
153	$HCCO+OH=C_2O+H_2O$	3.00E+13	0.00E+00	0.00E+00		
154	$C_2H_2(+M)=H_2CC(+M)$	8.00E+14	-5.00E-01	5.08E+04		
	Low pressure limit	0.00E+00	2.45E+15	-6.40E-01		
	Enhanced by	H2	H2O	CH4	CO	CO2
		2.00E+00	6.00E+00	2.00E+00	1.50E+00	2.00E+00
		C2H6	C2H4			
		3.00E+00	2.50E+00			
155	$C_2H_3(+M)=C_2H_2+H(+M)$		3.86E+08	1.60E+00	3.70E+04	
	Low pressure limit		0.00E+00	2.57E+27	-3.40E+00	
	TROE centering		1.98E+00	5.38E+03	4.29E+00	
	Enhanced by	H2	H2O	CH4	CO	CO2
		2.00E+00	6.00E+00	2.00E+00	1.50E+00	2.00E+00
		C2H6	AR	C2H2	C2H4	
		3.00E+00	7.00E-01	3.00E+00	3.00E+00	
156	$C_2H_2+O=C_2H+OH$	4.60E+19	-1.40E+00	2.90E+04		
157	$C_2H_2+O=CH_2+CO$	4.08E+06	2.00E+00	1.90E+03		
158	$C_2H_2+O=HCCO+H$	1.63E+07	2.00E+00	1.90E+03		
159	$C_2H_2+OH=CH_2CO+H$	2.18E-04	4.50E+00	-1.00E+03		
160	$C_2H_2+OH=HCCOH+H$	5.04E+05	2.30E+00	1.35E+04		
161	$C_2H_2+OH=C_2H+H_2O$	3.37E+07	2.00E+00	1.40E+04		
162	$C_2H_2+OH=CH_3+CO$	4.83E-04	4.00E+00	-2.00E+03		
163	$C_2H_2+HCO=C_2H_3+CO$	1.00E+07	2.00E+00	6.00E+03		
164	$C_2H_2+CH_2=C_3H_3+H$	1.20E+13	0.00E+00	6.62E+03		
165	$C_2H_2+CH_2^*=C_3H_3+H$	2.00E+13	0.00E+00	0.00E+00		
166	$C_2H_2+C_2H=C_4H_2+H$	9.60E+13	0.00E+00	0.00E+00		
167	$C_2H_2+C_2H(+M)=nC_4H_3(+M)$	8.30E+10	9.00E-01	-3.63E+02		
	Low pressure limit	0.00E+00	1.24E+31	-4.72E+00		
	TROE centering	1.00E+00	1.00E+02	5.61E+03		
	Enhanced by	H2	H2O	CH4	CO	CO2
		2.00E+00	6.00E+00	2.00E+00	1.50E+00	2.00E+00
		C2H6	C2H2	C2H4		
		3.00E+00	2.50E+00	2.50E+00		
168	$C_2H_2+C_2H(+M)=iC_4H_3(+M)$		8.30E+10	9.00E-01	-3.63E+02	
	Low pressure limit		0.00E+00	1.24E+31	-4.72E+00	
	TROE centering		1.00E+00	1.00E+02	5.61E+03	
	Enhanced by	H2	H2O	CH4	CO	CO2
		2.00E+00	6.00E+00	2.00E+00	1.50E+00	2.00E+00
		C2H6	C2H2	C2H4		
		3.00E+00	2.50E+00	2.50E+00		
169	$C_2H_2+HCCO=C_3H_3+CO$	1.00E+11	0.00E+00	3.00E+03		
170	$C_2H_2+CH_3=pC_3H_4+H$	2.56E+09	1.10E+00	1.36E+04		
171	$C_2H_2+CH_3=aC_3H_4+H$	5.14E+09	9.00E-01	2.22E+04		
172	$C_2H_2+CH_3=CH_3CCH_2$	4.99E+22	-4.40E+00	1.89E+04		
173	$C_2H_2+CH_3=CH_3CHCH$	3.20E+35	-7.80E+00	1.33E+04		
174	$C_2H_2+CH_3=aC_3H_5$	2.68E+53	-1.28E+01	3.57E+04		
175	$H_2CC+H=C_2H_2+H$	1.00E+14	0.00E+00	0.00E+00		
176	$H_2CC+OH=CH_2CO+H$	2.00E+13	0.00E+00	0.00E+00		
177	$H_2CC+O_2=HCO+HCO$	1.00E+13	0.00E+00	0.00E+00		
178	$H_2CC+C_2H_2(+M)=C_4H_4(+M)$	3.50E+05	2.10E+00	-2.40E+03		
	Low pressure limit	0.00E+00	1.40E+60	-1.26E+01		
	TROE centering		9.80E-01	5.60E+01	5.80E+02	
	Enhanced by	H2	H2O	CH4	CO	CO2
		2.00E+00	6.00E+00	2.00E+00	1.50E+00	2.00E+00
		C2H6	C2H2	C2H4		
		3.00E+00	3.00E+00	3.00E+00		
179	$H_2CC+C_2H_4=C_4H_6$	1.00E+12	0.00E+00	0.00E+00		
180	$CH_2CO+H(+M)=CH_2CHO(+M)$	3.30E+14	-1.00E-01	8.50E+03		
	Low pressure limit	0.00E+00	3.80E+41	-7.64E+00		
	TROE centering		3.37E-01	1.71E+03	3.20E+03	

Enhanced by	H2	H2O	CH4	CO	CO2
	2.00E+00	6.00E+00	2.00E+00	1.50E+00	2.00E+00
	C2H6	AR	C2H2	C2H4	
	3.00E+00	7.00E-01	3.00E+00	3.00E+00	
181 CH2CO+H=HCCO+H2		5.00E+13	0.00E+00	8.00E+03	
182 CH2CO+H=CH3+CO		1.50E+09	1.40E+00	2.69E+03	
183 CH2CO+O=HCCO+OH		1.00E+13	0.00E+00	8.00E+03	
184 CH2CO+O=CH2+CO2		1.75E+12	0.00E+00	1.35E+03	
185 CH2CO+OH=HCCO+H2O		7.50E+12	0.00E+00	2.00E+03	
186 HCCOH+H=CH2CO+H		1.00E+13	0.00E+00	0.00E+00	
187 C2H3+H(+M)=C2H4(+M)		6.08E+12	3.00E-01	2.80E+02	
Low pressure limit		0.00E+00	1.40E+30	-3.86E+00	
TROE centering		7.82E-01	2.08E+02	2.66E+03	
Enhanced by	H2	H2O	CH4	CO	CO2
	2.00E+00	6.00E+00	2.00E+00	1.50E+00	2.00E+00
	C2H6	AR	C2H2	C2H4	
	3.00E+00	7.00E-01	3.00E+00	3.00E+00	
188 C2H3+H=C2H2+H2		9.00E+13	0.00E+00	0.00E+00	
189 C2H3+H=H2CC+H2		6.00E+13	0.00E+00	0.00E+00	
190 C2H3+O=CH2CO+H		4.80E+13	0.00E+00	0.00E+00	
191 C2H3+O=CH3+CO		4.80E+13	0.00E+00	0.00E+00	
192 C2H3+OH=C2H2+H2O		3.01E+13	0.00E+00	0.00E+00	
193 C2H3+O2=C2H2+HO2		1.34E+06	1.60E+00	-3.83E+02	
194 C2H3+O2=CH2CHO+O		3.00E+11	3.00E-01	1.10E+01	
195 C2H3+O2=HCO+CH2O		4.60E+16	-1.40E+00	1.01E+03	
196 C2H3+HO2=CH2CHO+OH		1.00E+13	0.00E+00	0.00E+00	
197 C2H3+H2O2=C2H4+HO2		1.21E+10	0.00E+00	-5.96E+02	
198 C2H3+HCO=C2H4+CO		9.03E+13	0.00E+00	0.00E+00	
199 C2H3+HCO=C2H3CHO		1.80E+13	0.00E+00	0.00E+00	
200 C2H3+CH3=C2H2+CH4		3.92E+11	0.00E+00	0.00E+00	
201 C2H3+CH3(+M)=C3H6(+M)		2.50E+13	0.00E+00	0.00E+00	
Low pressure limit		0.00E+00	4.27E+58	-1.19E+01	
TROE centering		1.75E-01	1.34E+03	6.00E+04	
Enhanced by	H2	H2O	CH4	CO	CO2
	2.00E+00	6.00E+00	2.00E+00	1.50E+00	2.00E+00
	C2H6	AR	C2H2	C2H4	
	3.00E+00	7.00E-01	3.00E+00		
202 C2H3+CH3=aC3H5+H		1.50E+24	-2.80E+00	1.86E+04	
203 C2H3+C2H2=C4H4+H		2.00E+18	-1.70E+00	1.06E+04	
204 C2H3+C2H2=nC4H5		9.30E+38	-8.80E+00	1.20E+04	
205 C2H3+C2H2=iC4H5		1.60E+46	-1.10E+01	1.86E+04	
206 C2H3+C2H3=C4H6		1.50E+42	-8.80E+00	1.25E+04	
207 C2H3+C2H3=iC4H5+H		1.20E+22	-2.40E+00	1.37E+04	
208 C2H3+C2H3=nC4H5+H		2.40E+20	-2.00E+00	1.54E+04	
209 C2H3+C2H3=C2H2+C2H4		9.60E+11	0.00E+00	0.00E+00	
210 CH2CHO=CH3+CO		7.80E+41	-9.10E+00	4.69E+04	
211 CH2CHO+H(+M)=CH3CHO(+M)		1.00E+14	0.00E+00	0.00E+00	
Low pressure limit		0.00E+00	5.20E+39	-7.30E+00	
TROE centering		5.50E-01	8.90E+03	4.35E+03	
Enhanced by	H2	H2O	CH4	CO	CO2
	2.00E+00	6.00E+00	2.00E+00	1.50E+00	2.00E+00
	C2H6	C2H2	C2H4		
	3.00E+00	3.00E+00	3.00E+00		
212 CH2CHO+H=CH3CO+H		5.00E+12	0.00E+00	0.00E+00	
213 CH2CHO+H=CH3+HCO		9.00E+13	0.00E+00	0.00E+00	
214 CH2CHO+H=CH2CO+H2		2.00E+13	0.00E+00	4.00E+03	
215 CH2CHO+O=CH2CO+OH		2.00E+13	0.00E+00	4.00E+03	
216 CH2CHO+OH=CH2CO+H2O		1.00E+13	0.00E+00	2.00E+03	
217 CH2CHO+O2=CH2CO+HO2		1.40E+11	0.00E+00	0.00E+00	
218 CH2CHO+O2=CH2O+CO+OH		1.80E+10	0.00E+00	0.00E+00	
219 CH3+CO(+M)=CH3CO(+M)		4.85E+07	1.60E+00	6.15E+03	
Low pressure limit		0.00E+00	7.80E+30	-5.40E+00	
TROE centering		2.58E-01	5.98E+02	2.10E+04	
Enhanced by	H2	H2O	CH4	CO	CO2
	2.00E+00	6.00E+00	2.00E+00	1.50E+00	2.00E+00
	C2H6	AR	C2H2	C2H4	
	3.00E+00	7.00E-01	3.00E+00	3.00E+00	
220 CH3CO+H(+M)=CH3CHO(+M)		9.60E+13	0.00E+00	0.00E+00	



Low pressure limit	0.00E+00	3.85E+44	-8.57E+00	
TROE centering	1.00E+00	2.90E+03	2.90E+03	
Enhanced by	H2	H2O	CH4	CO
	2.00E+00	6.00E+00	2.00E+00	1.50E+00
	C2H6	C2H2	C2H4	CO2
	3.00E+00	3.00E+00	3.00E+00	2.00E+00
221 CH3CO+H=CH3+HCO		9.60E+13	0.00E+00	0.00E+00
222 CH3CO+O=CH2CO+OH		3.90E+13	0.00E+00	0.00E+00
223 CH3CO+O=CH3+CO2		1.50E+14	0.00E+00	0.00E+00
224 CH3CO+OH=CH2CO+H2O		1.20E+13	0.00E+00	0.00E+00
225 CH3CO+OH=CH3+CO+OH		3.00E+13	0.00E+00	0.00E+00
226 CH3CO+HO2=CH3+CO2+OH		3.00E+13	0.00E+00	0.00E+00
227 CH3CO+H2O2=CH3CHO+HO2		1.80E+11	0.00E+00	8.23E+03
228 CH3+HCO(+M)=CH3CHO(+M)		1.80E+13	0.00E+00	0.00E+00
Low pressure limit		0.00E+00	2.20E+48	-9.59E+00
TROE centering		6.17E-01	1.31E+01	2.08E+03
Enhanced by	H2	H2O	CH4	CO
	2.00E+00	6.00E+00	2.00E+00	1.50E+00
	C2H6	C2H2	C2H4	CO2
	3.00E+00	3.00E+00	3.00E+00	2.00E+00
229 CH3CHO+H=CH3CO+H2		4.10E+09	1.20E+00	2.40E+03
230 CH3CHO+H=CH4+HCO		5.00E+10	0.00E+00	0.00E+00
231 CH3CHO+O=CH3CO+OH		5.80E+12	0.00E+00	1.80E+03
232 CH3CHO+OH=CH3CO+H2O		2.35E+10	7.00E-01	-1.11E+03
233 CH3CHO+CH3=CH3CO+CH4		2.00E-06	5.60E+00	2.46E+03
234 CH3CHO+HCO=CO+HCO+CH4		8.00E+12	0.00E+00	1.04E+04
235 CH3CHO+O2=CH3CO+HO2		3.00E+13	0.00E+00	3.91E+04
236 CH2OCH2=CH3+HCO		3.63E+13	0.00E+00	5.72E+04
237 CH2OCH2=CH3CHO		7.26E+13	0.00E+00	5.72E+04
238 CH2OCH2=CH4+CO		1.21E+13	0.00E+00	5.72E+04
239 CH2OCH2+H=CH2OCH+H2		2.00E+13	0.00E+00	8.30E+03
240 CH2OCH2+H=C2H3+H2O		5.00E+09	0.00E+00	5.00E+03
241 CH2OCH2+H=C2H4+OH		9.51E+10	0.00E+00	5.00E+03
242 CH2OCH2+O=CH2OCH+OH		1.91E+12	0.00E+00	5.25E+03
243 CH2OCH2+OH=CH2OCH+H2O		1.78E+13	0.00E+00	3.61E+03
244 CH2OCH2+CH3=CH2OCH+CH4		1.07E+12	0.00E+00	1.18E+04
245 CH2OCH+M=CH3+CO+M		3.16E+14	0.00E+00	1.20E+04
246 CH2OCH+M=CH2CHO+M		5.00E+09	0.00E+00	0.00E+00
247 CH2OCH+M=CH2CO+H+M		3.00E+13	0.00E+00	8.00E+03
248 C2H4(+M)=H2+H2CC(+M)		8.00E+12	4.00E-01	8.88E+04
Low pressure limit		0.00E+00	7.00E+50	-9.31E+00
TROE centering		7.35E-01	1.80E+02	1.04E+03
Enhanced by	H2	H2O	CH4	CO
	2.00E+00	6.00E+00	2.00E+00	1.50E+00
	C2H6	AR	CO	CO2
	3.00E+00	7.00E-01	2.00E+00	2.00E+00
249 C2H4+H(+M)=C2H5(+M)		1.37E+09	1.50E+00	1.36E+03
Low pressure limit		0.00E+00	2.03E+39	-6.64E+00
TROE centering		-5.69E-01	2.99E+02	9.15E+03
Enhanced by	H2	H2O	CH4	CO
	2.00E+00	6.00E+00	2.00E+00	1.50E+00
	C2H6	AR	CO	CO2
	3.00E+00	7.00E-01	2.00E+00	2.00E+00
250 C2H4+H=C2H3+H2		5.07E+07	1.90E+00	1.30E+04
251 C2H4+O=C2H3+OH		1.51E+07	1.90E+00	3.74E+03
252 C2H4+O=CH3+HCO		1.92E+07	1.80E+00	2.20E+02
253 C2H4+O=CH2+CH2O		3.84E+05	1.80E+00	2.20E+02
254 C2H4+OH=C2H3+H2O		3.60E+06	2.00E+00	2.50E+03
255 C2H4+HCO=C2H5+CO		1.00E+07	2.00E+00	8.00E+03
256 C2H4+CH=aC3H4+H		3.00E+13	0.00E+00	0.00E+00
257 C2H4+CH=pC3H4+H		3.00E+13	0.00E+00	0.00E+00
258 C2H4+CH2=aC3H5+H		2.00E+13	0.00E+00	6.00E+03
259 C2H4+CH2*=H2CC+CH4		5.00E+13	0.00E+00	0.00E+00
260 C2H4+CH2*=aC3H5+H		5.00E+13	0.00E+00	0.00E+00
261 C2H4+CH3=C2H3+CH4		2.27E+05	2.00E+00	9.20E+03
262 C2H4+CH3=nC3H7		3.30E+11	0.00E+00	7.70E+03
263 C2H4+C2H=C4H4+H		1.20E+13	0.00E+00	0.00E+00
264 C2H4+O2=C2H3+HO2		4.22E+13	0.00E+00	6.08E+04

265	$C_2H_4 + C_2H_3 = C_4H_7$	7.93E+38	-8.50E+00	1.42E+04	
266	$C_2H_4 + HO_2 = CH_2OCH_2 + OH$	2.82E+12	0.00E+00	1.71E+04	
267	$C_2H_5 + H(+M) = C_2H_6(+M)$	5.21E+17	-1.00E+00	1.58E+03	
	Low pressure limit	0.00E+00	1.99E+41	-7.08E+00	
	TROE centering	8.42E-01	1.25E+02	2.22E+03	
	Enhanced by	H2	H2O	CH4	CO
		2.00E+00	6.00E+00	2.00E+00	1.50E+00
		C2H6	AR		CO2
		3.00E+00	7.00E-01		2.00E+00
268	$C_2H_5 + H = C_2H_4 + H_2$	2.00E+12	0.00E+00	0.00E+00	
269	$C_2H_5 + O = CH_3 + CH_2O$	1.60E+13	0.00E+00	0.00E+00	
270	$C_2H_5 + O = CH_3CHO + H$	8.02E+13	0.00E+00	0.00E+00	
271	$C_2H_5 + O_2 = C_2H_4 + HO_2$	2.00E+10	0.00E+00	0.00E+00	
272	$C_2H_5 + HO_2 = C_2H_6 + O_2$	3.00E+11	0.00E+00	0.00E+00	
273	$C_2H_5 + HO_2 = C_2H_4 + H_2O_2$	3.00E+11	0.00E+00	0.00E+00	
274	$C_2H_5 + HO_2 = CH_3 + CH_2O + OH$	2.40E+13	0.00E+00	0.00E+00	
275	$C_2H_5 + H_2O_2 = C_2H_6 + HO_2$	8.70E+09	0.00E+00	9.74E+02	
276	$C_2H_5 + CH_3(+M) = C_3H_8(+M)$	4.90E+14	-5.00E-01	0.00E+00	
	Low pressure limit	0.00E+00	6.80E+61	-1.34E+01	
	TROE centering	1.00E+00	1.00E+03	1.43E+03	
	Enhanced by	H2	H2O	CH4	CO
		2.00E+00	6.00E+00	2.00E+00	1.50E+00
		C2H6	AR		CO2
		3.00E+00	7.00E-01		2.00E+00
277	$C_2H_5 + C_2H_3(+M) = C_4H_8(+M)$	1.50E+13	0.00E+00	0.00E+00	
	Low pressure limit	0.00E+00	1.55E+56	-1.18E+01	
	TROE centering	1.98E-01	2.28E+03	6.00E+04	
	Enhanced by	H2	H2O	CH4	CO
		2.00E+00	6.00E+00	2.00E+00	1.50E+00
		C2H6	AR		CO2
		3.00E+00	7.00E-01		2.00E+00
278	$C_2H_5 + C_2H_3 = aC_3H_5 + CH_3$	3.90E+32	-5.20E+00	1.97E+04	
279	$C_2H_6 + H = C_2H_5 + H_2$	1.15E+08	1.90E+00	7.53E+03	
280	$C_2H_6 + O = C_2H_5 + OH$	8.98E+07	1.90E+00	5.69E+03	
281	$C_2H_6 + OH = C_2H_5 + H_2O$	3.54E+06	2.10E+00	8.70E+02	
282	$C_2H_6 + CH_2^* = C_2H_5 + CH_3$	4.00E+13	0.00E+00	-5.50E+02	
283	$C_2H_6 + CH_3 = C_2H_5 + CH_4$	6.14E+06	1.70E+00	1.05E+04	
284	$C_3H_3 + H = pC_3H_4$	1.50E+13	0.00E+00	0.00E+00	
285	$C_3H_3 + H = aC_3H_4$	2.50E+12	0.00E+00	0.00E+00	
286	$C_3H_3 + O = CH_2O + C_2H$	2.00E+13	0.00E+00	0.00E+00	
287	$C_3H_3 + O_2 = CH_2CO + HCO$	3.00E+10	0.00E+00	2.87E+03	
288	$C_3H_3 + HO_2 = OH + CO + C_2H_3$	8.00E+11	0.00E+00	0.00E+00	
289	$C_3H_3 + HO_2 = aC_3H_4 + O_2$	3.00E+11	0.00E+00	0.00E+00	
290	$C_3H_3 + HO_2 = pC_3H_4 + O_2$	2.50E+12	0.00E+00	0.00E+00	
291	$C_3H_3 + HCO = aC_3H_4 + CO$	2.50E+13	0.00E+00	0.00E+00	
292	$C_3H_3 + HCO = pC_3H_4 + CO$	2.50E+13	0.00E+00	0.00E+00	
293	$C_3H_3 + HCCO = C_4H_4 + CO$	2.50E+13	0.00E+00	0.00E+00	
294	$C_3H_3 + CH = iC_4H_3 + H$	5.00E+13	0.00E+00	0.00E+00	
295	$C_3H_3 + CH_2 = C_4H_4 + H$	5.00E+13	0.00E+00	0.00E+00	
296	$C_3H_3 + CH_3(+M) = C_4H_6(+M)$	1.50E+12	0.00E+00	0.00E+00	
	Low pressure limit	0.00E+00	2.60E+57	-1.19E+01	
	TROE centering	1.75E-01	1.34E+03	6.00E+04	
	Enhanced by	H2	H2O	CH4	CO
		2.00E+00	6.00E+00	2.00E+00	1.50E+00
		C2H6	AR		CO2
		3.00E+00	7.00E-01		2.00E+00
297	$C_3H_3 + C_2H_2 = C_5H_5$	6.87E+55	-1.25E+01	4.20E+04	
298	$C_3H_3 + C_3H_3 = >C_6H_5 + H$	5.00E+12	0.00E+00	0.00E+00	
299	$C_3H_3 + C_3H_3 = >C_6H_6$	2.00E+12	0.00E+00	0.00E+00	
300	$C_3H_3 + C_4H_4 = C_6H_5CH_2$	6.53E+05	1.30E+00	-4.61E+03	
301	$C_3H_3 + C_4H_6 = C_6H_5CH_3 + H$	6.53E+05	1.30E+00	-4.61E+03	
302	$aC_3H_4 + H = C_3H_3 + H_2$	1.30E+06	2.00E+00	5.50E+03	
303	$aC_3H_4 + H = CH_3CHCH$	5.40E+29	-6.10E+00	1.63E+04	
304	$aC_3H_4 + H = CH_3CCH_2$	9.46E+42	-9.40E+00	1.12E+04	
305	$aC_3H_4 + H = aC_3H_5$	1.52E+59	-1.35E+01	2.69E+04	
306	$aC_3H_4 + O = C_2H_4 + CO$	2.00E+07	1.80E+00	1.00E+03	
307	$aC_3H_4 + OH = C_3H_3 + H_2O$	5.30E+06	2.00E+00	2.00E+03	
308	$aC_3H_4 + CH_3 = C_3H_3 + CH_4$	1.30E+12	0.00E+00	7.70E+03	

309	aC3H4+CH3=iC4H7	2.00E+11	0.00E+00	7.50E+03				
310	aC3H4+C2H=C2H2+C3H3	1.00E+13	0.00E+00	0.00E+00				
311	pC3H4=cC3H4	1.20E+44	-9.90E+00	6.93E+04				
312	pC3H4=aC3H4	5.15E+60	-1.39E+01	9.11E+04				
313	pC3H4+H=aC3H4+H	6.27E+17	-9.00E-01	1.01E+04				
314	pC3H4+H=CH3CCH2	1.66E+47	-1.06E+01	1.37E+04				
315	pC3H4+H=CH3CHCH	5.50E+28	-5.70E+00	4.30E+03				
316	pC3H4+H=aC3H5	4.91E+60	-1.44E+01	3.16E+04				
317	pC3H4+H=C3H3+H2	1.30E+06	2.00E+00	5.50E+03				
318	pC3H4+C3H3=aC3H4+C3H3	6.14E+06	1.70E+00	1.05E+04				
319	pC3H4+O=HCCO+CH3	7.30E+12	0.00E+00	2.25E+03				
320	pC3H4+O=C2H4+CO	1.00E+13	0.00E+00	2.25E+03				
321	pC3H4+OH=C3H3+H2O	1.00E+06	2.00E+00	1.00E+02				
322	pC3H4+C2H=C2H2+C3H3	1.00E+13	0.00E+00	0.00E+00				
323	pC3H4+CH3=C3H3+CH4	1.80E+12	0.00E+00	7.70E+03				
324	cC3H4=aC3H4	4.89E+41	-9.20E+00	4.96E+04				
325	aC3H5+H(+M)=C3H6(+M)	2.00E+14	0.00E+00	0.00E+00				
	Low pressure limit	0.00E+00	1.33E+60	-1.20E+01				
	TROE centering	2.00E-02	1.10E+03	1.10E+03				
	Enhanced by	H2	H2O	CH4	CO	CO2		
		2.00E+00	6.00E+00	2.00E+00	1.50E+00	2.00E+00		
		C2H6	AR					
		3.00E+00	7.00E-01					
326	aC3H5+H=aC3H4+H2	1.80E+13	0.00E+00	0.00E+00				
327	aC3H5+O=C2H3CHO+H	6.00E+13	0.00E+00	0.00E+00				
328	aC3H5+OH=C2H3CHO+H+H	4.20E+32	-5.20E+00	3.01E+04				
329	aC3H5+OH=aC3H4+H2O	6.00E+12	0.00E+00	0.00E+00				
330	aC3H5+O2=aC3H4+HO2	4.99E+15	-1.40E+00	2.24E+04				
331	aC3H5+O2=CH3CO+CH2O	1.19E+15	-1.00E+00	2.01E+04				
332	aC3H5+O2=C2H3CHO+OH	1.82E+13	-4.00E-01	2.29E+04				
333	aC3H5+HO2=C3H6+O2	2.66E+12	0.00E+00	0.00E+00				
334	aC3H5+HO2=OH+C2H3+CH2O	6.60E+12	0.00E+00	0.00E+00				
335	aC3H5+HCO=C3H6+CO	6.00E+13	0.00E+00	0.00E+00				
336	aC3H5+CH3(+M)=C4H8(+M)	1.00E+14	-3.00E-01	-2.62E+02				
	Low pressure limit	0.00E+00	3.91E+60	-1.28E+01				
	TROE centering	1.04E-01	1.61E+03	6.00E+04				
	Enhanced by	H2	H2O	CH4	CO	CO2		
		2.00E+00	6.00E+00	2.00E+00	1.50E+00	2.00E+00		
		C2H6	AR					
		3.00E+00	7.00E-01					
337	aC3H5+CH3=aC3H4+CH4	3.00E+12	-3.00E-01	-1.31E+02				
338	aC3H5=CH3CCH2	7.06E+56	-1.41E+01	7.59E+04				
339	aC3H5=CH3CHCH	5.00E+51	-1.30E+01	7.33E+04				
340	aC3H5+C2H2=IC5H7	8.38E+30	-6.20E+00	1.28E+04				
341	CH3CCH2=CH3CHCH	1.50E+48	-1.27E+01	5.39E+04				
342	CH3CCH2+H=pC3H4+H2	3.34E+12	0.00E+00	0.00E+00				
343	CH3CCH2+O=CH3+CH2CO	6.00E+13	0.00E+00	0.00E+00				
344	CH3CCH2+OH=CH3+CH2CO+H	5.00E+12	0.00E+00	0.00E+00				
345	CH3CCH2+O2=CH3CO+CH2O	1.00E+11	0.00E+00	0.00E+00				
346	CH3CCH2+HO2=CH3+CH2CO+OH	2.00E+13	0.00E+00	0.00E+00				
347	CH3CCH2+HCO=C3H6+CO	9.00E+13	0.00E+00	0.00E+00				
348	CH3CCH2+CH3=pC3H4+CH4	1.00E+11	0.00E+00	0.00E+00				
349	CH3CCH2+CH3=iC4H8	2.00E+13	0.00E+00	0.00E+00				
350	CH3CHCH+H=pC3H4+H2	3.34E+12	0.00E+00	0.00E+00				
351	CH3CHCH+O=C2H4+HCO	6.00E+13	0.00E+00	0.00E+00				
352	CH3CHCH+OH=C2H4+HCO+H	5.00E+12	0.00E+00	0.00E+00				
353	CH3CHCH+O2=CH3CHO+HCO	1.00E+11	0.00E+00	0.00E+00				
354	CH3CHCH+HO2=C2H4+HCO+OH	2.00E+13	0.00E+00	0.00E+00				
355	CH3CHCH+HCO=C3H6+CO	9.00E+13	0.00E+00	0.00E+00				
356	CH3CHCH+CH3=pC3H4+CH4	1.00E+11	0.00E+00	0.00E+00				
357	C3H6+H(+M)=nC3H7(+M)	1.33E+13	0.00E+00	3.26E+03				
	Low pressure limit	0.00E+00	6.26E+38	-6.66E+00				
	TROE centering	1.00E+00	1.00E+03	1.31E+03				
	Enhanced by	H2	H2O	CH4	CO	CO2		
		2.00E+00	6.00E+00	2.00E+00	1.50E+00	2.00E+00		
		C2H6	AR					
		3.00E+00	7.00E-01					
358	C3H6+H(+M)=iC3H7(+M)	1.33E+13	0.00E+00	1.56E+03				

Low pressure limit		0.00E+00	8.70E+42	-7.50E+00	
TROE centering		1.00E+00	1.00E+03	6.45E+02	
Enhanced by	H2	H2O	CH4	CO	CO2
	2.00E+00	6.00E+00	2.00E+00	1.50E+00	2.00E+00
	C2H6	AR			
	3.00E+00	7.00E-01			
359 C3H6+H=C2H4+CH3		8.00E+21	-2.40E+00	1.12E+04	
360 C3H6+H=aC3H5+H2		1.73E+05	2.50E+00	2.49E+03	
361 C3H6+H=CH3CCH2+H2		4.00E+05	2.50E+00	9.79E+03	
362 C3H6+H=CH3CHCH+H2		8.04E+05	2.50E+00	1.23E+04	
363 C3H6+O=CH2CO+CH3+H		8.00E+07	1.60E+00	3.27E+02	
364 C3H6+O=C2H3CHO+H+H		4.00E+07	1.60E+00	3.27E+02	
365 C3H6+O=C2H5+HCO		3.50E+07	1.60E+00	-9.72E+02	
366 C3H6+O=aC3H5+OH		1.80E+11	7.00E-01	5.88E+03	
367 C3H6+O=CH3CCH2+OH		6.00E+10	7.00E-01	7.63E+03	
368 C3H6+O=CH3CHCH+OH		1.21E+11	7.00E-01	8.96E+03	
369 C3H6+OH=aC3H5+H2O		3.10E+06	2.00E+00	-2.98E+02	
370 C3H6+OH=CH3CCH2+H2O		1.10E+06	2.00E+00	1.45E+03	
371 C3H6+OH=CH3CHCH+H2O		2.14E+06	2.00E+00	2.78E+03	
372 C3H6+HO2=aC3H5+H2O2		9.60E+03	2.60E+00	1.39E+04	
373 C3H6+CH3=aC3H5+CH4		2.20E+00	3.50E+00	5.68E+03	
374 C3H6+CH3=CH3CCH2+CH4		8.40E-01	3.50E+00	1.17E+04	
375 C3H6+CH3=CH3CHCH+CH4		1.35E+00	3.50E+00	1.28E+04	
376 C3H6+C2H3=C4H6+CH3		7.23E+11	0.00E+00	5.00E+03	
377 C3H6+HO2=CH3CHOCH2+OH		1.09E+12	0.00E+00	1.42E+04	
378 C2H3CHO+H=C2H4+HCO		1.08E+11	5.00E-01	5.82E+03	
379 C2H3CHO+O=C2H3+OH+CO		3.00E+13	0.00E+00	3.54E+03	
380 C2H3CHO+O=CH2O+CH2CO		1.90E+07	1.80E+00	2.20E+02	
381 C2H3CHO+OH=C2H3+H2O+CO		3.43E+09	1.20E+00	-4.47E+02	
382 C2H3CHO+CH3=CH2CHCO+CH4		2.00E+13	0.00E+00	1.10E+04	
383 C2H3CHO+C2H3=C4H6+HCO		2.80E+21	-2.40E+00	1.47E+04	
384 CH2CHCO=C2H3+CO		1.00E+14	0.00E+00	2.70E+04	
385 CH2CHCO+H=C2H3CHO		1.00E+14	0.00E+00	0.00E+00	
386 CH3CHOCH2=CH3CH2CHO		1.84E+14	0.00E+00	5.85E+04	
387 CH3CHOCH2=C2H5+HCO		2.45E+13	0.00E+00	5.85E+04	
388 CH3CHOCH2=CH3+CH2CHO		2.45E+13	0.00E+00	5.88E+04	
389 CH3CHOCH2=CH3COCH3		1.01E+14	0.00E+00	5.99E+04	
390 CH3CHOCH2=CH3+CH3CO		4.54E+13	0.00E+00	5.99E+04	
391 iC3H7+H(+M)=C3H8(+M)		2.40E+13	0.00E+00	0.00E+00	
Low pressure limit		0.00E+00	1.70E+58	-1.21E+01	
TROE centering		6.49E-01	1.21E+03	1.21E+03	
Enhanced by	H2	H2O	CH4	CO	CO2
	2.00E+00	6.00E+00	2.00E+00	1.50E+00	2.00E+00
	C2H6	AR			
	3.00E+00	7.00E-01			
392 iC3H7+H=CH3+C2H5		1.40E+28	-3.90E+00	1.59E+04	
393 iC3H7+H=C3H6+H2		3.20E+12	0.00E+00	0.00E+00	
394 iC3H7+O=CH3CHO+CH3		9.60E+13	0.00E+00	0.00E+00	
395 iC3H7+OH=C3H6+H2O		2.40E+13	0.00E+00	0.00E+00	
396 iC3H7+O2=C3H6+HO2		1.30E+11	0.00E+00	0.00E+00	
397 iC3H7+HO2=CH3CHO+CH3+OH		2.40E+13	0.00E+00	0.00E+00	
398 iC3H7+HCO=C3H8+CO		1.20E+14	0.00E+00	0.00E+00	
399 iC3H7+CH3=CH4+C3H6		2.20E+14	-7.00E-01	0.00E+00	
400 nC3H7+H(+M)=C3H8(+M)		3.60E+13	0.00E+00	0.00E+00	
Low pressure limit		0.00E+00	3.01E+48	-9.32E+00	
TROE centering		4.98E-01	1.31E+03	1.31E+03	
Enhanced by	H2	H2O	CH4	CO	CO2
	2.00E+00	6.00E+00	2.00E+00	1.50E+00	2.00E+00
	C2H6	AR			
	3.00E+00	7.00E-01			
401 nC3H7+H=C2H5+CH3		3.70E+24	-2.90E+00	1.25E+04	
402 nC3H7+H=C3H6+H2		1.80E+12	0.00E+00	0.00E+00	
403 nC3H7+O=C2H5+CH2O		9.60E+13	0.00E+00	0.00E+00	
404 nC3H7+OH=C3H6+H2O		2.40E+13	0.00E+00	0.00E+00	
405 nC3H7+O2=C3H6+HO2		9.00E+10	0.00E+00	0.00E+00	
406 nC3H7+HO2=C2H5+OH+CH2O		2.40E+13	0.00E+00	0.00E+00	
407 nC3H7+HCO=C3H8+CO		6.00E+13	0.00E+00	0.00E+00	
408 nC3H7+CH3=CH4+C3H6		1.10E+13	0.00E+00	0.00E+00	

409	C3H8+H=H2+nC3H7	1.30E+06	2.50E+00	6.76E+03
410	C3H8+H=H2+iC3H7	1.30E+06	2.40E+00	4.47E+03
411	C3H8+O=nC3H7+OH	1.90E+05	2.70E+00	3.72E+03
412	C3H8+O=iC3H7+OH	4.76E+04	2.70E+00	2.11E+03
413	C3H8+OH=nC3H7+H2O	1.40E+03	2.70E+00	5.27E+02
414	C3H8+OH=iC3H7+H2O	2.70E+04	2.40E+00	3.93E+02
415	C3H8+O2=nC3H7+HO2	4.00E+13	0.00E+00	5.09E+04
416	C3H8+O2=iC3H7+HO2	4.00E+13	0.00E+00	4.76E+04
417	C3H8+HO2=nC3H7+H2O2	4.76E+04	2.50E+00	1.65E+04
418	C3H8+HO2=iC3H7+H2O2	9.64E+03	2.60E+00	1.39E+04
419	C3H8+CH3=CH4+nC3H7	9.03E-01	3.60E+00	7.15E+03
420	C3H8+CH3=CH4+iC3H7	1.51E+00	3.50E+00	5.48E+03
421	C4H2+H=nC4H3	1.10E+42	-8.70E+00	1.53E+04
422	C4H2+H=iC4H3	1.10E+30	-4.90E+00	1.08E+04
423	C4H2+OH=H2C4O+H	6.60E+12	0.00E+00	-4.10E+02
424	C4H2+C2H=C6H2+H	9.60E+13	0.00E+00	0.00E+00
425	C4H2+C2H=C6H3	4.50E+37	-7.70E+00	7.10E+03
426	H2C4O+H=C2H2+HCCO	5.00E+13	0.00E+00	3.00E+03
427	H2C4O+OH=CH2CO+HCCO	1.00E+07	2.00E+00	2.00E+03
428	nC4H3=iC4H3	4.10E+43	-9.50E+00	5.30E+04
429	nC4H3+H=iC4H3+H	2.50E+20	-1.70E+00	1.08E+04
430	nC4H3+H=C2H2+H2CC	6.30E+25	-3.30E+00	1.00E+04
431	nC4H3+H=C4H4	2.00E+47	-1.03E+01	1.31E+04
432	nC4H3+H=C4H2+H2	3.00E+13	0.00E+00	0.00E+00
433	nC4H3+OH=C4H2+H2O	2.00E+12	0.00E+00	0.00E+00
434	nC4H3+C2H2=l-C6H4+H	2.50E+14	-6.00E-01	1.06E+04
435	nC4H3+C2H2=C6H5	9.60E+70	-1.78E+01	3.13E+04
436	nC4H3+C2H2=o-C6H4+H	6.90E+46	-1.00E+01	3.01E+04
437	iC4H3+H=C2H2+H2CC	2.80E+23	-2.50E+00	1.08E+04
438	iC4H3+H=C4H4	3.40E+43	-9.00E+00	1.21E+04
439	iC4H3+H=C4H2+H2	6.00E+13	0.00E+00	0.00E+00
440	iC4H3+OH=C4H2+H2O	4.00E+12	0.00E+00	0.00E+00
441	iC4H3+O2=HCCO+CH2CO	7.86E+16	-1.80E+00	0.00E+00
442	C4H4+H=nC4H5	1.30E+51	-1.19E+01	1.65E+04
443	C4H4+H=iC4H5	4.90E+51	-1.19E+01	1.77E+04
444	C4H4+H=nC4H3+H2	6.65E+05	2.50E+00	1.22E+04
445	C4H4+H=iC4H3+H2	3.33E+05	2.50E+00	9.24E+03
446	C4H4+OH=nC4H3+H2O	3.10E+07	2.00E+00	3.43E+03
447	C4H4+OH=iC4H3+H2O	1.55E+07	2.00E+00	4.30E+02
448	C4H4+O=C3H3+HCO	6.00E+08	1.40E+00	-8.60E+02
449	C4H4+C2H=l-C6H4+H	1.20E+13	0.00E+00	0.00E+00
450	nC4H5=iC4H5	1.50E+67	-1.69E+01	5.91E+04
451	nC4H5+H=iC4H5+H	3.10E+26	-3.40E+00	1.74E+04
452	nC4H5+H=C4H4+H2	1.50E+13	0.00E+00	0.00E+00
453	nC4H5+OH=C4H4+H2O	2.00E+12	0.00E+00	0.00E+00
454	nC4H5+HCO=C4H6+CO	5.00E+12	0.00E+00	0.00E+00
455	nC4H5+HO2=C2H3+CH2CO+OH	6.60E+12	0.00E+00	0.00E+00
456	nC4H5+H2O2=C4H6+HO2	1.21E+10	0.00E+00	-5.96E+02
457	nC4H5+HO2=C4H6+O2	6.00E+11	0.00E+00	0.00E+00
458	nC4H5+O2=CH2CHCHCHO+O	3.00E+11	3.00E-01	1.10E+01
459	nC4H5+O2=HCO+C2H3CHO	9.20E+16	-1.40E+00	1.01E+03
460	nC4H5+C2H2=C6H6+H	1.60E+16	-1.30E+00	5.40E+03
461	nC4H5+C2H3=C6H6+H2	1.84E-13	7.10E+00	-3.61E+03
462	iC4H5+H=C4H4+H2	3.00E+13	0.00E+00	0.00E+00
463	iC4H5+H=C3H3+CH3	2.00E+13	0.00E+00	2.00E+03
464	iC4H5+OH=C4H4+H2O	4.00E+12	0.00E+00	0.00E+00
465	iC4H5+HCO=C4H6+CO	5.00E+12	0.00E+00	0.00E+00
466	iC4H5+HO2=C4H6+O2	6.00E+11	0.00E+00	0.00E+00
467	iC4H5+HO2=C2H3+CH2CO+OH	6.60E+12	0.00E+00	0.00E+00
468	iC4H5+H2O2=C4H6+HO2	1.21E+10	0.00E+00	-5.96E+02
469	iC4H5+O2=CH2CO+CH2CHO	2.16E+10	0.00E+00	2.50E+03
470	C4H5-2=iC4H5	1.50E+67	-1.69E+01	5.91E+04
471	iC4H5+H=C4H5-2+H	3.10E+26	-3.40E+00	1.74E+04
472	C4H5-2+HO2=OH+C2H2+CH3CO	8.00E+11	0.00E+00	0.00E+00
473	C4H5-2+O2=CH3CO+CH2CO	2.16E+10	0.00E+00	2.50E+03
474	C4H5-2+C2H2=C6H6+H	5.00E+14	0.00E+00	2.50E+04
475	C4H5-2+C2H4=C5H6+CH3	5.00E+14	0.00E+00	2.50E+04
476	C4H6=iC4H5+H	5.70E+36	-6.30E+00	1.12E+05

477	C4H6=nC4H5+H	5.30E+44	-8.60E+00	1.24E+05		
478	C4H6=C4H4+H2	2.50E+15	0.00E+00	9.47E+04		
479	C4H6+H=nC4H5+H2	1.33E+06	2.50E+00	1.22E+04		
480	C4H6+H=iC4H5+H2	6.65E+05	2.50E+00	9.24E+03		
481	C4H6+H=C2H4+C2H3	1.46E+30	-4.30E+00	2.16E+04		
482	C4H6+H=pC3H4+CH3	2.00E+12	0.00E+00	7.00E+03		
483	C4H6+H=aC3H4+CH3	2.00E+12	0.00E+00	7.00E+03		
484	C4H6+O=nC4H5+OH	7.50E+06	1.90E+00	3.74E+03		
485	C4H6+O=iC4H5+OH	7.50E+06	1.90E+00	3.74E+03		
486	C4H6+O=CH3CHCHCO+H	1.50E+08	1.40E+00	-8.60E+02		
487	C4H6+O=CH2CHCHCHO+H	4.50E+08	1.40E+00	-8.60E+02		
488	C4H6+OH=nC4H5+H2O	6.20E+06	2.00E+00	3.43E+03		
489	C4H6+OH=iC4H5+H2O	3.10E+06	2.00E+00	4.30E+02		
490	C4H6+HO2=C4H6O25+OH	1.20E+12	0.00E+00	1.40E+04		
491	C4H6+HO2=C2H3CHOCH2+OH	4.80E+12	0.00E+00	1.40E+04		
492	C4H6+CH3=nC4H5+CH4	2.00E+14	0.00E+00	2.28E+04		
493	C4H6+CH3=iC4H5+CH4	1.00E+14	0.00E+00	1.98E+04		
494	C4H6+C2H3=nC4H5+C2H4	5.00E+13	0.00E+00	2.28E+04		
495	C4H6+C2H3=iC4H5+C2H4	2.50E+13	0.00E+00	1.98E+04		
496	C4H6+C3H3=nC4H5+aC3H4	1.00E+13	0.00E+00	2.25E+04		
497	C4H6+C3H3=iC4H5+aC3H4	5.00E+12	0.00E+00	1.95E+04		
498	C4H6+aC3H5=nC4H5+C3H6	1.00E+13	0.00E+00	2.25E+04		
499	C4H6+aC3H5=iC4H5+C3H6	5.00E+12	0.00E+00	1.95E+04		
500	C4H6+C2H3=C6H6+H2+H	5.62E+11	0.00E+00	3.24E+03		
501	C4H612=iC4H5+H	4.20E+15	0.00E+00	9.26E+04		
502	C4H612+H=C4H6+H	2.00E+13	0.00E+00	4.00E+03		
503	C4H612+H=iC4H5+H2	1.70E+05	2.50E+00	2.49E+03		
504	C4H612+H=aC3H4+CH3	2.00E+13	0.00E+00	2.00E+03		
505	C4H612+H=pC3H4+CH3	2.00E+13	0.00E+00	2.00E+03		
506	C4H612+CH3=iC4H5+CH4	7.00E+13	0.00E+00	1.85E+04		
507	C4H612+O=CH2CO+C2H4	1.20E+08	1.60E+00	3.27E+02		
508	C4H612+O=iC4H5+OH	1.80E+11	7.00E-01	5.88E+03		
509	C4H612+OH=iC4H5+H2O	3.10E+06	2.00E+00	-2.98E+02		
510	C4H612=C4H6	3.00E+13	0.00E+00	6.50E+04		
511	C4H6-2=C4H6	3.00E+13	0.00E+00	6.50E+04		
512	C4H6-2=C4H612	3.00E+13	0.00E+00	6.70E+04		
513	C4H6-2+H=C4H612+H	2.00E+13	0.00E+00	4.00E+03		
514	C4H6-2+H=C4H5-2+H2	3.40E+05	2.50E+00	2.49E+03		
515	C4H6-2+H=CH3+pC3H4	2.60E+05	2.50E+00	1.00E+03		
516	C4H6-2=H+C4H5-2	5.00E+15	0.00E+00	8.73E+04		
517	C4H6-2+CH3=C4H5-2+CH4	1.40E+14	0.00E+00	1.85E+04		
518	C2H3CHOCH2=C4H6O23	2.00E+14	0.00E+00	5.06E+04		
519	C4H6O23=CH3CHCHCHO	1.95E+13	0.00E+00	4.94E+04		
520	C4H6O23=C2H4+CH2CO	5.75E+15	0.00E+00	6.93E+04		
521	C4H6O23=C2H2+CH2OCH2	1.00E+16	0.00E+00	7.58E+04		
522	C4H6O25=C4H4O+H2	5.30E+12	0.00E+00	4.85E+04		
523	C4H4O=CO+pC3H4	1.78E+15	0.00E+00	7.75E+04		
524	C4H4O=C2H2+CH2CO	5.01E+14	0.00E+00	7.75E+04		
525	CH3CHCHCHO=C3H6+CO	3.90E+14	0.00E+00	6.90E+04		
526	CH3CHCHCHO+H=CH2CHCHCHO+H2	1.70E+05	2.50E+00	2.49E+03		
527	CH3CHCHCHO+H=CH3CHCHCHO+H2	1.00E+05	2.50E+00	2.49E+03		
528	CH3CHCHCHO+H=CH3+C2H3CHO	4.00E+21	-2.40E+00	1.12E+04		
529	CH3CHCHCHO+H=C3H6+HCO	4.00E+21	-2.40E+00	1.12E+04		
530	CH3CHCHCHO+CH3=CH2CHCHCHO+CH4	2.10E+00	3.50E+00	5.68E+03		
531	CH3CHCHCHO+CH3=CH3CHCHCO+CH4	1.10E+00	3.50E+00	5.68E+03		
532	CH3CHCHCHO+C2H3=CH2CHCHCHO+C2H4	2.21E+00	3.50E+00	4.68E+03		
533	CH3CHCHCHO+C2H3=CH3CHCHCO+C2H4	1.11E+00	3.50E+00	4.68E+03		
534	CH3CHCHCO=CH3CHCH+CO	1.00E+14	0.00E+00	3.00E+04		
535	CH3CHCHCO+H=CH3CHCHCHO	1.00E+14	0.00E+00	0.00E+00		
536	CH2CHCHCHO=aC3H5+CO	1.00E+14	0.00E+00	2.50E+04		
537	CH2CHCHCHO+H=CH3CHCHCHO	1.00E+14	0.00E+00	0.00E+00		
538	C4H7=C4H6+H	2.48E+53	-1.23E+01	5.20E+04		
539	C4H7+H(+M)=C4H81(+M)	3.60E+13	0.00E+00	0.00E+00		
	Low pressure limit	0.00E+00	3.01E+48	-9.32E+00		
	TROE centering	4.98E-01	1.31E+03	1.31E+03		
	Enhanced by	H2	H2O	CH4	CO	CO2
		2.00E+00	6.00E+00	2.00E+00	1.50E+00	2.00E+00
		C2H6	AR			

	3.00E+00	7.00E-01			
540 C4H7+H=CH3+aC3H5		2.00E+21	-2.00E+00	1.10E+04	
541 C4H7+H=C4H6+H2		1.80E+12	0.00E+00	0.00E+00	
542 C4H7+O2=C4H6+HO2		1.00E+11	0.00E+00	0.00E+00	
543 C4H7+HO2=CH2O+OH+aC3H5		2.40E+13	0.00E+00	0.00E+00	
544 C4H7+HCO=C4H81+CO		6.00E+13	0.00E+00	0.00E+00	
545 C4H7+CH3=C4H6+CH4		1.10E+13	0.00E+00	0.00E+00	
546 iC4H7+H(+M)=iC4H8(+M)		2.00E+14	0.00E+00	0.00E+00	
Low pressure limit		0.00E+00	1.33E+60	-1.20E+01	
TROE centering		2.00E-02	1.10E+03	1.10E+03	
Enhanced by	H2	H2O	CH4	CO	CO2
	2.00E+00	6.00E+00	2.00E+00	1.50E+00	2.00E+00
	C2H6	AR			
	3.00E+00	7.00E-01			
547 iC4H7+H=CH3CCH2+CH3		2.60E+45	-8.20E+00	3.79E+04	
548 iC4H7+O=CH2O+CH3CCH2		9.00E+13	0.00E+00	0.00E+00	
549 iC4H7+HO2=CH3CCH2+CH2O+OH		4.00E+12	0.00E+00	0.00E+00	
550 C4H81+H(+M)=pC4H9(+M)		1.33E+13	0.00E+00	3.26E+03	
Low pressure limit		0.00E+00	6.26E+38	-6.66E+00	
TROE centering		1.00E+00	1.00E+03	1.31E+03	
Enhanced by	H2	H2O	CH4	CO	CO2
	2.00E+00	6.00E+00	2.00E+00	1.50E+00	2.00E+00
	C2H6	AR			
	3.00E+00	7.00E-01			
551 C4H81+H(+M)=sC4H9(+M)		1.33E+13	0.00E+00	1.56E+03	
Low pressure limit		0.00E+00	8.70E+42	-7.50E+00	
TROE centering		1.00E+00	1.00E+03	6.45E+02	
Enhanced by	H2	H2O	CH4	CO	CO2
	2.00E+00	6.00E+00	2.00E+00	1.50E+00	2.00E+00
	C2H6	AR			
	3.00E+00	7.00E-01			
552 C4H81+H=C2H4+C2H5		1.60E+22	-2.40E+00	1.12E+04	
553 C4H81+H=C3H6+CH3		3.20E+22	-2.40E+00	1.12E+04	
554 C4H81+H=C4H7+H2		6.50E+05	2.50E+00	6.76E+03	
555 C4H81+O=nC3H7+HCO		3.30E+08	1.40E+00	-4.02E+02	
556 C4H81+O=C4H7+OH		1.50E+13	0.00E+00	5.76E+03	
Declared duplicate reaction					
557 C4H81+O=C4H7+OH		2.60E+13	0.00E+00	4.47E+03	
Declared duplicate reaction					
558 C4H81+OH=C4H7+H2O		7.00E+02	2.70E+00	5.27E+02	
559 C4H81+O2=C4H7+HO2		2.00E+13	0.00E+00	5.09E+04	
560 C4H81+HO2=C4H7+H2O2		1.00E+12	0.00E+00	1.43E+04	
561 C4H81+CH3=C4H7+CH4		4.50E-01	3.60E+00	7.15E+03	
562 C4H82+H(+M)=sC4H9(+M)		1.33E+13	0.00E+00	1.56E+03	
Low pressure limit		0.00E+00	8.70E+42	-7.50E+00	
TROE centering		1.00E+00	1.00E+03	6.45E+02	
Enhanced by	H2	H2O	CH4	CO	CO2
	2.00E+00	6.00E+00	2.00E+00	1.50E+00	2.00E+00
	C2H6	AR			
	3.00E+00	7.00E-01			
563 C4H82+H=C4H7+H2		3.40E+05	2.50E+00	2.49E+03	
564 C4H82+O=C2H4+CH3CHO		2.40E+08	1.60E+00	3.27E+02	
565 C4H82+OH=C4H7+H2O		6.20E+06	2.00E+00	-2.98E+02	
566 C4H82+O2=C4H7+HO2		5.00E+13	0.00E+00	5.33E+04	
567 C4H82+HO2=C4H7+H2O2		1.90E+04	2.60E+00	1.39E+04	
568 C4H82+CH3=C4H7+CH4		4.40E+00	3.50E+00	5.68E+03	
569 iC4H8+H(+M)=iC4H9(+M)		1.33E+13	0.00E+00	3.26E+03	
Low pressure limit		0.00E+00	6.26E+38	-6.66E+00	
TROE centering		1.00E+00	1.00E+03	1.31E+03	
Enhanced by	H2	H2O	CH4	CO	CO2
	2.00E+00	6.00E+00	2.00E+00	1.50E+00	2.00E+00
	C2H6	AR			
	3.00E+00	7.00E-01			
570 iC4H8+H=iC4H7+H2		1.20E+06	2.50E+00	6.76E+03	
571 iC4H8+H=C3H6+CH3		8.00E+21	-2.40E+00	1.12E+04	
572 iC4H8+O=CH3+CH3+CH2CO		1.20E+08	1.60E+00	3.27E+02	
573 iC4H8+O=iC3H7+HCO		3.50E+07	1.60E+00	-9.72E+02	
574 iC4H8+O=iC4H7+OH		2.90E+05	2.50E+00	3.64E+03	

575	iC4H8+OH=iC4H7+H2O	1.50E+08	1.50E+00	7.75E+02		
576	iC4H8+HO2=iC4H7+H2O2	2.00E+04	2.50E+00	1.55E+04		
577	iC4H8+O2=iC4H7+HO2	2.70E+13	0.00E+00	5.09E+04		
578	iC4H8+CH3=iC4H7+CH4	9.10E-01	3.60E+00	7.15E+03		
579	C2H4+C2H5=pC4H9	1.50E+11	0.00E+00	7.30E+03		
580	pC4H9+H(+M)=C4H10(+M)	3.60E+13	0.00E+00	0.00E+00		
	Low pressure limit	0.00E+00	3.01E+48	-9.32E+00		
	TROE centering	4.98E-01	1.31E+03	1.31E+03		
	Enhanced by	H2	H2O	CH4	CO	CO2
		2.00E+00	6.00E+00	2.00E+00	1.50E+00	2.00E+00
		C2H6	AR			
		3.00E+00	7.00E-01			
581	pC4H9+H=C2H5+C2H5	3.70E+24	-2.90E+00	1.25E+04		
582	pC4H9+H=C4H8+H2	1.80E+12	0.00E+00	0.00E+00		
583	pC4H9+O=nC3H7+CH2O	9.60E+13	0.00E+00	0.00E+00		
584	pC4H9+OH=C4H8+H2O	2.40E+13	0.00E+00	0.00E+00		
585	pC4H9+O2=C4H8+HO2	2.70E+11	0.00E+00	0.00E+00		
586	pC4H9+HO2=nC3H7+OH+CH2O	2.40E+13	0.00E+00	0.00E+00		
587	pC4H9+HCO=C4H10+CO	9.00E+13	0.00E+00	0.00E+00		
588	pC4H9+CH3=C4H8+CH4	1.10E+13	0.00E+00	0.00E+00		
589	C3H6+CH3(+M)=sC4H9(+M)	1.70E+11	0.00E+00	7.40E+03		
	Low pressure limit	0.00E+00	2.31E+28	-4.27E+00		
	TROE centering	5.65E-01	6.00E+04	5.34E+02		
	Enhanced by	H2	H2O	CH4	CO	CO2
		2.00E+00	6.00E+00	2.00E+00	1.50E+00	2.00E+00
		C2H6	AR			
		3.00E+00	7.00E-01			
590	sC4H9+H(+M)=C4H10(+M)	2.40E+13	0.00E+00	0.00E+00		
	Low pressure limit	0.00E+00	1.70E+58	-1.21E+01		
	TROE centering	6.49E-01	1.21E+03	1.21E+03		
	Enhanced by	H2	H2O	CH4	CO	CO2
		2.00E+00	6.00E+00	2.00E+00	1.50E+00	2.00E+00
		C2H6	AR			
		3.00E+00	7.00E-01			
591	sC4H9+H=C2H5+C2H5	1.40E+28	-3.90E+00	1.59E+04		
592	sC4H9+H=C4H8+H2	3.20E+12	0.00E+00	0.00E+00		
593	sC4H9+H=C4H8+H2	2.10E+12	0.00E+00	0.00E+00		
594	sC4H9+O=CH3CHO+C2H5	9.60E+13	0.00E+00	0.00E+00		
595	sC4H9+OH=C4H8+H2O	2.40E+13	0.00E+00	0.00E+00		
596	sC4H9+OH=C4H8+H2O	1.60E+13	0.00E+00	0.00E+00		
597	sC4H9+O2=C4H8+HO2	5.10E+10	0.00E+00	0.00E+00		
598	sC4H9+O2=C4H8+HO2	1.20E+11	0.00E+00	0.00E+00		
599	sC4H9+HO2=CH3CHO+C2H5+OH	2.40E+13	0.00E+00	0.00E+00		
600	sC4H9+HCO=C4H10+CO	1.20E+14	0.00E+00	0.00E+00		
601	sC4H9+CH3=CH4+C4H8	2.20E+14	-7.00E-01	0.00E+00		
602	sC4H9+CH3=CH4+C4H8	1.50E+14	-7.00E-01	0.00E+00		
603	C3H6+CH3(+M)=iC4H9(+M)	9.60E+10	0.00E+00	8.00E+03		
	Low pressure limit	0.00E+00	1.30E+28	-4.27E+00		
	TROE centering	5.65E-01	6.00E+04	5.34E+02		
	Enhanced by	H2	H2O	CH4	CO	CO2
		2.00E+00	6.00E+00	2.00E+00	1.50E+00	2.00E+00
		C2H6	AR			
		3.00E+00	7.00E-01			
604	iC4H9+H(+M)=iC4H10(+M)	3.60E+13	0.00E+00	0.00E+00		
	Low pressure limit	0.00E+00	3.27E+56	-1.17E+01		
	TROE centering	5.06E-01	1.27E+03	1.27E+03		
	Enhanced by	H2	H2O	CH4	CO	CO2
		2.00E+00	6.00E+00	2.00E+00	1.50E+00	2.00E+00
		C2H6	AR			
		3.00E+00	7.00E-01			
605	iC4H9+H=iC3H7+CH3	1.90E+35	-5.80E+00	2.25E+04		
606	iC4H9+H=iC4H8+H2	9.00E+11	0.00E+00	0.00E+00		
607	iC4H9+O=iC3H7+CH2O	9.60E+13	0.00E+00	0.00E+00		
608	iC4H9+OH=iC4H8+H2O	1.20E+13	0.00E+00	0.00E+00		
609	iC4H9+O2=iC4H8+HO2	2.40E+10	0.00E+00	0.00E+00		
610	iC4H9+HO2=iC3H7+CH2O+OH	2.41E+13	0.00E+00	0.00E+00		
611	iC4H9+HCO=iC4H10+CO	3.60E+13	0.00E+00	0.00E+00		
612	iC4H9+CH3=iC4H8+CH4	6.00E+12	-3.00E-01	0.00E+00		



613	tC4H9(+M)=iC4H8+H(+M)	8.30E+13	0.00E+00	3.82E+04	
	Low pressure limit	0.00E+00	1.90E+41	-7.36E+00	
	TROE centering	2.93E-01	6.49E+02	6.00E+04	
	Enhanced by	H2	H2O	CH4	CO
		2.00E+00	6.00E+00	2.00E+00	1.50E+00
		C2H6	AR		CO2
		3.00E+00	7.00E-01		2.00E+00
614	tC4H9+H(+M)=iC4H10(+M)	2.40E+13	0.00E+00	0.00E+00	
	Low pressure limit	0.00E+00	1.47E+61	-1.29E+01	
	TROE centering	0.00E+00	1.46E+03	1.00E+03	
	Enhanced by	H2	H2O	CH4	CO
		2.00E+00	6.00E+00	2.00E+00	1.50E+00
		C2H6	AR		CO2
		3.00E+00	7.00E-01		2.00E+00
615	tC4H9+H=iC3H7+CH3	2.60E+36	-6.10E+00	2.56E+04	
616	tC4H9+H=iC4H8+H2	5.42E+12	0.00E+00	0.00E+00	
617	tC4H9+O=iC4H8+OH	1.80E+14	0.00E+00	0.00E+00	
618	tC4H9+O=CH3COCH3+CH3	1.80E+14	0.00E+00	0.00E+00	
619	tC4H9+OH=iC4H8+H2O	1.80E+13	0.00E+00	0.00E+00	
620	tC4H9+O2=iC4H8+HO2	4.80E+11	0.00E+00	0.00E+00	
621	tC4H9+HO2=CH3+CH3COCH3+OH	1.80E+13	0.00E+00	0.00E+00	
622	tC4H9+HCO=iC4H10+CO	6.00E+13	0.00E+00	0.00E+00	
623	tC4H9+CH3=iC4H8+CH4	3.80E+15	-1.00E+00	0.00E+00	
624	CH3COCH3+H=H2+CH2CO+CH3	1.30E+06	2.50E+00	6.76E+03	
625	CH3COCH3+O=OH+CH2CO+CH3	1.90E+05	2.70E+00	3.72E+03	
626	CH3COCH3+OH=H2O+CH2CO+CH3	3.20E+07	1.80E+00	9.34E+02	
627	CH3+CH3CO=CH3COCH3	4.00E+15	-8.00E-01	0.00E+00	
628	nC3H7+CH3(+M)=C4H10(+M)	1.93E+14	-3.00E-01	0.00E+00	
	Low pressure limit	0.00E+00	2.68E+61	-1.32E+01	
	TROE centering	1.00E+00	1.00E+03	1.43E+03	
	Enhanced by	H2	H2O	CH4	CO
		2.00E+00	6.00E+00	2.00E+00	1.50E+00
		C2H6	AR		CO2
		3.00E+00	7.00E-01		2.00E+00
629	C2H5+C2H5(+M)=C4H10(+M)	1.88E+14	-5.00E-01	0.00E+00	
	Low pressure limit	0.00E+00	2.61E+61	-1.34E+01	
	TROE centering	1.00E+00	1.00E+03	1.43E+03	
	Enhanced by	H2	H2O	CH4	CO
		2.00E+00	6.00E+00	2.00E+00	1.50E+00
		C2H6	AR		CO2
		3.00E+00	7.00E-01		2.00E+00
630	C4H10+H=pC4H9+H2	9.20E+05	2.50E+00	6.76E+03	
631	C4H10+H=sC4H9+H2	2.40E+06	2.40E+00	4.47E+03	
632	C4H10+O=pC4H9+OH	4.90E+06	2.40E+00	5.50E+03	
633	C4H10+O=sC4H9+OH	4.30E+05	2.60E+00	2.58E+03	
634	C4H10+OH=pC4H9+H2O	3.30E+07	1.80E+00	9.54E+02	
635	C4H10+OH=sC4H9+H2O	5.40E+06	2.00E+00	-5.96E+02	
636	C4H10+O2=pC4H9+HO2	4.00E+13	0.00E+00	5.09E+04	
637	C4H10+O2=sC4H9+HO2	8.00E+13	0.00E+00	4.76E+04	
638	C4H10+HO2=pC4H9+H2O2	4.76E+04	2.50E+00	1.65E+04	
639	C4H10+HO2=sC4H9+H2O2	1.90E+04	2.60E+00	1.39E+04	
640	C4H10+CH3=pC4H9+CH4	9.03E-01	3.60E+00	7.15E+03	
641	C4H10+CH3=sC4H9+CH4	3.00E+00	3.50E+00	5.48E+03	
642	iC3H7+CH3(+M)=iC4H10(+M)	1.40E+15	-7.00E-01	0.00E+00	
	Low pressure limit	0.00E+00	4.16E+61	-1.33E+01	
	TROE centering	9.31E-01	6.00E+04	1.27E+03	
	Enhanced by	H2	H2O	CH4	CO
		2.00E+00	6.00E+00	2.00E+00	1.50E+00
		C2H6	AR		CO2
		3.00E+00	7.00E-01		2.00E+00
643	iC4H10+H=iC4H9+H2	1.80E+06	2.50E+00	6.76E+03	
644	iC4H10+H=tC4H9+H2	6.00E+05	2.40E+00	2.58E+03	
645	iC4H10+O=iC4H9+OH	4.30E+05	2.50E+00	3.64E+03	
646	iC4H10+O=tC4H9+OH	1.57E+05	2.50E+00	1.11E+03	
647	iC4H10+OH=iC4H9+H2O	2.30E+08	1.50E+00	7.75E+02	
648	iC4H10+OH=tC4H9+H2O	5.73E+10	5.00E-01	6.40E+01	
649	iC4H10+HO2=iC4H9+H2O2	3.00E+04	2.50E+00	1.55E+04	
650	iC4H10+HO2=tC4H9+H2O2	3.60E+03	2.50E+00	1.05E+04	

651	iC4H10+O2=iC4H9+HO2	4.00E+13	0.00E+00	5.09E+04		
652	iC4H10+O2=tC4H9+HO2	4.00E+13	0.00E+00	4.40E+04		
653	iC4H10+CH3=iC4H9+CH4	1.36E+00	3.60E+00	7.15E+03		
654	iC4H10+CH3=tC4H9+CH4	9.00E-01	3.50E+00	4.60E+03		
655	C6H2+H=C6H3	1.10E+30	-4.90E+00	1.08E+04		
656	C6H3+H=C4H2+C2H2	2.80E+23	-2.50E+00	1.08E+04		
657	C6H3+H=l-C6H4	3.40E+43	-9.00E+00	1.21E+04		
658	C6H3+H=C6H2+H2	3.00E+13	0.00E+00	0.00E+00		
659	C6H3+OH=C6H2+H2O	4.00E+12	0.00E+00	0.00E+00		
660	l-C6H4+H=C6H5	1.70E+78	-1.97E+01	3.14E+04		
661	l-C6H4+H=o-C6H4+H	1.40E+54	-1.17E+01	3.45E+04		
662	l-C6H4+H=C6H3+H2	1.33E+06	2.50E+00	9.24E+03		
663	l-C6H4+OH=C6H3+H2O	3.10E+06	2.00E+00	4.30E+02		
664	C4H2+C2H2=o-C6H4	5.00E+78	-1.93E+01	6.79E+04		
665	o-C6H4+OH=CO+C5H5	1.00E+13	0.00E+00	0.00E+00		
666	C6H5+CH3=C6H5CH3	1.38E+13	0.00E+00	4.60E+01		
667	C6H5CH3+O2=C6H5CH2+HO2	3.00E+14	0.00E+00	4.30E+04		
668	C6H5CH3+OH=C6H5CH2+H2O	1.62E+13	0.00E+00	2.77E+03		
669	C6H5CH3+OH=C6H4CH3+H2O	1.33E+08	1.40E+00	1.45E+03		
670	C6H5CH3+H=C6H5CH2+H2	1.26E+14	0.00E+00	8.36E+03		
671	C6H5CH3+H=C6H6+CH3	1.93E+06	2.20E+00	4.16E+03		
672	C6H5CH3+O=OC6H4CH3+H	2.60E+13	0.00E+00	3.80E+03		
673	C6H5CH3+CH3=C6H5CH2+CH4	3.16E+11	0.00E+00	9.50E+03		
674	C6H5CH3+C6H5=C6H5CH2+C6H6	2.10E+12	0.00E+00	4.40E+03		
675	C6H5CH3+HO2=C6H5CH2+H2O2	3.98E+11	0.00E+00	1.41E+04		
676	C6H5CH3+HO2=C6H4CH3+H2O2	5.42E+12	0.00E+00	2.88E+04		
677	C6H5CH2+H(+M)=C6H5CH3(+M)	1.00E+14	0.00E+00	0.00E+00		
	Low pressure limit	0.00E+00	NaN	-2.46E+01		
	TROE centering	4.31E-01	3.83E+02	1.52E+02		
	Enhanced by	H2	H2O	CH4	CO	CO2
		2.00E+00	6.00E+00	2.00E+00	1.50E+00	2.00E+00
		C2H6				
		3.00E+00				
678	C6H5CH2+H=C6H5+CH3	1.50E+66	-1.39E+01	6.46E+04		
679	C6H5CH2+O=C6H5CHO+H	4.00E+14	0.00E+00	0.00E+00		
680	C6H5CH2+OH=C6H5CH2OH	2.00E+13	0.00E+00	0.00E+00		
681	C6H5CH2+HO2=C6H5CHO+H+OH	5.00E+12	0.00E+00	0.00E+00		
682	C6H5CH2+C6H5OH=C6H5CH3+C6H5O	1.05E+11	0.00E+00	9.50E+03		
683	C6H5CH2+HOC6H4CH3=C6H5CH3+OC6H4CH3	1.05E+11	0.00E+00	9.50E+03		
684	C6H5CH2OH+OH=C6H5CHO+H2O+H	5.00E+12	0.00E+00	0.00E+00		
685	C6H5CH2OH+H=C6H5CHO+H2+H	8.00E+13	0.00E+00	8.24E+03		
686	C6H5CH2OH+H=C6H6+CH2OH	1.20E+13	0.00E+00	5.15E+03		
687	C6H5CH2OH+C6H5=C6H5CHO+C6H6+H	1.40E+12	0.00E+00	4.40E+03		
688	C6H5+HCO=C6H5CHO	1.00E+13	0.00E+00	0.00E+00		
689	C6H5CHO=C6H5CO+H	3.98E+15	0.00E+00	8.69E+04		
690	C6H5CHO+O2=C6H5CO+HO2	1.02E+13	0.00E+00	3.90E+04		
691	C6H5CHO+OH=C6H5CO+H2O	2.35E+10	7.00E-01	-1.11E+03		
692	C6H5CHO+H=C6H5CO+H2	4.10E+09	1.20E+00	2.40E+03		
693	C6H5CHO+H=C6H6+HCO	1.93E+06	2.20E+00	4.16E+03		
694	C6H5CHO+O=C6H5CO+OH	5.80E+12	0.00E+00	1.80E+03		
695	C6H5CHO+C6H5CH2=C6H5CO+C6H5CH3	2.00E-06	5.60E+00	2.46E+03		
696	C6H5CHO+CH3=C6H5CO+CH4	2.00E-06	5.60E+00	2.46E+03		
697	C6H5CHO+C6H5=C6H5CO+C6H6	2.10E+12	0.00E+00	4.40E+03		
698	C6H5CO+H2O2=C6H5CHO+HO2	1.80E+11	0.00E+00	8.23E+03		
699	OC6H4CH3+H(+M)=HOC6H4CH3(+M)	1.00E+14	0.00E+00	0.00E+00		
	Low pressure limit	0.00E+00	4.00E+93	-2.18E+01		
	TROE centering	4.30E-02	3.04E+02	6.00E+04		
	Enhanced by	H2	H2O	CH4	CO	CO2
		2.00E+00	6.00E+00	2.00E+00	1.50E+00	2.00E+00
700	OC6H4CH3+H=C6H5O+CH3	1.93E+06	2.20E+00	4.16E+03		
701	OC6H4CH3+O=C6H4O2+CH3	8.00E+13	0.00E+00	0.00E+00		
702	HOC6H4CH3+OH=OC6H4CH3+H2O	6.00E+12	0.00E+00	0.00E+00		
703	HOC6H4CH3+H=OC6H4CH3+H2	1.15E+14	0.00E+00	1.24E+04		
704	HOC6H4CH3+H=C6H5CH3+OH	2.21E+13	0.00E+00	7.91E+03		
705	HOC6H4CH3+H=C6H5OH+CH3	1.20E+13	0.00E+00	5.15E+03		
706	C6H5CO=C6H5+CO	5.27E+14	0.00E+00	2.90E+04		
707	C6H5+H(+M)=C6H6(+M)	1.00E+14	0.00E+00	0.00E+00		
	Low pressure limit	0.00E+00	6.60E+75	-1.63E+01		

TROE centering		1.00E+00	1.00E-01	5.85E+02	
Enhanced by	H2	H2O	CH4	CO	CO2
708 C6H6+OH=C6H5+H2O	2.00E+00	6.00E+00	2.00E+00	1.50E+00	2.00E+00
709 C6H6+OH=C6H5OH+H		3.98E+05	2.30E+00	1.06E+03	
710 C6H6+O=C6H5O+H		1.30E+13	0.00E+00	1.06E+04	
711 C6H6+O=C5H5+HCO		1.39E+13	0.00E+00	4.91E+03	
712 C6H5+H2=C6H6+H		1.39E+13	0.00E+00	4.53E+03	
713 C6H5(+M)=o-C6H4+H(+M)		5.71E+04	2.40E+00	6.27E+03	
Low pressure limit		4.30E+12	6.00E-01	7.73E+04	
TROE centering		0.00E+00	1.00E+84	-1.89E+01	
Enhanced by	H2	H2O	CH4	CO	CO2
714 C6H5+H=o-C6H4+H2	2.00E+00	6.00E+00	2.00E+00	1.50E+00	2.00E+00
715 C6H5+O2=C6H5O+O		2.00E+11	1.10E+00	2.45E+04	
716 C6H5+O2=C6H4O2+H		2.60E+13	0.00E+00	6.12E+03	
717 C6H5+O=C5H5+CO		3.00E+13	0.00E+00	8.98E+03	
718 C6H5+OH=C6H5O+H		1.00E+14	0.00E+00	0.00E+00	
719 C6H5+HO2=C6H5O+OH		3.00E+13	0.00E+00	0.00E+00	
720 C6H5+HO2=C6H6+O2		3.00E+13	0.00E+00	0.00E+00	
721 C6H5+CH4=C6H6+CH3		1.00E+12	0.00E+00	0.00E+00	
722 C6H5+C2H6=C6H6+C2H5		3.89E-03	4.60E+00	5.26E+03	
723 C6H5+CH2O=C6H6+HCO		2.10E+11	0.00E+00	4.44E+03	
724 C6H5+C2H2=n-A1C2H2		8.55E+04	2.20E+00	3.80E+01	
725 C6H5+C2H2=C6H5C2H+H		7.00E+38	-8.00E+00	1.64E+04	
726 C6H5C2H+H=n-A1C2H2		3.30E+33	-5.70E+00	2.55E+04	
727 C6H5C2H+H=i-A1C2H2		3.00E+43	-9.20E+00	1.53E+04	
728 C6H5C2H+H=A1C2H*+H2		3.00E+43	-9.20E+00	1.53E+04	
729 C6H5C2H+OH=A1C2H*+H2O		2.50E+14	0.00E+00	1.60E+04	
730 C6H5C2H+C2H=A1C2H)2+H		1.60E+08	1.40E+00	1.45E+03	
731 C6H5+C2H4=C6H5C2H3+H		5.00E+13	0.00E+00	0.00E+00	
732 C6H5+C4H4=C10H8+H		2.51E+12	0.00E+00	6.19E+03	
733 C6H5C2H3+H=n-A1C2H2+H2		3.30E+33	-5.70E+00	2.55E+04	
734 C6H5C2H3+H=i-A1C2H2+H2		6.65E+06	2.50E+00	1.22E+04	
735 C6H4O2=C5H4O+CO		3.33E+05	2.50E+00	9.24E+03	
736 C6H4O2+H=CO+C5H5O(1,3)		7.40E+11	0.00E+00	5.90E+04	
737 C6H4O2+O=2CO+C2H2+CH2CO		4.30E+09	1.40E+00	3.90E+03	
738 C6H5O+H=C5H5+HCO		3.00E+13	0.00E+00	5.00E+03	
739 C6H5O+H=C5H6+CO		1.00E+13	0.00E+00	1.20E+04	
740 C6H5O=CO+C5H5		5.00E+13	0.00E+00	0.00E+00	
741 C6H5O+O=C6H4O2+H		3.76E+54	-1.21E+01	7.28E+04	
742 C6H5OH=C5H6+CO		2.60E+10	5.00E-01	7.95E+02	
743 C6H5OH+OH=C6H5O+H2O		1.00E+12	0.00E+00	6.08E+04	
744 C6H5OH+H=C6H5O+H2		2.95E+06	2.00E+00	-1.31E+03	
745 C6H5OH+O=C6H5O+OH		1.15E+14	0.00E+00	1.24E+04	
746 C6H5OH+C2H3=C6H5O+C2H4		2.81E+13	0.00E+00	7.35E+03	
747 C6H5OH+nC4H5=C6H5O+C4H6		6.00E+12	0.00E+00	0.00E+00	
748 C6H5OH+C6H5=C6H5O+C6H6		6.00E+12	0.00E+00	0.00E+00	
749 C5H6+H=C2H2+aC3H5		4.91E+12	0.00E+00	4.40E+03	
750 C5H6+H=1C5H7		7.74E+36	-6.20E+00	3.29E+04	
751 C5H6+H=C5H5+H2	NaN		-3.23E+01	8.23E+04	
752 C5H6+O=C5H5+OH		3.03E+08	1.70E+00	5.59E+03	
753 C5H6+O=C5H5O(1,3)+H		4.77E+04	2.70E+00	1.11E+03	
Declared duplicate reaction		8.91E+12	-1.00E-01	5.90E+02	
754 C5H6+O=C5H5O(1,3)+H		5.60E+12	-1.00E-01	2.00E+02	
Declared duplicate reaction					
755 C5H6+O=nC4H5+CO+H		8.70E+51	-1.11E+01	3.32E+04	
756 C5H6+OH=C5H5+H2O		3.08E+06	2.00E+00	0.00E+00	
757 C5H6+HO2=C5H5+H2O2		1.10E+04	2.60E+00	1.29E+04	
758 C5H6+O2=C5H5+HO2		4.00E+13	0.00E+00	3.72E+04	
759 C5H6+HCO=C5H5+CH2O		1.08E+08	1.90E+00	1.60E+04	
760 C5H6+CH3=C5H5+CH4		1.80E-01	4.00E+00	0.00E+00	
761 C5H5+H(+M)=C5H6(+M)		1.00E+14	0.00E+00	0.00E+00	
Low pressure limit		0.00E+00	4.40E+80	-1.83E+01	
TROE centering		6.80E-02	4.01E+02	4.14E+03	
Enhanced by	H2	H2O	CH4	CO	CO2
762 C5H5+O2=C5H5O(2,4)+O	2.00E+00	6.00E+00	2.00E+00	1.50E+00	2.00E+00
763 C5H5+O=C5H5O(2,4)		7.78E+15	-7.00E-01	4.87E+04	
		1.12E-12	5.90E+00	-1.73E+04	

764	$C_5H_5+O=C_5H_4O+H$	5.81E+13	0.00E+00	2.00E+01		
765	$C_5H_5+O=nC_4H_5+CO$	3.20E+13	-2.00E-01	4.40E+02		
766	$C_5H_5+OH=C_5H_4OH+H$	3.51E+57	-1.22E+01	4.84E+04		
767	$C_5H_5+OH=C_5H_5O(2,4)+H$	1.36E+51	-1.05E+01	5.71E+04		
768	$C_5H_5+HO_2=C_5H_5O(2,4)+OH$	6.27E+29	-4.70E+00	1.17E+04		
769	$C_5H_5+OH=C_5H_5OH$	6.49E+14	-8.00E-01	-2.73E+03		
	Declared duplicate reaction					
770	$C_5H_5+OH=C_5H_5OH$	1.15E+43	-8.80E+00	1.87E+04		
	Declared duplicate reaction					
771	$C_5H_5+OH=C_5H_5OH$	1.06E+59	-1.31E+01	3.35E+04		
	Declared duplicate reaction					
772	$C_5H_5+O_2=C_5H_4O+OH$	1.80E+12	1.00E-01	1.80E+04		
773	$C_5H_5OH+H=C_5H_5O(2,4)+H_2$	1.15E+14	0.00E+00	1.54E+04		
774	$C_5H_5OH+H=C_5H_4OH+H_2$	1.20E+05	2.50E+00	1.49E+03		
775	$C_5H_5OH+OH=C_5H_5O(2,4)+H_2O$	6.00E+12	0.00E+00	0.00E+00		
776	$C_5H_5OH+OH=C_5H_4OH+H_2O$	3.08E+06	2.00E+00	0.00E+00		
777	$C_5H_5O(2,4)+H=C_5H_5OH$	1.00E+14	0.00E+00	0.00E+00		
778	$C_5H_5O(2,4)=C_5H_4O+H$	2.00E+13	0.00E+00	3.00E+04		
779	$C_5H_5O(2,4)+O_2=C_5H_4O+HO_2$	1.00E+11	0.00E+00	0.00E+00		
780	$C_5H_4O+H=C_5H_5O(1,3)$	2.00E+13	0.00E+00	2.00E+03		
781	$C_5H_5O(1,3)=c-C_4H_5+CO$	1.00E+12	0.00E+00	3.60E+04		
782	$C_5H_5O(1,3)+O_2=C_5H_4O+HO_2$	1.00E+11	0.00E+00	0.00E+00		
783	$C_5H_4OH=C_5H_4O+H$	2.10E+13	0.00E+00	4.80E+04		
784	$C_5H_4O=2C_2H_2+CO$	6.20E+41	-7.90E+00	9.87E+04		
785	$C_5H_4O+H=CO+c-C_4H_5$	4.30E+09	1.40E+00	3.90E+03		
786	$C_5H_4O+O=CO+HCO+C_3H_3$	6.20E+08	1.40E+00	-8.58E+02		
787	$c-C_4H_5+H=C_4H_6$	1.00E+13	0.00E+00	0.00E+00		
788	$c-C_4H_5+H=C_2H_4+C_2H_2$	1.00E+13	0.00E+00	0.00E+00		
789	$c-C_4H_5+O=CH_2CHO+C_2H_2$	1.00E+14	0.00E+00	0.00E+00		
790	$c-C_4H_5+O_2=CH_2CHO+CH_2CO$	4.80E+11	0.00E+00	1.90E+04		
791	$c-C_4H_5=C_4H_4+H$	3.00E+12	0.00E+00	5.20E+04		
792	$c-C_4H_5=C_2H_3+C_2H_2$	2.00E+12	0.00E+00	5.80E+04		
793	$aC_3H_5+C_2H_3=IC_5H_7+H$	1.00E+13	0.00E+00	0.00E+00		
794	$IC_5H_7+O=C_2H_3CHO+C_2H_3$	5.00E+13	0.00E+00	0.00E+00		
795	$IC_5H_7+OH=C_2H_3CHO+C_2H_4$	2.00E+13	0.00E+00	0.00E+00		
796	$C_6H_6+H=c-C_6H_7$	1.40E+51	-1.19E+01	1.61E+04		
797	$nC_4H_3+C_4H_2=A_1C_2H-$	9.60E+70	-1.78E+01	3.13E+04		
798	$C_6H_6+C_2H=C_6H_5C_2H+H$	5.00E+13	0.00E+00	0.00E+00		
799	$C_6H_5C_2H+H=A_1C_2H-+H_2$	2.50E+14	0.00E+00	1.60E+04		
800	$C_6H_5C_2H+OH=A_1C_2H-+H_2O$	1.60E+08	1.40E+00	1.45E+03		
801	$A_1C_2H-+H(+M)=C_6H_5C_2H(+M)$	1.00E+14	0.00E+00	0.00E+00		
	Low pressure limit	0.00E+00	6.60E+75	-1.63E+01		
	TROE centering	1.00E+00	1.00E-01	5.85E+02		
	Enhanced by	H2	H2O	CH4	CO	CO2
		2.00E+00	6.00E+00	2.00E+00	1.50E+00	2.00E+00
		C2H6				
		3.00E+00				
802	$A_1C_2H^*+H(+M)=C_6H_5C_2H(+M)$	1.00E+14	0.00E+00	0.00E+00		
	Low pressure limit	0.00E+00	6.60E+75	-1.63E+01		
	TROE centering	1.00E+00	1.00E-01	5.85E+02		
	Enhanced by	H2	H2O	CH4	CO	CO2
		2.00E+00	6.00E+00	2.00E+00	1.50E+00	2.00E+00
		C2H6				
		3.00E+00				
803	$C_6H_6+C_2H_3=C_6H_5C_2H_3+H$	7.90E+11	0.00E+00	6.40E+03		
804	$C_6H_5+C_2H_3=C_6H_5C_2H_3$	1.20E+27	-4.20E+00	7.24E+03		
805	$C_6H_5+C_2H_3=i-A_1C_2H_2+H$	8.50E-02	4.70E+00	1.84E+04		
806	$C_6H_5+C_2H_3=n-A_1C_2H_2+H$	9.40E+00	4.10E+00	2.32E+04		
807	$C_6H_5C_2H_3=i-A_1C_2H_2+H$	5.30E+27	-3.60E+00	1.09E+05		
808	$C_6H_5C_2H_3=n-A_1C_2H_2+H$	1.10E+32	-4.80E+00	1.19E+05		
809	$C_6H_5C_2H_3+H=A_1C_2H_3^*+H_2$	2.50E+14	0.00E+00	1.60E+04		
810	$C_6H_5C_2H_3+OH=A_1C_2H_3^*+H_2O$	1.60E+08	1.40E+00	1.45E+03		
811	$A_1C_2H_3^*+H(+M)=C_6H_5C_2H_3(+M)$	1.00E+14	0.00E+00	0.00E+00		
	Low pressure limit	0.00E+00	6.60E+75	-1.63E+01		
	TROE centering	1.00E+00	1.00E-01	5.85E+02		
	Enhanced by	H2	H2O	CH4	CO	CO2
		2.00E+00	6.00E+00	2.00E+00	1.50E+00	2.00E+00
		C2H6				

	3.00E+00				
812 C6H5C2H3+OH=n-A1C2H2+H2O	3.10E+06	2.00E+00	3.43E+03		
813 C6H5C2H3+OH=i-A1C2H2+H2O	1.55E+06	2.00E+00	4.30E+02		
814 n-A1C2H2+H=C6H5C2H+H2	1.50E+13	0.00E+00	0.00E+00		
815 i-A1C2H2+H=C6H5C2H+H2	3.00E+13	0.00E+00	0.00E+00		
816 n-A1C2H2+H=i-A1C2H2+H	9.90E+04	3.40E+00	2.20E+04		
817 n-A1C2H2+OH=C6H5C2H+H2O	2.50E+12	0.00E+00	0.00E+00		
818 i-A1C2H2+OH=C6H5C2H+H2O	5.00E+12	0.00E+00	0.00E+00		
819 A1C2H*+C2H2=A2-1	2.20E+62	-1.46E+01	3.31E+04		
820 A1C2H*+C2H2=A1C2H)2+H	1.80E+19	-1.70E+00	1.88E+04		
821 A1C2H*+C2H2=naphthylene+H	5.70E+64	-1.44E+01	5.70E+04		
822 A1C2H)2+H=A2-1	1.40E+64	-1.46E+01	2.99E+04		
823 A1C2H)2+H=naphthylene+H	1.90E+73	-1.63E+01	6.09E+04		
824 naphthylene+H=A2-1	4.90E+52	-1.24E+01	3.30E+04		
825 A1C2H3*+C2H2=C10H8+H	1.60E+16	-1.30E+00	6.60E+03		
826 n-A1C2H2+C2H2=C10H8+H	1.60E+16	-1.30E+00	5.40E+03		
827 C10H8+H=A2-1+H2	2.50E+14	0.00E+00	1.60E+04		
828 C10H8+H=A2-2+H2	2.50E+14	0.00E+00	1.60E+04		
829 C10H8+OH=A2-1+H2O	1.60E+08	1.40E+00	1.45E+03		
830 C10H8+OH=A2-2+H2O	1.60E+08	1.40E+00	1.45E+03		
831 A2-1+H(+M)=C10H8(+M)	1.00E+14	0.00E+00	0.00E+00		
Low pressure limit	0.00E+00	NaN	-3.14E+01		
TROE centering	2.00E-01	1.23E+02	4.78E+02		
Enhanced by	H2	H2O	CH4	CO	CO2
	2.00E+00	6.00E+00	2.00E+00	1.50E+00	2.00E+00
	C2H6				
	3.00E+00				
832 A2-2+H(+M)=C10H8(+M)	1.00E+14	0.00E+00	0.00E+00		
Low pressure limit	0.00E+00	NaN	-3.21E+01		
TROE centering	8.70E-01	4.93E+02	1.18E+02		
Enhanced by	H2	H2O	CH4	CO	CO2
	2.00E+00	6.00E+00	2.00E+00	1.50E+00	2.00E+00
	C2H6				
	3.00E+00				
833 A2-1+H=A2-2+H	2.40E+24	-1.80E+00	4.53E+04		
834 C10H8+C2H=A2C2HA+H	5.00E+13	0.00E+00	0.00E+00		
835 C10H8+C2H=A2C2HB+H	5.00E+13	0.00E+00	0.00E+00		
836 A2-1+C2H2=A2C2H2	1.70E+43	-9.10E+00	2.11E+04		
837 A2-1+C2H2=A2C2HA+H	1.30E+24	-3.10E+00	2.26E+04		
838 A2C2HA+H=A2C2H2	5.90E+46	-1.00E+01	1.91E+04		
839 A2C2H2+H=A2C2HA+H2	1.50E+13	0.00E+00	0.00E+00		
840 A2C2H2+OH=A2C2HA+H2O	2.50E+12	0.00E+00	0.00E+00		
841 A2C2HA+H=A2C2HA*+H2	2.50E+14	0.00E+00	1.60E+04		
842 A2C2HB+H=A2C2HB*+H2	2.50E+14	0.00E+00	1.60E+04		
843 A2C2HA+OH=A2C2HA*+H2O	1.60E+08	1.40E+00	1.45E+03		
844 A2C2HB+OH=A2C2HB*+H2O	1.60E+08	1.40E+00	1.45E+03		
845 A2C2HB*+H(+M)=A2C2HB(+M)	1.00E+14	0.00E+00	0.00E+00		
Low pressure limit	0.00E+00	NaN	-3.14E+01		
TROE centering	2.00E-01	1.23E+02	4.78E+02		
Enhanced by	H2	H2O	CH4	CO	CO2
	2.00E+00	6.00E+00	2.00E+00	1.50E+00	2.00E+00
	C2H6				
	3.00E+00				
846 A2C2HA*+H(+M)=A2C2HA(+M)	1.00E+14	0.00E+00	0.00E+00		
Low pressure limit	0.00E+00	NaN	-3.21E+01		
TROE centering	8.70E-01	4.93E+02	1.18E+02		
Enhanced by	H2	H2O	CH4	CO	CO2
	2.00E+00	6.00E+00	2.00E+00	1.50E+00	2.00E+00
	C2H6				
	3.00E+00				
847 A2C2HB*+C2H2=A3-1	1.10E+62	-1.46E+01	3.31E+04		
848 A2C2HB*+C2H2=A2C2H)2+H	1.80E+19	-1.70E+00	1.88E+04		
849 A2C2H)2+H=A3-1	6.90E+63	-1.46E+01	2.99E+04		
850 A2C2HA*+C2H2=A3-4	1.10E+62	-1.46E+01	3.31E+04		
851 A2C2HA*+C2H2=A2C2H)2+H	1.80E+19	-1.70E+00	1.88E+04		
852 A2C2H)2+H=A3-4	6.90E+63	-1.46E+01	2.99E+04		
853 A2C2HA+C2H=A2C2H)2+H	5.00E+13	0.00E+00	0.00E+00		
854 A2C2HB+C2H=A2C2H)2+H	5.00E+13	0.00E+00	0.00E+00		

855	A3+H=A3-1+H2	2.50E+14	0.00E+00	1.60E+04	
856	A3+H=A3-4+H2	2.50E+14	0.00E+00	1.60E+04	
857	A3+OH=A3-1+H2O	1.60E+08	1.40E+00	1.45E+03	
858	A3+OH=A3-4+H2O	1.60E+08	1.40E+00	1.45E+03	
859	A3-1+H(+M)=A3(+M)	1.00E+14	0.00E+00	0.00E+00	
	Low pressure limit	0.00E+00	NaN	-3.75E+01	
	TROE centering	1.00E+00	5.36E+02	1.45E+02	
	Enhanced by	H2	H2O	CH4	CO
		2.00E+00	6.00E+00	2.00E+00	1.50E+00
		C2H6			CO2
		3.00E+00			2.00E+00
860	A3-4+H(+M)=A3(+M)	1.00E+14	0.00E+00	0.00E+00	
	Low pressure limit	0.00E+00	NaN	-3.48E+01	
	TROE centering	1.00E-03	1.71E+02	1.71E+02	
	Enhanced by	H2	H2O	CH4	CO
		2.00E+00	6.00E+00	2.00E+00	1.50E+00
		C2H6			CO2
		3.00E+00			2.00E+00
861	A3-1+H=A3-4+H	3.80E+40	-6.30E+00	6.18E+04	
862	A2-1+C4H4=A3+H	3.30E+33	-5.70E+00	2.55E+04	
863	A2-2+C4H4=A3+H	3.30E+33	-5.70E+00	2.55E+04	
864	A2R5+H=A2R5+H2	2.50E+14	0.00E+00	1.60E+04	
865	A2R5+OH=A2R5+H2O	1.60E+08	1.40E+00	1.45E+03	
866	A2R5+H(+M)=A2R5(+M)	1.00E+14	0.00E+00	0.00E+00	
	Low pressure limit	0.00E+00	6.60E+75	-1.63E+01	
	TROE centering	1.00E+00	1.00E-01	5.85E+02	
	Enhanced by	H2	H2O	CH4	CO
		2.00E+00	6.00E+00	2.00E+00	1.50E+00
		C2H6			CO2
		3.00E+00			2.00E+00
867	A2-1+C2H2=A2R5+H	9.70E+30	-5.30E+00	2.16E+04	
868	A2C2HA+H=A2R5+H	4.60E+37	-7.00E+00	2.31E+04	
869	A2C2H2=A2R5+H	1.56E+46	-1.03E+01	4.13E+04	
870	A1C2H*+C6H6=A3+H	1.10E+23	-2.90E+00	1.59E+04	
871	C6H5+C6H5C2H=A3+H	1.10E+23	-2.90E+00	1.59E+04	
872	A3+C2H=A3C2H+H	5.00E+13	0.00E+00	0.00E+00	
873	A3-4+C2H2=A3C2H2	8.00E+61	-1.45E+01	3.48E+04	
874	A3-4+C2H2=A3C2H+H	1.20E+26	-3.40E+00	3.02E+04	
875	A3-4+C2H2=A4+H	6.60E+24	-3.40E+00	1.78E+04	
876	A3C2H+H=A3C2H2	1.90E+64	-1.51E+01	2.93E+04	
877	A3C2H+H=A4+H	9.00E+38	-7.40E+00	2.07E+04	
878	A3C2H2=A4+H	2.00E+63	-1.53E+01	4.32E+04	
879	A4+H=A4+H2	2.50E+14	0.00E+00	1.60E+04	
880	A4+OH=A4+H2O	1.60E+08	1.40E+00	1.45E+03	
881	A4+H=A4	1.00E+14	0.00E+00	0.00E+00	
882	C6H6+C6H5=P2+H	1.10E+23	-2.90E+00	1.59E+04	
883	C6H6+C6H5=P2-H	3.70E+32	-6.70E+00	9.87E+03	
884	P2-H=P2+H	3.80E+37	-8.00E+00	2.79E+04	
885	C6H5+C6H5=P2	2.00E+19	-2.00E+00	2.90E+03	
886	C6H5+C6H5=P2+H	2.30E-01	4.60E+00	2.90E+04	
887	P2=P2+H	1.10E+25	-2.70E+00	1.14E+05	
888	P2+H=P2+H2	2.50E+14	0.00E+00	1.60E+04	
889	P2+OH=P2+H2O	1.60E+08	1.40E+00	1.45E+03	
890	P2+C2H2=A3+H	4.60E+06	2.00E+00	7.30E+03	
891	C6H5O+O=HCO+2C2H2+CO	3.00E+13	0.00E+00	0.00E+00	
892	C6H5O+H(+M)=C6H5OH(+M)	2.50E+14	0.00E+00	0.00E+00	
	Low pressure limit	0.00E+00	1.00E+94	-2.18E+01	
	TROE centering	4.30E-02	3.04E+02	6.00E+04	
	Enhanced by	H2	H2O	CH4	CO
		2.00E+00	6.00E+00	2.00E+00	1.50E+00
		C2H6			CO2
		3.00E+00			2.00E+00
893	C5H4OH+H=CH2O+2C2H2	3.00E+13	0.00E+00	0.00E+00	
894	C5H4OH+O=CO2+nC4H5	3.00E+13	0.00E+00	0.00E+00	
895	C5H4O+O=CO2+2C2H2	3.00E+13	0.00E+00	0.00E+00	
896	C6H5C2H+OH=>C6H5+CH2CO	2.18E-04	4.50E+00	-1.00E+03	
897	A1C2H)2+OH=>A1C2H+CH2CO	2.18E-04	4.50E+00	-1.00E+03	
898	A2C2HA+OH=>A2-1+CH2CO	2.18E-04	4.50E+00	-1.00E+03	

899	A2C2HB+OH=>A2-2+CH2CO	2.18E-04	4.50E+00	-1.00E+03
900	A3C2H+OH=>A3-4+CH2CO	2.18E-04	4.50E+00	-1.00E+03
901	C6H5C2H+OH=>C6H5O+C2H2	1.30E+13	0.00E+00	1.06E+04
902	C6H5C2H3+OH=>C6H5O+C2H4	1.30E+13	0.00E+00	1.06E+04
903	A1C2H)2+OH=>C4H2+C6H5O	1.30E+13	0.00E+00	1.06E+04
904	C10H8+OH=>C6H5C2H+CH2CO+H	1.30E+13	0.00E+00	1.06E+04
905	A2C2HA+OH=>C6H5C2H+H2C4O+H	1.30E+13	0.00E+00	1.06E+04
906	A2C2HB+OH=>C6H5C2H+H2C4O+H	1.30E+13	0.00E+00	1.06E+04
907	A3+OH=>A2C2HB+CH2CO+H	6.50E+12	0.00E+00	1.06E+04
908	A3+OH=>A2C2HA+CH2CO+H	6.50E+12	0.00E+00	1.06E+04
909	A3C2H+OH=>A2C2HA+H2C4O+H	6.50E+12	0.00E+00	1.06E+04
910	A3C2H+OH=>A2C2HB+H2C4O+H	6.50E+12	0.00E+00	1.06E+04
911	A4+OH=>A3-4+CH2CO	1.30E+13	0.00E+00	1.06E+04
912	C6H5C2H+O=>HCCO+C6H5	2.04E+07	2.00E+00	1.90E+03
913	A1C2H)2+O=>HCCO+A1C2H-	2.04E+07	2.00E+00	1.90E+03
914	C6H5C2H3+O=>C6H5+CH3+CO	1.92E+07	1.80E+00	2.20E+02
915	A2C2HA+O=>HCCO+A2-1	2.04E+07	2.00E+00	1.90E+03
916	A2C2HB+O=>HCCO+A2-2	2.04E+07	2.00E+00	1.90E+03
917	C6H5C2H+O=>C2H+C6H5O	2.20E+13	0.00E+00	4.53E+03
918	C6H5C2H3+O=>C2H3+C6H5O	2.20E+13	0.00E+00	4.53E+03
919	A1C2H)2+O=>C6H5O+C4H	2.20E+13	0.00E+00	4.53E+03
920	C10H8+O=>CH2CO+C6H5C2H	2.20E+13	0.00E+00	4.53E+03
921	A2C2HA+O=>A1C2H)2+CH2CO	2.20E+13	0.00E+00	4.53E+03
922	A2C2HB+O=>A1C2H)2+CH2CO	2.20E+13	0.00E+00	4.53E+03
923	A3+O=>A2C2HA+CH2CO	1.10E+13	0.00E+00	4.53E+03
924	A3+O=>A2C2HB+CH2CO	1.10E+13	0.00E+00	4.53E+03
925	A3C2H+O=>A2C2HA+H2C4O	1.10E+13	0.00E+00	4.53E+03
926	A3C2H+O=>A2C2HB+H2C4O	1.10E+13	0.00E+00	4.53E+03
927	A4+O=>A3-4+HCCO	2.20E+13	0.00E+00	4.53E+03
928	A1C2H*+O2=>1-C6H4+CO+HCO	2.10E+12	0.00E+00	7.47E+03
929	A1C2H-+O2=>1-C6H4+CO+HCO	2.10E+12	0.00E+00	7.47E+03
930	A1C2H3*+O2=>1-C6H6+CO+HCO	2.10E+12	0.00E+00	7.47E+03
931	n-A1C2H2+O2=>C6H5+CO+CH2O	1.00E+11	0.00E+00	0.00E+00
932	A2-1+O2=>C6H5C2H+HCO+CO	2.10E+12	0.00E+00	7.47E+03
933	A2-2+O2=>C6H5C2H+HCO+CO	2.10E+12	0.00E+00	7.47E+03
934	A2C2HA*+O2=>A2-1+CO+CO	2.10E+12	0.00E+00	7.47E+03
935	A2C2HB*+O2=>A2-2+CO+CO	2.10E+12	0.00E+00	7.47E+03
936	A3-4+O2=>A2C2HB+HCO+CO	2.10E+12	0.00E+00	7.47E+03
937	A3-1+O2=>A2C2HA+HCO+CO	2.10E+12	0.00E+00	7.47E+03
938	A4+O2=>A3-4+CO+CO	2.10E+12	0.00E+00	7.47E+03

# Appendix C

## 30 kWth Coal Combustor Standard Operating Procedure (SOP)

### C.1 Preliminaries

1. Calibrate oxygen sensor, NO, and CO analyzers.
2. Replace filters and desiccants as necessary.
3. Verify oxygen sampling line is free of ash and moisture.
4. Start oxygen slipstream cooling water.
5. Verify all flow meters are shut off before beginning ignition procedure.

### C.2 Ignition

1. Close exhaust damper.
2. Remove ignition port cover.
3. Set secondary air flow to slightly lift the float from the bottom of the “SO Mix” flow meter and verify that all flow is being introduced tangentially (i.e. 100% SO swirl).
4. Open methane/propane tank. (NOTE: IT IS CRITICAL THAT THE PILOT FLOW METER VALVE IS CLOSED TO PREVENT THE BUILD UP OF A POTENTIALLY DANGEROUS PREMIXTURE IN THE COMBUSTOR)
5. Open ignition wand valve on flow panel.
6. Light ignition wand and insert into ignition port. Verify visually that ignition wand remained ignited.
7. Open pilot gas flow meter valve and set steel ball scale to 20-30.
8. Open exhaust baffle to marked position ( $\sim 0.04$  inH<sub>2</sub>O).



9. Increase SO air flow to 6-8 SCFM at 50 psig.
10. Verify pilot fuel is burning, close local ignition wand valve, and remove ignition wand.
11. Replace ignition port cover.

## **C.3 Coal Delivery**

1. Increase methane/propane pilot flow to a scale reading of 55 for the steel ball.
2. Begin sending air to the PO (eductor) and set the scale reading to 50 for the steel ball at 50 psig. (NOTE: IF EDUCTOR BAG IS INSTALLED BAG FLOW AIR SHOULD BE A MINIMUM OF 70 LPM BEFORE SENDING FLOW TO THE EDUCTOR)
3. Insert ear plugs.
4. Increase vibrator plate pressure to 60 psig.
5. Set coal feeder RPM to 180 (on low speed setting, default) and press the “run” button.
6. Wait approx. 30 seconds and verify that coal is burning steadily.
7. Shut pilot methane/propane tank off and close all pilot and ignition valves on flow panel.
8. Set desired flow settings and wait 45-80 minutes for steady state operation.

## **C.4 Shutdown**

1. Press the “stop” button on K-Tron coal feeder controller and turn off Schenk (sawdust) feeder if cofiring.
2. Wait 30 seconds for residual fuel to enter combustor and burn and then turn vibrator plate pressure regulator off.
- 3a. Under air-fired conditions reduce the air flow pressure to 15 psig, turn bag and eductor flows off, and leave 2-3 SCFM of flow at 50 psig flowing through the combustor for cooling

purposes. If experiments are to be run the following day, the air can be turned off to prevent rapid cooling such that the startup time on the following day can be reduced.

3b. Under oxy-fuel conditions, close the pressure builder and turn the oxygen dewar off to bleed the pressure from the oxygen lines. After the oxygen flow is eliminated, reduce the flow of carbon dioxide in half at the flow panel and keep the pressure under 50 psig. Reduce the voltages on the 3 Sylvania heaters and the ceiling heater in half. Close the CO<sub>2</sub> dewar pressure regulators. Close two of the CO<sub>2</sub> dewar valves. Turn the three Sylvania heaters down to 20 Volts and turn off the third CO<sub>2</sub> dewar. Turn all CO<sub>2</sub> heaters off. Turn off Sylvania thermocouple readout.

4. Turn off O<sub>2</sub> slipstream cooling water.

# References

- [1] M. Faraday, *The Chemical History of a Candle*. Dover: New York, 2002; p 223.
- [2] E.P.A. *Semiannual Regulatory Agenda--Spring 2009 pp.44*; 2009.
- [3] E.I.A. [www.eia.gov](http://www.eia.gov)
- [4] E.I.A. *International Energy Outlook 2009*; 2009.
- [5] J. Deutch, Moniz, E. J. *The Future of Coal*; MIT: 2007.
- [6] C. E. Baukal, *Oxygen Enhanced Combustion*. CRC Press LLC: Boca Raton, 1998; p 490.
- [7] H. Kobayashi *Oxygen enriched combustion system performance study: Phase 1, Interim/final report: Volume 1, Technical and economic analysis*; DOE/ID/12597-1; 1987.
- [8] S. J. Williams, Cuervo, L. A., Chapman, M. A. *High-Temperature Industrial Process Heating: Oxygen-Gas Combustion and Plasma Heating Systems*; Gas Research Institute: Chicago, 1989.
- [9] K. Callaghan, Nemsler, S., Poola, R. B., Stork, K. C., Sekar, R. R., Johnson, B. *Variable Air Composition with Polymer Membrane--A New Low Emissions Tool*; SAE International: 1998.
- [10] D. Assanis; E. Karvounis; R. Sekar; W. Marr, J. Eng. Gas Turb. Power 115 (4) (1993) 761-8.
- [11] R. R. Sekar; W. W. Marr; D. N. Assanis; R. L. Cole; T. J. Marciniak; J. E. Schaus, J. Eng. Gas Turb. Power 113 (3) (1991) 365-9.
- [12] R. B. Poola; R. Sekar, J. Eng. Gas Turb. Power 125 (2) (2003) 524-533.
- [13] R. Poola; R. Sekar, ICE (American Society of Mechanical Engineers) 37-1 (Diesel Combustion and Emissions, Fuel Injections and Sprays) (2001) 77-88.
- [14] D. N. Assanis; R. B. Poola; R. Sekar; G. R. Cataldi, J. Eng. Gas Turb. Power 123 (1) (2001) 157-166.
- [15] D. Lahiri; P. S. Mehta; R. B. Poola; R. Sekar, ICE (American Society of Mechanical Engineers) 29-3 (Engine Combustion Performance and Emissions, Vol. 3) (1997) 119-127.
- [16] R. B. Poola; R. Sekar; D. N. Assanis; G. R. Cataldi, ICE (American Society of Mechanical Engineers) 27-4 (Natural Gas Engines, Combustion, Emissions and Simulation) (1996) 115-125.
- [17] H. S. Coombe; S. Nieh, Energy Conversion and Management 48 (5) (2007) 1499-1505.
- [18] B. J. P. Buhre; L. K. Elliott; C. D. Sheng; R. P. Gupta; T. F. Wall, Prog. Energy Combust. Sci. 31 (4) (2005) 283-307.
- [19] A. F. Sarofim in: 2nd IEAGHG International Oxy-Combustion Workshop, *Oxy-fuel Combustion: Progress and Remaining Issues*, January 25-26, 2007, 2007; Windsor, CT.
- [20] A. J. Mackrory; D. R. Tree, Proceedings of the International Technical Conference on Coal Utilization & Fuel Systems 33rd (Vol. 1) (2008) 162-173.
- [21] A. J. Mackrory. A Mechanistic Investigation of Nitrogen Evolution in Pulverized Coal Oxy-Fuel Combustion. Brigham Young University, 2008.
- [22] D. A. Tillman *EPRI-USDOE Cooperative Agreement: Cofiring Biomass with Coal*; FC22-96PC96252--18, National Energy Technology Lab., Pittsburgh, PA (US); National Energy Technology Lab., Morgantown, WV (US): 2001.

- [23] D. A. Tillman, Proceedings - Annual International Pittsburgh Coal Conference 20th (2003) 712-722.
- [24] M. Sami; K. Annamalai; M. Wooldridge, Prog. Energy Combust. Sci. 27 (2) (2001) 171-214.
- [25] S. Van Loo; J. Koppejan, *Handbook of Biomass Combustion and Co-Firing*. Earthscan Publications: 2007.
- [26] C. S. Allred; D. Arnold; T. J. Barrett; A. Beehler; A. Bement; G. Buchanan; T. C. Dorr; G. Gray; S. Hays; A. Karsner; R. Orbach; P. Swagel; J. Turner, in: D. o. Energy, (Ed.) 2008.
- [27] A. Demirbas, Prog. Energy Combust. Sci. 31 (2) (2005) 171-192.
- [28] G. Sugiyama, Proc. Combust. Inst. 25 (1994) 601-8.
- [29] K. C. Lin; G. M. Faeth, J. Prop. Power 12 (4) (1996) 691-698.
- [30] J. Du, Axelbaum, R. L., Combust. Flame 100 (3) (1995) 367-75.
- [31] A. Atreya, C. Zhang, H.K. Kim, T. Shamim, J. Suh, Proc. Combust. Inst. 26 (2) (1996) 2181-2189.
- [32] B. H. Chao; S. Liu; R. L. Axelbaum, Combust. Sci. Tech. 138 (1-6) (1998) 105-135.
- [33] C. J. Sun; C. J. Sung; H. Wang; C. K. Law, Combust. Flame 107 (4) (1996) 321-335.
- [34] P. B. Sunderland; R. L. Axelbaum; D. L. Urban, NASA Conference Publication 208917 (Fifth International Microgravity Combustion Workshop, 1999) (1999) 475-478.
- [35] P. B. Sunderland; R. L. Axelbaum; D. L. Urban; B. H. Chao; S. Liu, Combust. Flame 132 (1/2) (2003) 25-33.
- [36] P. B. Sunderland; D. L. Urban; D. P. Stocker; B. H. Chao; R. L. Axelbaum, Combust. Sci. Tech. 176 (12) (2004) 2143-2164, 1 plate.
- [37] B. M. Kumfer; S. A. Skeen; R. Chen; R. L. Axelbaum, Combust. Flame 147 (3) (2006) 233-242.
- [38] B. M. Kumfer; S. A. Skeen; R. L. Axelbaum, Combust. Flame 154 (3) (2008) 546-556.
- [39] R. Chen; R. L. Axelbaum, Combust. Flame 142 (1-2) (2005) 62-71.
- [40] I. M. Kennedy, Combust. Sci. Tech. 59 (1) (1988) 107-121.
- [41] D. X. Du; R. L. Axelbaum; C. K. Law, Proc. Combust. Inst. 22 (1988) 387-94.
- [42] K. C. Lin; G. M. Faeth, Combust. Flame 115 (4) (1998) 468-480.
- [43] Z. Cheng; J. A. Wehrmeyer; R. W. Pitz, Combust. Sci. Tech. 178 (12) (2006) 2145 - 2163.
- [44] S. Nakayama; Y. Noguchi; T. Kiga; S. Miyamae; U. Maeda; M. Kawai; T. Tanaka; K. Koyata; H. Makino, Energy Conversion and Management 33 (5-8) (1992) 379-86.
- [45] N. Kimura; K. Omata; T. Kiga; S. Takano; S. Shikisima, Energy Conversion and Management 36 (6-9) (1995) 805-8.
- [46] T. Nozaki; S.-i. Takano; T. Kiga; K. Omata; N. Kimura, Energy (Oxford) 22 (2/3) (1997) 199-205.
- [47] K. Okazaki; T. Ando, Energy (Oxford) 22 (2/3) (1997) 207-215.
- [48] T. Kiga; S. Takano; N. Kimura; K. Omata; M. Okawa; T. Mori; M. Kato, Energy Conversion and Management 38 (Suppl., Proceedings of the Third International Conference on Carbon Dioxide Removal, 1996) (1997) S129-S134.
- [49] T. Kiga, in: *Advanced Coal Combustion*, T. Miura, (Ed.) Nova Science Publishers Inc.: 2001; pp 185-41.
- [50] Y. Q. Hu; N. Kobayashi; M. Hasatani, Fuel 80 (13) (2001) 1851-1855.

- [51] Y. Q. Hu; N. Kobayashi; M. Hasatani, *Energy Conversion and Management* 44 (14) (2003) 2331-2340.
- [52] R. Sangras; F. Chatel-Pelage; P. Pranda; H. Farzan; S. J. Vecci; Y. Lu; S. Chen; M. Rostam-Abadi; A. C. Bose, *Proceedings of the International Technical Conference on Coal Utilization & Fuel Systems* 2004.
- [53] Y. Tan; E. Croiset, *Proceedings of the International Technical Conference on Coal Utilization & Fuel Systems 30th (Vol.1)* (2005) 529-536.
- [54] H. Farzan; S. J. Vecci; F. Chatel-Pelage; P. Pranda; A. C. Bose, *Proceedings - Annual International Pittsburgh Coal Conference 22nd* (2005) 244/1-244/12.
- [55] Y. Tan; E. Croiset; M. A. Douglas; K. V. Thambimuthu, *Fuel* 85 (4) (2006) 507-512.
- [56] J. Maier; B. Dhungel; P. Moenckert; G. Scheffknecht, *Proceedings of the International Technical Conference on Coal Utilization & Fuel Systems 31st (Vol. 1)* (2006) 65-75.
- [57] S. Hjaertstam; K. Andersson; F. Johnsson, *Proceedings of the International Technical Conference on Coal Utilization & Fuel Systems 32nd (Vol. 1)* (2007) 201-212.
- [58] G. J. Scheffknecht; B. D. Maier; P. Monckert in: *Third International Conference on Clean Coal Technologies for our Future, Investigation of Oxy-Coal Combustion in Semi-technical Test Facilities*, May 15-17, 2007; Cagliari, Sardinia, Italy.
- [59] B. Dhungel; J. Maier; G. Scheffknecht in: *AICHE 2007 Annual Meeting, Emission Behaviour during Oxy-Coal Combustion*, November 4-9, 2007; Salt Lake City, UT.
- [60] D. K. McDonald; T. J. Flynn; D. J. DeVault; R. Varagani; S. Levesque; W. Castor, *Proceedings of the International Technical Conference on Coal Utilization & Fuel Systems 33rd (Vol. 1)* (2008) 1-12.
- [61] J. Du, Axelbaum, R. L., *Proc. Combust. Inst.* 26 (1) (1996) 1137-1142.
- [62] A. Kitajima; H. Torikai; M. Takeuchi; M. Oya, *Combust. Flame* 137 (2004) 93-108.
- [63] C. K. Law, *Combustion Physics*. 1st ed.; Cambridge: New York, 2006.
- [64] F. A. Williams, *Combustion Theory; the Fundamental Theory of Chemically Reacting Flow Systems*. 2nd ed. ed.; Benjamin/Cummings Pub. Co.: Menlo Park, CA, 1985; p 680 pp.
- [65] D. W. Dockery; C. A. Pope; X. Xu; J. D. Spengler; J. H. Ware; M. E. Fay; B. G. Ferris; F. E. Speizer, *New England Journal of Medicine* 329 (24) (1993) 1753-1759.
- [66] K. Siegmann; H. C. Siegmann, *Current Problems in Condensed Matter*, [Proceedings of an International Workshop on Current Problems in Condensed Matter: Theory and Experiment], Cocoyoc, Mex., Jan. 5-9, 1997 (1998) 143-160.
- [67] J. L. Durant; W. F. Busby, Jr.; A. L. Lafleur; B. W. Penman; C. L. Crespi, *Mutation research* 371 (3-4) (1996) 123-57.
- [68] D. A. Kaden; R. A. Hites; W. G. Thilly, *Cancer Research* 39 (10) (1979) 4152-9.
- [69] A. W. Wood; W. Levin; R. L. Chang; M.-T. Huang; D. E. Ryan; P. E. Thomas; R. E. Lehr; S. Kumar; M. Koreeda; et al., *Cancer Research* 40 (3) (1980) 642-9.
- [70] P. P. Fu; F. A. Beland; S. K. Yang, *Carcinogenesis* 1 (8) (1980) 725-7.
- [71] W. F. Busby, Jr.; E. K. Stevens; E. R. Kellenbach; J. Cornelisse; J. Lugtenburg, *Carcinogenesis FIELD Full Journal Title: Carcinogenesis* 9 (5) (1988) 741-6.
- [72] A. L. Lafleur; J. P. Longwell; L. Shirname-More; P. A. Monchamp; W. A. Peters; E. F. Plummer, *Energy & Fuels* 4 (3) (1990) 307-19.
- [73] S. Menon; J. Hansen; L. Nazarenko; Y. Luo, in: 2002; Vol. 297, pp 2250-2253.
- [74] V. Ramanathan; G. Carmichael, *Nature Geoscience* 1 (4) (2008) 221-227.

- [75] M. Z. Jacobson, *Journal of Climate* 17 (15) (2004) 2909-2926.
- [76] W. L. Chameides; M. Bergin, in: 2002; Vol. 297, pp 2214-2215.
- [77] J. Hansen; L. Nazarenko, *Proceedings of the national academy of sciences* 101 (2) (2004) 423-428.
- [78] G. T. Wolff, *Environment International* 11 (2-4) (1985) 259-69.
- [79] H. B. Palmer; C. F. Cullis, *Chemistry and Physics of Carbon* 1 (1965) 265.
- [80] K. Tian; F. Liu; K. A. Thomson; D. R. Snelling; G. J. Smallwood; D. Wang, *Combust. Flame* 138 (1/2) (2004) 195-198.
- [81] U. O. Koçylu; G. M. Faeth; T. L. Farias; M. G. Carvalho, *Combust. Flame* 100 (4) (1995) 621-33.
- [82] I. Glassman, *Combustion*. Academic Press: San Diego, 1996; p 632.
- [83] J. A. Miller; C. F. Melius, *Combust. Flame* 91 (1991) 21-39.
- [84] N. M. Marinov; W. J. Pitz; C. K. Westbrook; M. J. Castaldi; S. M. Senkan, *Combust. Sci. Tech.* 116 (1) (1996) 211-287.
- [85] H. Richter; J. B. Howard, *Prog. Energy Combust. Sci.* 26 (4-6) (2000) 565-608.
- [86] C. J. Pope; J. A. Miller, *Proc. Combust. Inst.* 28 (2) (2000) 1519-1528.
- [87] J. A. Miller; S. J. Klippenstein, *J. Phys. Chem. A* 107 (39) (2003) 7783-7799.
- [88] J. A. Miller; M. J. Pilling; J. Troe, *Proc. Combust. Inst.* 30 (1) (2005) 43-88.
- [89] C. S. McEnally; L. D. Pfefferle; B. Atakan; K. Kohse-Höinghaus, *Prog. Energy Combust. Sci.* 32 (3) (2006) 247-294.
- [90] Y. Georgievskii; J. A. Miller; S. J. Klippenstein, *Physical Chemistry Chemical Physics* 9 (31) (2007) 4259-4268.
- [91] N. Hansen; T. A. Cool; P. R. Westmoreland; K. Kohse-Höinghaus, *Prog. Energy Combust. Sci.* 35 (2) (2009) 168-191.
- [92] C. A. Schuetz; M. Frenklach, *Proc. Combust. Inst.* 29 (Pt. 2) (2002) 2307-2314.
- [93] B. S. Haynes; H. G. Wagner, *Prog. Energy Combust. Sci.* 7 (4) (1981) 229-273.
- [94] H. Bockhorn, *Soot Formation in Combustion*. Springer-Verlag: 1994.
- [95] I. M. Kennedy, *Prog. Energy Combust. Sci.* 23 (2) (1997) 95.
- [96] I. S. McLintock, *Combust. Flame* 12 (3) (1968) 217-25.
- [97] I. Glassman; P. Yaccarino, *Proc. Combust. Inst.* 18 (1981) 1175-83.
- [98] R. L. Axelbaum; W. L. Flower; C. K. Law, *Combust. Sci. Tech.* 61 (1-3) (1988) 51-73.
- [99] R. L. Axelbaum; C. K. Law, *Chemical and Physical Processes in Combustion* (1989) 60/1-60/4.
- [100] R. L. Axelbaum; C. K. Law, *Proc. Combust. Inst.* 23 (1991) 1517-23.
- [101] R. L. Axelbaum; C. K. Law; W. L. Flower, *Proc. Combust. Inst.* 22 (1989) 379-86.
- [102] I. Glassman, *Proc. Combust. Inst.* 27 (1998) 1589-1596.
- [103] H. S. Hura; I. Glassman, *Chemical and Physical Processes in Combustion* (1985) Paper 50, 6 pp.
- [104] H. S. Hura; I. Glassman, *Proc. Combust. Inst.* 22nd (1989) 371-8.
- [105] G. Sugiyama; L. Xie; M. Kono, *Nippon Kikai Gakkai Ronbunshu, B-hen* 55 (519) (1989) 3532-7.
- [106] D. X. Du; R. L. Axelbaum; C. K. Law, *Proc. Combust. Inst.* 23 (1990) 1501-7.
- [107] F. Liu; H. Guo; G. J. Smallwood; O. L. Gulder, *Combust. Flame* 125 (1/2) (2001) 778-787.
- [108] I. Glassman; P. Yaccarino, *Combust. Sci. Tech.* 24 (3-4) (1980) 107-14.
- [109] K. C. Lin; G. M. Faeth, *J. Prop. Power* 12 (1) (1996) 10-17.
- [110] K. C. Lin; P. B. Sunderland; G. M. Faeth, *Combust. Flame* 104 (3) (1996) 369-75.

- [111] K. T. Kang; J. Y. Hwang; S. H. Chung; W. Lee, *Combust. Flame* 109 (1/2) (1997) 266-281.
- [112] S. Liu; B. H. Chao; R. L. Axelbaum, *Combust. Flame* 140 (1-2) (2005) 1-23.
- [113] D. X. Du; R. L. Axelbaum; C. K. Law, *Combust. Flame* 102 (1/2) (1995) 11-20.
- [114] A. Gomez; M. G. Littman; I. Glassman, *Combust. Flame* 70 (2) (1987) 225-41.
- [115] K. Saito; A. S. Gordon; F. A. Williams; W. F. Stickle, *Combust. Sci. Tech.* 80 (1-3) (1991) 103-19.
- [116] C. S. McEnally; L. D. Pfefferle, *Combust. Flame* 117 (1/2) (1999) 362-372.
- [117] R. A. Dobbins, *Combust. Flame* 130 (3) (2002) 204-214.
- [118] J. Y. Hwang; S. H. Chung, *Combust. Flame* 125 (1) (2001) 752.
- [119] A. Kitajima; T. Hatanaka; M. Takeuchi; H. Torikai; T. Miyadera, *Combust. Sci. Tech.* 142 (2005) 72-88.
- [120] G. W. Sidebotham; I. Glassman, *Combust. Flame* 90 (3-4) (1992) 269-83.
- [121] G. W. Sidebotham; I. Glassman, *Combust. Sci. Tech.* 81 (4-6) (1992) 207-19.
- [122] D. B. Makel; I. M. Kennedy, *Combust. Sci. Tech.* 97 (4-6) (1994) 303-30.
- [123] R. L. Vander Wal, *Combust. Flame* 26 (1996) 2269-2275.
- [124] L. G. Blevins; R. A. Fletcher; B. A. Benner, Jr.; E. B. Steel; G. W. Mulholland, *Proc. Combust. Inst.* 29 (2002) 2325-2333.
- [125] K. C. Oh; U. D. Lee; H. D. Shin; E. J. Lee, *Combust. Flame* 140 (2005) 249-254.
- [126] C. R. Kaplan; K. Kailasanath, *Combust. Flame* 124 (1/2) (2001) 275-294.
- [127] B. J. McBride; S. Gordon *Computer program for calculation of complex chemical equilibrium compositions and applications*; NASA-RP-1311-P2; Cleveland, 1996.
- [128] I. Glassman; O. Nishida; G. Sidebotham, *Critical temperatures of soot formation*. Springer-Verlag: Heidelberg, 1994; Vol. 59, p 316-24.
- [129] S. J. Harris; A. M. Weiner; C. C. Ashcraft, *Combust. Flame* 64 (1) (1986) 65-81.
- [130] R. J. Kee; J. A. Miller; G. H. Evans; G. Dixon-Lewis, *Proc. Combust. Inst.* 22nd (1989) 1479-94.
- [131] A. E. Lutz; R. J. Kee; J. F. Grcar; F. M. Rupley *OPPDIF: A Fortran program for computing opposed-flow diffusion flames*; SAND96-8243; Sandia National Laboratories: Livermore, CA, 1997.
- [132] H. Wang; M. Frenklach, *Combust. Flame* 110 (1/2) (1997) 173-221.
- [133] J. Appel; H. Bockhorn; M. Frenklach, *Combust. Flame* 121 (1/2) (2000) 122-136.
- [134] T. P. Pandya; F. J. Weinberg, *Proceedings of the Royal Society of London. Series A, Mathematical and Physical Sciences* 1964.
- [135] T. P. Pandya; N. K. Srivastava, *Combust. Sci. Tech.* 11 (5) (1975) 165-180.
- [136] R. W. Bilger, *Combust. Flame* 30 (1977) 277.
- [137] X. Y. Hai Wang, Ameya V. Joshi, Scott G. Davis, Alexander Laskin, Fokion Egolfopoulos, Chung K. Law USC Mech Version II. High-Temperature Combustion Reaction Model of H<sub>2</sub>/CO/C<sub>1</sub>-C<sub>4</sub> Compounds. <http://ignis.usc.edu>
- [138] R. W. Bilger, *Proc. Combust. Inst.* 22nd (1989) 475-88.
- [139] V. R. Lecoustre; B. H. Chao; P. B. Sunderland; D. L. Urban; D. P. Stocker; R. L. Axelbaum, *Chemical and Physical Processes in Combustion* (2007) c12/1-c12/10.
- [140] S. A. Skeen, Yablonsky, G., Axelbaum, R. L., *Combust. Flame* (2009), doi:10.1016/j.combustflame.2009.07.009.
- [141] C. Cavallotti; R. Rota; S. Carra, *The Journal of Physical Chemistry A* 106 (34) (2002) 7769-7778.
- [142] K. M. Leung; R. P. Lindstedt; W. P. Jones, *Combust. Flame* 87 (3-4) (1991) 289-305.

- [143] J. Szekeley; J. W. Evans; H. Y. Sohn, *Gas-solid reactions*. Academic Pr: 1976.
- [144] D. A. Tillman, *The combustion of solid fuels and wastes*. Academic Press New York: 1991.
- [145] S. R. Turns, *An Introduction to Combustion*. McGraw-Hill: New York, 1999.
- [146] P. Glarborg; A. D. Jensen; J. E. Johnsson, *Prog. Energy Combust. Sci.* 29 (2) (2003) 89-113.
- [147] J. Tomeczek, *Coal Combustion*. Krieger: Malabar, 1994; p 166.
- [148] J. G. Speight, *Handbook of coal analysis*. Wiley-Interscience: 2005.
- [149] *BP Statistical Review of World Energy June 2009*; British Petroleum: 2009.
- [150] E.I.A. Coal Prices. <http://www.eia.doe.gov/neic/infosheets/coalprice.html>
- [151] T. A. Torp; J. Gale, *Energy* 29 (9-10) (2004) 1361-1369.
- [152] CO2 Sequestration.  
[http://www.basinelectric.com/Energy\\_Resources/Gas/CO2\\_Sequestration/](http://www.basinelectric.com/Energy_Resources/Gas/CO2_Sequestration/)
- [153] M. Lotz; A. C. Brent, *Journal of Energy in Southern Africa* 19 (1) (2008) 13.
- [154] S. M. Benson; D. R. Cole, *ELEMENTS* 4 (5) (2008) 325-331.
- [155] J. D. Figueroa; T. Fout; S. Plasynski; H. McIlvried; R. D. Srivastava, *International Journal of Greenhouse Gas Control* 2 (1) (2008) 9-20.
- [156] M. C. Trachtenberg; R. M. Cowan; D. A. Smith; D. A. Horazak; M. D. Jensen; J. D. Laumb; A. P. Vucelic; H. Chen; L. Wang; X. Wu, *Energy Procedia* 1 (1) (2009) 353-360.
- [157] Y. Lu; S. Chen; M. Rostam-Abadi; R. K. Varagani; F. Chatel-Pelage; P. Pranda; A. C. Bose, *Proc. - Annu. Int. Pittsburgh Coal Conf. 22nd (2005)* 277/1-277/15.
- [158] H. Liu; K. Okazaki, *Fuel* 82 (11) (2003) 1427-1436.
- [159] R. Varagani; F. Chatel-Pelage; P. Pranda; Y. Lu; S. Chen; M. Rostam-Abadi; H. Farzan; S. J. Vecci; A. C. Bose in: *Third Annual Conference on Carbon Sequestration, Oxycombustion in pulverized coal-fired boiler: a promising technology for CO2 capture*, May 3-6, 2004; Alexandria, VA.
- [160] J. Hong; G. Chaudhry; J. G. Brisson; R. Field; M. Gazzino; A. F. Ghoniem, *Energy* 34 (9) (2009) 1332-1340.
- [161] F. Chatel-Pelage; R. Varagani; P. Pranda; N. Perrin; H. Farzan; S. J. Vecci; Y. Lu; S. Chen, *Therm. Sci.* 10 (3) (2006) 119-142.
- [162] K. J. McCauley; H. Farzan; K. C. Alexander; D. K. McDonald; R. Varagani; R. Prabhakar; J. P. Tranier; N. Perrin, *Energy Procedia* 1 (1) (2009) 439-446.
- [163] B. Metz, *IPCC Special Report on Carbon Dioxide Capture and Storage*. Cambridge University Press: 2005.
- [164] A. L. Robinson; J. S. Rhodes; D. W. Keith, *Environ. Sci. Technol* 37 (22) (2003) 5081-5089.
- [165] J. Goldemberg; S. Teixeira Coelho, *Energy Policy* 32 (6) (2004) 711-714.
- [166] E. Hughes, *Biomass and Bioenergy* 19 (6) (2000) 457-465.
- [167] R. D. Perlack; L. L. Wright; A. F. Turhollow; R. L. Graham; B. J. Stokes; D. C. Erbach, in: *Storming Media*: 2005.
- [168] J. R. Hess; T. D. Foust; L. Wright; S. Sokhansanj *Roadmap for Agriculture Biomass Feedstock Supply in the United States*; DOE/NE-ID-11129. US Department of Energy, Washington (DC): 2003.
- [169] National Fire Plan and National Energy Plan: An Untapped Opportunity.  
<http://www.amforest.org/resource/issue-papers/AFRC%20IssuePapers%20NationalFire.pdf>
- [170] DOE Bioenergy Research Centers. <http://genomicsgtl.energy.gov/centers/>



- [171] M. Sami; K. Annamalai; S. Dhanapalan; M. Wooldridge, HTD (Am. Soc. Mech. Eng.) FIELD Full Journal Title:HTD (American Society of Mechanical Engineers) 364-2 (Proceedings of the ASME Heat Transfer Division--1999, Vol. 2) (1999) 363-371.
- [172] B. Arias; C. Pevida; F. Rubiera; J. J. Pis, Fuel 87 (12) (2008) 2753-2759.
- [173] K. R. G. Hein; J. M. Bemtgen, Fuel Processing Technology 54 (1-3) (1998) 159-169.
- [174] H. Spliethoff; K. R. G. Hein, Fuel processing technology 54 (1-3) (1998) 189-205.
- [175] J. B. Howard, Chemistry of coal utilization (1981) 665-784.
- [176] G. R. Gavalas, *Coal Pyrolysis*. Elsevier Scientific Publishing Co., Amsterdam, Netherland: 1982.
- [177] P. R. Solomon; M. A. Serio; E. M. Suuberg, Prog. Energy Combust. Sci. 18 (2) (1992) 133-220.
- [178] D. B. Anthony; J. B. Howard; H. C. Hottel; H. P. Meissner, Proc. Combust. Inst. 15 (1975) 1303-17.
- [179] D. B. Anthony; J. B. Howard, AIChE Journal 22 (4) (1976) 625-56.
- [180] D. J. Seery; J. D. Freihaut; W. M. Proscia; J. B. Howard; W. Peters; J. Hsu; M. Hajaligol; A. Sarofim; R. Jenkins; et al. *Kinetics of coal pyrolysis: Volume 1, Sections 1-5: final report*; United Technol. Res. Cent., East Hartford, CT, USA.: 1989; p 438 pp.
- [181] H. Kobayashi; J. B. Howard; A. F. Sarofim, Proc. Combust. Inst. 16 (1977) 411-25.
- [182] W. J. McLean; D. R. Hardesty; J. H. Pohl, Proc. Combust. Inst. 18 (1) (1981) 1239-1248.
- [183] W. R. Seeker; G. S. Samuelsen; M. P. Heap; J. D. Trolinger, Proc. Combust. Inst. 18 (1) (1981) 1213-1226.
- [184] D. J. Seery; J. D. Freihaut; R. G. Jenkins; R. H. Essenhigh; J. B. Howard; W. A. Peters; A. F. Sarofim *Kinetics of coal pyrolysis and devolatilization*; United Technol. Res. Cent., East Harford, CT, USA.: 1985; pp 364-72.
- [185] K. L. Smith; L. D. Smoot; T. H. Fletcher, Coal Science and Technology 20 (Fundamentals of Coal Combustion for Clean and Efficient Use) (1993) 131-298.
- [186] C. Di Blasi, Fuel 76 (10) (1997) 957-964.
- [187] P. Raman; W. P. Walawender; L. T. Fan; J. A. Howell, Industrial & Engineering Chemistry Process Design and Development 20 (4) (1981) 630-636.
- [188] E. Biagini; F. Lippi; L. Petarca; L. Tognotti, Fuel 81 (8) (2002) 1041-1050.
- [189] A. Bharadwaj; L. L. Baxter; A. L. Robinson, Energy Fuels 18 (4) (2004) 1021-1031.
- [190] E. Kastanaki; D. Vamvuka; P. Grammelis; E. Kakaras, Fuel Processing Technology 77 (2002) 159-166.
- [191] C. Sheng; J. L. T. Azevedo, Proc. Combust. Inst. 29 (1) (2002) 407-414.
- [192] E. Biagini; F. Barontini; L. Tognotti, Ind. Eng. Chem. Res 45 (13) (2006) 4486-4493.
- [193] R. Zanzi; K. Sjöström; E. Björnbom, Biomass and Bioenergy 23 (5) (2002) 357-366.
- [194] S. Niksa, PROCEEDINGS-COMBUSTION INSTITUTE 28 (2) (2000) 2727-2734.
- [195] A. A. Rostami; M. R. Hajaligol; S. E. Wrenn, Fuel 83 (11-12) (2004) 1519-1525.
- [196] L. D. Smoot; P. J. Smith, *Coal combustion and gasification*. Plenum Press New York: 1985.
- [197] S. Godoy; K. Hirji; R. C. Lockwood; J. Miller, Combust. Sci. Tech. 44 (5) (1986) 319 - 335.
- [198] N. N. Semenov, Z. Phys. Chem 48 (1928) 571-582.
- [199] A. Adrover; F. Creta; M. Giona; M. Valorani, Chemical Engineering Science 62 (4) (2007) 1171-1183.
- [200] A. Molina; C. R. Shaddix, Proc. Combust. Inst. 31 (Pt. 2) (2007) 1905-1912.

- [201] J. M. Beer; N. A. Chigier, *Journal of the Institute of Fuel* 42 (347) (1969) 443-50.
- [202] J. M. Beer, *Journal of the Institute of Fuel* 37 (1964).
- [203] P. Wolanski; S. Wojcicki, *Proc. Combust. Inst.* 15 (1975) 1295-302.
- [204] N. Syred; J. M. Beér, *Combust. Flame* 23 (2) (1974) 143-201.
- [205] F. C. Lockwood; T. Mahmud, *Combust. Sci. Tech.* 66 (4) (1989) 319 - 328.
- [206] J. S. Truelove; D. Holcombe, *Proc. Combust. Inst.* 23rd (1991) 963-71.
- [207] J. P. Smart; R. Weber, *Journal of the Institute of Energy* 62 (453) (1989) 237-45.
- [208] S. P. Khare; T. F. Wall; A. Z. Farida; Y. Liu; B. Moghtaderi; R. P. Gupta, *Fuel* 87 (7) (2008) 1042-1049.
- [209] L. A. Rosendahl; C. Yin; S. K. Kaer; K. Friborg; P. Overgaard, *Biomass and Bioenergy* 31 (5) (2007) 318-325.
- [210] S. K. Kaer; L. A. Rosendahl; C. Yin; S. Berg; H. Junker, *Proceedings of the International Technical Conference on Coal Utilization & Fuel Systems 30th* (Vol. 2) (2005) 1191-1202.
- [211] C. Yin; L. Rosendahl; S. Knudsen Kaer; H. Sorensen, *Chemical Engineering Science* 58 (15) (2003) 3489-3498.
- [212] S. K. Kaer; L. Rosendahl; P. Overgaard in: *Numerical Analysis of Co-firing Coal and Straw in Utility Boiler at MIDTKRAFT ENERGY COMPANY, Denmark.*
- [213] L. Rosendahl; H. Soerensen; C. Yin; J. Eriksson, *Proceedings of the International Technical Conference on Coal Utilization & Fuel Systems 31st* (Vol. 2) (2006) 891-899.
- [214] F. Normann; K. Andersson; B. Leckner; F. Johnsson, *Fuel* 87 (17-18) (2008) 3579-3585.
- [215] K. Andersson; F. Normann; F. Johnsson; B. Leckner, *Industrial & Engineering Chemistry Research* 47 (6) (2008) 1835-1845.
- [216] J. A. Miller; C. T. Bowman, *Prog. Energy Combust. Sci.* 15 (4) (1989) 287-338.
- [217] C. T. Bowman, *Proc. Combust. Inst.* 24th (1992) 859-78.
- [218] L. L. Baxter; R. E. Mitchell; T. H. Fletcher; R. H. Hurt, *Energy & Fuels* 10 (1) (1996) 188-196.
- [219] D. W. Pershing; J. O. L. Wendt, *Proc. Combust. Inst.* 16 (1977) 389-99.
- [220] J. H. Pohl; A. F. Sarofim, *Proc. Combust. Inst.* 16 (1977) 491-501.
- [221] F. Chatel-Pelage; P. Pranda; N. Perrin; H. Farzan; S. J. Vecci, *Proceedings of the International Technical Conference on Coal Utilization & Fuel Systems 29th* (Vol. 1) (2004) 241-252.
- [222] J. O. L. Wendt; C. V. Sternling; M. A. Matovich, *Proc. Combust. Inst.* 14 (1) (1973) 897-904.
- [223] A. E. Weller; B. W. Rising; A. A. Boiarski; R. J. Nordstrom; R. E. Barrett; R. G. Luce *Experimental evaluation of firing pulverized coal in a CO<sub>2</sub>/O<sub>2</sub> atmosphere*; EDB-86-030601; 1985; p 342.
- [224] L. D. Smoot; Editor, *Fundamentals of Coal Combustion: For Clean and Efficient Use. [In: Coal Sci. Technol., 1993; 20].* 1993; p 755 pp.
- [225] Y. Hu; S. Naito; N. Kobayashi; M. Hasatani, *Fuel* 79 (15) (2000) 8.
- [226] L. D. Timothy; A. F. Sarofim; J. M. Beer, *Proc. Combust. Inst.* 19th (1982) 1123-30.
- [227] E. Croiset; K. V. Thambimuthu, *Fuel* 80 (14) (2001) 2117-2121.
- [228] H. Liu; R. Zailani; B. M. Gibbs, *Fuel* 84 (7-8) (2005) 833-840.
- [229] H. Liu; R. Zailani; B. M. Gibbs, *Fuel* 84 (16) (2005) 2109-2115.

- [230] K. W. Ragland; D. J. Aerts; C. Weiss, Bioenergy '96: Partnerships to Develop and Apply Biomass Technologies, Proceedings of the National Bioenergy Conference, 7th, Nashville, Sept. 15-20, 1996 1 (1996) 113-120.
- [231] D. J. Aerts; K. M. Bryden; J. M. Hoerning; K. W. Ragland; C. A. Weiss in: Proceedings of the American Power Conference., *Co-firing switchgrass in a 50 MW pulverized coal boiler*, 1997; pp 1180-1185.
- [232] V. Siegel; B. Schweitzer; H. Spliethoff; K. R. G. Hein in: Proceedings of the 9th European Bioenergy Conference, *Preparation and co-combustion of cereals with hard coal in a 500 kW pulverized-fuel test unit. Biomass for energy and the environment.* , 24-27 June, 1996; Copenhagen, Denmark, pp 1027-1032.
- [233] J. Brouwer; W. D. Owens; N. S. Harding; M. P. Heap; D. W. Pershing, Biomass Conference of the Americas: Energy, Environment, Agriculture and Industry, 2nd, Portland, Oreg., Aug. 21-24, 1995 (1995) 390-399.
- [234] J. Werther; M. Saenger; E. U. Hartge; T. Ogada; Z. Siagi, Prog. Energy Combust. Sci. 26 (1) (2000) 1-27.
- [235] J.-C. Chen; J.-S. Huang, Environmental Engineering Science 24 (3) (2007) 353-362.
- [236] B. M. Abraham; J. G. Asbury; E. P. Lynch; A. P. S. Teotia, Oil & Gas Journal 80 (11) (1982) 68-70, 75.
- [237] L. Bool; J. Bradley, *28th International Technical Conference on Coal Utilization and Fuel Systems* 2003.
- [238] L. Bool; H. Kobayashi; K. T. Wu; D. Thompson; E. Eddings; R. Okerlund; J. O. L. Wendt; M. Cremer; D. Wang, Proceedings - Annual International Pittsburgh Coal Conference 19th (2002) 2163-2175.
- [239] A. J. Mackrory; S. Lokare; L. L. Baxter; D. R. Tree, Proceedings of the International Technical Conference on Coal Utilization & Fuel Systems 32nd (Vol. 1) (2007) 109-119.
- [240] H. P. V. Kobayashi, NY), Bool III, Lawrence E. (East Aurora, NY), Snyder, William J. (Ossining, NY) NOx reduction in combustion with concentrated coal streams and oxygen injection. 2004.
- [241] A. Robinson; L. Baxter; H. Junker; C. Shaddix; M. Freeman; R. James; D. Dayton, BioEnergy '98, Oct (1998) 4-8.
- [242] D. W. Pershing; J. O. L. Wendt, Ind. Eng. Chem. Process Des. Dev. 18 (1) (1979) 60-67.

# Curriculum Vitae

## Scott A. Skeen

### PERSONAL

---

Date of Birth: 5 November 1978

Birthplace: Bend, Oregon

### EDUCATION

---

*Washington University in Saint Louis, Saint Louis, MO*

Ph.D. Energy, Environmental, and Chemical Engineering August 2009

M.S. Mechanical Engineering December 2007

B.S. Mechanical Engineering, *summa cum laude* May 2004

*The College of Idaho, Caldwell, ID*

B.A. Physics, *summa cum laude* May 2004

### PROFESSIONAL EXPERIENCE

---

#### Research

**Graduate Research Assistant**, Washington University in St. Louis, St. Louis, MO

*Department of Energy, Environmental, and Chemical Engineering* 8/2005-8/2009

**Control System Analyst**, *The Johns Hopkins University Applied Physics Laboratory, Laurel, MD*

Strategic Systems Department 8/2004-8/2005

**Undergraduate Research Assistant**, Washington University in St. Louis, St. Louis, MO

*Department of Mechanical Engineering* 6/2002-6/2004

#### Teaching

**Thermal Sciences Laboratory Instructor**, Washington University in St. Louis, St. Louis, MO

*Department of Mechanical, Aerospace, and Structural Engineering* 1/2006-12/2008

**Teaching Assistant**, Washington University in St. Louis, St. Louis, MO

*Department of Mechanical, Aerospace, and Structural Engineering* 1/2006-12/2008

**Mentor**, *NASA Missouri Space Grant Consortium*

2005-2008

### HONORS AND AWARDS

---

Dr. Lilia Abron Environmental Engineering Scholarship, 2006

President, Pi Tau Sigma Student Chapter, 2004

Pi Tau Sigma Mechanical Engineering Honorary, 2002-2004

Tau Beta Pi Student Service Award, 2004

The Gustav Mesmer Academic Achievement Award, 2004

Razek Prize for Outstanding Junior, 2003

Frank Dziama Memorial Scholarship, 2002-2003

Frank Mesmer Scholar 2002-2004

Dr. Frank Blood Memorial Award in Chemistry, 2001

Ralph and Merle Kyle Award in Math and Computer Science, 2001

Dean's List, 2000-2004

The College of Idaho Academic Athlete of the Year, 2002

Team Captain, College of Idaho Baseball, 2001-2002

NAIA Baseball All-American 2001-2002

NAIA Academic All-American 2000-2002

## PROFESSIONAL PUBLICATIONS AND PRESENTATIONS

---

- Skeen, S.A., Yablonsky, G., Axelbaum, R.L. "Structural effects on soot precursor kinetics resulting in soot-free flames", to be submitted *Combustion and Flame*.
- Skeen, S.A., Kumfer, B.M., Axelbaum, R.L. "Measurements of nitric oxide emissions during coal and coal/biomass combustion under air-fired and oxy-fuel conditions at 30 kWth", to be submitted *Energy and Fuels*
- Skeen, S.A., Yablonsky, G., Axelbaum, R.L. "Characteristics of non-premixed oxygen-enhanced combustion: I. The presence of appreciable oxygen at the location of peak temperature", *Combustion and Flame*, In Press.
- Kumfer, B.M., Skeen, S.A., Axelbaum, R.L. "Soot inception limits in laminar diffusion flames with application to oxy-fuel combustion", *Combustion and Flame*, 154, 546-556 (2008).
- Kumfer, B.M., Skeen, S.A., Chen, R., Axelbaum, R.L. "Measurement and analysis of soot inception limits of oxygen-enriched coflow flames", *Combustion and Flame*, 147, 233-242 (2006).
- Skeen, S.A., Kumfer, B.M., Axelbaum, R.L., "The effects of cofiring biomass with coal on NOx formation under air-fired and oxy-fuel conditions in a 20 kWth combustor", 6<sup>th</sup> U.S. National Combustion Meeting, Ann Arbor, MI, May 17-20, 2009
- Skeen, S.A., Kumfer, B.M., Axelbaum, R.L., "The effects of cofiring biomass with PRB coal on NOx formation under air-fired and oxy-fuel conditions", 34<sup>th</sup> International Technical Conference on Clean Coal and Fuel Systems, Clearwater, FL, May 31-June 4, 2009
- Skeen, S.A., Yablonsky, G., Axelbaum, R.L., "Effects of oxygen-enhanced combustion and fuel-dilution on the kinetics of soot formation in non-premixed flames of ethylene", 6<sup>th</sup> U.S. National Combustion Meeting, Ann Arbor, MI, May 17-20, 2009
- Skeen, S.A., Roisman, A.E., Holtmeyer, M.L., Axelbaum, R.L. "Flame stability in oxygen-enhanced combustion of coal", American Institute of Chemical Engineers Spring National Meeting, New Orleans, LA, April 6-10, 2008.
- Suriyawong, A., Skeen, S.A., Roisman, A.E., Axelbaum, R.L., Biswas, P.B. "Characterization of aerosol, mercury and trace elements under enriched oxygen coal combustion", American Institute of Chemical Engineers Annual Meeting, Salt Lake City, UT, November 4-9, 2007.
- Roisman, A.E., Holtmeyer, M.L., Skeen, S.A., Axelbaum, R.L. "Flame stability in oxygen-enhanced combustion of coal", American Institute of Chemical Engineers Annual Meeting, Salt Lake City, UT, November 4-9, 2007.
- Skeen, S.A., Axelbaum, R.L., "Modeling the effect of flame structure on the formation of aromatics in opposed flow diffusion flames", Eastern States Section Meeting of the Combustion Institute, Charlottesville, VA, October 21-24, 2007.
- Skeen, S.A., Kumfer, B.M., Axelbaum, R.L. "An experimental and theoretical approach to soot particle inception in laminar diffusion flames", 5<sup>th</sup> U.S. Combustion Meeting, San Diego, CA, March 25-27, 2007.
- Skeen, S.A., Kumfer, B.M., Axelbaum, R.L. "An experimental and theoretical approach to soot particle inception in laminar diffusion flames", 7<sup>th</sup> International Aerosol Conference, St. Paul, MN, September 10-15, 2006.